

Aus der **Neurologischen Universitätsklinik Heidelberg**
Abteilung: **Experimentelle Neuroradiologie**
Abteilungsleiterin: Prof. Dr. Sabine Heiland

In Kooperation mit dem
Deutschen Krebsforschungszentrum Heidelberg
Abteilung: **Radiologie**
Abteilungsleiter: Prof. Dr. Heinz-Peter Schlemmer

Development of methods, algorithms and applications
for the
robust and objective delineation of structures
in diffusion weighted MR images

Inauguraldissertation
zur Erlangung des Doctor scientiarum humanarum (Dr.sc.hum.)
an der
Medizinischen Fakultät Heidelberg
der
Ruprechts-Karls-Universität

vorgelegt von
Dirk Simon

aus
Trier
2011

Dekan: Prof. Dr. med. Claus R. Bartram
Doktormutter: Prof. Dr. rer. nat. Sabine Heiland

Abstract

Diffusion weighted imaging (DWI) derived parameters like the apparent diffusion coefficient (ADC) are known to correlate inversely to tumour-proliferation in brain tumours. In high grade gliomas, the heterogeneity makes it difficult to delineate high and low proliferative areas. Furthermore, this separation is impeded by partial volume effects and blurred borders. In addition to that, necrosis and cerebrospinal fluid increase the uncertainty of a proper delineation.

A second parameter derived by diffusion weighted imaging is the perfusion fraction f and can be used to differentiate pancreatic diseases like pancreatic carcinoma from healthy tissue and pancreatitis from pancreatic carcinoma, thanks to the hypoperfused nature of pancreatic carcinoma versus pancreatitis and healthy pancreatic tissue, respectively.

In this thesis, we present algorithms and approaches for these two cases to objectively determine the derived parameters. In the glioma case, an approach is presented to automatically delineate the mentioned heterogeneous regions and to probabilistically quantify the tissue inhomogeneity. Two methods were tested to achieve this aim. Firstly, a Gaussian mixture model, solely consisting of Gaussians and a partial volume aware technique using an additional class. Next, an Expectation Maximization algorithm has been applied onto these two models to separate these regions.

In the pancreatic case, we used linear rigid image registration, to spatially align the so called \mathbf{b} value stack, representing the diffusion raw data, and tried to improve the reproducibility of the derived parameters and the plausibility of the anatomical structure.

The results of the first study indicate that the Gaussian model excels the partial volume model in terms of reproducibility by using a systematic initialization routine automatically drawn onto the low and high-proliferative areas.

In the second study, we could show that linear image registration significantly improves the plausibility of the spatially alignment of the \mathbf{b} value stack and furthermore the reproducibility of the *IVIM* derived parameters such as f .

In conclusion, we can say that the first study yields an automatic, rapid, reproducible and objective determination of regions of signal inhomogeneity in high grade gliomas by an automatic initialization whereas the second study results in a reduction of residual motion and artifacts ending up in a degradation of the standard deviation of the perfusion fraction f to better delineate between the pancreatic entities. This leads to a development of a pancreatic screening tool which could be eventually expanded onto the usage of other organs.

1 Subtle is the Lord, but malicious He is not.

Albert Einstein

Contents

Abstract	II
2 Introduction	1
2.1 Aim and purpose	1
2.1.1 The reproducible determination of high- and low- proliferative areas in glioblastomas	2
2.1.2 The IVIM model and reproducible derived parameters	2
2.2 Motivation	2
2.3 Delineation to other works or scope of the thesis	3
2.3.1 The reproducible determination of high- and low- proliferative areas in glioblastomas	3
2.3.2 The IVIM model and reproducible derived parameters	4
2.4 Outline	4
3 Basics	5
3.1 Magnetic resonance imaging	5
3.1.1 Basics of MR imaging	5
History of MR imaging	6
Spins in MR imaging and analogy of a gyroscope	6
3.1.2 Relaxation	8
T_1 and T_2 relaxation	8
The Bloch equations	8
3.1.3 Image acquisition	9
The slice selection and the frequency encoding	9
The image reconstruction by the inverse Fourier transform ..	10
3.1.4 Imaging sequences	10
Spin echo sequence	10
Echo planar imaging	11
3.1.5 Signal to noise ratio and noise distribution	11

Signal to noise ratio	13
The noise dependence on the SNR	14
3.1.6 The partial volume effect	14
3.1.7 Diffusion weighted imaging	14
Basics of diffusion weighted imaging	15
Isotropic diffusion and scalar interpretation of diffusion	17
Anisotropic diffusion and tensorial interpretation of diffusion	19
Diffusion weighted imaging and brain tumours	20
Intravoxel incoherent motion model	22
Diffusion weighted imaging and pancreatic diseases	24
3.2 Image processing	25
3.2.1 ROI placement in heterogeneous tumours	26
3.2.2 Automatic and semi-automatic segmentation algorithms	27
Clustering as an example for a statistical algorithm	28
Adding spatial constraints by a Markov Random Field	30
3.2.3 Quantification	33
3.2.4 Validation of segmentation algorithms	35
Overlapping coefficients	35
Receiver operating characteristic curves	36
The intraclass coefficient	38
3.2.5 Medical image registration	39
Basics of rigid image registration	40
Monomodal image registration	41
Multimodal image registration	42
3.3 Tumour types	43
3.3.1 Brain tumours	43
3.3.2 Pancreatic tumours	47
4 Material and methods	51
4.1 Software development	51
4.1.1 A reproducible separation and quantification of high- and low-proliferative areas in gliomas	52
Illustration of the flow of information	52
Module based description	54
Realization	57
Including functional imaging such as perfusion as additional information	63
4.1.2 The IVIM model and reproducible derived parameters in diffusion weighted images	67
Illustration of the flow of information	67
Module based description	67

Realization	73
Application of the IVIM approach onto several organs	78
4.2 Preliminary experimental procedures	86
4.2.1 Design and theoretical workflow for a reproducible separation and quantification of high- and low-proliferative areas in gliomas	86
Principal flow of information	86
Including functional imaging such as perfusion as additional information.....	89
4.2.2 Design and theoretical workflow for the IVIM model and reproducible parameters in diffusion weighted images	90
Principal flow of information	90
Application of the IVIM approach onto several organs	91
The IVIM experimental values for the differentiation between pancreatitis and pancreatic carcinoma	94
4.3 Postprocessing	96
4.3.1 Application of the software for a reproducible separation and quantification of high- and low-proliferative areas in gliomas	96
Clustering	96
Probabilistic quantification	99
Application of the functional imaging technique such as perfusion as additional information.....	100
4.3.2 Application of the IVIM model and reproducible derived parameters in diffusion weighted images	102
Registration	102
Quantification	102
Evaluation	105
5 Results	106
5.1 A reproducible separation and quantification of high- and low-proliferative areas in gliomas.....	106
5.1.1 Indication of conservative ROIS and ADC distribution analysis	106
5.1.2 Qualitative evaluation.....	108
The GTV histogram model.....	108
Histogram clustering results	108
5.1.3 Quantitative evaluation	117
The GTV histogram model.....	117
Histogram clustering results	117
Statistical analysis of clustering results.....	120

Result of automatic initialization approach	122
5.1.4 Including functional imaging such as perfusion as additional information	122
Qualitative evaluation	122
Quantitative evaluation	122
5.2 The IVIM model and reproducible derived parameters	122
5.2.1 Evaluation of the intra-individual reproducibility	124
5.2.2 Evaluation of the plausibility	125
5.2.3 Application of the IVIM approach onto several organs	125
Adding an additional mono-exponential fitting routine and comparison to the IVIM fit	126
5.2.4 The IVIM experimental values for the differentiation between pancreatitis and pancreatic carcinoma	129
Qualitative evaluation	129
Quantitative evaluation	129
6 Discussion	134
6.1 Separation and quantification of high- and low-proliferative areas in glioblastomas	134
6.1.1 Interpretation of the results and limitations	134
6.1.2 Improvements of the used technique	138
6.1.3 Future research and practical applications	139
6.1.4 Conclusion	140
6.2 The IVIM model and reproducible derived parameters in diffusion weighted images	140
6.2.1 Interpretation of the results and limitations	141
Determining reproducible derived parameters and serial registration	141
The ducts and vessels segmentation	142
The IVIM fit	142
Adding an additional mono-exponential fitting routine	143
The IVIM experimental values for the differentiation between pancreatitis and pancreatic carcinoma	143
6.2.2 Improvements of results and future research	144
Determining reproducible derived parameters and serial registration	144
The ducts and vessels segmentation	144
The IVIM fit	144
The IVIM experimental values for the differentiation between pancreatitis and pancreatic carcinoma	145
Therapy issues concerning different organs	145

6.2.3 Conclusion	145
7 Summary	147
7.1 Quantitative parameters derived from diffusion weighted imaging	147
7.2 Reproducibility	148
7.3 Importance of this work for clinical applications	148
References	154
Own cited Contributions	163
Appendix	165
Curriculum Vitae	167
Acknowledgements	169

Introduction

Diffusion weighted imaging is a method of micro-anatomical imaging and has been vastly used in the brain and in the abdomen to yield surrogate parameters to monitor treatment response (Chenevert et al., 2000, Grünberg et al., 2011, Higano et al., 2006, Moffat et al., 2004, Riches et al., 2007). The exact, objective and reproducible derivation of these diffusion based parameters can be seen as a major goal of this thesis. As a matter of principle, the restriction, pertaining to the used technique, lays solely on **incoherent** motion, regarding the used intra voxel incoherent motion technique (IVIM), introduced by (Le Bihan et al., 1988, 2008). Where the microcirculation of blood, represented by the perfusion or parameter f , the combined diffusion and perfusion, represented by the so called ADC (Apparent diffusion coefficient or the averaged diffusion within a voxel) (Mori, 2007, Mori and Barker, 1999, Tofts, 2003) and the pure diffusion fraction D are being distinguished.

In the process, two major studies can be derived to obtain reproducible parameters. Firstly, a reproducible and objective determination of the ADC , reflecting the proliferation rate in heterogeneous high grade gliomas and secondly, the determination of reproducible parameters within pancreatic tumours and most importantly the perfusion fraction f , due to the hypoperfused nature of pancreatic tumours compared to healthy pancreatic tissue and pancreatic tumours compared to pancreatitis, respectively (Grünberg et al., 2011).

2.1 Aim and purpose

The aim and purpose of this study is firstly, to delineate objective reproducible parameters within heterogeneous high grade gliomas and secondly, to retrieve reproducible parameters in pancreatic diseases, such as pancreatic tumours and pancreatitis, respectively.

2.1.1 The reproducible determination of high- and low-proliferative areas in glioblastomas

For resections and biopsies and also chemoradiotherapy (Stadnik et al., 2001) concerning heterogeneous high grade gliomas, the objective and reproducible determination of the proliferation is a mandatory issue. This can be obtained by derivation of the inversely correlated ADC , regarding tissue cellularity (Simon et al., 2009). This delineation is impeded by partial volume effects, signal inhomogeneities and gliding borders due to the heterogeneity within high grade gliomas and between high grade gliomas and healthy tissue. This can be seen as a research niche and a challenging task (Moffat et al., 2004). Moreover, this delineation is especially useful, if oedema and necrotic areas are present within the heterogeneous tumour.

2.1.2 The IVIM model and reproducible derived parameters

The second study, pertaining to the *IVIM* model, aims at the determination of reproducible parameters considering the alignment of the single acquisitions, called the \mathbf{b} value stack, in different breathhold phases (Graf et al., 2010). This is being done to reduce residual motion by artifacts and to significantly improve the reproducibility of the derived parameters such as f . Furthermore, from a clinical point of view, the differentiation between pancreatic tumour versus healthy tissue on the one hand and pancreatitis versus pancreatic tumour on the other hand, plays, in terms of derived parameters by the *IVIM* model, an important role to ascertain an objective delineation.

2.2 Motivation

In his talk, Jones (2010a) emphasizes the importance of correct data by the statement 'Always look at your raw data'. He fills in on the background about the accuracy and objectivity of parameters derived by diffusion weighted imaging. The comparison between derived values plays an important role to strengthen the expressiveness of the quantitatively derived values.

Several issues concerning the objectivity and user independence are being described, such as 'distortion in spatially alignment of the images', and artifacts, such as eddy currents. The dependence on the measurement protocol, such as the \mathbf{b} value, if different acquisitions have to be compared, and moreover, systematic errors such as the signal to noise ratio.

He particularly draws his attention onto the ROI placement and its inherent dependency on the user, especially regarding large N and talks about a 'poor reproducibility' and the problems in isolating particular structures. However, he

also postulates advantages of manual ROI placements, such as the easy implementation and the transparency in explaining the work which has been done. Drawbacks are that the physician has to know where to look and has to use anatomical knowledge to draw the ROI, efficiently. This ROI drawing is tedious and can be errorprone, dependant on the to be designated structure. Furthermore, hard to delineate partial volume has to be excluded.

Similarly, the ROI issues are emphasized by Fallini (2010) and the tasks *reliability* and *repeatability* are being depicted which end up into a 'Development and validation of standardized systems for glioma recognition that will allow objective tumor identification and quantitative measurements' (Fallini, 2010). He postulates that this is especially important in the context of follow-up regarding therapy planning.

All these data issues lead to a strong motivation to develop *methods, algorithms and applications for the robust and objective delineation of structures in diffusion weighted MR images*, which is the title of this doctoral thesis.

2.3 Delineation to other works or scope of the thesis

The section delineates this work to other works in this field and defines the scope of the thesis of the two studies, separated in the glioma study ([Section 2.3.1](#)) and the pancreas study ([Section 2.3.2](#)).

2.3.1 The reproducible determination of high- and low-proliferative areas in glioblastomas

It should be clearly stated that we do not focus on the accuracy of the segmentation of the different areas of proliferation within the heterogeneous high grade gliomas due to a lack of a proper histopathological comparison or ground truth of the underlying proliferation within the tumour, in the glioma study. Instead, we try to derive objective and reproducible parameters derived by incoherent motion, reflecting the proliferation in inverse correlation by the *ADC*. This is being done by the application of a statistical soft clustering Expectation Maximization algorithm (Bishop, 2006, Dempster et al., 1977, Hastie et al., 2009).

The direct comparison can be only done in works where there is an underlying ground truth, such as white and grey matter segmentation as depicted in (Noe and Gee., 2001, van Leemput, 2001, van Leemput et al., 1999) while using similarity measures.

However, we also add an additional functional imaging technique such as *rCBV* (Giesel et al., 2005, Tofts, 2003) and tried to measure the overlap of the two competing modalities by application of a similarity measure and comparing two techniques.

2.3.2 The IVIM model and reproducible derived parameters

In this work, we try to derive reproducible parameters by the *IVIM* model and do not focus on an automatic segmentation of the pancreatic lesion. Instead, we try to improve the manual measurements of the physician by several techniques such as removing impeding ducts and vessels. But most importantly, we emphasize the delineation of the groups *pancreatic tumour*, *pancreatitis* and *healthy pancreatic tissue* by the improvement of the spatial alignment of the \mathbf{b} value stack by applying linear image registration.

2.4 Outline

This thesis is outlined as follows. First, in the basic chapter ([Section 3](#)), it fills in on the background of the main fundamental research topics, concerning the imaging technique from a physical point of view (*magnetic resonance imaging*), in basics like *image processing*, from a computer scientist's point of view and *tumour types*, from a medical point of view.

Second, the chapter material and methods ([Section 4](#)) covers the used experimental procedures to foster the two studies regarding objectivity and reproducibility concerning pancreatic diseases and brain tumours like gliomas. This chapter emphasizes the software development and is therefore mentioned as the first topic. Third, the results ([Section 5](#)) obtained by the two studies are given here and depict qualitatively and quantitatively derived statistical analyses.

Fourth, the discussion, regarding the two studies, is depicted in [Section 6](#) and fifth, a summary in [Section 7](#) sums up the major goals of this thesis, regarding the determination of incoherent flow parameters in diffusion weighted imaging, the reproducibility and objectiveness of the parameters and its value for clinical applications.

Basics

This basic chapter fills in on the background of the physics in [Section 3.1](#), explains the computer science related part in [Section 3.1](#) and closes with a chapter about tumour types ([Section 3.3](#)).

3.1 Magnetic resonance imaging

This chapter explains the basics of MR imaging ([Section 3.1.1](#)), including a historical timeline. Afterwards, fundamentals of MR imaging are described such as relaxation ([Section 3.1.2](#)), the image acquisition ([Section 3.1.3](#)), basically used sequences ([Section 3.1.4](#)), a short overview about the noise occurring in magnetic resonance imaging ([Section 3.1.5](#)) and closes with a succinct overview about the partial volume effect ([Section 3.1.6](#)).

This chapter finally ends with a thorough description about the here used functional imaging technique diffusion weighted imaging ([Section 3.1.7](#)).

3.1.1 Basics of MR imaging

Magnetic resonance imaging is an extraordinary versatile technique, providing a range of different weighting techniques (Hendee and Morgan, 1984, Mori and Barker, 1999, Tofts, 2003). In general, 5 weighting techniques can be differentiated which can be flexibly combined to perform multimodal acquisitions to end up in a multispectral qualitative and quantitative analysis of the subject.

1. The spin density or proton density ([Section 3.1.2](#)) (Tofts, 2003).
2. T_1 relaxation or longitudinal relaxation ([Section 3.1.2](#)) (Tofts, 2003).
3. T_2 relaxation or transversal relaxation ([Section 3.1.2](#)) (Tofts, 2003).
4. Motion
 - a) Flow shifts, such as flow motion (MR angiography (Lettau et al., 2011) such as time of flight imaging TOF (coherent motion), phase contrast or contrast enhanced angiography)

- b) Incoherent motion, such as diffusion or microperfusion (Le Bihan et al., 1988, 2008, Mori and Barker, 1999, Tofts, 2003) (Section 3.1.7) (DSCE (Dynamic susceptibility contrast enhanced), DCE (Dynamic contrast enhanced) and derived imaging techniques like functional BOLD MRI (Blood oxygen level dependency) (Tofts, 2003) or SWI (Susceptibility weighted imaging) (Haacke et al., 2009).
5. Spectral shifts such as NMR spectroscopy (Tofts, 2003).

History of MR imaging

The magnetic resonance phenomenon has been discovered independently in 1946 by Felix Bloch and Edward Purcell (Hornak, 2011). They have been awarded by the Nobel prize for this invention in 1952. However, the first publication in the field of magnetic resonance imaging, depicting the nuclear magnetism on the magnitude of deflection (Hendee and Morgan, 1984), is Rabi et al. (1939). The first spin-echo measurements (Hahn, 1950) have been pursued to lay the principles of diffusion weighted imaging (Section 3.1.7). The first tumour detection in the rat by magnetic resonance imaging, using T_1 and T_2 relaxation, respectively, has been elucidated by Damadian (1971). The first real MR images of a human finger, however, have been produced by Mansfield and Maudsley (2011).

Spins in MR imaging and analogy of a gyroscope

In Mori and Barker (1999), the NMR phenomenon is explained by the analogy of a gyroscope (Figure 3.1) and depicts the *spin* derived from quantum mechanics. The spin quantum number depicts 'how much spin the protons have' and only half-integer spin numbers can be used in magnetic resonance imaging. The most prominent nucleus is hydrogen and has a spin number of $\frac{1}{2}$. It behaves like a small dipolar magnet and can be aligned by an externally applied magnetic field B_0 (Tofts, 2003).

Application of a magnetic field B_0

By application of an external magnetic field B_0 , the protons align either in parallel direction (low energy state) of the field or antiparallel (high energy state) obeying quantum mechanics (Figure 3.2). In the process, the parallel state is preferred. Moreover, the angular momentum begins to precess according to the so called 'Lamor frequency' which is given in Equation 3.1. The gyromagnetic ratio γ is dependant on the given proton. It can be clearly seen that ω_0 is directly dependant on B_0 and for hydrogen it is depicted by 42.58 MHz or $2.68 \cdot 10^8 \text{ rad s}^{-1} \text{ T}^{-1}$.

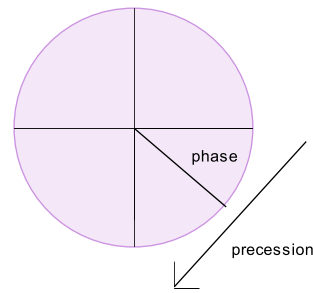


Fig. 3.1: Position of the gyroscope with projection to the horizontal plane. The phase is described by ω (adapted from Mori and Barker (1999)).

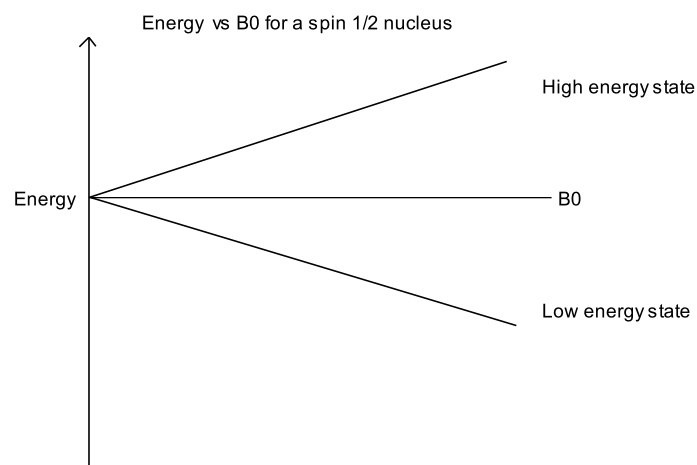


Fig. 3.2: Affect of the bulk magnetization onto the proton. The proton switches either into the parallel (low energy) or antiparallel (high energy) state according to quantum mechanics (adapted from Tofts (2003))

$$\omega_0 = \gamma \cdot B_0 \quad (3.1)$$

Application of a perpendicular field B_1

Next, a magnetic field perpendicular to B_0 is being applied with angular velocity $\omega = \omega_0$. To switch between the two states, an energy of ΔE has to be induced, which is given by Equation 3.2, where \hbar depicts Planck's constant and ν_0 the Lamor frequency.

By a short application of this high frequency pulse (HF field), the magnetization is being flipped into the transverse plane. First, starting to precess around B_0 and B_1 and then flipping completely to B_1 . The detectable signal is being

measurable through the time-dependant effect by Faraday's law which is eventually being transformed to the image (Haacke et al., 1999). Furthermore, important to note is that the so called isochromats, consisting of a volume containing a large number of spins, are now precessing *in phase* (Tofts, 2003).

$$\Delta E = \hbar \cdot \nu_0 \quad (3.2)$$

3.1.2 Relaxation

In this chapter, MR specific characteristics like the ' T_1 and T_2 relaxation' and the 'Bloch equations' are being described.

T_1 and T_2 relaxation

Immediately, after the excitation, the relaxation process begins and the system is trying to move into the state of equilibrium. Thereby, two different processes of relaxation are being distinguished (Tofts, 2003).

1. The T_1 relaxation, where the energy is being transported back to the lattice (*spin-lattice relaxation*). The z component of the signal is being recovered.
2. The T_2 relaxation, where the energy is going back into the spin-system (*spin-spin relaxation*) and the isochromats lose its phase coherence. This relaxation process is a lot faster than T_1 .

The whole relaxation process is depicted by the Bloch equations (Equation 3.3) (Haacke et al., 1999), where M_x, M_y, M_z depict the transversal (M_x, M_y) and the longitudinal relaxation M_z . M_0 describes the equilibrium longitudinal relaxation (Tofts, 2003) and ω_0 determined by the resonance frequency. The original Bloch equations are thoroughly depicted in Bloch (1946).

Visually, the whole relaxation process can be explained by a 'corkscrew' trajectory (Haacke et al., 1999).

The Bloch equations

$$\begin{bmatrix} \frac{\partial M_z}{\partial t} = \frac{M_0 - M_z}{T_1} \\ \frac{\partial M_x}{\partial t} = \omega_0 \cdot M_y - \frac{M_x}{T_2} \\ \frac{\partial M_y}{\partial t} = -\omega_0 \cdot M_x - \frac{M_y}{T_2} \end{bmatrix} \equiv \begin{bmatrix} \dot{M}_z = \gamma(M_x B_y - M_y B_x) - \frac{M_z - M_0}{T_1} \\ \dot{M}_x = \gamma(M_y B_z - M_z B_y) - \frac{M_x}{T_2} \\ \dot{M}_y = \gamma(M_z B_x - M_x B_z) - \frac{M_y}{T_2} \end{bmatrix} \quad (3.3)$$

The two processes are completely different and depend on molecular structure and chemical composition. The relationship between T_1 and T_2 can be depicted by Equation 3.4.

$$T_2 \leq T_1 \quad (3.4)$$

The longitudinal relaxation

By solving the Bloch equation (Equation 3.3), the longitudinal relaxation is depicted as given in Equation 3.5.

$$M_z(t) = M_0(1 - e^{-\frac{t}{T_1}}) + M_z(0)e^{-\frac{t}{T_1}} \quad (3.5)$$

The transversal relaxation

The T_2 relaxation can be described by an exponential decay, obeying Equation 3.6.

$$S(t) = S_0 \cdot e^{-\frac{t}{T_2}} \quad (3.6)$$

3.1.3 Image acquisition

The spin density $\rho(z)$ of a sample, dependant from the measurement of the signal as a function of time is the object of imaging (Haacke et al., 1999).

By applying linearly varying fields, also called gradients, the signal can be encoded to be later transformed by an inverse Fourier transformation to the image (Haacke et al., 1999).

The slice selection and the frequency encoding

The slice encoding is being performed by application of a linearly varying gradient in z direction resulting in a selective excitation of different slices z obeying Equation 3.7 (Haacke et al., 1999). This is called frequency encoding and is also applied in x direction, thus resulting in Equation 3.8. Similarly, the phase encoding is being performed by usage of Equation 3.9.

$$\omega(z, t) = \omega_0 + \omega_G(z, t) \quad (3.7)$$

$$\omega(x, t) = \omega_0 + \omega_G(x, t) \quad (3.8)$$

$$\omega(y, t) = \omega_0 + \omega_G(y, t) \quad (3.9)$$

The image reconstruction by the inverse Fourier transform

These three encoding schemes, depicted in Equation 3.7, Equation 3.8 and Equation 3.9 create the so called k -space. The spin density or the signal intensity $\rho(z)$ of a slice z can be explained by performing $\mathcal{F}^{-1}(s(k))$, where $s(k)$ depicts the signal in k -space. This process is thoroughly described by Equation 3.10.

$$\rho(z) = \int s(k)e^{+i2\pi kz} dk \quad (3.10)$$

3.1.4 Imaging sequences

In this section, common imaging sequences such as the 'Spin echo sequence' and 'Echo planar imaging' are being described.

Spin echo sequence

An illustration of a multi echo sequence, derived from the original spin echo sequence by Hahn (1950), is given in Figure 3.3 and includes the following consecutive steps:

1. Generate a maximum signal by application of a 90° pulse.
2. The so called *FID* (Free induction decay) is decaying within the short time T_2^* after the application of the 90° pulse and depends on additional effects $R' = \frac{1}{T_2'}$ which are being generated by inhomogeneous processes relating to B_0 .
3. Application of a 180° pulse to rephase the isochromats. The signal now only depends on irreversible effects denoted as time T_2 .
4. The maximum signal is being retrieved at time TE , where the complete synchronization occurs (Figure 3.3).

$$\frac{1}{T_2^*} = \frac{1}{T_2} + \frac{1}{T_2'} \quad (3.11)$$

For filling a k space consisting of $N \times N$ lines and columns, we need a repetition of the experiment for 256 times and are waiting for T_R . Several tissue contrasts can be generated by modifying T_E the echo time, and T_R the repetition time denoted as follows:

- Short T_E and short T_R generates a T_1 weighted image.
- Long T_E and long T_R generates a T_2 weighted image.
- Short T_E and long T_R is governed by the spin-density only.

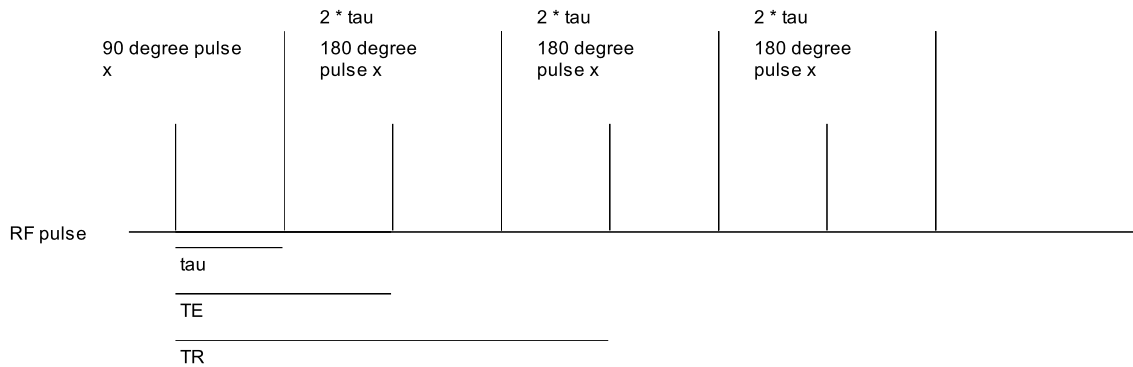


Fig. 3.3: A spin echo train by Carr and Purcell (1954) (adapted from Tofts (2003))

Echo planar imaging

The echo planar imaging sequence is a fast imaging sequence to reflect processes such as diffusion and perfusion effects. It is often used as a so called gradient sequence where gradients are being applied to generate the echo and not the used 180° pulse and was introduced by Mansfield and Maudsley (2011). It is able to cover an image within one second and one excitation. This technique can cover the k space in a 'line-by-line' way using a 'forward, backward' technique to end up in a more efficient technique (Haacke et al., 1999).

The contrast is governed by spin-density and T_2^* alone and no T_1 dependency occurs. To also gain T_1 weighted contrast, the experiment has to be repeated with repetition time T_R (Haacke et al., 1999).

Typically for the nature of gradient echo sequences is that a gradient is being applied to generate gradient echos for dephasing and rephasing (G_R). The slice selection gradient G_{SS} is selecting the slice and performs a 'fan-out' of the spin phases. The negative application of G_{SS} inverses this dephasing by rephasing for half of the dephasing time. The phase-encoding gradient G_{PE} changes the line in k space. It is called a 'blib' (Haacke et al., 1999).

The complete k space coverage is being illustrated in [Figure 3.5](#). The phase change is illustrated by the vertical arrows.

3.1.5 Signal to noise ratio and noise distribution

In this chapter the noise distribution in magnetic resonance imaging is being described in further detail. First, the signal to noise ratio is denoted in 'Signal to noise ratio' and second, 'The noise dependence on the SNR'.

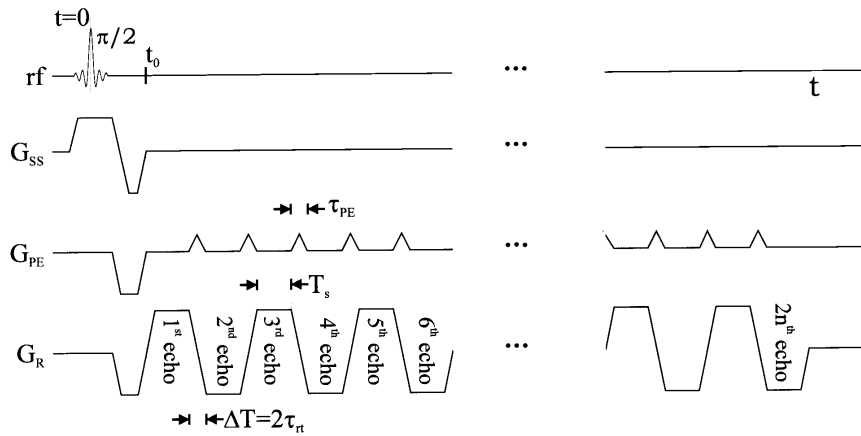


Fig. 3.4: The echo planar sequence (EPI) (Carr and Purcell, 1954), taken from Haacke et al. (1999)

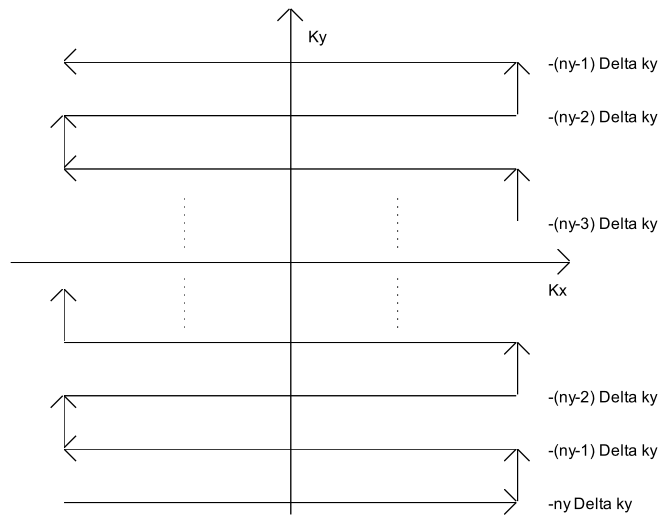


Fig. 3.5: The echo planar sequence (EPI) and the k space coverage (adapted from Haacke et al. (1999))

Signal to noise ratio

This section is subdivided into a theoretical and practical part to determine the signal to noise ratio. Firstly, the 'Theoretical determination of signal to noise ratio' and secondly, 'Practical aspects of determining the signal to noise ratio'.

Theoretical determination of signal to noise ratio

The systematic errors occurring during MR measurements can be quantitatively depicted by the SNR which describes the so called *Signal to Noise Ratio*. Interestingly, Haacke et al. (1999) explains that every factor of an improvement of $\sqrt{2}$ doubles the directional resolution and has therefore a tremendous impact onto the image quality.

Especially, when dealing with quantitative measurements, and more importantly, when reproducible measurements are being derived, the improvement of the SNR plays an important role. For reproducible diffusion based parameter estimation in particular, the SNR has an important impact on the determination of these values.

The SNR is depicted by Equation 3.12, where $\Delta x, \Delta y, \Delta z$ describe the voxel dimensions, N_{acq} the number of samples in k space in directions N_x, N_y, N_z and BW the bandwidth (Haacke et al., 1999). The SNR dependant on k can be determined by considering Equation 3.13, where $\sigma_m(k)$ denotes the noise variance and $s(k)$ the signal.

$$\frac{SNR}{voxel} \propto \frac{\Delta x \Delta y \Delta z \sqrt{N_{acq}}}{\sqrt{\frac{BW_{read}}{N_x N_y N_z}}} \quad (3.12)$$

$$SNR(k) = \sqrt{N_{acq}} \frac{s(k)}{\sigma_m(k)} \quad (3.13)$$

Practical aspects of determining the signal to noise ratio

According to Haacke et al. (1999), the SNR can be measured by dividing the retrieved μ of a signal in a region of interest S through a region with zero signal and complete noise, denoted by σ_0 .

$$SNR = \frac{S}{\sigma_0} \quad (3.14)$$

The noise dependence on the SNR

The noise occurring during image acquisition is dependant on the *Signal to Noise Ratio* or *SNR*. At low *SNR*, the noise is governed by a *Rayleigh distribution* whereas a high *SNR* turns out to be *Gaussian* (Tofts, 2003).

These distributions are completely described by a Rice distribution (Goodlett et al., 2007) (Equation 3.16), where R depicts the noise measurement, A the signal and σ^2 the noise variance. I_0 is the modified Bessel function of the first kind. The noise is depicted by pure Johnson noise in the real and imaginary components of the k space (Equation 3.15), explained by X and Y .

$$R = \sqrt{(A + X)^2 + Y^2}, X, Y \sim N(0, \sigma^2) \quad (3.15)$$

$$f(x|A, \sigma) = \frac{x}{\sigma^2} \cdot e^{-\frac{x^2+A^2}{2\sigma^2}} I_0\left(\frac{xA}{\sigma^2}\right) \quad (3.16)$$

3.1.6 The partial volume effect

The partial volume effect is a common issue, occurring during MR imaging and depicts the facts that voxels in the image can be a mixture of relative fractions of different tissue classes (Noe and Gee., 2001). Due to the discretization of the image matrix, these effects occur while trying to reflect fine details within the anatomical structure.

This has a tremendous effect onto derivation of quantitative parameters within images and can be minimized by using smaller voxels although the signal to noise ratio is being corrupted in these cases (Tofts, 2003). Another approach is given in Noe and Gee. (2001) and assumes a mixed model, consisting of a mixture of pure tissue. Over this histogram, the probability density can be marginalized to reduce this occurring partial volume effect.

3.1.7 Diffusion weighted imaging

The section elucidates the topic diffusion weighted imaging. Firstly, the basics are being described in 'Basics of diffusion weighted imaging', next, an 'Isotropic diffusion and scalar interpretation of diffusion' is given, explains 'Anisotropic diffusion and tensorial interpretation of diffusion' and eventually 'Diffusion weighted imaging and brain tumours'.

Basics of diffusion weighted imaging

This section fills in on the background of diffusion weighted imaging. It entails a historical wrap up of the developments in 'Historical development of diffusion weighted imaging and Fick's law' and 'The Stejskal-Tanner sequence and \mathbf{b} value'.

Historical development of diffusion weighted imaging and Fick's law

Diffusion weighted imaging is a method of microanatomical imaging and has been developed in 1965 by Stejskal and Tanner (Mori, 2007, Stejskal and Tanner, 1965, Tofts, 2003). Although, the first measurements were done by Hahn in 1950 (Hahn, 1950) and Carr and Purcell (1954) made experiments to eliminate the occurring diffusion by oscillating gradients. It has been introduced into clinical practice in the 1990th (Mori and Barker, 1999) and reflects the Brownian molecular motion of water. In Mori (2007), it is also called intra-voxel incoherent motion (IVIM) and its effect is a phase disruption by water motion onto the MR signal but measured as a signal loss (Mori, 2007). It has to be differentiated from *bulk motion*, such as moving the head in the scanner and flow motion with a direction (Mori, 2007) (coherent motion) which results in a phase-shift. Hence, the measured diffusion is not the motion in x -direction. Instead, it can be described as the diffusion along the x -axis (Jones, 2010b). A good illustration is a drop of ink into water and this self diffusion obeys a Gaussian distribution. This mean square displacement can be described by Einstein's equation (Laun et al., 2011, Mori, 2007) (Equation 3.17) where D_0 depicts the free diffusion constant and t the time. If we extract the root, we can derive σ , yielding the mean diffusion distance. This Gaussian probability density is depicted as given in Equation 3.18. A good derivation of this equation is given in Laun et al. (2011).

$$\langle x^2 \rangle = 2D_0 \cdot t \quad (3.17)$$

The central limit theorem (Elpelt and Hartung, 1992) yields that the probability density of the mean square displacement or the expectation value $\langle x^2 \rangle$ obeys a Gaussian distribution.

Fick's first law (Equation 3.19) was introduced in 1855 and depicts the analogy between heat conduction and diffusion, where F is the rate of transfer of the diffusion distance, through the unit area of the section and C depicts the concentration of the diffusion substance. x can be seen as a coordinate in space. One dimensional diffusion processes can be determined by Fick's second law (Equation 3.20).

Considering all three dimensions, we can use ∇ to describe the diffusion in all three dimension x , y and z , thus leading to Equation 3.21 (Tofts, 2003).

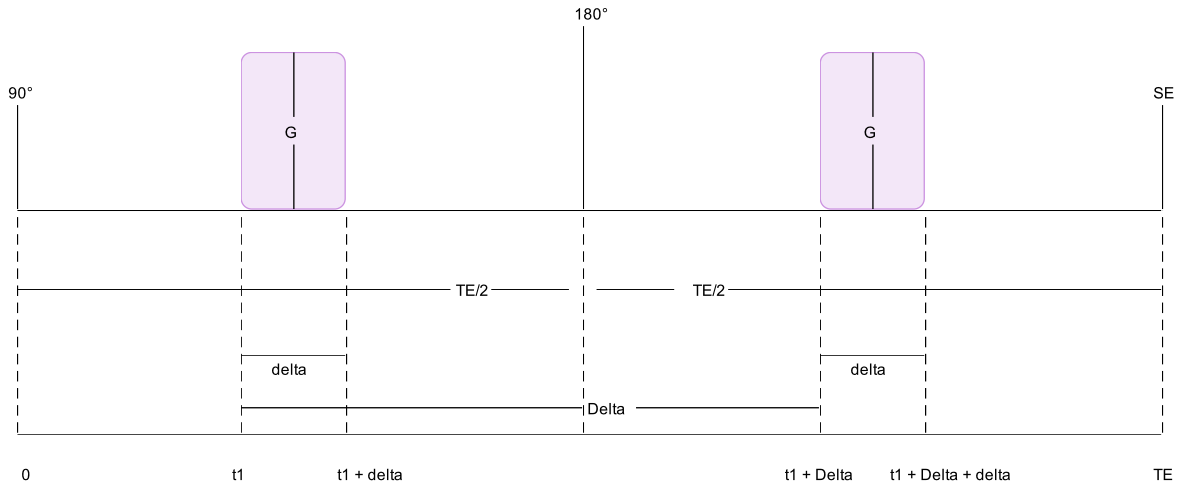


Fig. 3.6: The Stejskal Tanner Sequence (Stejskal and Tanner, 1965) (adapted from Tofts (2003))

$$P(x, t) = \frac{1}{\sqrt{4\pi D \cdot t}} \cdot e^{-\frac{x^2}{4Dt}} \quad (3.18)$$

$$F = -D \frac{\partial C}{\partial x} g t \quad (3.19)$$

$$\frac{\partial C}{\partial t} = D \cdot \frac{\partial^2 C}{\partial x^2} \quad (3.20)$$

$$\frac{\partial C}{\partial t} = D \left(\frac{\partial^2 C}{\partial x^2} + \frac{\partial^2 C}{\partial y^2} + \frac{\partial^2 C}{\partial z^2} \right) = D \cdot \nabla^2 C \quad (3.21)$$

The Stejskal-Tanner sequence and b value

The Stejskal-Tanner sequence (Figure 3.6) is described in (Stejskal and Tanner, 1965, Tofts, 2003). The crucial point of this sequence is that we have pulsed gradients in a spin echo sequence in contradiction to the experiments by (Carr and Purcell, 1954, Hahn, 1950).

The different steps can be explained as follows:

1. In the first step (0 to t_1), there is no gradient application and the signals are in phase.
2. The second step (t_1 to $t_1 + \delta$) consists of a gradient application where the phase of the signals is being dispersed with the gradient application (duration δ and strength G).
3. The 180 degree pulse inverts the phase.
4. The second gradient application $t_1 + \Delta$ to $t_1 + \Delta + \delta$ is subsequently being applied in the opposite direction but with the same magnitude.
5. The phase of the static spins, which have changed during time Δ , can be refocused completely but the spins with incoherent motion cannot be refocused and thus result in a loss of signal.

The **b** factor or **b** value can be calculated by [Equation 3.22](#) and can be seen as motion sensitization of the applied gradient scheme (Le Bihan et al. (2008)). It consists of γ the gyromagnetic ratio, G the gradient strength or amplitude of the spin echo (Tofts, 2003), δ the gradient application time or diffusion time and Δ the interpulse delay (Tofts, 2003).

$$b = \gamma^2 \cdot G^2 \cdot \delta^2 \cdot \left(\Delta - \frac{\delta}{3} \right) \quad (3.22)$$

An exact derivation of the **b** factor can be found in Mori (2007).

Isotropic diffusion and scalar interpretation of diffusion

The quantification of diffusion in a scalar way and the definition of the signal loss is denoted by [Equation 3.24](#). It depicts the so called *ADC*, the apparent diffusion coefficient, denoted as D .

$$\frac{S}{S_0} = e^{-\gamma^2 \delta^2 G^2 (\Delta - \frac{\delta}{3}) \cdot D} \Leftrightarrow \quad (3.23)$$

$$\ln \left(\frac{S}{S_0} \right) = -b \cdot D \quad (3.24)$$

This diffusion coefficient depicts the average diffusion (in the extracellular and intracellular space (Le Bihan, 2003)) in a voxel and is usually represented as a so called diffusion map or *ADC* map. At least two diffusion measurements are necessary to calculate this *ADC* which is essentially the slope of [Equation 3.24](#). However, the calculation of an *ADC* measurement of one gradient vector and in one direction is not enough if anisotropic effects have to be considered. Hence, the trace ([Equation 3.25](#)) can be calculated by measuring the mean *ADC* in all three gradient vector applications.

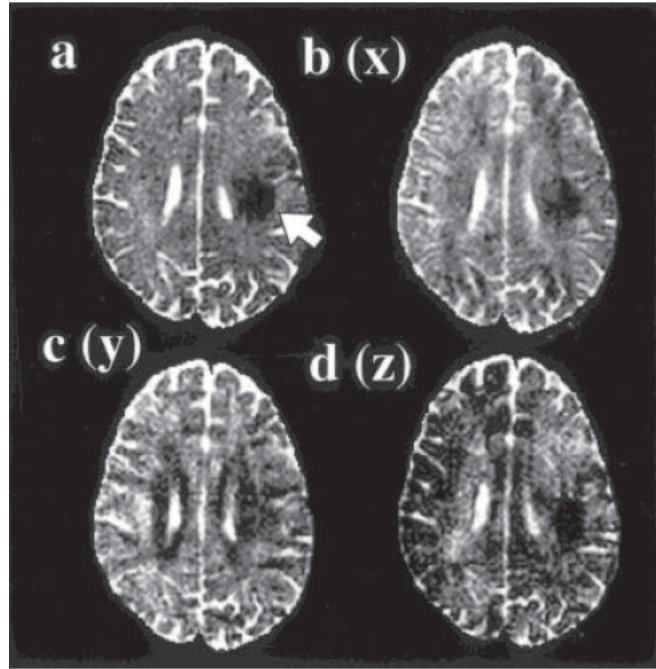


Fig. 3.7: Brain anisotropy of ischaemic stroke (taken from Mori and Barker (1999)). (a) The combined trace image calculated by Equation 3.25, (b) Single ADC measurement with application of the gradient in x direction, (c) ADC measurement with application of the gradient in y direction, (d) ADC measurement with application of the gradient in z direction.

In Figure 3.7, an ischaemic stroke is depicted while considering anisotropic effects. It can be clearly seen that the application of one gradient is not enough to detect the ischaemic stroke, visible by the dark patch.

To calculate this map, we need a direction independent measurement with an application of a b_0 weighted gradient. However, an application of an absolute b_0 measurement is often practically not feasible. There is always a small amount of diffusion weighting left. Hence, if anisotropic effects can be neglected like depicted in Figure 3.7, two arbitrary \mathbf{b} weighted images are enough to calculate the ADC map (Mori (2007)).

$$\langle ADC \rangle = \frac{-1}{3} \cdot \frac{\ln\left(\frac{S_x}{S_0}\right) + \ln\left(\frac{S_y}{S_0}\right) + \ln\left(\frac{S_z}{S_0}\right)}{b} \quad (3.25)$$

To improve the signal to noise ratio (SNR), an array of different measurements with different \mathbf{b} values can be made and thus the ADC can be calculated by applying a linear fitting to the signal loss equation (Equation 3.24).

Anisotropic diffusion and tensorial interpretation of diffusion

Anisotropic diffusion considers the effect of directionality and carries information about ordered environment. In the isotropic case, the information of the diffusion is described by one value, the diffusion constant ADC and is related to the diameter of a sphere. In the anisotropic case, however, diffusion is explained as an ellipsoid and can be explained by a so called diffusion tensor. By this tensor, the underlying anatomical architecture and more specifically the fiber integrity can be described (Equation 3.26) (Mori, 2007).

The parameters of the resulting ellipsoid can be described by $\lambda_1, \lambda_2, \lambda_3, v_1, v_2, v_3$ after a procedure called 'diagonalization' (Mori, 2007). $\lambda_1, \lambda_2, \lambda_3$ define the shape of the ellipsoid and v_1, v_2, v_3 the principal orientations. They form an orthonormal basis of eigenvalues and eigenvectors, thus resulting in Equation 3.27.

$$D = \begin{pmatrix} D_{xx} & D_{xy} & D_{xz} \\ D_{yx} & D_{yy} & D_{yz} \\ D_{zx} & D_{zy} & D_{zz} \end{pmatrix} \quad (3.26)$$

$$D' = \begin{pmatrix} \lambda_1 & 0 & 0 \\ 0 & \lambda_2 & 0 \\ 0 & 0 & \lambda_3 \end{pmatrix} \cdot \begin{pmatrix} v_1 \\ v_2 \\ v_3 \end{pmatrix} \quad (3.27)$$

The crucial point of these derived parameters by the diffusion tensor is that they are intrinsic properties of the underlying anatomical reference which do not depend on the applied gradient coordinate system (Tofts (2003)). It is a symmetric tensor with 6 independent elements, namely $D_{xx}, D_{yy}, D_{zz}, D_{xy}, D_{xz}, D_{yz}$. The first three elements depict the ADC values in x, y and z direction, respectively and the last three off diagonal elements contain information about the rotation of the tensor.

6 weighted plus 1 unweighted measurement ($S_x, S_y, S_z, S_{x+y}, S_{x+z}, S_{y+z}$) and S_0 , respectively, have to be performed to generate this diffusion tensor (Mori, 2007).

$$\gamma^2 \cdot \delta^2 \left(\Delta - \frac{\delta}{3} \right) \vec{G}^T \cdot \begin{pmatrix} D_{xx} & D_{xy} & D_{xz} \\ D_{yx} & D_{yy} & D_{yz} \\ D_{zx} & D_{zy} & D_{zz} \end{pmatrix} \cdot \vec{G} \quad (3.28)$$

They can be determined by applying Equation 3.27. E.g., D_{xz} can be calculated by applying Equation 3.29.

$$\frac{S_{xz}}{S_0} = e^{-\gamma^2 \delta^2 (\Delta - \frac{\delta}{3})(G_x^2 D_{xx} + 2 \cdot G_x G_z D_{xz} + G_z^2)} \quad (3.29)$$

Furthermore, the element vector of the diffusion tensor \vec{D} can be determined by linear least squares application on the signal vector \vec{S} and by using the gradient application matrix X , thus resulting in Equation 3.30.

$$\vec{D} = (X^T \cdot X)^{-1} \cdot X^T \cdot \frac{1}{b} \ln \left(\frac{\vec{S}}{S_0} \right) \quad (3.30)$$

The scalar rotationally invariant properties of the diffusion tensor can be described as mean diffusivity (MD) or as the mean ADC ($\langle ADC \rangle$) (Tofts, 2003).

$$\langle \lambda \rangle = \frac{\lambda_1 + \lambda_2 + \lambda_3}{3} = \frac{Trace}{3} \quad (3.31)$$

$$\langle ADC \rangle = \frac{ADC_x + ADC_y + ADC_z}{3} \quad (3.32)$$

Moreover, the FA (Basser and Pierpaoli, 1996, Jones, 2010b) or fractional anisotropy is proportional to the square root of the variance of the eigenvalues divided by the square root of the sum of the squares of the eigenvalues. Fully isotropic diffusion can be described with a value of 0 whereas completely anisotropic diffusion will have a value of 1. It quantitatively describes the amount of $\langle \lambda \rangle$ due to anisotropic diffusion (Tofts (2003)).

$$FA = \beta \cdot \sqrt{\frac{(\lambda_1 - \langle \lambda \rangle)^2 + (\lambda_2 - \langle \lambda \rangle)^2 + (\lambda_3 - \langle \lambda \rangle)^2}{\lambda_1^2 + \lambda_2^2 + \lambda_3^2}} \equiv \frac{\sigma_\lambda}{\lambda_{rms}} \quad (3.33)$$

$$\text{whereas } \beta = \sqrt{\frac{3}{2}} \quad (3.34)$$

$$(3.35)$$

Diffusion weighted imaging and brain tumours

This sections fills in on the background of diffusion weighted imaging and brain tumours. Firstly, the 'Importance of the ADC and application as a surrogate

marker', the 'Drawbacks concerning the usage of the *ADC* and separating different areas in brain tumours', and closes with 'Using more sophisticated parameters derived by diffusion tensor imaging' like the fractional anisotropy (*FA*) and finally describes 'Diffusion weighted imaging and pancreatic diseases'.

Importance of the ADC and application as a surrogate marker

In brain tumours, the measured *ADC* by applying the microanatomical functional imaging technique of diffusion weighted imaging, represents a surrogate marker. It has been shown that it increases after successful application of chemotherapy, radiotherapy or a combination of both and is also important for resections and biopsies (Stadnik et al., 2001).

The *ADC* indicates high cellular density and increased proliferation within a voxel whereas a high *ADC* is related to low cellular density and low proliferation (Chenevert et al., 2000, Moffat et al., 2004).

Drawbacks concerning the usage of the ADC and separating different areas in brain tumours

However, the mean *ADC* is also increased by water retention, e.g. caused by oedema or necrosis. In human brain tumours and especially in high grade gliomas, areas of high and low proliferation, oedema and necrosis are present within the tumour area and the boundaries between these regions are ill defined. This tissue heterogeneity remains a major challenge for the *ADC* as measure of cellular density in gliomas (Moffat et al., 2004). (Brunberg et al., 1995, Tien et al., 1994) report that a separation between these different heterogeneous areas is possible considering a separation between cystic, necrotic and solid tissue (Brunberg et al., 1995). In Tien et al. (1994), it is reported that a separation between progressive and non-progressive tumour could not be found (Simon et al., 2009).

However, the mean *ADC* cannot be used to differentiate various types of tumours considering gliomas, metastatic tumours and meningiomas (Fallini, 2010, Kono et al., 2001).

Using more sophisticated parameters derived by diffusion tensor imaging

Considering the usage of the fractional anisotropy (*FA*), there is no clear message concerning tumour cellularity. However, the tumour cell infiltration of white matter can be described by a low *FA* value. Especially for the pyramidal tract adjacent to brain tumours (Fallini, 2010, Stadlbauer et al., 2007).

Additionally, (Fallini, 2010, Price et al., 2001) describe a better delineation of the margins around gliomas and also white matter infiltration by the *FA*.

Final message

To sum up, it can be said that the *ADC* can be seen as a probable surrogate marker for brain tumours. However, the delineation between heterogeneous areas seems to be challenging due to ill defined regions. The *FA* can be used to build hypotheses about the infiltration of white matter. However, it cannot be used to differentiate regions of low and high cellularity or low and high proliferation.

Intravoxel incoherent motion model

The intravoxel incoherent motion model (Le Bihan et al., 1988, 2008, Lemke et al., 2011, Luciani et al., 2008) and Lemke et al. (2010) describes the signal loss in diffusion weighted imaging more precisely by the *IVIM* model given in [Equation 3.36](#) and can be used to separate the diffusion and perfusion compartment, where f depicts the perfusion fraction, D the pure diffusion coefficient and D^* the pseudo diffusion constant which is related to the velocity of the blood and about 10 times greater than D (Le Bihan et al., 1988). These derived values can be determined by a bi-exponential fitting routine.

$$\frac{S(b)}{S(0)} = (1 - f) \cdot e^{-b \cdot D} + f \cdot e^{-b \cdot (D + D^*)} \quad (3.36)$$

In [Figure 3.8](#), the interpretation of the *IVIM* model according to Le Bihan et al. (1988) is depicted. Important to note is that the perfusion fraction f is a combination of diffusion and perfusion and can be depicted by (a) and f .

Le Bihan et al. (1988) explains that the phase shift occurring by the attenuation, describing the perfusion only ($e^{-b \cdot D^*}$), depends on the capillary geometry and the blood velocity \vec{v} . He elucidates the capillary network by a succession of straight capillary segments and derives two different situations.

1. The blood flow changes its segments several times during spin-echo: The result is that the perfusion process looks like a random walk but consists also of the pseudo diffusion constant D^* depending on the mean length of the capillaries (\vec{l}) and the velocity of the blood, denoted by \vec{v} .
2. The blood flow does not change its segments during spin-echo, occurring in situations where \vec{l} is longer, \vec{v} is longer or the spin-echo delay is shorter. According to Le Bihan et al. (1988), $e^{-b \cdot D^*}$ can be still calculated by interpreting an incoherent motion at voxel level. However, and this is an important issue, coherent motion can not be measured (a net flow present in the voxel)

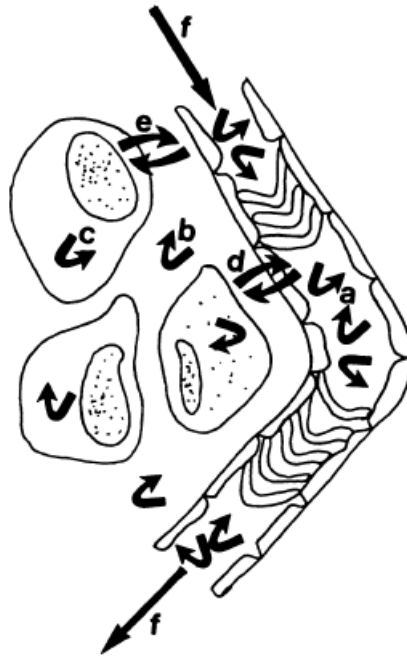


Fig. 3.8: The IVIM interpretation (taken from Le Bihan et al. (1988)): f depicts the incoherent flow and consists of perfusion and a small fraction of diffusion, whereas $1 - f$ consists of the pure diffusion compartment with intracellular (b) and extracellular (c) spaces. The exchanges between these compartments are designated by (d)

in any case by applying this model. Direct shift of the phase cannot be measured, since this technique is restricted onto the signal loss. Other methods, like phase-imaging or time of flight imaging, can also take these phase shifts into account (Section 3.1.1).

This model can be only applied if several \mathbf{b} values are used to describe the signal decay more precisely. In the brain, the effect has been reported to be very low (under 4 % (Lemke et al., 2011)). Thus, studies concerning the IVIM model are concentrated on much higher perfused organs such as the pancreas (Klauss et al., 2011, Lemke et al., 2009, Re et al., 2009), the liver (Luciani et al., 2008), the prostate (Riches et al., 2009) and the kidney (Zhang et al., 2009) where the perfusion fraction f yields more than 20 % (Lemke et al., 2011). However, organ motion is present and bulk motion can be eliminated by using several techniques.

1. Several b_0 values can be acquired as blocks with a weighted \mathbf{b} value as one acquisition (Klauss et al., 2011, Lemke et al., 2009).
2. To additional decrease the residual motion, registration can be applied to further improve the result (Graf et al., 2010).

At low \mathbf{b} values (from 0 to 200 (Le Bihan et al., 1988, 2008, Luciani et al., 2008)), D^* is most prominent, since the proton transport by vascular flow is considerably faster than that of molecular diffusion (Lemke et al., 2010) and can be seen as a signal drop in the signal decay diagram $\ln\left(\frac{S}{S_0}\right)$.

In Lemke et al. (2010), the perfusion fraction f is proven to represent the vascular compartment in the pancreas. Furthermore, under increasing TE, the perfusion fraction rises and can be explained by a faster transversal relaxation of the tissue compartment signal.

Moreover, Lemke et al. (2010) explains that the perfusion fraction f is mainly influenced by the arterial fraction and can be thus also called 'apparent arterial fraction'. Concerning Lemke et al. (2010), the venous compartment is argued to have the same decay as D . Otherwise, the signal would decay rather tri-exponentially than bi-exponentially. Lemke et al. (2010) concludes with the statement that it could be incorrect to just measure two signals with different \mathbf{b} values. Instead, an array of acquisitions has to be made by application of the IVIM model to also account for the arterial contribution in the signal decay caused by diffusion weighted imaging.

Diffusion weighted imaging and pancreatic diseases

This section elucidates the combination of diffusion weighted imaging and pancreatic diseases and starts with a 'Historical development of diffusion weighted imaging in the abdomen', explains 'Methods derived by diffusion weighted imaging to delineate pancreatic diseases', scrutinizes 'The ADC and its value as a surrogate marker' and closes with a word on 'The best derived diagnostic parameters regarding their diagnostic performance'.

Historical development of diffusion weighted imaging in the abdomen

Historically, diffusion weighted imaging has been restricted onto the brain. One reason is that motion artifacts have to be considered. These effects are most prominent if long echo times are used (Luciani et al., 2008). However, as mentioned earlier, these circumstances can be prevented by the application of breathhold acquisition blocks (Klauss et al., 2011, Lemke et al., 2009) and more sophisticatedly by the application of medical image registration (Graf et al., 2010).

Another reason of the application concerned on neurologic diseases is the directionality in white matter for the application of diffusion tensor imaging. The first prominent publication to segment white matter tracts while using diffusion tensor imaging is Stieltjes et al. (2001). This is potentially important for risk structure assessment and white matter infiltration by high grade brain tumours.

Methods derived by diffusion weighted imaging to delineate pancreatic diseases

In Grünberg et al. (2011), several methods concerning the differentiation between healthy pancreatic tissue are depicted. First, the application of two \mathbf{b} values, where the ADC in pancreatic carcinoma has been shown to be significantly lower than in pancreatitis and in healthy pancreatic tissue, respectively (Fattahi et al., 2009). Second, the application of at least two \mathbf{b} values (Lemke et al., 2009) and third, the usage of multiple \mathbf{b} values for the differentiation between pancreatic carcinoma and healthy pancreatic tissue, as well as pancreatic carcinoma and pancreatitis.

Moreover, as a third technique, the derived perfusion fraction f and the pure diffusion constant D have been used to perform these delineations (Klauss et al., 2011, Lemke et al., 2009). This is due to a hypoperfused pancreatic carcinoma compared to pancreatitis and healthy pancreatic tissue (Grünberg et al., 2011).

The ADC and its value as a surrogate marker

Grünberg et al. (2011) elucidates that the ADC in the pancreas is strongly influenced by the increase of collagen fibers, seen from a histopathological point of view and can be used as a surrogate, regarding (Grünberg et al., 2011, ECR), in a course of applied chemoradiation.

The best derived diagnostic parameters regarding their diagnostic performance

Pertaining to the diagnostic performance and as a message, it can be said that the derived perfusion fraction f is the outperforming parameter among the usage of all of the here depicted techniques, concerning the differentiation between pancreatic carcinoma and healthy pancreatic tissue with a diagnostic sensitivity performance of 95.7% and 100% for the specificity and should be used for its differentiation (Lemke et al., 2009).

The differentiation between pancreatitis and pancreatic carcinoma is thoroughly discussed in Klauss et al. (2011). In this study, again, the perfusion fraction f turned out to be the superior parameter amongst single \mathbf{b} value measurements and the pure diffusion fraction D . The combined sensitivity has been denoted as 80% and the specificity as 89.9%.

3.2 Image processing

The image processing part is subdivided into a section explaining the arbitrary nature and the inherent user dependency regarding the drawing of ROIs ([Section 3.2.1](#)), scrutinizes automatic and semi-automatic segmentation procedures in this context ([Section 3.2.2](#)), explains a quantification while taking statistical

methods into account (Section 3.2.3), continues with succinct overview about a validation of these segmentation algorithms (Section 3.2.4) and closes with a section filling in on the background of medical image registration (Section 3.2.5).

3.2.1 ROI placement in heterogeneous tumours

The issues of objectively segmenting and quantification of heterogeneous tumours like gliomas have been depicted in many articles and seem to be clearly identified as a research niche which is not well understood so far.

Commonly, DWI data are evaluated using region of interest (ROI) analysis. Using such analysis, a negative correlation between the *ADC* and the micro vessel density, as a marker of tumour proliferation was found in the tumour bulk (Sadeghi et al., 2004). However, this correlation was only weak in regions of tissue heterogeneity. This was attributed to the presence of heterogeneity and partial volume effects within the ROI.

In another study, the minimum *ADC* in astrocytic tumours (all WHO Grades I-IV) was found to be in general negatively correlated to the Ki-67 labelling index (LI), which is an index for cell proliferation (Higano et al., 2006). However, in the glioblastoma multiforme group (IV), this negative correlation could not be found. This again can be attributed to a high heterogeneity found in high grade gliomas. Considering the ROI placement, round- or oval-shaped regions were placed on the *ADC* map, excluding necrotic, cystic or haemorrhagic areas to determine a minimum *ADC* of the whole tumour. However, since the borders between solid tumour regions and necrotic and cystic areas are ill defined, the ROI placement is inherently user-dependant.

In Rana and Wardlaw (2003), the observer variability considering brain tumours is investigated and it is pointed out that it has an important impact on *ADC* measurements. Considering Sadeghi et al. (2004), the authors try to correlate *ADC* and *rCBV* values with cell and microvessel density in gliomas and thus try to investigate the usage of the *ADC* as a biomarker of cellularity in gliomas. They are pointing out clearly that the heterogeneity has to be recognized if the *ADC* or perfusion markers like *rCBV* are correlated to histological samples in terms of stereotactic biopsies. Notwithstanding, a correlation pertaining micro vessel density could be found, considering the bulk tumour samples, only a weak correlation could be identified in the heterogeneous regions. The authors are depicting this fact as a constitution of necrosis and extracellular matrix. Due to the mentioned manual region of interest placement, there seems to be a lack of objectively delineating the heterogeneous regions to find an accurate correlation between micro vessel densities.

In Moffat et al. (2005), the authors try to encompass the clinical response and therefore incorporate the dynamic behaviour of the *ADC* due to receive of

radiation, chemotherapy or a combination of both. They argue about an automatic segmentation of the tumour regions and create clusters in which the *ADC* increases significantly (a), where the *ADC* decreases significantly (b) and for which the *ADC* does not change significantly (c).

Doubtlessly, it has to be pointed out that this is a first step towards an objective tumour response to therapy. However, there seems to be a lack in terms of objective quantification. Objective *ADC* values within the tumour cannot be identified. Moreover, the amount of work in preprocessing the images, especially in terms of registration appears to be considerably high. Thus, the clusters are likely to be impeded by registration errors and inaccuracy in the cluster size. The arising partial volume effects between the different clusters are completely ignored.

The problems, which rise up here, are that the regions of interest are dependant on the physician due to visual inspection of the *ADC* map (Fallini, 2010). An approach of automatic tumour heterogeneity quantification of the different areas is mandatory which enables the determination of an objective *ADC* value of the tumour. This remains a major challenge in quantifying gliomas and taking the heterogeneity into account.

3.2.2 Automatic and semi-automatic segmentation algorithms

Segmentation is a challenging task that has previously been addressed using among others by the following methods (Zhang et al., 2005): region growing, shape-based and more recently introduced statistical segmentation approaches.

The disadvantages of region growing methods are that there is a user interaction needed to initialize the algorithm and that a certain threshold needs to be defined to denote the end of the region growing algorithm. Furthermore, region growing only works for homogeneous sharply delineated regions. Thus, such approaches are successfully applied for CT-based lung or trachea segmentation, where mostly homogeneous regions are being segmented (Fabijanska et al., 2009) but are less suitable for brain tumour clustering.

A prominent example of a shape-based segmentation method is live wire segmentation (Falcão and Jayaram, 2000) and is often used for liver segmentation based on CT images (Bourquain et al., 2002). The segmentation result is dependant on an initial contour and does not necessarily guarantee to be satisfactory in all cases (Zhang et al., 2005). Thus user-based variance may reduce the reproducibility. Moreover, the convergence speed has been reported to be very slow (Zhang et al., 2005). Another limitation, as in region growing, is the need for relatively sharp borders.

The intensity distribution of the signal in heterogeneous tumour regions can be described using statistical methods (Hongmin et al., 2007, Kaus et al., 1999,

Menze et al., 2010, Noe and Gee., 2001, Prastawa et al., 2004, 2003, Riklin-Raviv et al., 2010, Schlüter et al., 2005, Stieltjes et al., 2006, van Leemput, 2001). Statistical methods comprise a quantitative outcome which should be predicted by a set of features. By observing the outcome (training set) and feature measurements for a set of objects, a prediction model can be build to accurately predict the outcome (Hastie et al., 2009). Statistical approaches are promising in cases where soft and gliding borders between segments occur. In Prastawa et al. (2003), this behaviour is described as overlapping intensities and in the case of glioblastomas as ragged boundaries. An important first requirement for statistical segmentation approaches is that the distributions of the measurement value (e.g. the ADC) within the expected different segments (e.g. high vs. low cellularity) can be separated into a superpositions of two Gaussians. If this is given for each voxel within the tumour, the probability can be calculated that this voxel belongs to one of the expected clusters (Simon et al., 2009, 2011). Based on these individual probabilities, using an expectation maximization (EM) approach (Bishop, 2006, Dempster et al., 1977, Hastie et al., 2009), the assumed tissue groups can be found. The overall probability of the found cluster, which can be seen as a quality measurement of the complete approach, is then given by the so called posterior probability. Furthermore, the given probabilities within the tumour area can be used to take partial volume effects into account (Noe and Gee., 2001, Schlüter et al., 2005, Stieltjes et al., 2006).

Clustering as an example for a statistical algorithm

The K-means clustering algorithm

The *K-means* clustering technique, as the basis of the Expectation Maximization algorithm is introduced in this section.

It is an unsupervised machine learning algorithm, where the input vectors $\vec{x}_1, \dots, \vec{x}_N$ are given to discover similar groups within the data and to generate the output vectors (Bishop, 2006). The so called 'distortion measure' (Equation 3.37) (Bishop, 2006) is being minimized to achieve new cluster sets and to perform a *hard assignment*. Thus, this clustering algorithm belongs to the partitioned clustering procedures where no overlap of the output vectors will occur.

$$J = \sum_{n=1}^N \sum_{k=1}^K r_{nk} \|\vec{x}_n - \vec{\mu}_k\|^2 \quad (3.37)$$

Equation 3.37 describes the squares of the distances of each data point to the center vector $\vec{\mu}_k$ (Bishop, 2006), r_{nk} is a binary indicator function, where n denotes the data point and k the assigned cluster.

After an arbitrary initialization of the center vectors $\vec{\mu}_k$, two basic steps can be derived which are called 'Expectation' and 'Maximization'.

Expectation step Minimization with respect to r_{nk} , where $r_{nk} = 1$ in case of $k = \operatorname{argmin}_j |\vec{x}_n - \vec{\mu}_j|^2$ and an assignment to the cluster is being performed (Quality measurement of approach and new assignment).

Maximization step Use new assignment r_{nk} to estimate the new model parameter vector $\vec{\mu}_k$.

The derivative of the distortion function and the determination of $\vec{\mu}_k$ results in [Equation 3.38](#) (Bishop, 2006).

$$2 \cdot \sum_{n=1}^N r_{nk} (\vec{x}_n - \vec{\mu}_k) = 0 \Leftrightarrow \vec{\mu}_k = \frac{\sum_n r_{nk} \cdot \vec{x}_n}{\sum_n r_{nk}} \quad (3.38)$$

Advantages of this algorithm are that a minimum of the distortion function [Equation 3.37](#) is guaranteed. However, this minimum can be a local minimum instead of a global one (Bishop, 2006). Furthermore, it can be described as 'intuitive' and creates compact, easy clusters (Hastie et al., 2009).

However, a big disadvantage is the strong dependence on the initialization $\vec{\mu}_k$, the number of clusters and the partition property (Bishop, 2006).

The general Expectation Maximization algorithm

An algorithm, also known of the 'soft variant' of *K-means* is the probabilistic clustering algorithm *Expectation Maximization* with a probabilistic model. Most prominent is the usage of a Gaussian mixture model $p(x)$ with an n dimensional multivariate Gaussian ([Equation 3.39](#)). These superpositions are linear combinations using the normalized mixture coefficient π and can approximate any continuous probability density to arbitrary accuracy (Bishop, 2006).

$$\mathcal{N}(\vec{x} | \vec{\mu}, \Sigma) = \frac{1}{(2 \cdot \pi)^{\frac{n}{2}}} \cdot \frac{1}{|\Sigma|^{\frac{1}{2}}} e^{-0.5(\vec{x} - \vec{\mu})^T \Sigma^{-1} (\vec{x} - \vec{\mu})} \quad (3.39)$$

$$p(\vec{x}) = \sum_{k=1}^K \pi_k \mathcal{N}(\vec{x} | \vec{\mu}_k, \Sigma_k) \quad (3.40)$$

The general Expectation Maximization algorithm defines model parameters θ , which can be determined as latent or hidden variables Z and can denote the

labelling or the segmentation of the data. In the multivariate Gaussian case, these model parameters are defined as the parameters of the Gaussian mixture model ($\theta = \{\vec{\mu}, \vec{\Sigma}, \vec{\pi}\}$). In the *K-means* case, the model parameters can be defined as $\vec{\mu}_k$.

The quality measurement of the whole approach is given by the probability function $p(Z|X, \theta)$. In the multivariate Gaussian case, this parameter is defined as the responsibilities or posterior probability $\gamma(z_k) \equiv p(z_k = 1 | \vec{x})$, where z_k denotes these latent variables and is defined as a binary vector. z_k denotes to which class the voxel belongs (Bishop, 2006).

The general EM algorithm is denoted given the following steps (adapted from Bishop (2006)).

$$\gamma(z)_k \equiv p(z_k = 1 | \vec{x}) = \frac{p(z_k = 1)p(\vec{x} | z_k = 1)}{\sum_{j=1}^K p(z_j = 1)p(\vec{x} | z_j = 1)} = \quad (3.41)$$

$$\frac{\pi_k \mathcal{N}(\vec{x} | \vec{\mu}_k, \vec{\Sigma}_k)}{\sum_{j=1}^K \pi_j \mathcal{N}(\vec{x} | \vec{\mu}_j, \vec{\Sigma}_j)} \quad (3.42)$$

Expectation step Estimate $p(Z|X, \theta^{old})$ (Estimate posterior probability and evaluate the latent variables given the joint distribution of the parameters θ^{old} and the observations X)

Maximization step Optimize the model parameters θ^{new} given by [Equation 3.43](#) and [Equation 3.44](#). In this step, the posterior probability, determined in the Expectation step, is being used to maximize the Log-likelihood and to estimate the new parameter set θ^{new} .

$$\theta^{new} = \operatorname{argmax}_{\theta} \mathcal{Q}(\theta, \theta^{old}) \quad (3.43)$$

$$\mathcal{Q}(\theta, \theta^{old}) = \sum_Z p(Z|X, \theta^{old}) \ln(p(X, Z|\theta)) \quad (3.44)$$

The Log-likelihood function is checked for convergence in a last step.

Adding spatial constraints by a Markov Random Field

By adding spatial constraints by means of a Markov Random Field (MRF) (Bishop, 2006, Li et al., 1995, Perez et al., 1998, van Leemput, 2001, van Leemput

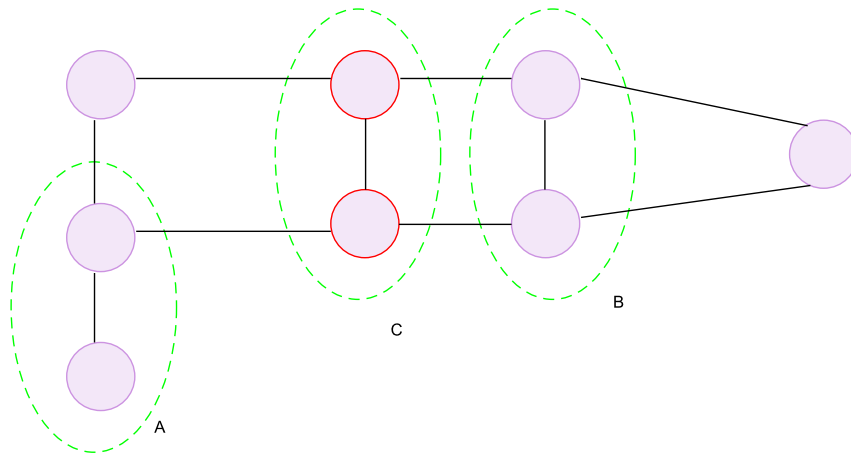


Fig. 3.9: The independence property (adapted from Bishop (2006))

et al., 1999), the segmentation is based not on the intensity only. Instead, the context or the spatial clustering of the voxels can be taken into account. In this way, outliers can be erased and configurations are preferred where neighbours for the same class occur (van Leemput, 2001). The posterior probability, denoted by $p(Z|X, \theta^{old})$, or the fractions π_k in the multidimensional Gaussian case, can be determined, dependant on the context in which the labels reside.

Independence properties

Markov Random fields are probabilistic undirected graphical models. In [Figure 3.9](#), a graphical model is showing an independence property denoted by [Equation 3.45](#). It says that A is conditionally independent of B given C . Hence C is blocking the path to B (Bishop, 2006).

$$A \perp\!\!\!\perp B | C \quad (3.45)$$

Factorization properties and joint distribution of graph

The factorization properties can be described as a locality definition or the joint distribution $p(x)$ as a product over all functions (Bishop, 2006). The illustration in [Figure 3.10](#), yields that the middle node, which is conditioned on all of the variables in the graph, is only dependant on a small subset which is called a 'Markov blanket' (Bishop, 2006).

The factorization properties are derived by this locality assumption. If we take for instance the two lower nodes in [Figure 3.10](#), there is no direct link

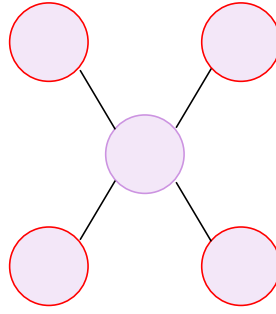


Fig. 3.10: Illustration of a Markov blanket (adapted from Bishop (2006))

between them. That is why a so called conditional independence assumption yields such as that they do not belong to the same factor (Equation 3.46).

$$p(x_i, x_j | \vec{x}_{\setminus i,j}) = p(x_i | \vec{x}_{\setminus i,j}) p(x_j | \vec{x}_{\setminus i,j}) \quad (3.46)$$

The independence assumption leads to the model of maximum cliques. The joint distribution is written as a product of potential functions over the maximum cliques of the graph $\psi_c(x_c)$ (Equation 3.47 and Equation 3.48) (Bishop, 2006).

$$p(x) = \frac{1}{Z} \prod_C \psi_C(x_c) \quad (3.47)$$

$$Z = \sum_x \prod_C \psi_C(x_c) \quad (3.48)$$

Now, the Hammersley Clifford theorem (Li et al., 1995) states that the Markov Random Field obeys a *Gibbs* distribution (van Leemput, 2001). A *Gibbs* measure is derived from the Ising model in statistical mechanics as a probability measure on all sequences of dipol experiments (up and down spins) (Kindermann and Snell, 2000).

These maximum cliques can be defined by a *Boltzmann distribution* as an exponential representation (Bishop, 2006) using Equation 3.49.

$$\psi_C(x_c) = e^{-E(x_c)} \quad (3.49)$$

Markov Random Fields and the Expectation Maximization algorithm

By adding contextual constraints to the Expectation Maximization algorithm, an expansion onto the Potts model using more than 2 classes can be made in the way such as neighbours for the same class are preferred (van Leemput, 2001).

Recalling the Expectation Maximization algorithm, and the posterior probability depicted in Equation 3.42, the new posterior probability function can be described as Equation 3.50 and the energy of the MRF, defined by the *Boltzmann distribution*, as Equation 3.51 (adapted from van Leemput et al. (1999) and Bishop (2006)).

In the last step, the Markov Random Field is additionally included into the posterior probability evaluation where θ_y determines the parameters of the Gaussian model Equation 3.42 ($\theta = \vec{\mu}_k, \vec{\Sigma}, \pi$) and θ_z denotes the Markov Random Field configuration and \mathcal{N}_i a three dimensional neighbourhood around voxel i .

$$\gamma(z)_k \equiv p(z_k = 1 | \vec{x}) = \frac{p(\vec{x} | z_k = 1, \theta_y^{old}) p(z_k = 1 | P_{\mathcal{N}_k}^{old}, \theta_z^{old})}{\sum_{j=1}^K p(\vec{x} | z_j = 1, \theta_y^{old}) p(z_j = 1 | P_{\mathcal{N}_i}^{old}, \theta_z^{old})} \quad (3.50)$$

$$p(z_k = 1 | P_{\mathcal{N}_k}^{old}, \theta_z^{old}) = \frac{e^{-U_{mrf}(z_k | P_{\mathcal{N}_k}^{old}, \theta_z^{old})}}{\sum_{j=1}^K e^{-U_{mrf}(z_j | P_{\mathcal{N}_k}^{old}, \theta_z^{old})}} \quad (3.51)$$

This is known as the dependant case. The classification now depends on the surrounding voxels \mathcal{N}_i .

3.2.3 Quantification

The likelihoods, derived from a probabilistic approach, can be used to come to a probabilistic quantification that allows for a reproducible quantification in regions of tissue inhomogeneity (Schlüter et al., 2005, Stieltjes et al., 2006). Important to note is that the probabilistic quantification does not necessarily ensure a better delineation. However, the objectivity of the quantification increases by applying probabilistic assumptions.

Moments of the probability distribution can be calculated to derive probabilistic reproducible values such as μ_{prob} , σ_{prob} ($\sqrt{\mu_{prob}^2}$), the skewness (μ_{prob}^3) and the kurtosis (μ_{prob}^4).

Usually, the expected value or the first moment of a discrete random variable X is defined as [Equation 3.52](#) (Elpelt and Hartung, 1992).

$$E(X) = \sum_{i=1}^{\infty} x_i \cdot P(X = x_i) \quad (3.52)$$

The second moment of a discrete random variable X or the variance σ^2 can be denoted as [Equation 3.53](#) (Elpelt and Hartung, 1992).

$$Var(X) = \sum_{i=1}^{\infty} [x_i - E(X)]^2 \cdot P(X = x_i) \quad (3.53)$$

In general, the moments can be derived by [Equation 3.54](#) (Elpelt and Hartung (1992)).

$$Moment(X)_n = \sum_{i=1}^{\infty} [x_i - E(X)]^n \cdot P(X = x_i) \Leftrightarrow E[(X - E[X])^n] \quad (3.54)$$

The probabilistic quantification, while considering a Gaussian mixture model ([Equation 3.40](#)) with a discrete posterior probability $\gamma(z_{nk})$ ([Equation 3.42](#)) can be performed by using [Equation 3.52](#) and dividing through the probabilistic observations inside one cluster N_k , denoted as $N_k = \sum_{n=1}^N \gamma(z_{nk})$ (Bishop, 2006) resulting in [Equation 3.55](#). The derived standardized moments $\mu_{prob}^2 \dots \mu_{prob}^4$ can be determined accordingly as denoted in ([Equation 3.56](#), [Equation 3.57](#), [Equation 3.58](#)) where σ depicts the standard deviation (Bishop, 2006).

$$\mu_{prob} = \frac{1}{N_k} \cdot \sum_{n=1}^N \gamma(z_{nk}) \cdot x_n \quad (3.55)$$

$$\mu_{prob}^2 = \frac{1}{N_k} \cdot \sum_{n=1}^N (x_n - \mu_{prob})^2 \cdot \gamma(z_{nk}) \quad (3.56)$$

$$\mu_{prob}^3 = \frac{\frac{1}{N_k} \cdot \sum_{n=1}^N (x_n - \mu_{prob})^3 \cdot \gamma(z_{nk})}{\sigma_{prob}^3} \quad (3.57)$$

$$\mu_{prob}^4 = \frac{\frac{1}{N_k} \cdot \sum_{n=1}^N (x_n - \mu_{prob})^4 \cdot \gamma(z_{nk})}{\sigma_{prob}^4} \quad (3.58)$$

Despite the efforts made so far, there is still a lack of an automatic, rapid, quantifiable and partial volume aware method which considers the heterogeneous nature of brain tumours. In Hongmin et al. (2007), tumour cellularity is taken into account as a quantification method, but partial volume modelling is not addressed. (Noe and Gee., 2001, Schlüter et al., 2005, Stieltjes et al., 2006, van Leemput, 2001) are promising methods to tackle the outlined issues.

3.2.4 Validation of segmentation algorithms

This chapter gives a succinct overview about common methods of the validation of segmentation algorithms. First, it introduces 'Overlapping coefficients', explains 'Receiver operator characteristic curves' and ends with the variance analysis based 'intraclass coefficient'.

Overlapping coefficients

In Haenelt (2007), a good introduction into common similarity measures is given. Four different coefficients shall be explained here to be applied onto different volumes.

1. The simple overlap, determined by the intersection, is explained in [Equation 3.59](#).
2. The Jaccard or Tanimoto coefficient (Jaccard, 1912) is defined by [Equation 3.60](#) and penalizes small common entries in contradiction to the Dice coefficient (Dice, 1945).
3. The Dice coefficient is explained by [Equation 3.61](#) and can be transformed to the Jaccard index $J = \frac{D}{(2-D)}$. The opposite transformation is denoted as $\frac{2 \cdot J}{1+J}$.
4. The overlap coefficient is determined in [Equation 3.62](#) with the property that if X is a subset of Y or vice-versa, then it will sum to one.

$$\text{SimpleOverlap}(X, Y) = |X \cap Y| \quad (3.59)$$

$$\text{JaccardCoefficient}(X, Y) = \frac{|X \cap Y|}{|X \cup Y|} \quad (3.60)$$

$$DiceCoefficient(X, Y) = \frac{2|X \cap Y|}{|X| + |Y|} \quad (3.61)$$

$$OverlapCoefficient(X, Y) = \frac{|X \cap Y|}{\min(|X|, |Y|)} \quad (3.62)$$

$$\frac{2 \cdot J}{1 + J} = \frac{2 \cdot \left(\frac{|A \cup B|}{|A \cap B|}\right)}{1 + \left(\frac{|A \cup B|}{|A \cap B|}\right)} \Leftrightarrow \frac{2}{\frac{|A \cap B|}{|A \cup B|} + 1} \Leftrightarrow \frac{2 \cdot |A \cap B|}{|A \cup B| + |A \cap B|} \equiv \quad (3.63)$$

$$D = \frac{2|X \cap Y|}{|X| + |Y|} \quad (3.64)$$

Receiver operating characteristic curves

This chapter introduces the 'Theory of ROC curves', explains the 'ROC space' and ends with the quantitative parameter of the 'Area under the curve'.

Theory of ROC curves

Receiver operator characteristic curves or ROC curves can be e.g. used in the medical field to decide between cancer or non cancer as two hypotheses H_0 : target is not present and H_1 : target is present (Fawcett, 2004, Kerekes, 2008).

Four outcomes can be derived (Figure 3.11).

1. FN: The False Negatives explain a missed detection in the test classification of a positive in reality (Equation 3.65).
2. TP: The True Positives determine the correct detection of the correctly classified positives in the test classification of the total positives in reality. This is also called 'Sensitivity' (Equation 3.66).
3. FP: The False Positives elucidate the false alarm rate or that the test classification detects a positive where there is a negative in reality (Equation 3.67).
4. TN: The True Negatives elaborate a correctly determined negative by the test of the negatives. This is also called specificity (Equation 3.68).

$$P(\text{negative detection} | \text{positive in reality}) \quad (3.65)$$

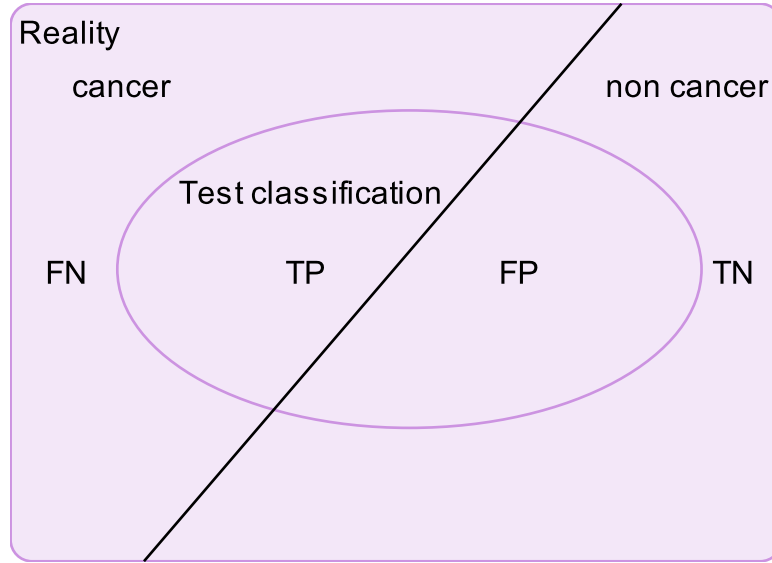


Fig. 3.11: A ROC classification illustration by sets

$$P(\text{negative detection} | \text{positive in reality}) \quad (3.66)$$

$$P(\text{positive detection} | \text{negative in reality}) \quad (3.67)$$

$$P(\text{negative detection} | \text{negative in reality}) \quad (3.68)$$

The ROC space

The ROC space (Fawcett, 2004) is depicted by a two-dimensional graph showing the sensitivity (Equation 3.66 and Equation 3.69) (ordinate) and the false positive rate (Equation 3.67) (abscissa).

$$\text{Sensitivity} = \frac{\text{Positives correctly classified}}{\text{Total positives} + \text{False negatives}} \quad (3.69)$$

$$\text{False positiverate} = \frac{\text{Negatives incorrectly classified}}{\text{Total negatives}} \quad (3.70)$$

$$\text{Specificity} = \frac{\text{True negatives}}{\text{False positives} + \text{True negatives}} \quad (3.71)$$

Some important points can be denoted as follows (Fawcett, 2004).

- (0,0) No positive classification can be denoted and no false positive errors.
 (1,1) This is the contradictory case where the result is positive but also with 100 % false positives.
 (0,1) This is a perfect classification with 100 % sensitivity and no false positives.

In general, points compared to the north-west are better and classifiers near the X axis and left-hand side are called 'conservative' whereas the classifiers on the right-hand side can be denoted as 'liberal' with strong evidence and a high false alarm rate. A classifier on the middle line can be explained as a random guessing classifier (Fawcett, 2004).

Additionally, cut off values can be determined for every sensitivity and false positive pair (Fawcett, 2004).

Area under the curve

The area under the curve of a ROC space considering sensitivity and the false positives can be calculated to get additional information about the performance of the classifier. This value is equivalent to the Wilcoxon test of ranks (Elpelt and Hartung, 1992) and explains that a randomly taken positive detection (e.g. cancer) will be higher than a randomly chosen negative one (e.g. non cancer) (Fawcett, 2004).

The intraclass coefficient

The intraclass coefficient can be used to measure the reproducibility of a quantification value during a series of segmented areas j of a patient i . This measurement considers both the intra-subject and the inter-subject variability retrieved from a variance analysis (Handl, 2002) with model depicted in Equation 3.72. The random variable \vec{y}_{ij} depicts the j^{th} observation or segmented area of a patient with index i and obeys a multivariate normal distribution with covariance matrix Σ , expectation value vector $\hat{\theta}$ and error vector \vec{e}_{ij} .

$$\vec{y} = X \cdot \hat{\theta} + \vec{e} \quad (3.72)$$

The ICC is determined as denoted in Equation 3.74 (adapted from Tofts (2003)) where the subjects can be denoted as the patients.

$$ICC = \frac{\text{variance between subjects}}{\text{variance between subjects} + \text{variance within subjects}} \quad (3.73)$$

$$\equiv \frac{\text{variance}(\hat{\theta})}{\text{variance}(\hat{\theta}) + \text{variance}(\vec{e})} \quad (3.74)$$

3.2.5 Medical image registration

Viola and Wells III (1997) describes the image alignment or the image registration process by [Equation 3.75](#).

$$v(T(x)) = F(u(x), \vec{q}) + \eta \Leftrightarrow v(y) = F(u(T^{-1}(y)), \vec{q}) + \eta \quad (3.75)$$

This equation denotes the transformation T or pose between a model $u(x)$ and an image $v(y)$. T can be explained as the relation between the coordinate frame of the model to the coordinate frame of the image. The imaging function $F(u(x), \vec{q})$ elucidates the value of the point $v(T(x))$ in space. η represents a random variable to model the noise in the imaging process (Viola and Wells III, 1997) and \vec{q} a vector of the exogenous factors such as the lightning.

In medical imaging, this process is especially important if multimodal image acquisitions have to be combined to complete the whole picture of a patient's diagnosis. Moreover, tumour growth can be investigated, a treatment can be verified and a comparison with atlases can be made to find deviations (Zitová and Flusser, 2003).

In Zitová and Flusser (2003), four different methodologies are being described.

Different viewpoints Here, a set of acquisitions of different viewpoints are being combined to get a full view of the scene in 3D.

Different times In Maintz and Viergever (1997), this registration technique is called *serial registration* where images of the same scene are acquired at different times and circumstances. In medical imaging, this can be done for monitoring and followup analysis concerning tumour progression.

Different sensors This task covers the combination of multimodal acquisitions of the same image to perform a sensor fusion of multispectral information. This can be performed for different subjects (inter-subject registration) and for the same subject (intra-subject registration) (Schnabel and Rueckert, 2009).

Scene to model registration In this case, a computer representation of a scene is being matched with images of a scene.

A complete registration process usually encapsulates the following consecutive steps (Zitová and Flusser, 2003):

- **Feature detection:** In this step, features of the images are being detected manually or automatically detected denoted as control points.
- **Feature matching:** In this consecutive step, the detected features are being aligned.

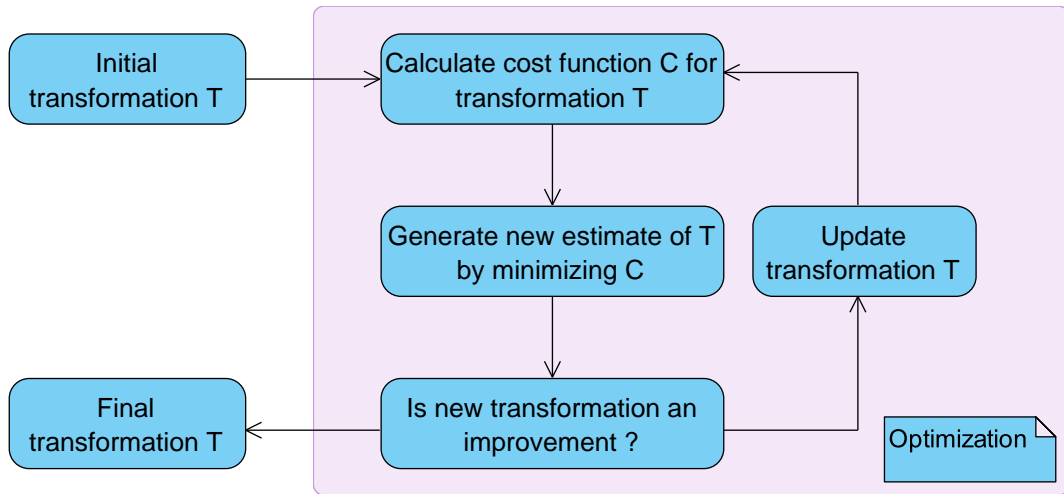


Fig. 3.12: A registration algorithm (adapted from Schnabel and Rueckert (2009))

- Transform model estimation: The mapping function T (Equation 3.75) is being calculated to map the model $u(x)$ and an image $v(y)$.
- Image resampling and transformation: The last step covers the appropriate interpolation technique to the voxel coordinates of the image by a designated interpolation technique.

A typical image registration algorithm as an optimization process is depicted in Figure 3.12. A metric is being iteratively minimized to achieve a final transformation T . This transformation can be either *local* if the transformation is being applied to subsections of the image and every subsection has its own transformation T (Maintz and Viergever, 1997) or *global* if the transformation is being applied to the whole image.

Basics of rigid image registration

Rigid image registration incorporates 6 degrees of freedom with the operations *translation* (3) and *rotation* (3). In homogeneous coordinates, the transformation T can be described as denoted in Equation 3.76. The translations are described by t_x, t_y, t_z and the rotations by r_{11}, \dots, r_{33} around x, y, z (Schnabel and Rueckert, 2009).

$$T_{rigid}(x, y, z) = \begin{pmatrix} x' \\ y' \\ z' \\ 1 \end{pmatrix} = \begin{pmatrix} r_{01} & r_{02} & r_{03} & t_x \\ r_{11} & r_{12} & r_{13} & t_y \\ r_{21} & r_{22} & r_{23} & t_z \\ 0 & 0 & 0 & 1 \end{pmatrix} \cdot \begin{pmatrix} x \\ y \\ z \\ 1 \end{pmatrix} \quad (3.76)$$

Monomodal image registration

Monomodal image registration describes the alignment process between images of the same modality. In Maintz and Viergever (1997), the following modalities are depicted:

1. Auto-radiographic
2. CT or CTA (Computer Tomography Angiography)
3. MR (Magnetic Resonance Imaging)
4. PET (Positron Emission Tomography)
5. Portal (Control images for radiotherapy)
6. SPECT (Single Photon Emission Computed Tomography)
7. US (Ultrasound)
8. Video (Video Images)
9. X-ray or DSA (Digital Subtraction Angiography)

Because of the higher similarity in a mono-modal environment than in a multi-modal environment, the registration problem is easier to solve (Maintz and Viergever, 1997) and the functional relationship between the two images consists of either an identity function or a linear dependency. The following metrics are being used for the mono-modal task (Schnabel and Rueckert, 2009) where I_A depicts image intensity of image a (fixed image) and I_B image intensity of image b (moving image) of point p_i (Figure 3.13). C depicts a function of voxel similarity between these two images.

SSD The sum of squared differences (SSD) can be used if an identity transformation exists in both images, i.e. $f(x) = x$ and assumes Gaussian noise between the images.

SSA The sum of absolute differences (SAD) equivalently needs an identity transformation and is less sensitive to outliers compared to SSD.

NCC The normalized cross correlation (NCC) is related to Pearson's correlation coefficient (Equation 3.78) and depicted by Equation 3.76 (Elpelt and Hartung, 1992) and has to obey a linear relationship between the two images and is especially useful if the acquisition has been achieved with scaled intensity.

$$C(I_A, I_B, T) = \frac{1}{N} \sum_i (I_A(p_i) - I_B(T(p_i)))^2 \quad (3.77)$$

$$\text{Corr}(X, Y) = \sigma_{xy} = \frac{\sigma_{XY}}{\sigma_X \cdot \sigma_Y} \quad (3.78)$$

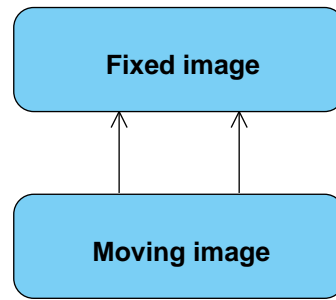


Fig. 3.13: Illustrated fixed and moving image

$$NCC(I_A, I_B, T) = \frac{\sum (I_A(p) - \mu_A)(I_B(T(p)) - \mu_B)}{\sqrt{((\sum (I_A(p) - \mu_A)^2)(\sum (I_B(T(p)) - \mu_B)^2))}} \quad (3.79)$$

Multimodal image registration

In multimodal image registration, two different modalities are being registered where the functional dependence between the images is not known. Even in the monomodal case, it could be beneficial (Graf and Nix, 2009). In the process, the following common modalities are being considered (Maintz and Viergever, 1997) where *TMS* describes the Transcranial magnetic stimulation.

1. CT-MR
2. CT-PET
3. CT-SPECT
4. DSA-MR
5. PET-MR
6. PET-US
7. SPECT-MR
8. SPECT-US
9. *TMS^a*-MR
10. US-CT
11. US-MR
12. X-ray-CT
13. X-ray-MR
14. X-ray-portal
15. Video-CT
16. Video-MR

A commonly used metric considering multi modal registration tasks is normalized mutual information (NMI) (Maes et al., 1997, Viola and Wells III, 1997) and based on information theory given by [Equation 3.80](#). This is known as *Shannon entropy* (Pluim et al., 2003).

$$H = \sum_i p_i \log \frac{1}{p_i} = - \sum_i p_i \log p_i \quad (3.80)$$

Now, the mutual information regarding [Equation 3.75](#) can be defined as [Equation 3.82](#) (Viola and Wells III, 1997). In this case, $H(u(x))$ and $H(v(T(x)))$ denote the *Shannon entropy* of the model $u(x)$ and the image $H(v(T(x)))$, respectively and $H(u(x), v(T(x)))$ the joint entropy.

The normalized information, as an index between 0 and 1 is defined as [Equation 3.83](#) and illustrated in [Figure 3.14](#) where $I(u(x); v(T(x)))$ depicts the mutual information.

$$I(u(x), v(T(x))) \equiv H(u(x)) + H(v(T(x))) - H(u(x), v(T(x))) \quad (3.81)$$

$$\Leftrightarrow \sum_{u(x), v(T(x))} p(u(x), v(T(x))) \cdot \log \frac{p(u(x), v(T(x)))}{p(u(x))p(v(T(x)))} \quad (3.82)$$

$$NMI(u(x), v(T(x))) = \frac{H(u(x)) + H(v(T(x)))}{H(u(x)), H(v(T(x)))} \quad (3.83)$$

3.3 Tumour types

This section is subdivided into a general introduction pertaining to brain tumours ([Section 3.3.1](#)) and gives a succinct overview about pancreatic tumours ([Section 3.3.2](#)).

3.3.1 Brain tumours

In [Figure 3.15](#), a 3D model of the brain is given.

General characteristics of brain tumours

In Prastawa et al. (2003), the following general characteristics and assumptions concerning brain tumours are given. Due to these properties, they are not easy to be segmented.

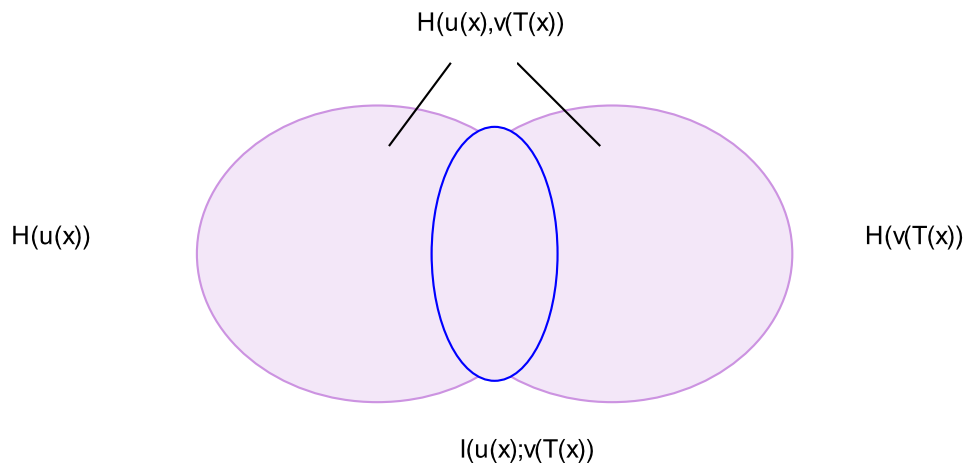


Fig. 3.14: Mutual Information (adapted from Schnabel and Rueckert (2009))

- Vary greatly in size and position.
- Vary greatly in the way they show up in MRI.
- May have overlapping intensities with normal tissue.
- May be space occupying or infiltrating.
- May enhance fully, partially, or not at all, with contrast agent.
- May be enhanced by surrounding oedema.

Gliomas and grading

Half of the common brain tumours are gliomas (Synowitz, 2008). The WHO classifies these tumours in tumours with and without stable histology and thus separates the WHO grades at grade II but often transforms to higher grade tumours in the majority (Stieltjes et al., 2006). Moreover, the differentiation between benign and malignant can be made by the infiltration of the tumour in healthy tissue and a clear delineation (Synowitz, 2008). Approximately 12 to 15 % belong to the highest malignant group, the glioblastoma multiforme (Synowitz, 2008). There are two ranges where most of the cases of glioblastomas occur. The first range between 20 and 30 and the second range between the age of 50 and 60, where the probability of a glioblastoma is considerably higher (Synowitz, 2008). The complete grading of brain tumours is given in [Table 3.1](#).

The main reason for the development of gliomas are deformed gliacells and they are classified into *microglia*, *oligodendrocytes* and *astrocytes* (Krebs et al., 2004). The respective derived gliomas belonging to these abnormal tumour cells are *microglioma*, *oligodendroglioma* and *astrocytoma*.

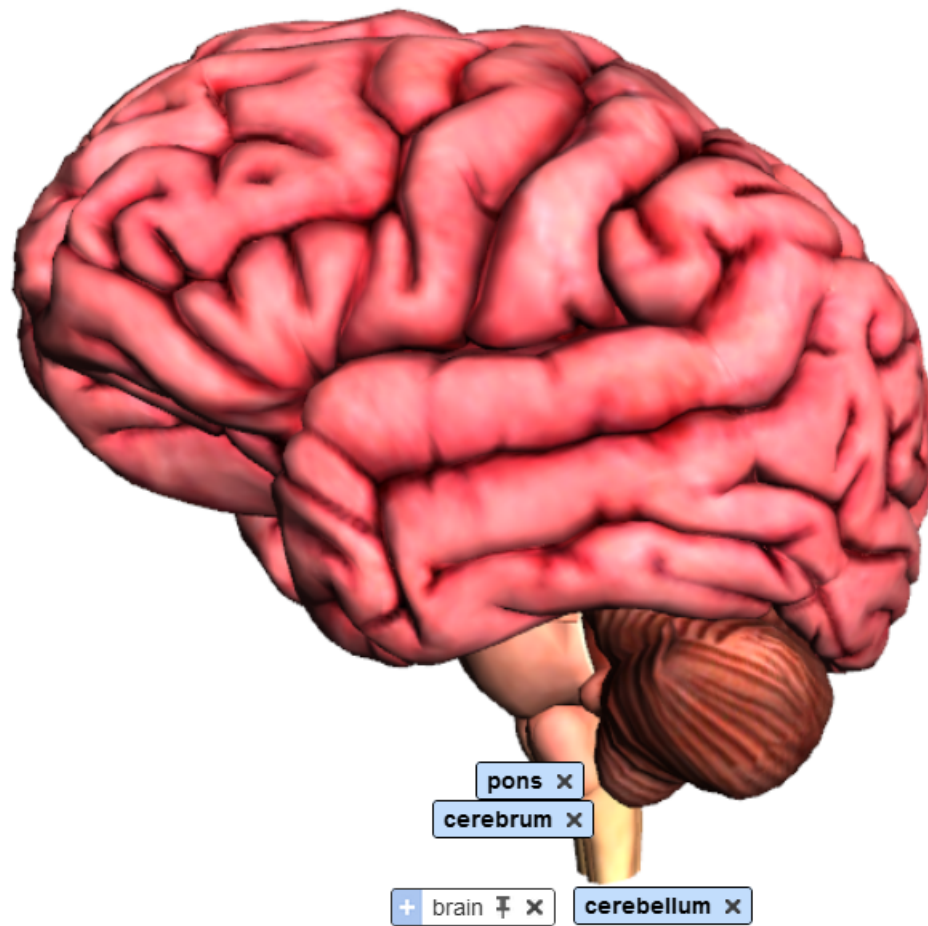


Fig. 3.15: The central nervous system (GoogleLabs, 2011a). Highlighted are the cerebrum, the cerebellum, the pons and medulla oblongata.

WHO - Grade	Properties	Prognosis
Grade I	benign, slow tumour growth	very good healing chances
Grade II	still benign Survival rate: to 5 years	
Grade III	malignant after operation radiation or chemotherapy necessary Survival rate: 2-3 years	
Grade IV	very malignant high tumour growth after operation radiation or chemotherapy necessary Survival rate: glioblastoma: up to one year other types: up to 5 years	poor healing prognosis

Table 3.1: Grading of brain tumours (Synowitz, 2008), Survival rates (Louis et al., 2007)

Contradictory to that, novel research identifies stem cells as the real source for developing glioblastomas which are genetically disrupted. Furthermore, the cell division seems to be disturbed and results in a heterogeneous speed of growth (Synowitz, 2008).

Prastawa et al. (2003) denotes the basic characteristics of gliomas as

- Ragged boundaries
- Initially only in white matter, possibly later spreading outside white matter.
- Margins enhance with contrast agent, inside does not.
- Accompanied by oedema
- Infiltrating at first, possibly becoming space occupying when larger.

Therapy issues concerning gliomas

Referring to Synowitz (2008), effective therapies for gliomas are not easy to pursue due to a lack of thorough knowledge of the development. Thereby, the high-proliferation and the infiltration issue, raised by Prastawa et al. (2003) are crucial points.

After an operative resection of the tumour, a consecutive chemo- and radiotherapy or immunotherapy or gentherapy can be applied to lengthen the actuarial survival rate (Synowitz, 2008).

It has been reported that the average actuarial survival rate can be denoted with 10 months. The maximum survival rate amounts to one year (Synowitz, 2008).

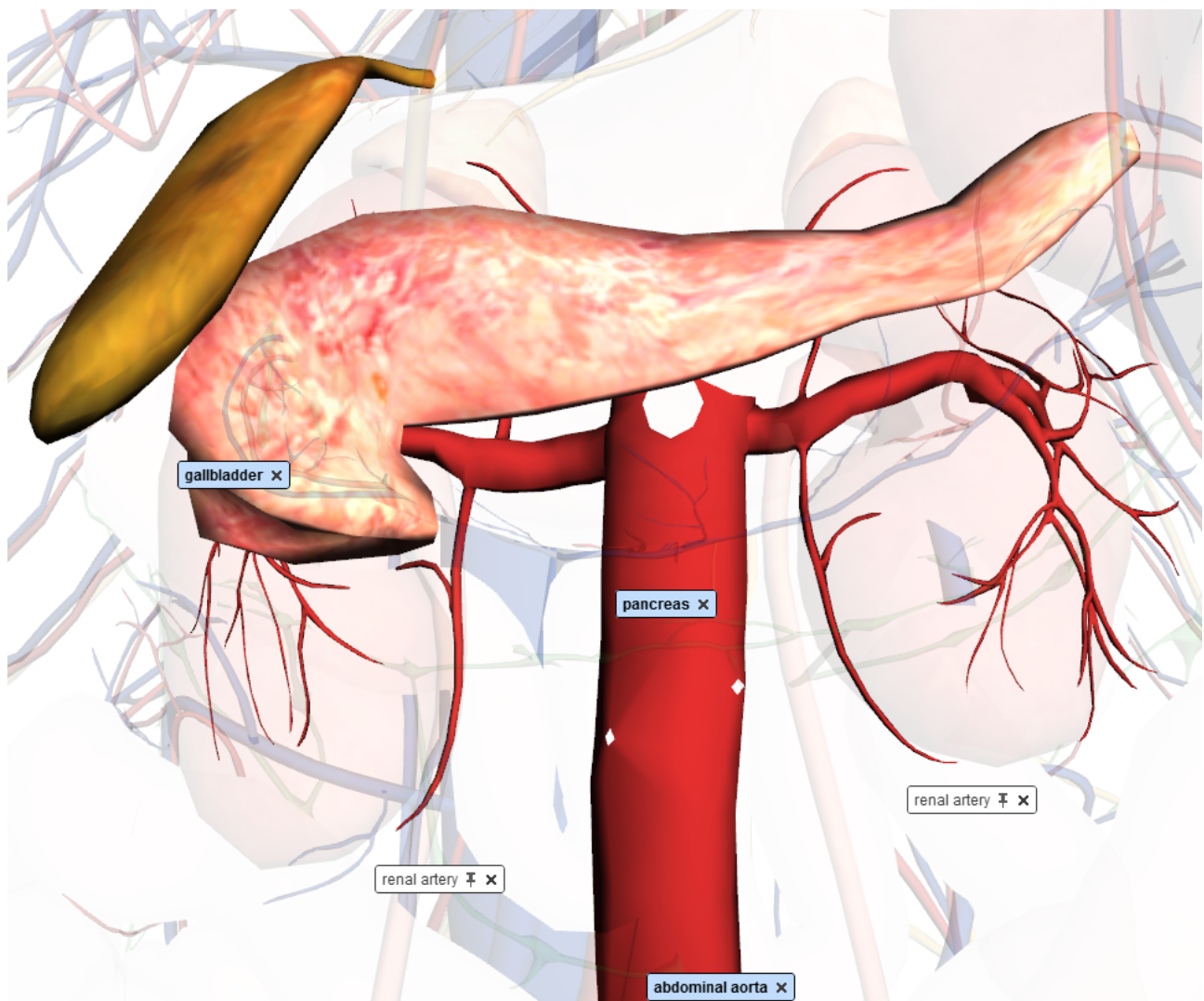


Fig. 3.16: The pancreas, the aorta, the renal artery and the gallbladder (GoogleLabs, 2011b)

This proliferation rate can be seen as the main surrogate marker (Chenevert et al., 2000, Higano et al., 2006, Moffat et al., 2004) ([Section 3.1.7](#)).

3.3.2 Pancreatic tumours

In [Figure 3.16](#), the pancreas, the aorta, the renal artery and the gallbladder are shown in a 3D projection.

General characteristics of pancreatic tumours

Pancreatic cancer is a severe disease with a poor overall 5-year survival rate of about 4% and the fourth most common cause of cancer both in the U.S.A. and internationally (Ades et al., 2010). There is no proper screening-method at present which turns out to be a clear research niche. However, mendelian risk-prediction programmes, ultrasound and highly accurate blood markers can be used for a preliminary screening (Vincent et al., 2011).

It is the most common pancreatic disease among other typical diseases like autoimmune pancreatitis. Pancreatic tumours are divided into solid tumours (exocrine and endocrine) and cystic neoplasias. The ductal adenocarcinoma is the most common type of pancreatic cancer (75 % to 90 % of pancreatic carcinomas (Grünberg et al., 2011)).

In terms of pathophysiology, pancreatic ductal adenocarcinomas develop by intraepithelial neoplasias, intraductal papillary mucinous neoplasms or mucinous cystic neoplasms (Vincent et al., 2011).

As a general marker, it can be stated that pancreatic carcinoma is lower perfused than healthy pancreatic tissue ((Grünberg et al., 2011, Lemke et al., 2009, ECR) and Grünberg et al. (2011)) and pancreatitis, respectively (Klauss et al., 2011).

Staging of pancreatic tumours

Clinical staging of pancreatic tumours is being performed while considering the *TNM classification* (Table 3.2, Table 3.3, Table 3.4, Table 3.5) (Vincent et al., 2011).

Stage	TNM
Stage 0	(Tis, N0, M0)
Stage IA	(T1, N0, M0)
Stage IB	(T2, N0, M0)
Stage IIA	(T3, N0, M0)
Stage III	(T4, any N, M0)
Stage IV	(any T, any N, M1)

Table 3.2: Grading of pancreatic cancer (Vincent et al., 2011): *TNM classification*

Therapy of pancreatic tumours

Therapies include adjuvant and neoadjuvant treatment, radiation therapy, chemotherapy alone or a combined chemoradiotherapy (Vincent et al., 2011).

Tumour	Diagnosis
Tx	primary cannot be assessed
T0	no evidence of primary tumour
Tis	carcinoma in situ
T1	tumour restricted to the pancreas ≤ 2 cm greatest dimension
T2	tumour restricted to the pancreas > 2 cm greatest dimension
T3	tumour extends beyond the pancreas no involvement of coeliac axis or superior mesenteric artery (resectable)
T4	tumour affects the coeliac axis or superior mesenteric artery (unresectable)

Table 3.3: Grading of pancreatic cancer (tumour) (Vincent et al., 2011)

Lymph node	Diagnosis
Nx	regional lymph nodes cannot be assessed
N0	no regional lymph-node metastasis
N1	regional lymph-node metastasis

Table 3.4: Grading of pancreatic cancer (nodes) (Vincent et al., 2011)

Metastasis	Diagnosis
M0	no distant metastasis
M1	distant metastasis

Table 3.5: Grading of pancreatic cancer (metastasis) (Vincent et al., 2011)

An adjuvant therapy is being performed only for curative purpose in terms of a surgical resection and a radiation therapy in addition is discussed controversially and remains unproven.

The neoadjuvant treatment can be used for patients with a rapidly progressing disease and can filter the patients who would not benefit from surgery. Specifically and in contradiction to adjuvant therapy, patients with borderline resectable disease are preferred for neoadjuvant therapy.

A typical radiotherapy is delivering 45-60 Gy over about 6 weeks.

30 % are being downstaged by chemotherapy and it is currently under research if chemotherapy alone could be more efficient than a combined radiotherapy Vincent et al. (2011).

Surrogate markers In (Grünberg et al., 2011, ECR), it has been reported that the perfusion in the pancreas also changes under therapy (Section 3.1.7). Vincent

et al. (2011) describes the standard RECIST (response evaluation criteria in solid tumours) measured by CT as a marker and additionally explains mutant DNA or changes in mutant DNA as probable surrogates.

Material and methods

In this chapter, the material and methods concerning two basic studies are depicted, regarding the reproducible quantification of parameters while using diffusion weighted imaging.

Firstly, the automated, objective and reproducible delineation and quantification of high- and low-proliferating areas in heterogeneous high grade gliomas, while using a statistical machine learning Expectation Maximization (EM) (Bishop, 2006, Dempster et al., 1977, Hastie et al., 2009) algorithm.

Secondly, the application of the *IVIM* model and the reproducible determination of derived parameters such as ADC , f and D through rigid linear image registration.

For both studies, the software development as the main task, is described in the beginning in [Section 4.1](#). In 'Preliminary experimental procedures', the principal workflow, used devices and sequences are described ([Section 4.2](#)).

This chapter finishes with a postprocessing section ([Section 4.3](#)) and encapsulates the application of the developed software.

Note: To emphasize the software development, it has been shifted to the first place but with the disadvantage of forward references to the respective equations.

4.1 Software development

This section describes the software development of the two basic studies. First, a reproducible separation and quantification of high- and low-proliferative areas ([Section 4.1.1](#)), and second, the *IVIM* model and reproducible parameters in diffusion weighted images ([Section 4.1.2](#)).

4.1.1 A reproducible separation and quantification of high- and low-proliferative areas in gliomas

In this section, the software development of an automated, objective and reproducible delineation and quantification of high- and low-proliferating areas in high grade gliomas is illustrated.

This delineation is impeded by partial volume effects, signal inhomogeneities and gliding borders due to the heterogeneous nature of high grade gliomas. Here, we present an algorithm to objectively delineate and probabilistically quantify areas of high- and low-proliferation in heterogeneous high grade gliomas, resulting in a reproducible quantification in regions of tissue inhomogeneity.

Firstly, we used an Expectation Maximization (EM) algorithm, applied on a Gaussian mixture model, consisting of pure superpositions of Gaussian distributions and secondly, we used a model which additionally considers partial volume effects to assign voxels to a high- and low-proliferating class, respectively.

Both methods were tested in terms of reproducibility by initialization seeds onto low-proliferating and high-proliferating samples. The pure Gaussian clustering excelled the partial volume model concerning objectivity and could be automatically initialized. This model has to be tested using more statistical data in further studies. Thus, a new, rapid, reproducible and automatic method to separate and quantify these regions in a nearly user independent manner has been achieved.

The first section 'Illustration of the flow of information' explains the principal flow of information as an activity diagram. 'Module based description' explains the software based on MeVisLab (Fraunhofer MEVIS, Bremen) modules. Finally, the realization of the software is given in 'Realization' with help of UML diagrams.

The application to include additional functional information such as $rCBV$ is described consecutively in the end of the section.

Illustration of the flow of information

The principal flow of information ([Figure 4.1](#)) is divided into 'Acquisition' and 'Preprocessing' ([Section 4.2.1](#)) and the postprocessing part consists of 'Clustering' and 'Quantification' ([Section 4.3.1](#)). The statistical evaluation is taking place in [Section 5.1](#).

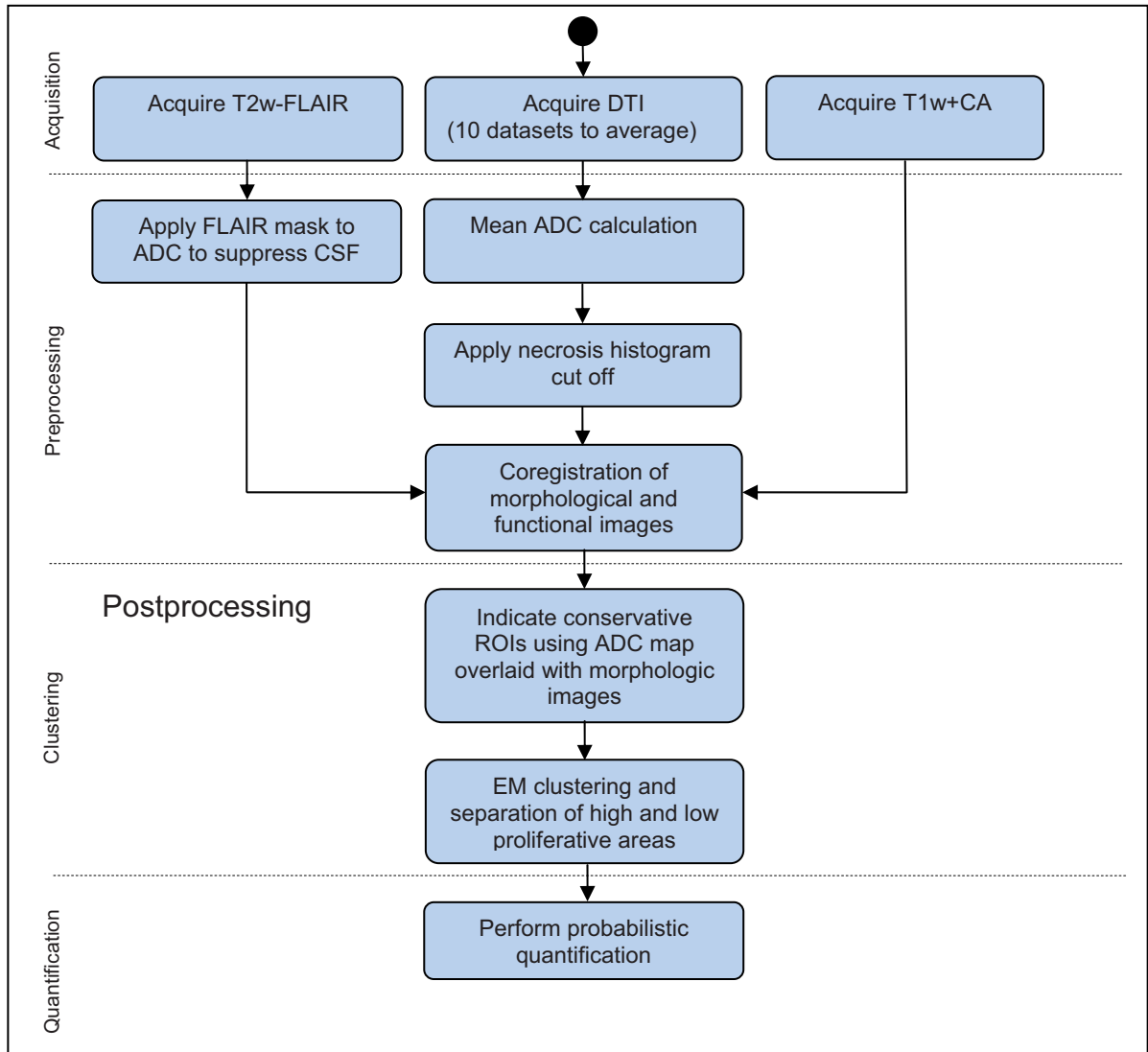


Fig. 4.1: The principal flow of information is shown as an activity diagram (taken from Simon et al. (2011))

Module based description

This section entails a MeVisLab (Fraunhofer, MEVIS, Bremen, Germany) module based description of the existing modules.

Firstly, the preprocessing modules are elucidated in 'Preprocessing' and secondly, the clustering and quantification modules are depicted in 'Clustering and Quantification'.

Preprocessing

The main part of the preprocessing has been performed independently in NeuroQLab (Fraunhofer MEVIS, Bremen, Germany). The spatially matched, B-spline interpolated and resampled datasets were retrieved by this software. The co-registration and trilinear interpolation (Section 3.2.5) between the multimodal datasets have been done by an automatic matching of the different world coordinate systems, an integrated manual rigid pre registration, an automatic linear registration module based on the downhill simplex optimizer using the normalized mutual information metric to achieve an objective spatial realignment independent from the user (Section 3.2.5). The ADC (Section 3.1.7) calculation or strength for the study is taking place within the already given module `DiffusionTensorAnalysis`. The ADC can be calculated in a scaled and non scaled way. The non scaled variant implements Equation 4.3. The scaled variant has been used for display properties pertaining to the histogram and the fixed bin size and is calculated by Equation 4.1.

$$(\lambda_1 + \lambda_2 + \lambda_3) \cdot (3 \cdot 0.003 \cdot 65535 = 21845000) \quad (4.1)$$

In Figure 4.3, the preprocessing modules are shown. Here, the multimodal images are being orthogonally reformatted onto the calculated ADC map. Furthermore, the extraction of necrotic areas and CSF is being performed. The `ScalingToUInt` module scales the image to a fixed size of unsigned int. The macro module `GenerateROISForCluster` is responsible for the ROI generation. An external ROI can be loaded by `LoadCSOGTV`. The scaled conservative ROIs can be loaded by `(loadLow, loadHigh)` and the automatic seed points are being generated in `GenerateROIHighMalignantTumour` and `GenerateROILowMalignantTumour`, respectively. Both modules are interconnected so that the drawn ROI is available in both viewer modules. The two non visible modules `generateInitROIs` and `determineCOG` within the macro module `GenerateROIHighMalignantTumour` and `GenerateROILowMalignantTumour` generate the ROIs in concentric circles around the calculated center of gravity. Eventually, the ROIs are being concatenated.

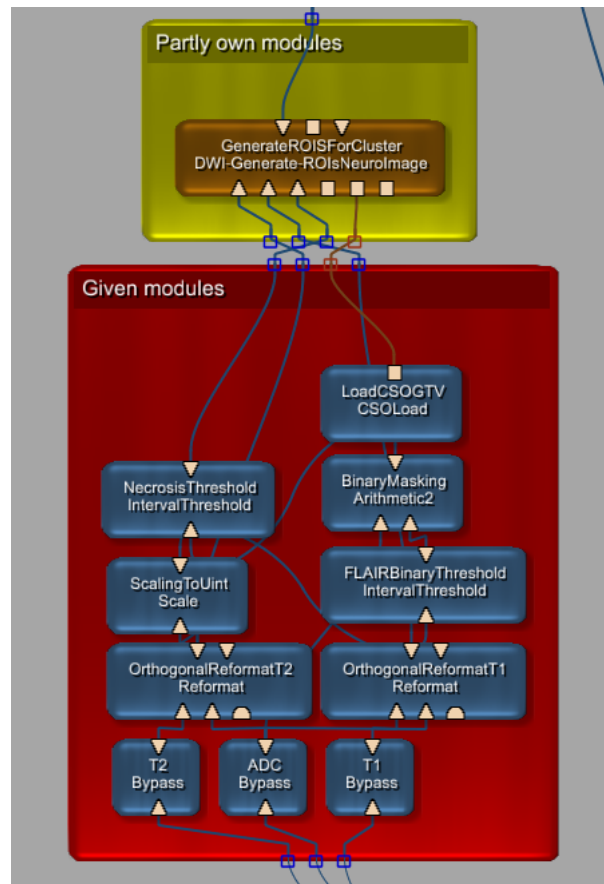


Fig. 4.2: A MeVisLab based description of the preprocessing modules

Clustering and quantification

Clustering The modules, which are responsible for the clustering and quantification, are shown in Figure 4.4. The given module `ParameterGeneration` determines an initial guess for a Gaussian mixture model given in Equation 4.21. The generated initialization ROIs can be used to create the model. In `ManualParameters` the parameters can be generated manually using the initialization procedure in Equation 4.19. The EM optimization process by itself is taking place in `EMParameterOptimization` and uses the upscaled histogram of the GTV as input. The Expectation process is optimizing the parameters, i.e. γ_k by Equation 4.24 and the Maximization procedure generates a Gaussian mixture model until the Log-likelihood optimization is completed (Equation 4.28). The completed parameters are evaluated by determining the final γ_k in `PosteriorProbability`. The module has been modified to generate also

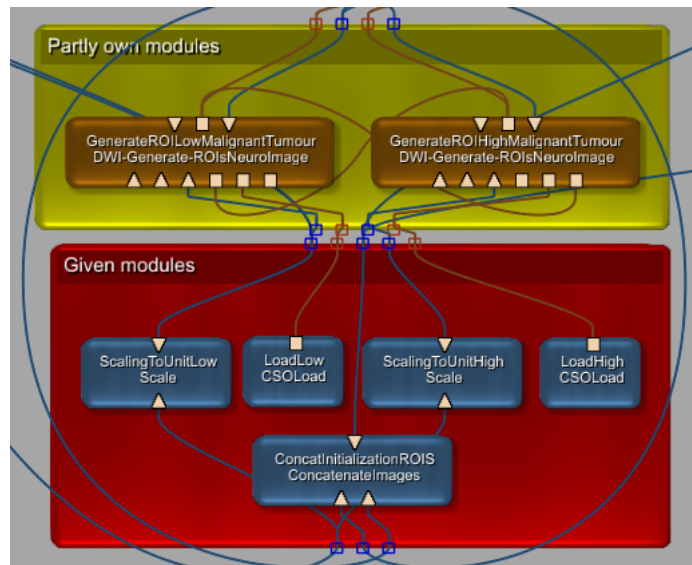


Fig. 4.3: A MeVisLab based description of the initialization modules

the direct posterior probability apart from the upscaled probability for visualization purposes.

Quantification

The final probabilistic quantification given in (Equation 4.24, Equation 4.32, Equation 4.33, Equation 4.34 and Equation 4.35) is taking place in the own developed module `ProbabilisticADCQuantification` and uses the original ADC values as input and mask. The third input delivers the posterior probability γ_k .

Important to note is that the original ADC can be replaced with every diffusion weighted derived value, covering the same region following Stieltjes et al. (2006). Furthermore, if the ADC is transformed to another representation within the clustering via an 'one-way function', the quantification can be always done via the described module. Thus, this approach enables a novel probabilistic quantification based on γ_k , an arbitrary quantity Q to calculate 4 moments and to determine the probabilistic volume within the calculated clusters.

Visualization of the histograms The visualization of the histograms is displayed in Figure 4.5. The 10 sample histograms can be loaded by the respective histogram modules which have been saved previously by a MeVisLab specific XML format. The macro module `AverageHistograms` consists of the own combination of developed modules `HistogramArithmetic` and `HistogramArithmeticConst` where arbitrary arithmetic functions on a transformed

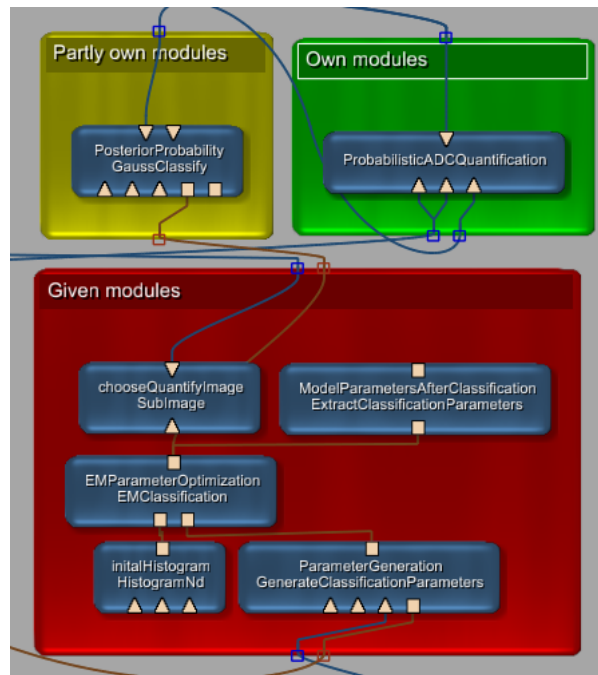


Fig. 4.4: A MeVisLab based description of the EM Clustering modules and probabilistic quantification

Curvelist can be performed by Equation 5.1. The module DWIGaussApproximation is a multipurpose tool to fit an univariate Gaussian by application of the toolkit root (root, CERN, Switzerland) and the max voxelsize can be automatically detected by the image input, to visualize a Gaussian mixture model (Equation 4.22) and especially in combination with the partial volume class (Equation 4.38). The module Merge10Histograms is displaying the given Curvelists in combination with their μ in one diagram.

Realization

The realization of the software is explained by an UML description of the required modules in 'Implementation and UML description of required modules'. The user interface is depicted in 'Implementation and user interface'.

Implementation and UML description of required modules

The following modules are described consecutively by an UML approach: The 'Preprocessing modules' and the 'Quantification modules'.

Preprocessing modules For initialization, the center of gravity module DWIDetermineCOG is being used to determine the center of gravity of the ROI in world and voxel coordinates by a three dimensional vector (Figure 4.6a). The

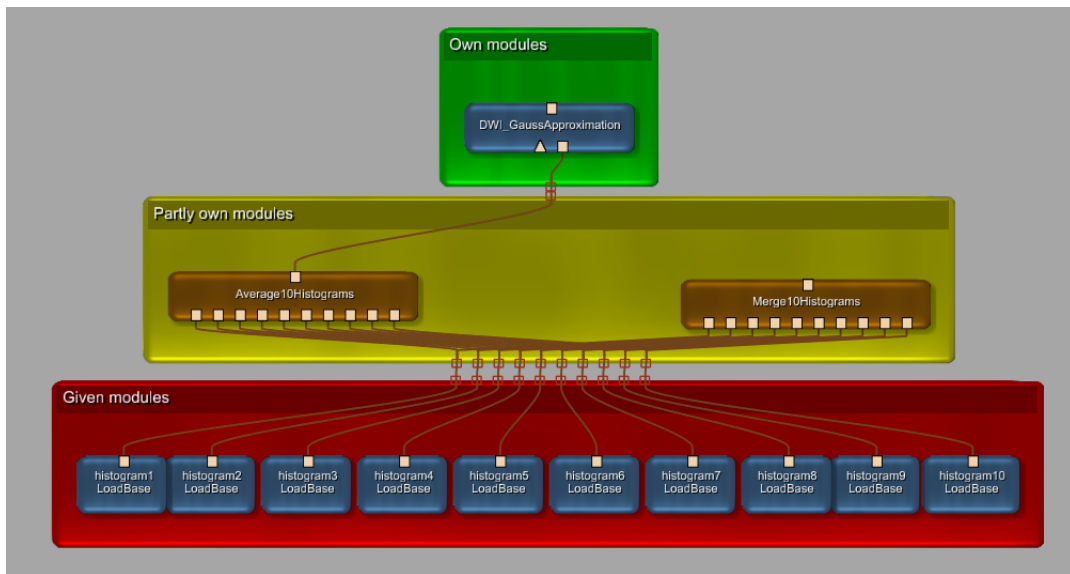


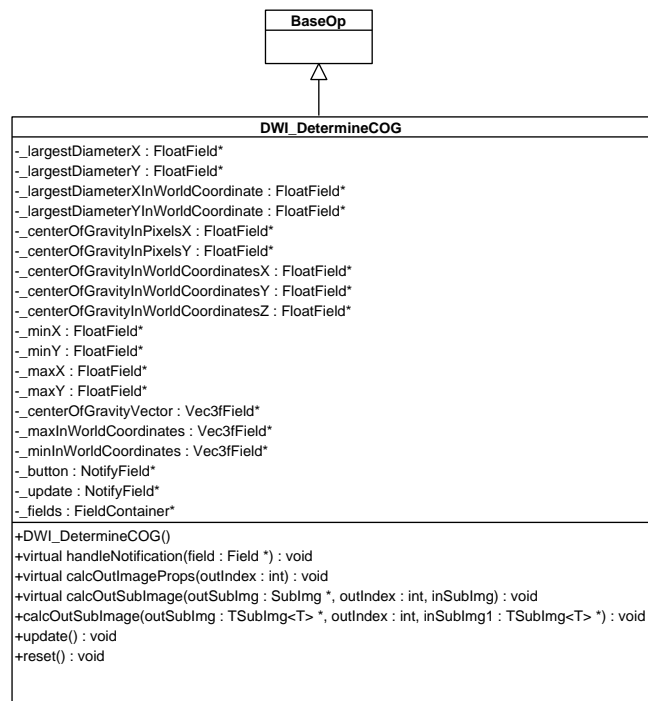
Fig. 4.5: A MeVisLab based description of the histogram displaying and averaging

interconnected module `DWICreateCSOList` is determining the seed ROIs by taking the center of gravity of the ROI by the parameter `myCOGInWorldCoordinates` (Figure 4.6b). The minimum and maximum can be adjusted by `_myMinInWorldCoordinates` and `_myMaxInWorldCoordinates`.

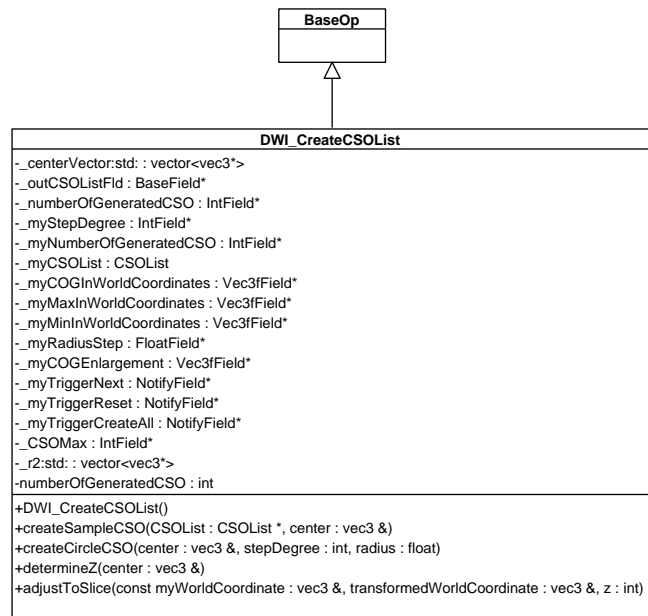
Quantification modules In Figure 4.7, the UML diagram of the probabilistic quantification is depicted. The main image processing operation `calcOutSubImage(...)` is operating on the three images simultaneously (`ADC` as input and mask plus posterior probability γ_k).

Visualization of the histograms For the histogram combination, the modules `HistogramArithmetic` (Figure 4.8b) and `HistogramArithmeticConst` (Figure 4.8a) are used. In the first case two curve data objects `_myCurveData` and `myCurveData2` are being arithmetically transformed to result in an outputlist `_myCurveData3`. The `const` variant is transforming the curve data object `_myCurveData` by a scalar value to `_myCurveData2`.

In `DWIGaussApproximation` (see Figure 4.9) an input histogram `_histo` can be fitted by an univariate Gaussian. The range of the Gaussian fit can be adjusted by `DWIGaussApproximationB` and `DWIGaussApproximationE`, respectively. Furthermore, a complete Gaussian mixture model can be displayed with and without the partial volume class (by activating the switch `_myPartialVolumeSwitch`).



(a)



(b)

Fig. 4.6: (a) UML description of DWIDetermineCOG and (b) DWICreateCSOList

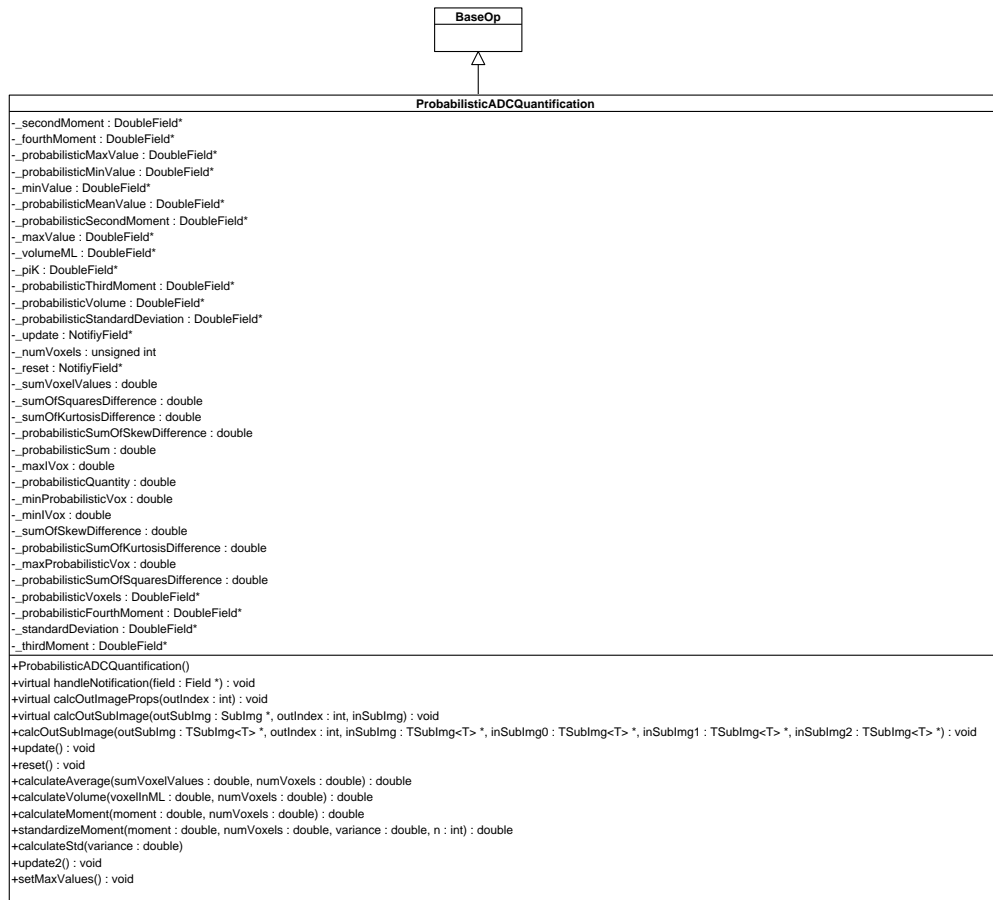


Fig. 4.7: UML description of ProbabilisticADCQuantification

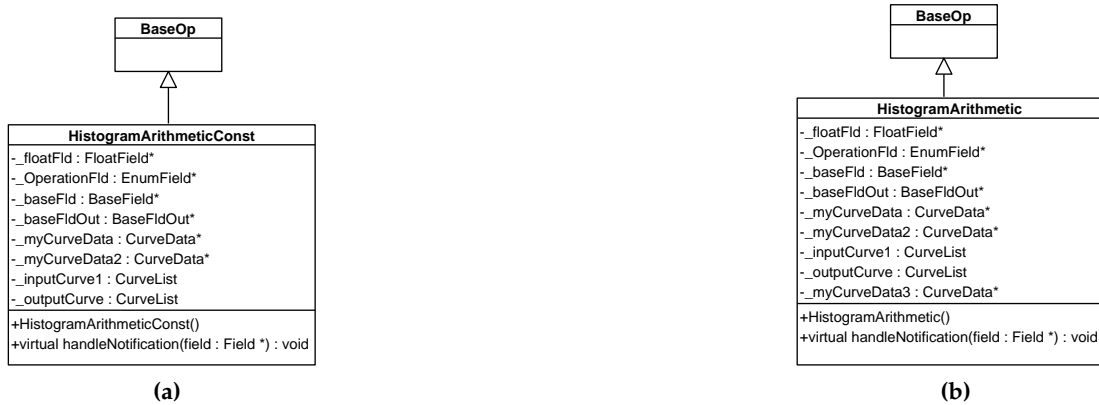


Fig. 4.8: (a) UML diagrams of HistogramArithmeticConst and (b) HistogramArithmetic

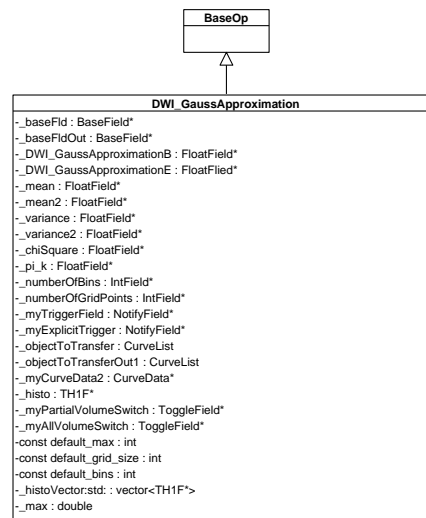


Fig. 4.9: UML description of DWIGaussApproximation

Implementation and user interface

Here, the user interface is described by a 'Clustering prototype'.

Clustering prototype A screenshot of the clustering prototype is shown in [Figure 4.10](#). Three automatic quantification modes can be chosen:

1. Automatic initialization by concentric clustering seeds and an automatic quantification per clustering seed using the standard Gaussian mixture model ([Equation 4.23](#)).
2. Automatic initialization by concentric clustering seeds and an automatic quantification per clustering seed using the partial volume model ([Equation 4.37](#)).
3. Using the initialization Equation given in [Equation 4.19](#).

In all three procedures, the clustering result screenshot and the probabilistic quantification ([Equation 4.24](#), [Equation 4.32](#), [Equation 4.33](#), [Equation 4.34](#)) and [Equation 4.35](#) are saved into a special folder. Furthermore, a screenshot of the clustered GTV in a high-proliferating and low-proliferating region is recorded as well. A histogram sample of the posterior probability γ_k is also shown to complete the probabilistic quantification.

The properties of the automatic initialization procedure can be adjusted in (`Radiushighmalignant`, `Radiuslowmalignant`, `Degreehighmalignant`, `Degreelowmalignant`). The iterations can be modified in `numberofruns`. Underneath, the center of gravity and the surrounding bounding box can be modified, accordingly.

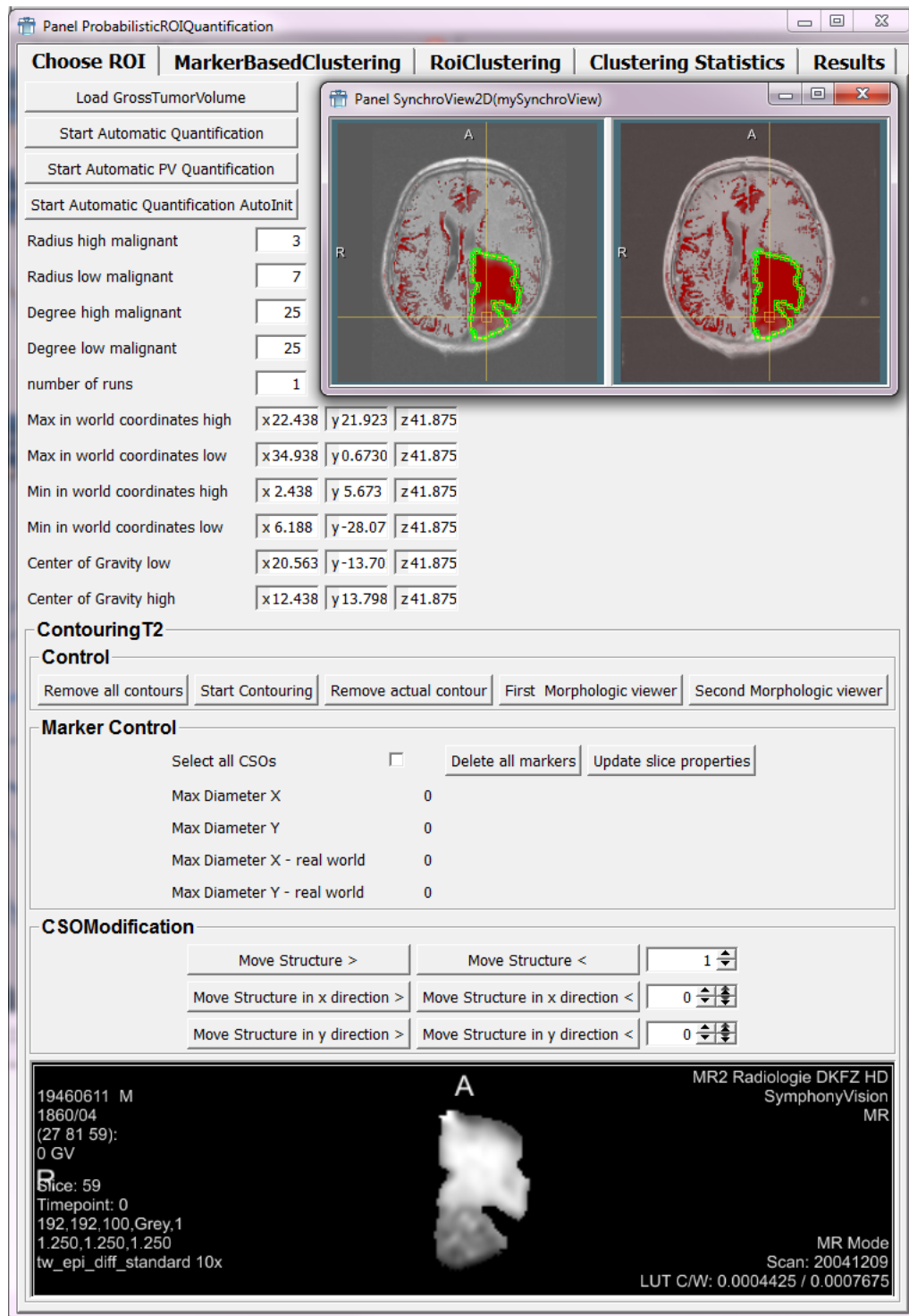


Fig. 4.10: UML description of clustering prototype

The multimodal viewer is showing the *GTV* und structures can be loaded via `Load GrossTumorVolume` or drawn directly onto the viewer. Apart from the multimodal `Synchroviewer` which shows the functional *ADC* map in red with overlaid T1 and T2-FLAIR, respectively, the morphologic images can be also displayed in an exclusive independent viewer by pressing on the morphologic viewer buttons.

Markers can be also added to measure the diameter of the *GTV* in an automatic and in a manual way by application of a ruler to encompass certain regions within the *GTV*.

The `CSOModification` section establishes the possibility to move the drawn *GTV* in x and y direction. Furthermore, the CSO can be copied to an arbitrary number of slices in z direction.

An additional experimental initialization of the clustering can be performed by choosing `MarkerBasedClustering`, where markers can be used to build the Gaussian initialization set with gray value samples.

In the `ROIclustering` section, conservative ROIs as shown in [Figure 4.1](#), can be drawn manually to form the Gaussian mixture model.

Including functional imaging such as perfusion as additional information

In this section, the software development concerning the additional functional imaging technique such as perfusion (*rCBV*) is given. Firstly, the flow of information is illustrated in 'Illustration of the flow of information'. A module based description with help of MeVisLab (Fraunhofer MEVIS, Bremen) modules is elaborated and second the realization of the software is depicted by UML diagrams in 'Realization'.

Illustration of the flow of information

The principal flow of information is divided into 'Acquisition' and 'Preprocessing' [Section 4.2.1](#) and 'Segmentation' and 'Quantification', respectively, which belongs to the 'Postprocessing' [Section 4.3.1](#) ([Section 4.11](#)). The evaluation is shown in [Section 5.1.4](#).

Module based description

In [Figure 4.12](#) the modules pertaining to the *percentile thresholding* are shown. The delineated *GTV* is being firstly processed by an `ImagePropertyConvert`. The module transforms the image to **unsigned int**. Afterwards, the `interval-Threshold` clamps the image by $\theta_{low} = \min(GTV) + 1$ and $\theta_{high} = \max(GTV) - 1$. By the first clamping, all background values are switched to -1 so that the background is excluded by performing the *percentile thresholding* and does not

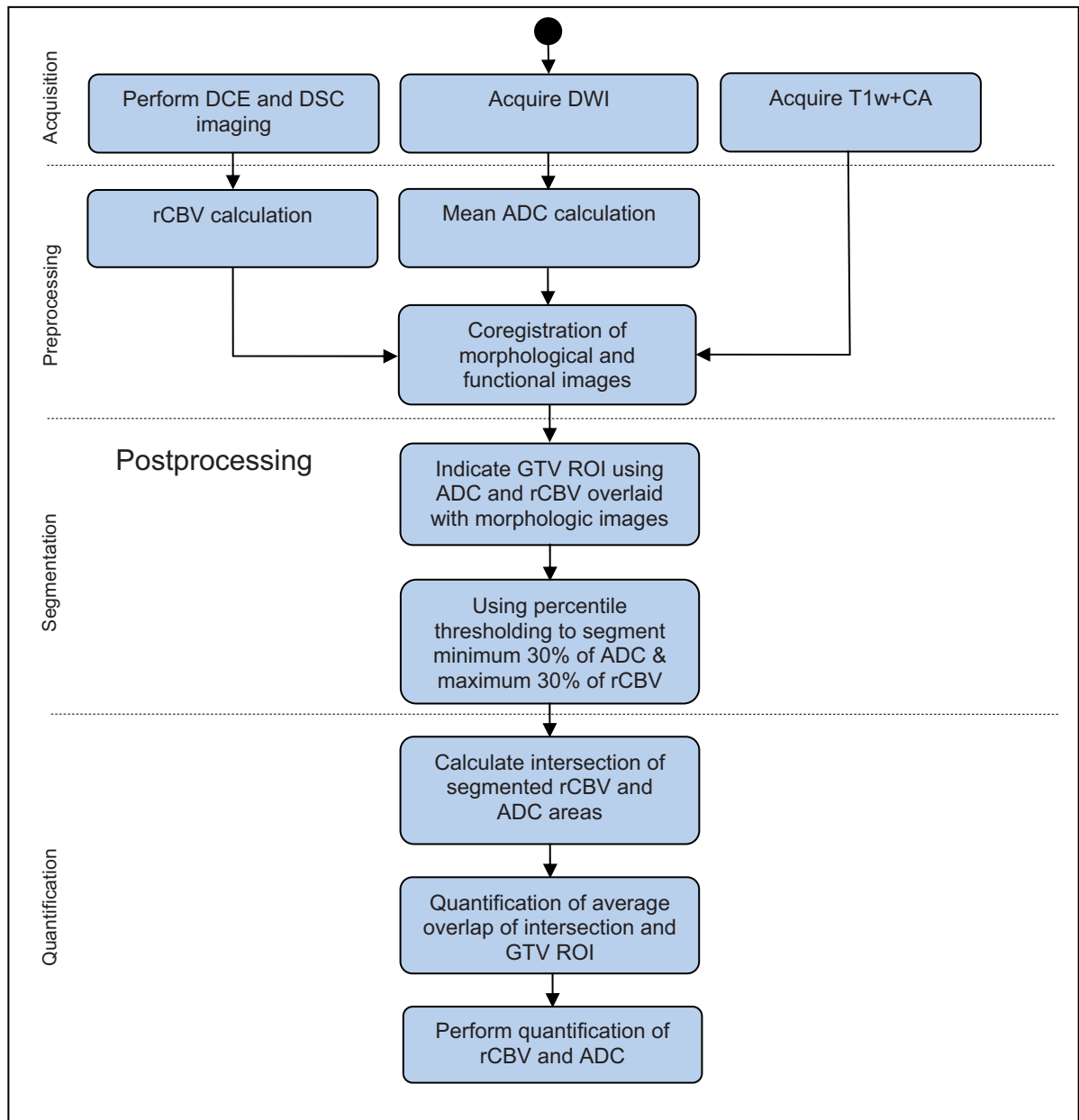


Fig. 4.11: The principal flow of information is shown as an activity diagram of the rCBV study

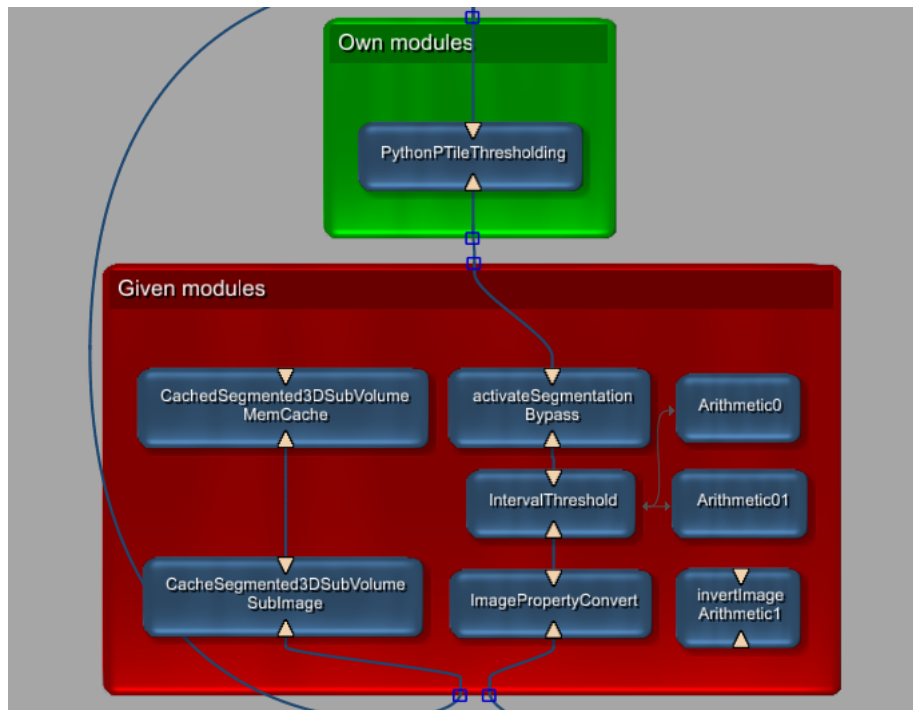


Fig. 4.12: MeVisLab based module description of the percentile thresholding

count to the integral of the probability distribution. The second clamp operation is being used in the inverted case to exclude the zero values from the statistical information. The inversion is being done by activation of the module `invertImage`.

Due to performance issues, the *percentile thresholding* can be locked by activating and deactivating `activateSegmentation`. A complete locking of the *percentile thresholding* is being performed by copying the subvolume in `CacheSegmented3DSubVolume` to the cache in `CachedSegmented3DSubVolume`. In the last step, the quantification can be performed without recalculating the percentile.

The module `PythonPTileThresholding` performs the thresholding of the GTV given by (Equation 4.39 Equation 4.40, Equation 4.40, Equation 4.41 and Equation 4.42).

Realization

The realization consists of the implementation and UML description ('Implementation and UML description of required modules') and of screenshots of the user interface in 'Implementation and user interface'.

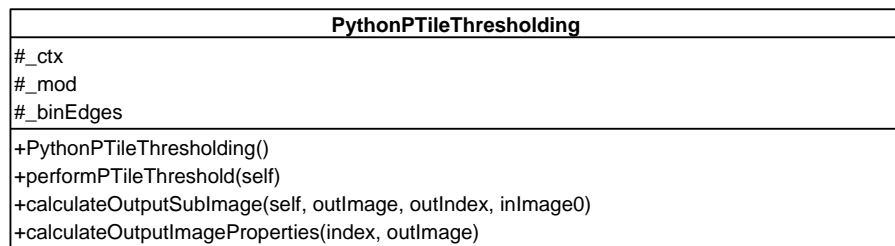


Fig. 4.13: UML description of PythonPTileThresholding

Implementation and UML description of required modules In Figure 4.13, the UML diagram of the implemented module PythonPTileThresholding is shown. In `calculateOutputSubImage(self, outImage, outIndex, inImage0)` the whole thresholding is being performed onto the whole delineated GTV by setting a threshold value θ . The method `performPTileThreshold(self)` calculates the normalized cumulative probability histogram (Equation 4.40, and Equation 4.41). The threshold value θ is being determined by Equation 4.42.

Implementation and user interface This section is subdivided into a segmentation part ('Segmentation') where the user interface of the segmentation is described in further detail and a quantification part ('Quantification') where the derived quantification values can be found.

Segmentation An example of the user interface of the segmentation module can be found in Figure 4.14. In the centre, the delineated glioblastoma is shown in a Synchronviewer, displaying the *rCBV* map with underlying *T1 postCM* (left). On the right side, the *ADC* map is shown. Underneath, the pure *ADC* map, the *rCBV* map and the *T1 postCM* is depicted. 30 % of the pixels of the lower bend of the *ADC* map are shown on the left in the lower quantification viewer and determine 30 % of the highest malignant area. 30 % of the pixels of the highest malignant area of the *rCBV* map are shown in the right quantification viewer. The *rCBV* map is inverted and thus is showing 30 % of the upper bend of the pixels. Both segmentations are transferred to the cache so that the percentile thresholding is deactivated.

In *QuantificationControl*, the connected multimodal viewers can be raised. Furthermore, the quantification image can be chosen by switching `Push - background image`. `Invert the quantification image` performs the operation: $\max(GTV) - GTV(x)$. `pushCSO` copies the segmentation object to the next modality shown in the right viewer. Moreover, the segmentation can be activated and deactivated. The cache is being filled by pressing on `transfer segmentation to cache` and a subvolume can be chosen by pressing on `Take subvolume`.

In the *Overlay control* tab, the different multimodal viewers can be activated and deactivated.

The *CSOModification* tab enables the arbitrarily moving of the contour segmentation object in x and y direction. Furthermore, contour segmentation objects can be copied arbitrarily into z dimension. Moreover, the contour segmentation objects can be selected and deleted.

Quantification The first quantification on [Figure 4.14](#) in the marker control box can be used to determine the diameter in x, y and z. Furthermore, arbitrary markers can be drawn as a ruler onto the `SynchroViewer` to perform certain manual measurements.

The main quantification is depicted on [Figure 4.14](#). The viewer shows the *ADC* map in green, the *rCBV* map in blue and the intersection by red colour. The quantification values depicted by ([Equation 4.43](#)) ([Section 3.2.4](#)), [Equation 4.46](#), [Equation 4.47](#)) and derived values are shown here.

4.1.2 The IVIM model and reproducible derived parameters in diffusion weighted images

In this section, the software development of a reproducible determination of parameters in diffusion weighted images by the application of the *IVIM* model ([Section 3.1.7](#)) is shown. Three derived parameters are evaluated here in terms of reproducibility: f , D and the *ADC*.

The principal flow of information is illustrated in 'Illustration of the flow of information'.

A MeVisLab (Fraunhofer MEVIS, Bremen) module based description is depicted in 'Module based description'.

In the consecutive part, the realization by an UML approach and user interface is depicted in 'Realization'.

Illustration of the flow of information

The principal flow of information is shown in [Figure 4.16](#) and is divided into 'Acquisition' and 'Preprocessing' ([Section 4.2.2](#)) on the one hand and 'Registration' and 'Quantification' on the other hand as 'Postprocessing' ([Section 4.3.2](#)). The 'Evaluation' is being done in [Section 5.2](#).

Module based description

The module based description entails the 'Preprocessing', elucidates the 'Registration' and 'Quantification' depicts the used quantification modules.

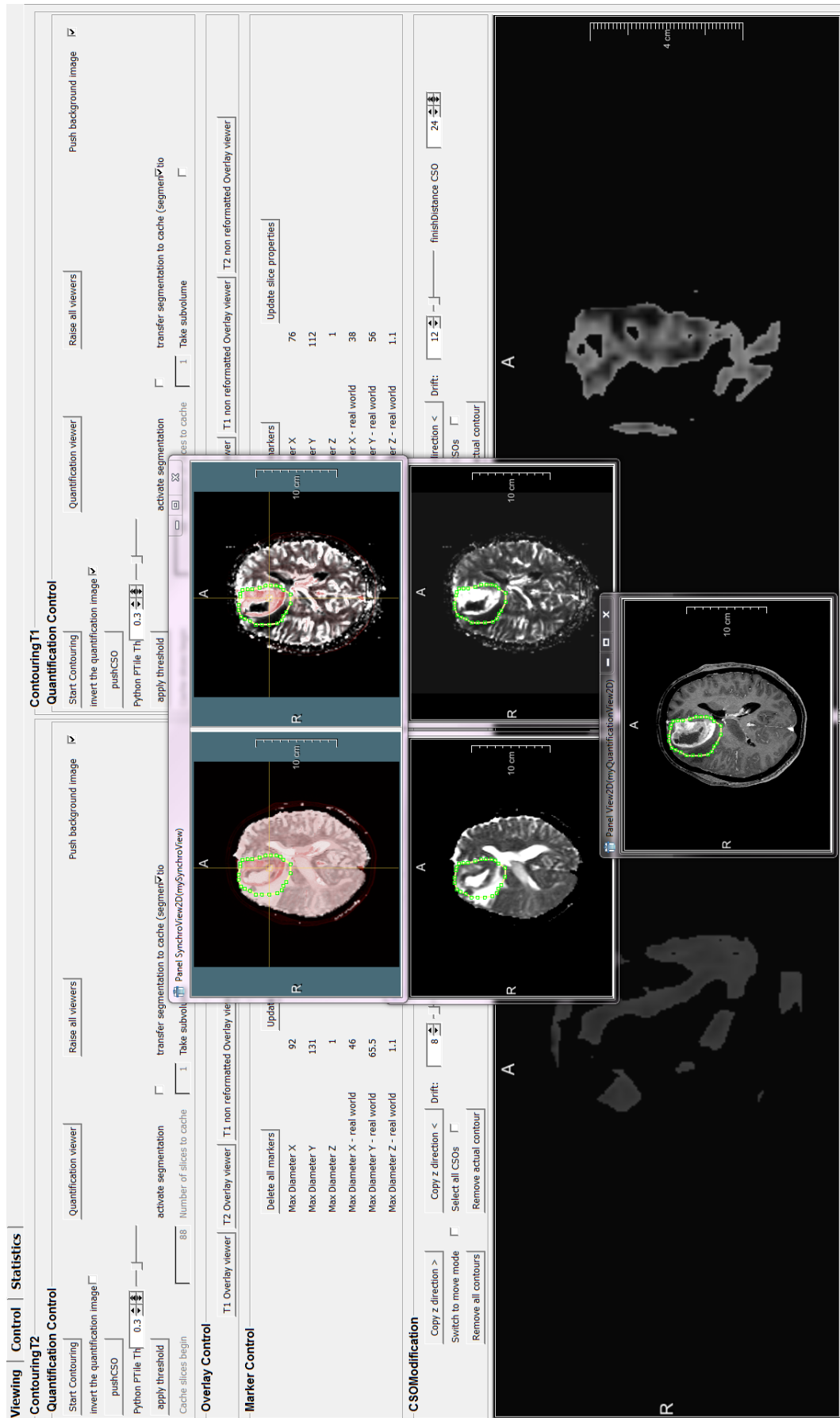


Fig. 4.14: Sample of the multimodal percentile segmentation

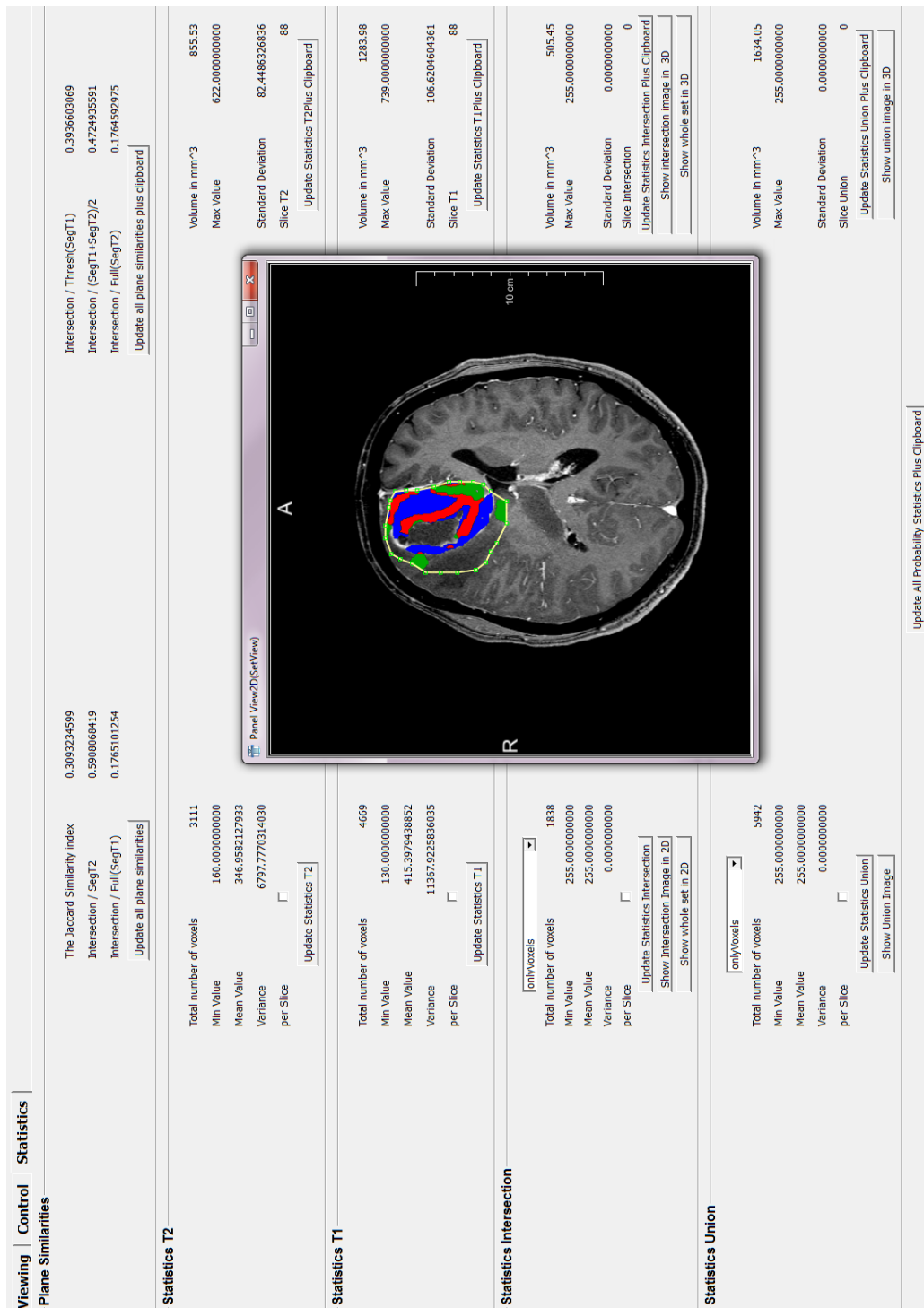


Fig. 4.15: Sample quantification. The ADC map is shown in green whereas the rCBV map is highlighted in blue. The intersection is delineated by the red colour.

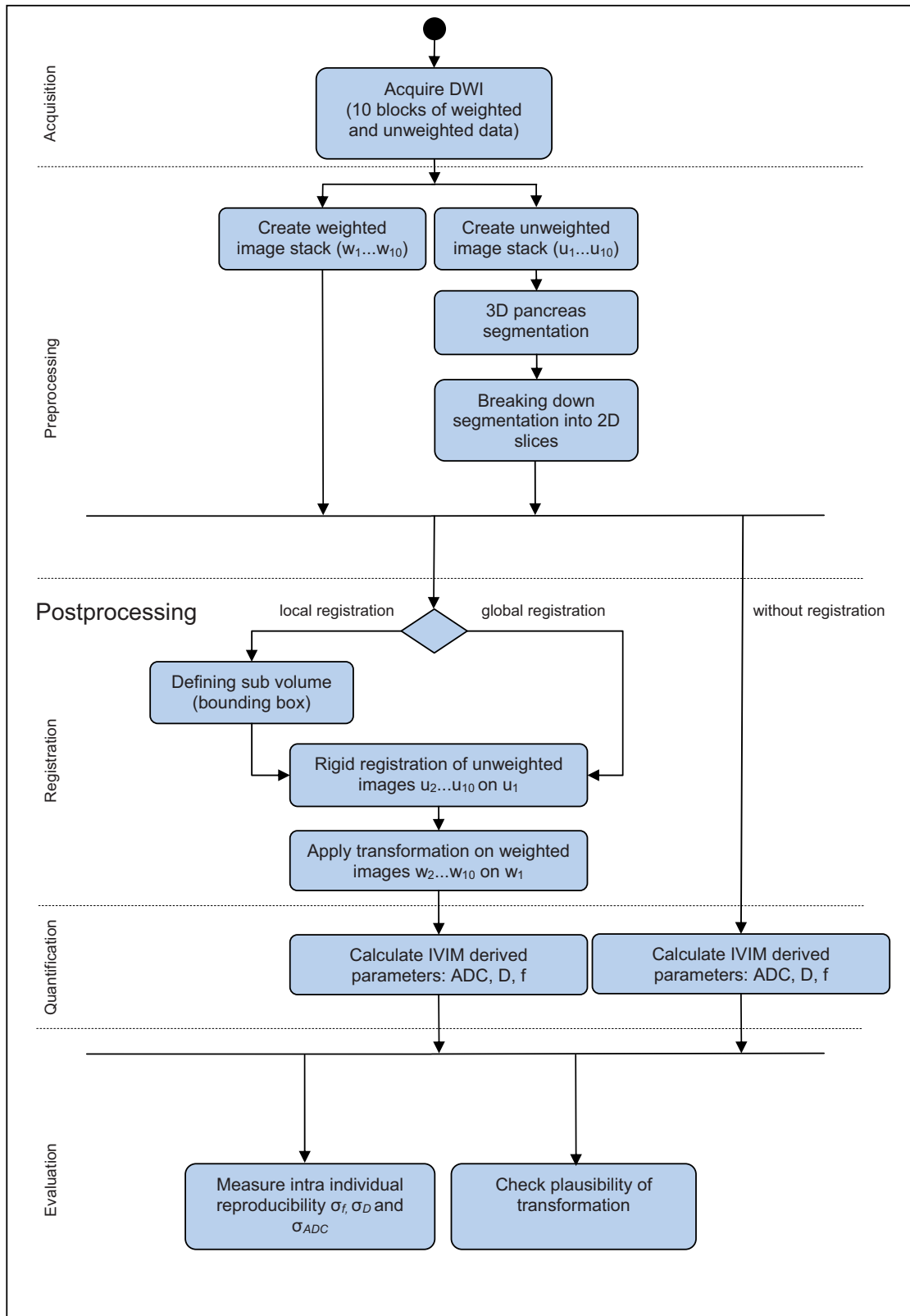


Fig. 4.16: Flow of IVIM model and reproducible parameters in diffusion weighted images

Preprocessing

The automatic preprocessing of the data and splitting is being done in an exclusive macro module 'Breathholdsorter'. Here, the data sets are being copied into their respective breathhold phase and **b** value.

Registration

The stack registration (Section 3.2.5) onto the unweighted images is being performed by a given rigid registration module `myLinearRegistrationGUI` (Figure 4.17). The obtained transformation matrices are saved and then being applied subsequently onto the weighted images in the pair of the acquisition. The inputs are on demand automatically being filled by the *fixedImage* (input0) (interconnected by input0 of `PancreasRegistration`, *movingImage* (*Subvolume*) (input1) (interconnected by input1 of `PancreasRegistration`). The third input contains the complete *movingImage* (delivered by input 2 of `PancreasRegistration`). The linearly registered images are saved in `ImageComposerValued` and `ImageComposerNonValued`, respectively, to perform a quantification step onto the newly registered image stacks.

In Figure 4.18, the transformation matrices \mathcal{T}_u are being used to transform the weighted images with image matrix \mathcal{I}_w , obtained by module `info`. The operation $\mathcal{T}_u \cdot \mathcal{I}_w$ is then being performed, consecutively. `ImagePropertyConvert` sets the matrix within the image. The `Reformat` performs a linear interpolation and `WriteTraceTag` writes the information into the **DICOM-Tag** to be eventually saved with `DicomTool` using the **b** value vector \vec{b} in `bvalueList`. This saving capability is also available in `myLinearRegistrationGUI` to save the unweighted images.

With `CropByBoundingBox`, a subvolume of the image can be used as a moving subimage to perform a bounding box registration.

Quantification

The main quantification is taking place in Figure 4.19. Firstly, the signal is being normalized in `PancreasNormalizer` (Equation 4.48). This module has two inputs. The first input is being filled with the non weighted and weighted image stack (Figure 4.34). The second input can contain an external vector of **b** values. In this case, it is done internally by an extraction of the DICOM values. The first output is delivering the normalized images plus an artificially normalized zero valued image (i.e. $\frac{S}{S_0} = 1$) and is directly interconnected with the module `IVIMCalculator`. The second output contains the changed **b** value vector plus the additional 0.

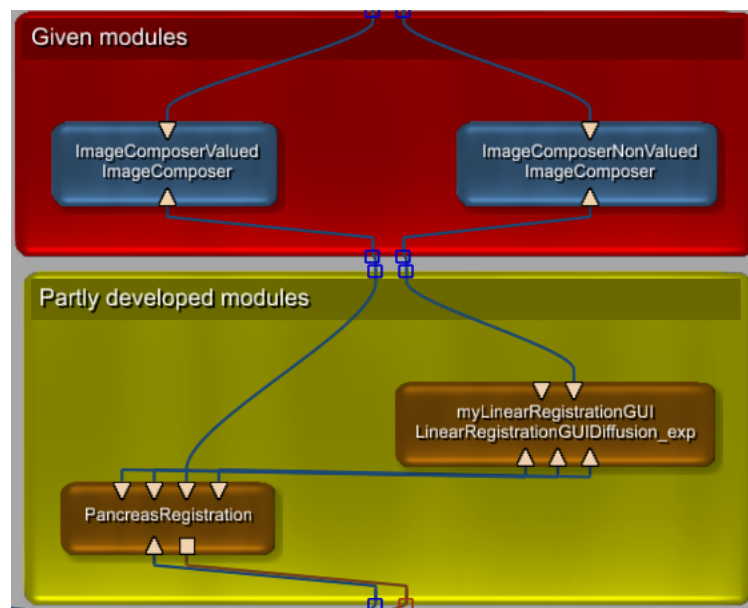


Fig. 4.17: MeVisLab based module description of registration modules

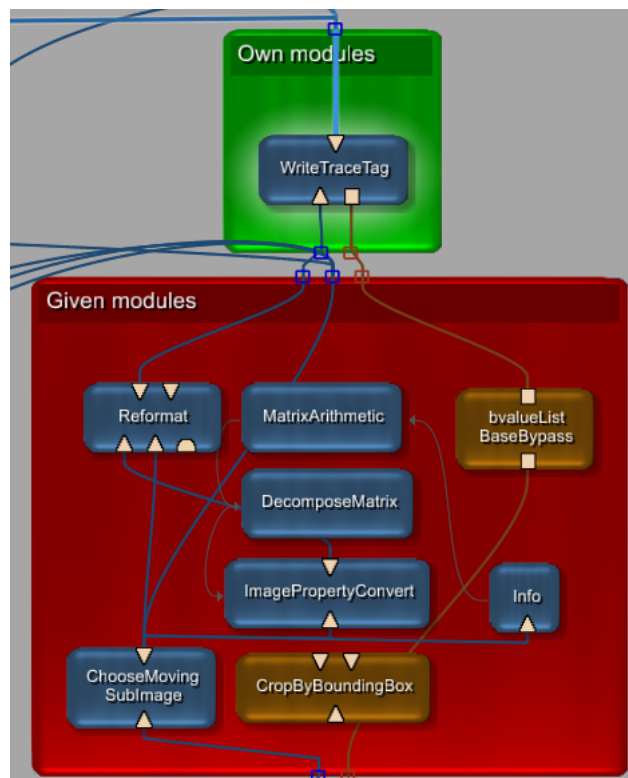


Fig. 4.18: MeVisLab based module description of the registration modules part 2

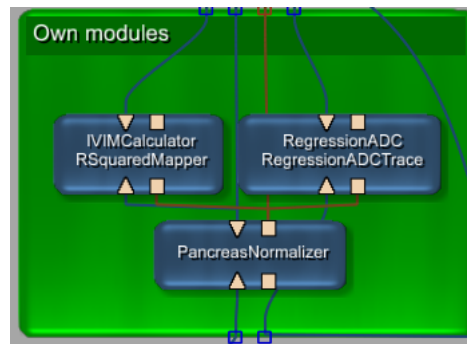


Fig. 4.19: MeVisLab based module description of the quantification modules

In `IVIMCalculator`, the *IVIM* (Equation 4.52) derived parameters, such as f and D are being calculated by the Levenberg Marquardt approach (Equation 4.54, Equation 4.54) delivered by the first output as an f or D map. The \mathbf{b} values are delivered via the second \mathbf{b} value output.

The *ADC* in two versions is derived by Equation 4.50 (fixed model) and Equation 4.49 (non fixed model) and solved by Equation 4.51. This calculation is taking place in module `RegressionADC`. The first output delivers the calculated *ADC* map in the two mentioned versions. The second output contains the unchanged version of the \mathbf{b} value vector and can be used in further operations.

Realization

The realization of the software is explained in this section. Firstly, the 'Implementation and UML description of required modules' is elucidated. Secondly, the 'Implementation and user interface' is described.

Implementation and UML description of required modules

Preprocessing In Figure 4.20, the UML diagram of the processing unit of module `Breathholdsorter` is shown. The \mathbf{b} values are being extracted by `getPrincipalBValues(self)` and used to create unweighted and weighted folders to perform a resorting dependant on the specific \mathbf{b} value.

Registration The scripting modules concerning the registration are shown in Figure 4.21. `PancreasRegistration` is the main class and steering the serial registration in `FullyAutomaticRegistration` and subsequent quantification of f , D and *ADC*. The mentioned 'Breaking down segmentation into 2D slices' is done via the function `performQuantificationForSlice(self, x)` in `FullyAutomaticQuantification`. The *IVIM* calculation itself is being executed via an object oriented scripting access onto the objects directly connected to the *IVIM* macro module in `doNewPFWICalculation(self)`.

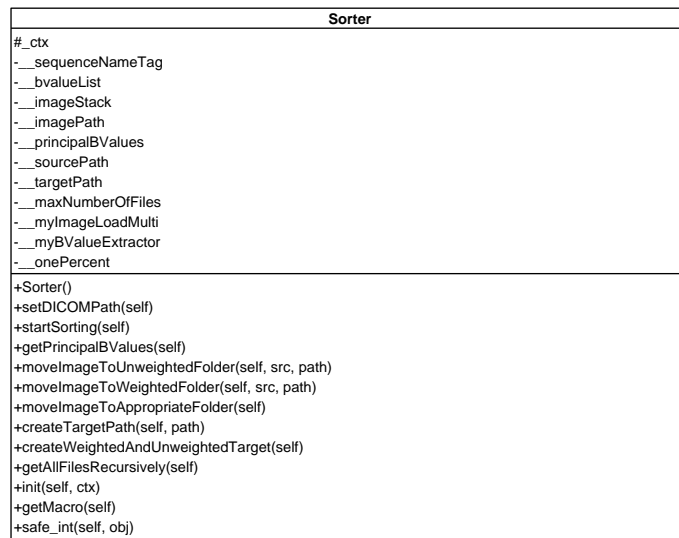


Fig. 4.20: An UML Diagram of the Python Sorter

Quantification Figure 4.22 explains the implementation of the quantification modules given in Figure 4.19. `INormalizer` is an abstract interface, describing operations pertaining to the internal extraction of the **b** value list (`bValueImportInternally()`), external acquisition (`bValueImportExternally`) and operations onto the **b** value list and finally the export (`bValueOperation`). `Normalizer` implements these basic operations. The `PancreasNormalizer` implements the normalization procedure given in Equation 4.2. The `IVIM` parameters such as f and D are calculated in `RSquaredMapper`. `IVIMFunction` (Equation 4.52) encapsulates the function given in Equation 4.52 and the Jacobian matrix (Equation 4.54). The **b** value extraction is encapsulated in `BValueClass`.

Implementation and user interface

The automatic bounding box registration is shown in Figure 4.23. In an orthogonally reformatted viewer (`CropByBoundingBox`), the encompassed pancreas is shown in an axial, coronal and sagittal view. The fixed image is shown in the upper viewer whereas the moving image is displayed in the lower part. The free hand delineated pancreas on the *ADC* map is shown in the lower left corner.

Several options can be made in the lower right corner. `Start Registration` can be used to perform a manual sample registration. `Reset Registration` is resetting the registration to start a new automatic registration plus quantification. `Start Fully Automated Registration` performs an automatic registration and the derived quantification maps are automatically be-

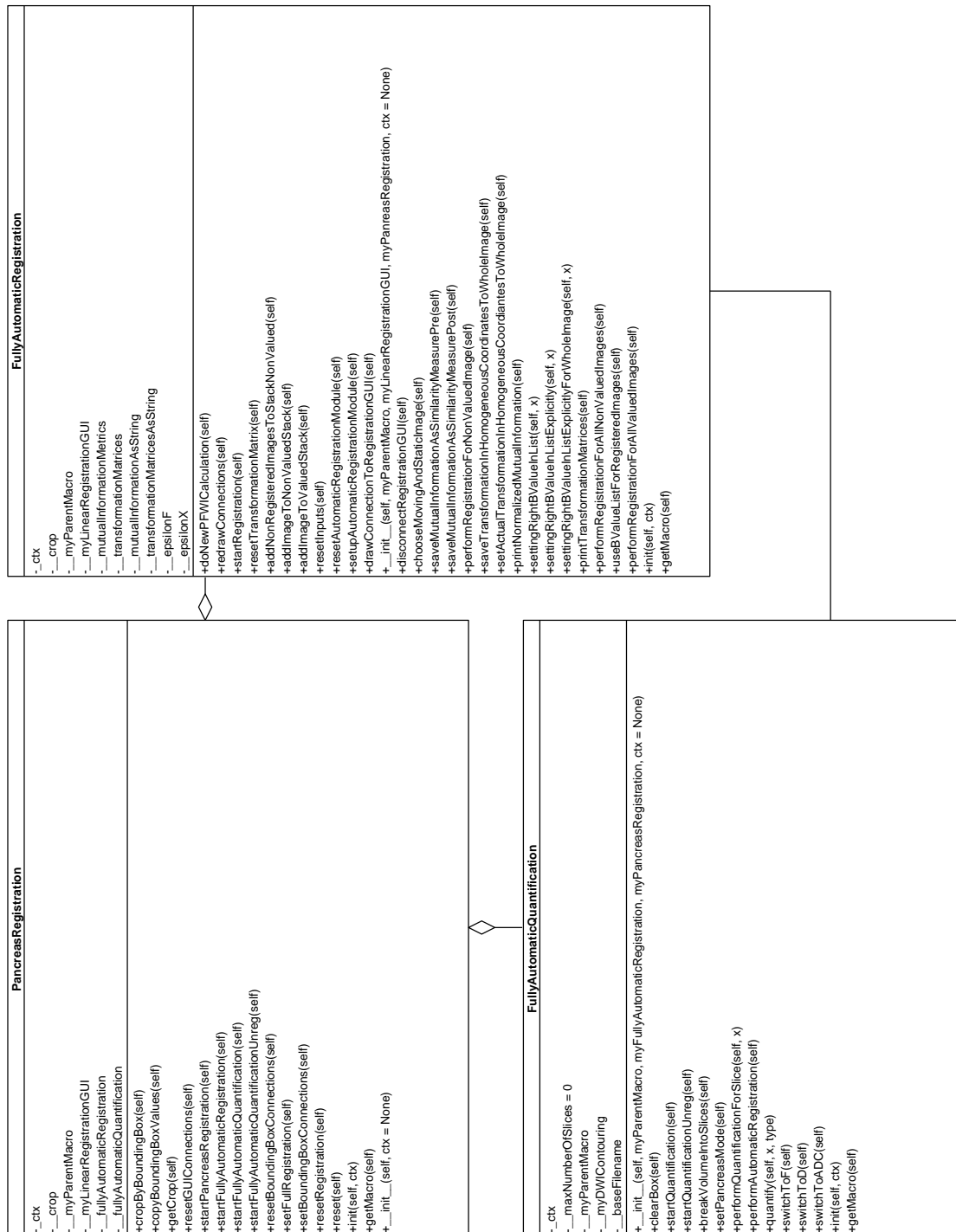


Fig. 4.21: UML Diagram of the registration modules

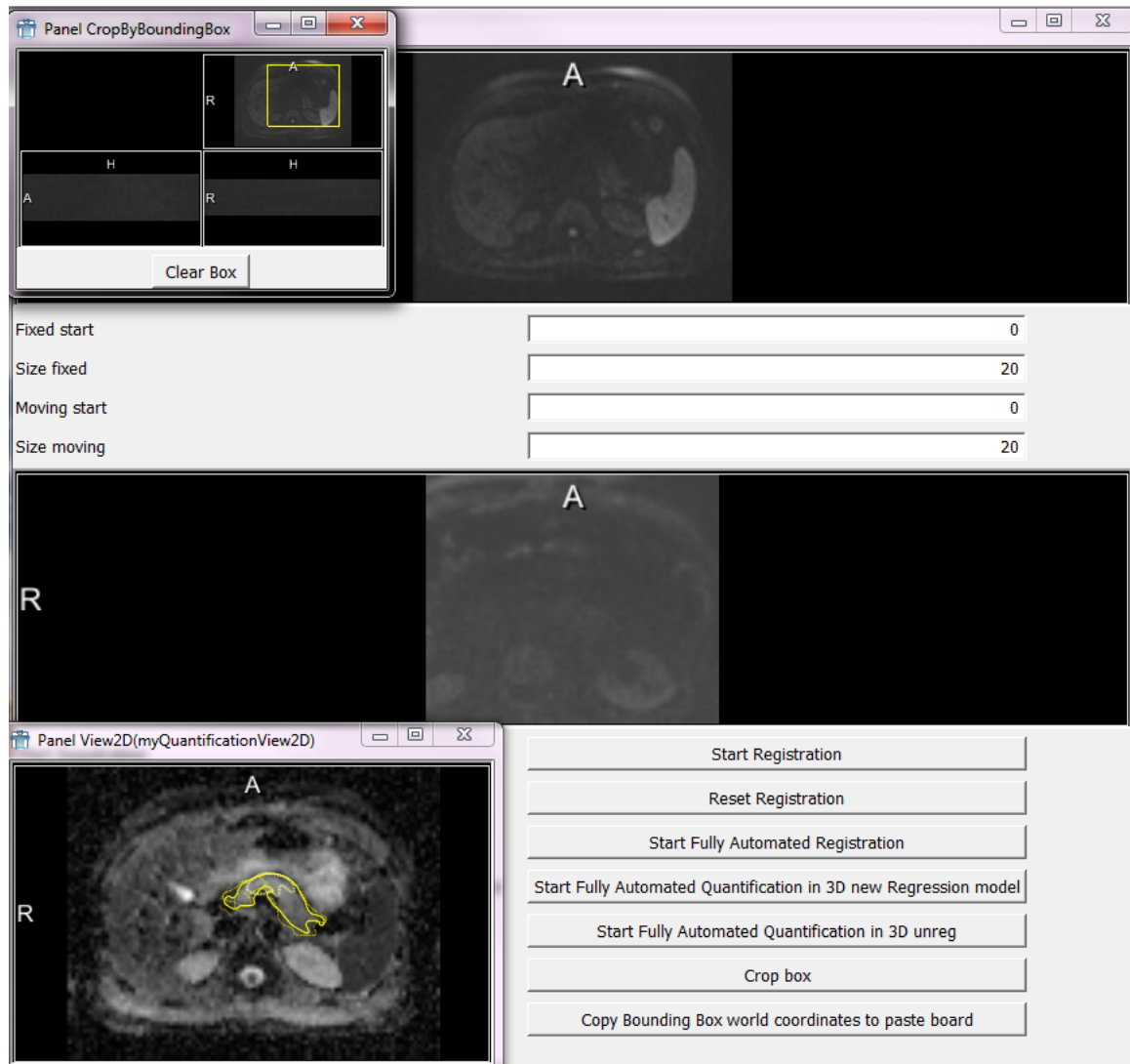


Fig. 4.23: Illustration of the automatic bounding box registration

ing calculated. The quantification can be done manually via Start Fully - Automated Quantification in 3D unreg. A complete run with registration and consecutive automatic quantification can be done via Start - Fully Automated Quantification in 3D new Regression model. Here, the old and new regression model can be chosen (Equation 4.49 and Equation 4.50). The crop box can be displayed and adjusted via Crop Box and the coordinates of the box can be copied to the clipboard via Copy bounding Box world coordinates to paste board.

Application of the IVIM approach onto several organs

The IVIM approach (Equation 4.52) has been successfully applied onto several different organs.

In lung tumours (Koyama et al., 2011), the contribution of the perfusion fraction f to the ADC and therewith the correlation between these derived parameters has been elucidated.

It has been thoroughly discussed in Hillengass et al. (2011) for multiple myeloma as a useful technique, where the ADC unexpectedly decreased after therapy due to a decrease of microvessel density in histology.

In Hauser et al. (2011), the therapy monitoring in head and neck tumours considering the IVIM model has been evaluated. The rise of f , D and ADC could be found. This can be explained as a decrease in cellularity and an increase of the blood volume under radiochemotherapy.

Most importantly, the application onto the pancreas should be further evaluated in this section. The significant differentiation between healthy pancreas and pancreatic carcinoma as well as pancreatitis and pancreatic carcinoma should be emphasized here (Klauss et al., 2011, Lemke et al., 2009, Re et al., 2009). Moreover, the improvement through ducts and vessel segmentation is explained, as well (Re et al., 2011).

Furthermore, the application, regarding the usage of combined chemoradiation, is discussed in (Grünberg et al., 2011, ECR) (Section 3.3.2). Here, IVIM derived parameters such as f were measured in patients with primary inoperable pancreatic carcinoma during a course of combined chemoradiation. The pure diffusion parameter D and the combined ADC showed a significant increase compared to the initial therapy and 4 weeks after the end of radiation. It could be elaborated that f showed an increase. Nonetheless, the rise could not be significantly proved.

This section starts with a MeVisLab 'Module based description' and continues with a 'Realization' to show the UML diagrams of the developed software.

Module based description

The module based description of MeVisLab modules (Fraunhofer MEVIS, Bremen) is depicted here. The section is subdivided into the 'Automatic preprocessing', 'Ducts and vessels segmentation' and 'Plotting modules'.

Automatic preprocessing In Figure 4.24, the second normalization procedure is carried out (Equation 4.13). In addition to Figure 4.19, the PFWINormalizer can be connected automatically in the case of data without breath-hold blocks.

The several ADC calculations elucidated in Section 4.1.2 are switched appropriately in the macro module DWIMetaADCCalculation (Figure 4.25). The

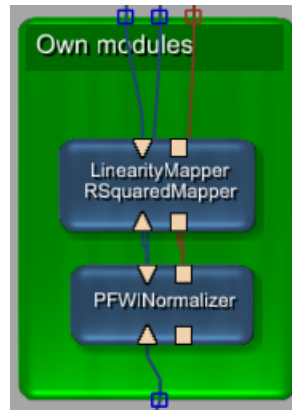


Fig. 4.24: MeVisLab module based description of additional quantification modules for IVIM

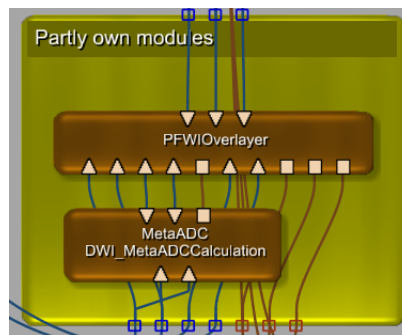


Fig. 4.25: MeVisLab module based description of the preprocessing modules

two inputs are automatically being filled with the unweighted and weighted data.

The outputs deliver the calculated *ADC* map (first output) and the raw diffusion weighted data. The last input contains the **b** value list.

All of the *IVIM* calculations are taking place in `PFWIOverlayer`. The first two inputs consist of the unweighted and weighted data. The third input delivers the precalculated *ADC* map, the raw diffusion weighted data and the **b** value list. The last two image inputs contain the morphological data and the three rectangle inputs are being filled with ROIs coming from three different viewers. The image inputs and rectangle inputs are needed for the plotting facility.

The first output contains the *IVIM* derived parameters, whereas the second output delivers the *ADC* map. The last input consists of the raw diffusion weighted data.

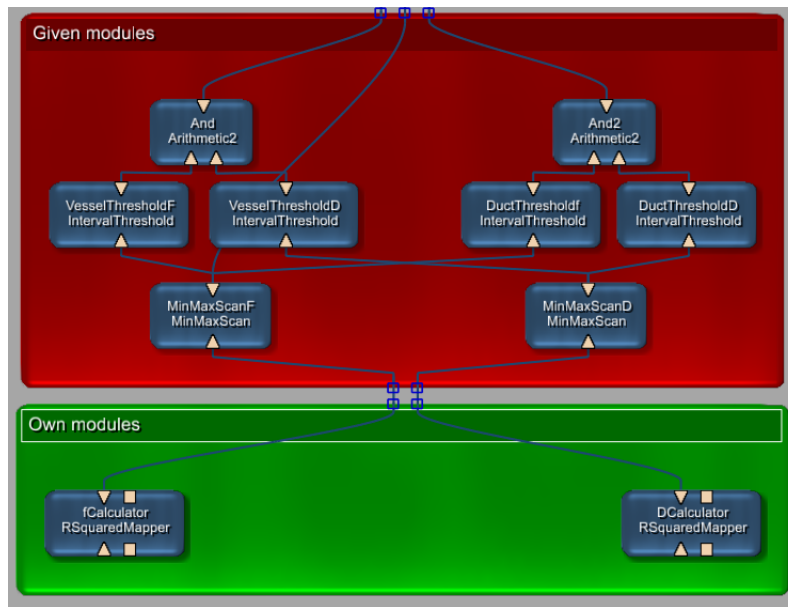


Fig. 4.26: The ducts and vessels segmentation modules

Ducts and vessels segmentation The module based description of the ducts and vessels segmentation is depicted in Figure 4.26. The logical circuit described in the state chart diagram in Figure 4.35 is shown here. The functional values relating to D and f are calculated in the own modules `fCalculator` and `DCalculator`. A maximum LUT is being calculated by `MinMaxScanF` and `MinMaxScanD`. Afterwards, the threshold range is being determined by the respective threshold modules. The logical function is carried out by the two `And` modules.

Plotting modules The main plotting routine is taking place in Figure 4.27. The two inputs consist of the normalized signals, either using normalization procedure of Equation 4.48 or Equation 4.13 (first input) and the \mathbf{b} value vector \vec{b} (second input). The first output delivers the raw signal plotted against the \mathbf{b} value. The second output consists of the linear regression using Equation 4.49 or Equation 4.50. The residuals are given by the third output. The fourth output can perform a normalization using Equation 4.13, if the signal has not been normalized before. The last output delivers the Levenberg Marquardt fitted signal.

Realization

The realization part covers the 'Implementation and UML description of required modules', the 'Implementation of the plotting module' and the 'Implementation and user interface' of the software for the *IVIM* calculation.

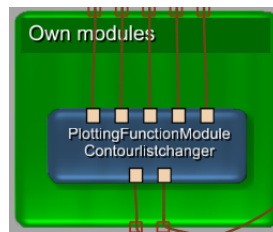


Fig. 4.27: The plotting module

Implementation and UML description of required modules

Automatic preprocessing The second normalization procedure combined with the whole quantification is depicted in [Figure 4.28](#). The normalization in [Equation 4.13](#) is taking place in `PFWINormalizer`. The other calculations are done via graphical programming and scripting, concealed in module `DWIMeta-ADCCalculation` ([Figure 4.25](#)).

Implementation of the plotting module

The whole plotting facility is shown in [Figure 4.29](#).

Implementation and user interface

Automatic preprocessing In [Figure 4.30](#), an automatically generated f map pancreas quantification is shown. Shown are the multimodal viewers with T1 post plus contrastmedium (left) and T2 (right). The quantification f map is shown as the red overlay in the upper `synchroViewer` and separately in the lower functional quantification viewer. The ROI can be delineated synchronously in the multimodal way. In the middle lower viewer, the zoomed pancreatic adenocarcinoma slice is depicted.

The viewer has the same functionality as described in [Section 4.1.1](#). Furthermore, the control tab enables the functionality to load and save ROIs. Moreover, we have the possibility to combine three viewers in total as shown in [Figure 4.30](#) to establish a combined quantification. This is especially of value, if necrosis has to be subtracted from the tumour mass. The contoured regions are displayed synchronously in all open viewers by different colours.

A screenshot of the ducts and vessels segmentation in a multimodal context is shown in [Figure 4.31](#). The gallbladder (GB), the renal artery (RA), the tumour (T) and the aorta (A) are shown in the T1 weighted image (A), the T2 weighted image (B), the f map (C) and the segmented f map, showing vessels in red and highlighting ducts in green. A 3D image of this scene is given in [Figure 3.16](#).

The plotting facility is depicted in [Figure 4.32](#). It shows the fitting routines pertaining to the 3D tumour VOI. In (A), the linear regression using model

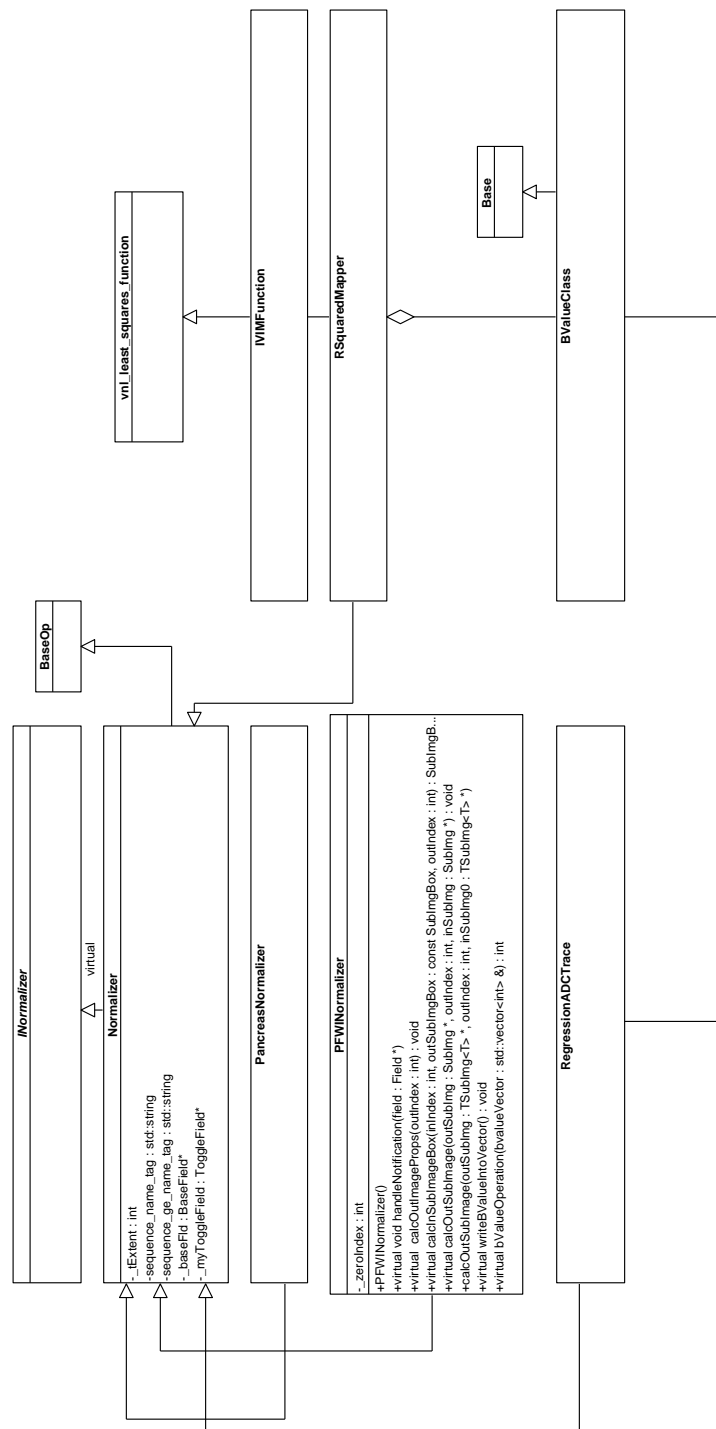


Fig. 4.28: IVIM quantification UML with additional normalizer

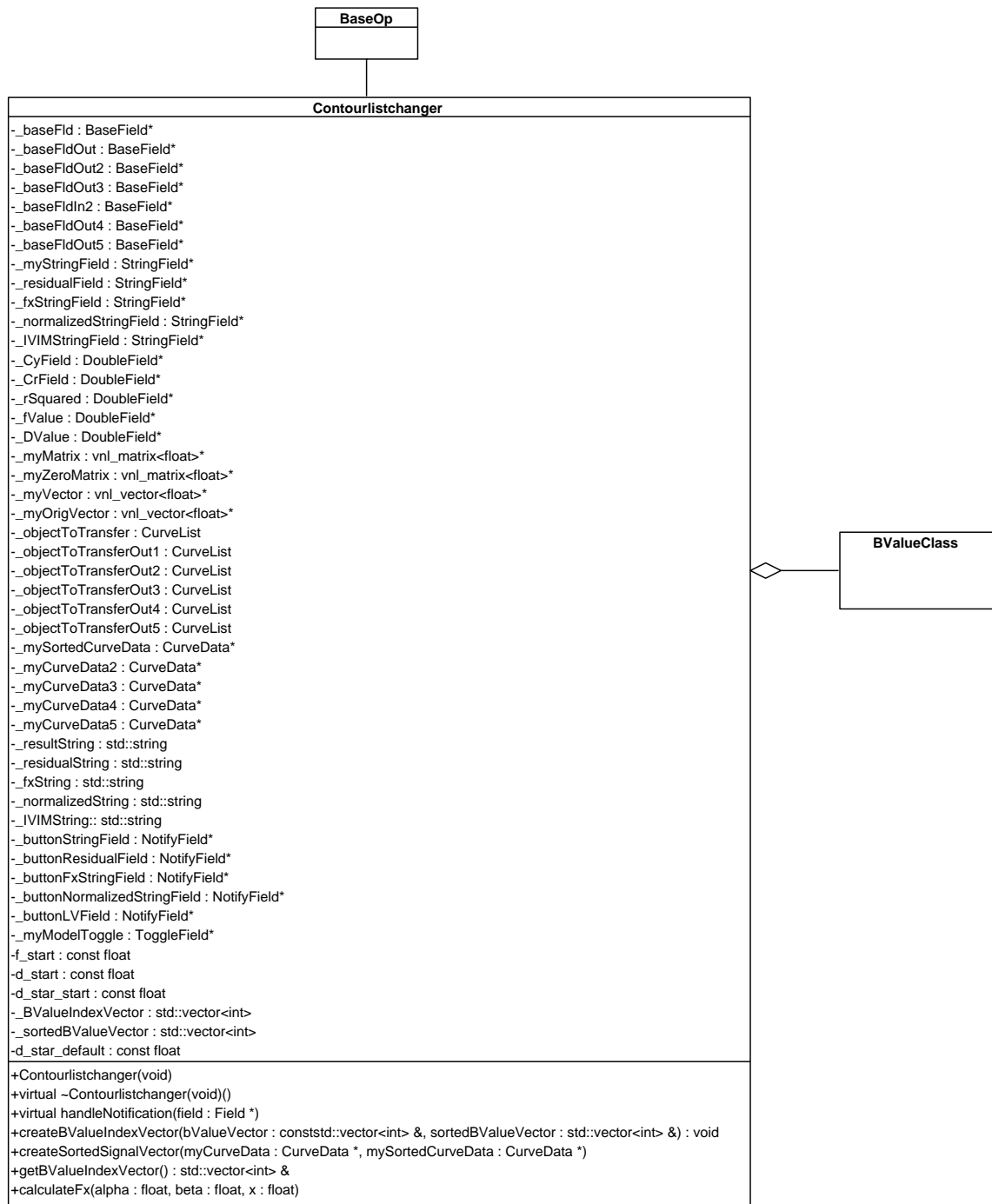


Fig. 4.29: The plotting facility UML

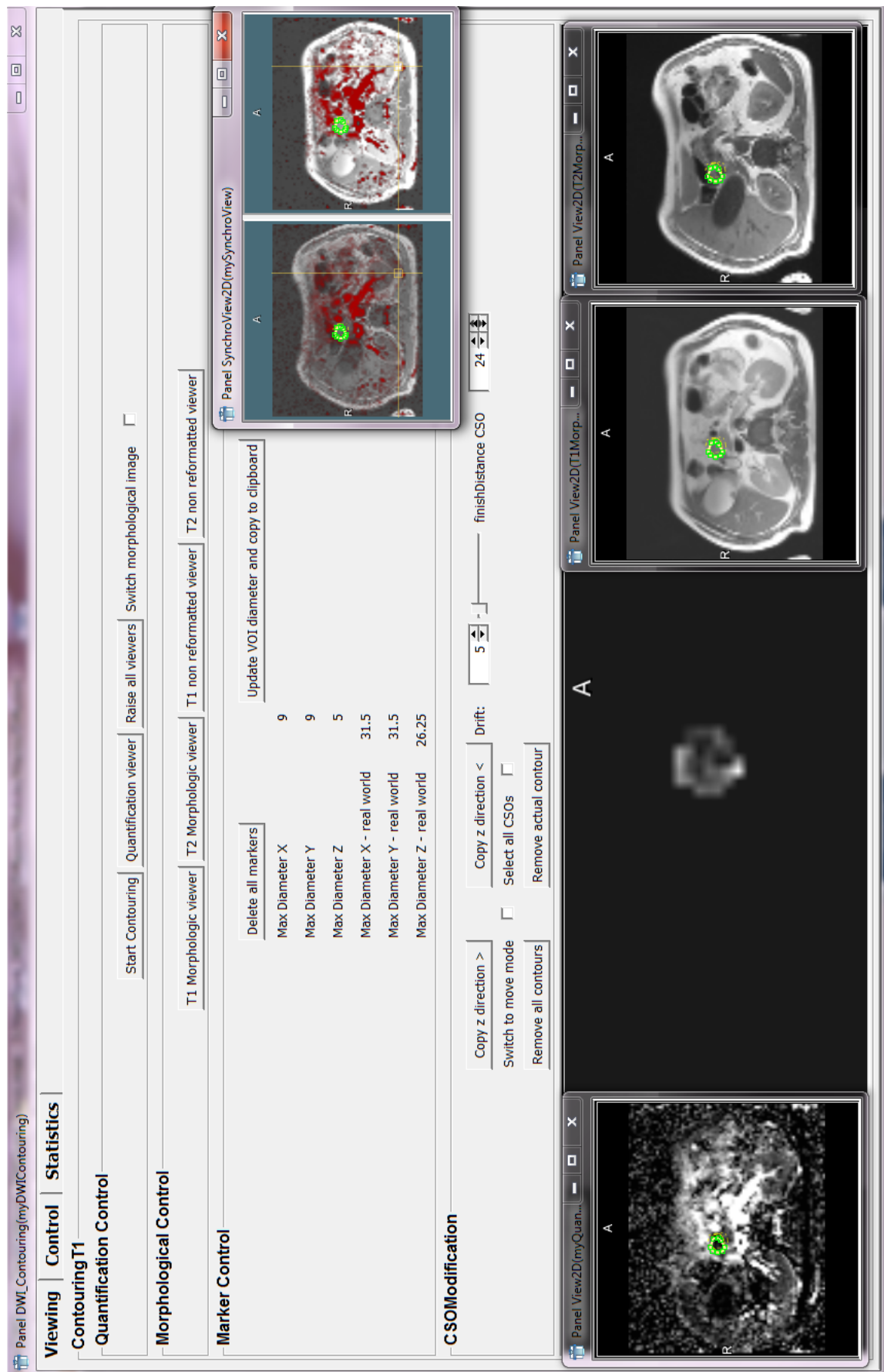


Fig. 4.30: The automatic preprocessing: Contouring

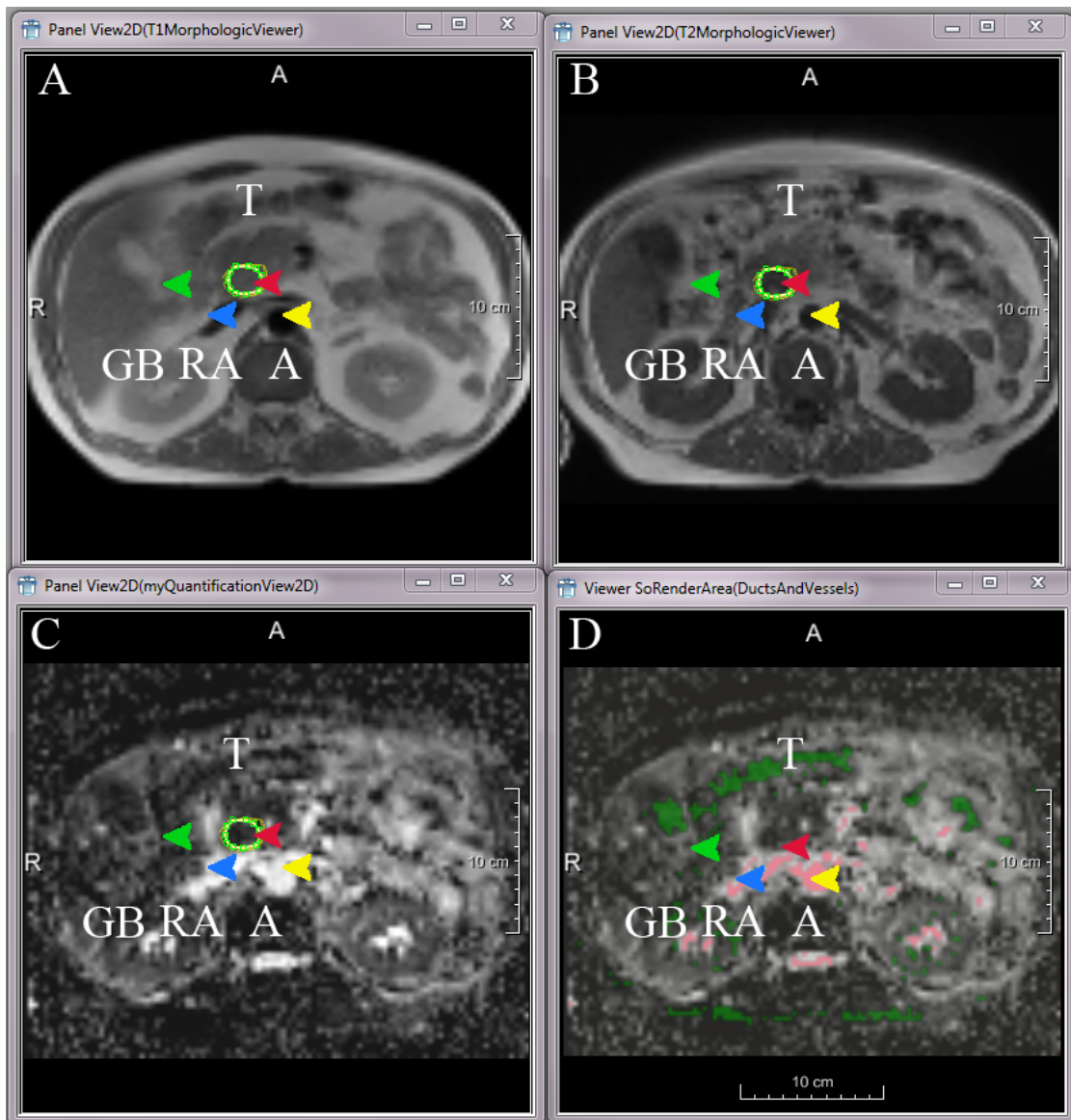


Fig. 4.31: The automatic preprocessing: Ducts and vessels segmentation. The gallbladder (GB), the renal artery (RA), the tumour (T) and the aorta (A) are shown in the T1 weighted image (A), the T2 weighted image (B), the f map (C) and the segmented f map showing vessels in red and highlighting ducts in green.

(Equation 4.49) is shown. In (B), the Levenberg Marquardt algorithm (Equation 4.54) concerning to the IVIM fit is depicted. (C) shows the normalized signal $\ln\left(\frac{S}{S_0}\right)$ versus b . In (D), the residuals of the signal are visualized.

4.2 Preliminary experimental procedures

The design and theoretical workflow for both studies is depicted here. This section additionally entails the used devices, sequences and patients. Firstly, the reproducible separation and quantification of high- and low-proliferative areas (Section 4.2.1) and secondly, for the IVIM model and reproducible parameters in diffusion weighted images (Section 4.2.2).

4.2.1 Design and theoretical workflow for a reproducible separation and quantification of high- and low-proliferative areas in gliomas

In this section, the design and theoretical workflow of the study is elaborated (Figure 4.1).

The application design approach, including an activity diagram is depicted in 'Application design approach'.

A module based description of MeVisLab modules (Fraunhofer MEVIS, Bremen) is given in 'Module based description'.

Principal flow of information

In Figure 4.1, the principal flow of information is shown.

Acquisition of MR data

Three multispectral datasets of ten patients with biopsy proven glioblastoma have been acquired on a 1.5 T whole-body clinical MRI scanner equipped with a quadrature head coil (Magnetom Symphony, Siemens Healthcare, Erlangen, Germany). The extent of the gross tumour volume (*GTV*) with biopsy proven glioblastoma was delineated manually by an experienced clinical radiologist on a FLAIR (Fluid attenuated inversion recovery) sequence.

1. T2-FLAIR weighted images (parameters: 24 axial slices, TR/TE : 9000/114; voxel size: $0.469 \times 0.469 \times 6.5 \text{ mm}^3$; resolution 448×512 ; field of view: $210.11 \times 210.11 \text{ mm}^2$).
2. T1 contrast enhanced images (parameters: 24 axial slices, TR/TE : 700/18; voxel size: $0.469 \times 0.469 \times 5.500 \text{ mm}^3$; resolution 512×512 ; field of view: $240.13 \times 240.13 \text{ mm}^2$).

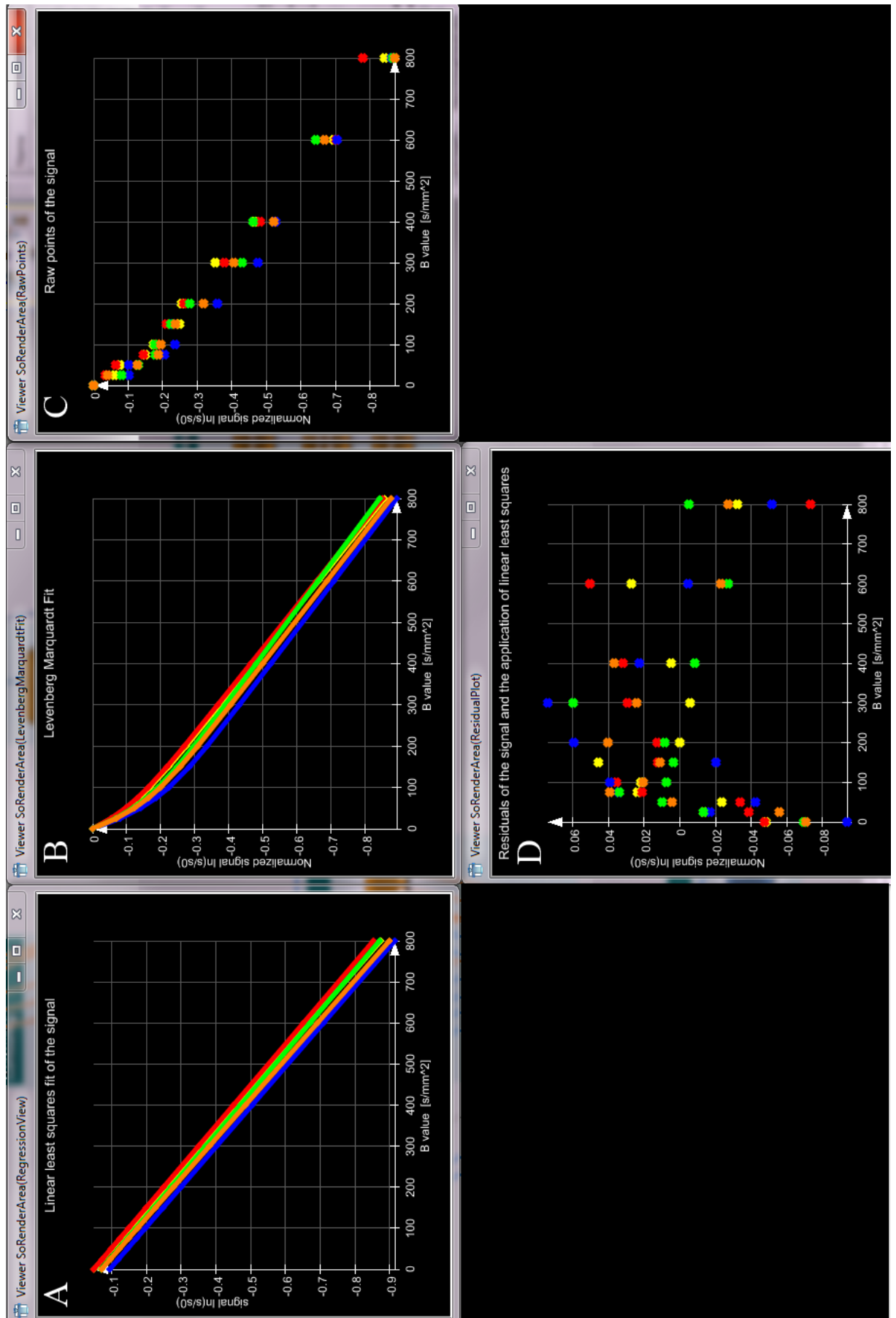


Fig. 4.32: The automatic preprocessing: Plotting of a 3D pancreatic lesion. (A): Linearly fitted signal decay by linear least squares (Elpelt and Hartung, 1992) using Equation 4.49. (B): Signal fitted by non linear least squares (C): Raw points of the signal decay. (D): Residuals of the fitting by linear least squares.

3. Diffusion weighted images: 50 axial slices were acquired using 6 gradient directions and two b-values (0 and $1000 \frac{\text{sec}}{\text{mm}^2}$ TR/TE: 8400/108; voxel size $2.5 \times 2.5 \times 2.5$; resolution 96×96 ; field of view $240 \times 240 \text{mm}^2$); 10 averages.

ADC calculation

The mean ADC $\langle ADC \rangle$, which is denoted as the mean diffusivity MD $\langle ADC \rangle \approx MD$, was calculated by using a log linear model. The normalized signals were calculated by [Equation 4.2](#).

$$\vec{s}_{norm} = \ln \left(\frac{\vec{S}}{S_0} \right) \quad (4.2)$$

and tensor components were estimated by linear least squares calculation (Elpelt and Hartung, 1992) ([Equation 4.3](#)).

$$\vec{D} = (X^T \cdot X)^{-1} X^T \cdot -\frac{1}{b} \cdot \ln \left(\frac{\vec{S}}{S_0} \right) \quad (4.3)$$

where the matrix X comprises the gradient directions. The diagonalization results in an orthonormal basis of eigenvectors and eigenvalues $e_1, e_2, e_3, \lambda_1, \lambda_2, \lambda_3$. The mean ADC $\langle ADC \rangle$ is determined by ([Equation 4.4](#)).

$$\langle ADC \rangle \approx MD = \frac{\lambda_1 + \lambda_2 + \lambda_3}{3} \quad (4.4)$$

In the following, the mean ADC $\langle ADC \rangle$ is referred to as ADC.

Preprocessing

In order to improve the SNR ([Section 3.1.5](#)) of the diffusion data, we combined 10 DTI datasets and matched them spatially with a linear registration model and used normalized cross correlation as a similarity measure and performed a trilinear interpolation. To further improve the matching, we resampled the data to a finer grid of an isotropic voxel size of 1.25 mm using a cubic B-spline for the interpolation. Then, we registered the axial T1 contrast enhanced weighted image onto the ADC map using normalized mutual information due to different image modalities ([Section 3.2.5](#)). Afterwards, a trilinear interpolation was performed.

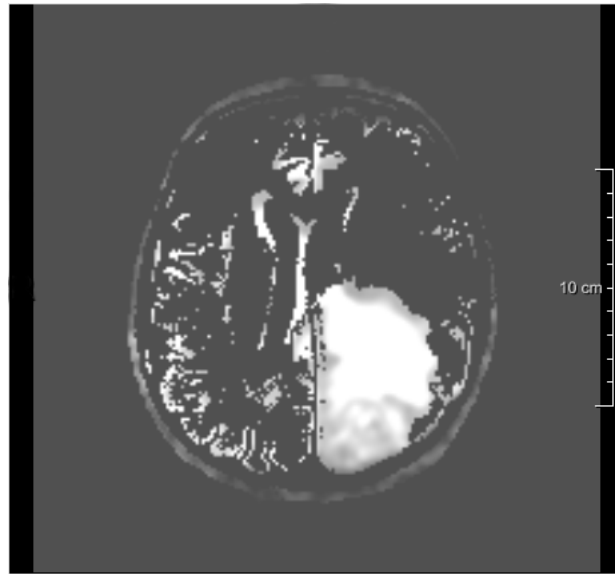


Fig. 4.33: Applied binary mask onto ADC map (taken from Simon et al. (2009))

Application of T2-FLAIR mask We used a binary T2-FLAIR mask to resolve the potential overlapping intensities of low proliferating tumour with cerebrospinal fluid (Simon et al., 2011, 2009). Therefore, we used the registered T2-FLAIR image where cerebrospinal fluid appeared hypointense. After a binarization of the image, where a threshold $\theta = 17450$ denotes the threshold cut off, was applied to the scaled T2-FLAIR image to a fixed index; values below this threshold were set to 1 so that only cerebrospinal fluid was visible. Thus, cerebrospinal fluid could be cut off by applying this binary mask to the ADC map (Figure 4.33).

Necrosis cut off The ADC in necrotic areas may overlap with that of low-proliferating tumour areas (Simon et al., 2011, 2009). However, the necrosis ADC exceeds that of the low-proliferating areas and thus a cut off value can be used to separate the two. The cut off value was empirically determined by a physician and set to $\theta = 0.001 \frac{\text{mm}^2}{\text{sec}}$.

Including functional imaging such as perfusion as additional information

In this section, an additional functional imaging technique is evaluated to describe the part of high-malignancy in high-grade gliomas.

Firstly, the preliminary assumptions and a principal flow of information is described in 'Design'. Secondly, the 'Realization' depicts the UML description and the user interface.

Design

The workflow given in [Figure 4.11](#) has been developed using a software platform based on MeVisLab (Fraunhofer MEVIS, Bremen, Germany) (Radbruch et al., 2011).

Acquisition of MR data Three multispectral datasets have been acquired of twenty patients with newly diagnosed and histologically proven glioblastoma before surgery on a 3 Tesla MR system (Magnetom Tim Trio, Siemens Healthcare, Erlangen, Germany).

1. T1 contrast enhanced images (parameters: 147 axial slices, TR/TE : 1710/4.04; voxel size: $0.5 \times 0.5 \times 1.1 \text{ mm}^3$; resolution 512×512 ; field of view: $256 \times 256 \text{ mm}^2$).
2. Dynamic susceptibility contrast enhanced images (DSC imaging) (Giesel et al., 2005) (parameters: 25 axial slices, TR/TE : 5.44/2.47; voxel size: $1.797 \times 1.797 \times 5.5 \text{ mm}^3$; resolution 128×128 ; field of view: $230 \times 230 \text{ mm}^2$).
3. Diffusion weighted images (parameters: 20 axial slices TR/TE : 4700/109; voxel size: $1.769 \times 1.769 \times 5.5 \text{ mm}^3$; resolution 130×130 ; field of view: $230 \times 180 \text{ mm}^2$ 6 gradient directions and two b-values (0 and $1200 \frac{\text{sec}}{\text{mm}^2}$).

Preprocessing $rCBV$ and ADC maps have been previously calculated using Siemens Syngo-Software and were available as pre calculated functional maps. We performed a global linear rigid registration between the morphologic T1 weighted image+CA (reference image) and the functional images (moving images) because of an expectation of a higher intensity similarity between these two different sets. A normalized mutual information (NMI) ([Section 3.2.5](#)) was used as a similarity measure and a downhill simplex optimization algorithm determined the transformation between the images. Afterwards, a trilinear interpolation was being executed to upscale the functional images to the finer voxelsize.

4.2.2 Design and theoretical workflow for the IVIM model and reproducible parameters in diffusion weighted images

This section consists of the 'Principal flow of information' of the main study and additionally entails the 'Application of the IVIM approach onto several organs' as an expand of the IVIM approach onto other organs.

Principal flow of information

The workflow given in [Figure 4.16](#) has been developed using a software platform based on MeVisLab (Fraunhofer MEVIS, Bremen, Germany) 'DWIQuant-Classic' (Simon et al., 2009). The registration study itself is given in Graf et al. (2010) and implemented in 'DWIQuantExperimental'.

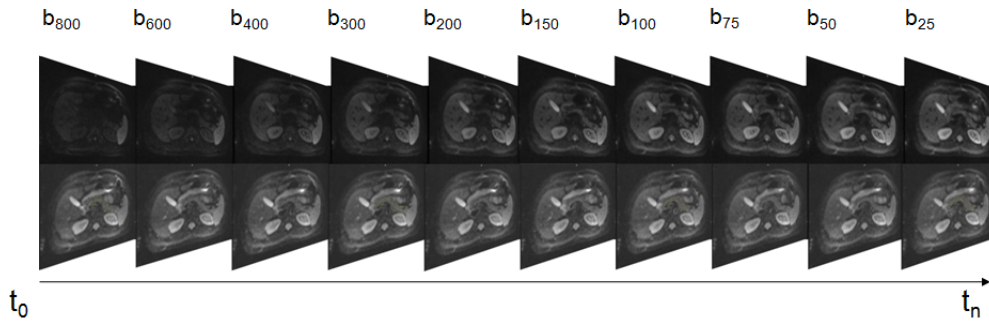


Fig. 4.34: *The original sequence*

Acquisition of MR data

Three consecutive measurements of ten healthy volunteers have been acquired on a 1.5 T scanner (Magnetom Avanto, Siemens Medical Solutions, Erlangen, Germany). Axial DWI was performed using a single-shot echo-planar imaging TR/TE : 1300/60; voxel size $3.5 \times 3.5 \times 5.25 \text{ mm}^3$; resolution 100×78 and 4 averages. The acquisition was separated into 10 blocks consisting of one unweighted and one weighted image $(b_0, b_{25}), (b_0, b_{50}) \dots (b_0, b_{800})$. This was performed in a single breathhold to avoid motion artifacts. However, residual organic motion between these blocks may be still present.

Preprocessing

The weighted and unweighted stack is being created automatically by splitting up the sequence (Figure 4.34) (taken from Graf et al. (2010)) into a weighted and unweighted part belonging to their respective breath hold phase and \mathbf{b} value to directly perform the calculation in MeVisLab.

The pancreas was delineated manually in 3D by an experienced physician and physicist. This was performed onto the unweighted image in the breath-hold pair due to higher and more equalized signal to noise ratio. Afterwards, this segmentation was being applied onto the corresponding weighted image in the set. In total, three manual sample segmentations of the pancreas have been performed (Figure 4.37) (taken from Graf et al. (2010)).

To reduce the potentially high σ of the quantification parameters, we splitted the 3D VOIs into 2D ROIs and performed the quantification onto these ROIs.

Application of the IVIM approach onto several organs

In 'Consistent calculation scheme and automatic preprocessing', the design of an automatic preprocessing of diffusion weighted images is described and continues with a break down of the Siemens diffusion sequences given in Table 4.1.

Afterwards, the ducts and vessel segmentation is being described in 'Design of an automatic ducts and vessels segmentation' and the description of the design of a plotting facility is given in 'Design of a plotting facility'.

Consistent calculation scheme and automatic preprocessing

As described in (Simon et al., 2009, SPIE) and Simon et al. (2009), an automatic preprocessing has been designed and implemented to distinguish between different diffusion weighted magnetic resonance sequences. The *Advanced Preprocessing* has been implemented into the software platform **RONDO** (Woetzel et al., 2010) to foster an automatic and user independent calculation scheme to support several organs and sequences (Table 4.1) (Table 3.1.4).

Sequence Type	Diffusion Sequence
ECHO PLANAR IMAGING	DIFFMODE ORTHOGONAL DIFFMODE SLICE DIFFMODE READ DIFFMODE PHASE DIFFMODE THREE SCAN TRACE DIFFMODE TENSOR
HASTE	DIFFMODE DIAGONAL DIFFMODE ORTHOGONAL DIFFMODE SLICE DIFFMODE READ DIFFMODE PHASE

Table 4.1: Siemens MR sequences ((Simon et al., 2009, SPIE), (Simon et al., 2009))

Orthogonal ADC

The orthogonal ADC map $\langle ADC \rangle$ is being calculated by Equation 4.5.

$$\langle ADC \rangle = \frac{ADC_x + ADC_y + ADC_z}{3} \quad (4.5)$$

$$\text{where, } ADC = \frac{-1}{b} \cdot \ln \left(\frac{S}{S_0} \right) \cdot \Leftrightarrow \quad (4.6)$$

$$\langle ADC \rangle = \frac{1}{3} \cdot \frac{-1}{b} \cdot \left(\ln \left(\frac{S_x}{S_0} \right) + \ln \left(\frac{S_y}{S_0} \right) + \ln \left(\frac{S_z}{S_0} \right) \right) \cdot \quad (4.7)$$

Trace ADC

The trace-image can be derived from [Equation 4.5](#). The trace calculation itself is shown in [Equation 4.8](#).

$$\langle ADC \rangle = \frac{-1}{3} \cdot \frac{\ln\left(\frac{S_x}{S_0}\right) + \ln\left(\frac{S_y}{S_0}\right) + \ln\left(\frac{S_z}{S_0}\right)}{b} \Leftrightarrow \quad (4.8)$$

$$\langle ADC \rangle = \frac{-1}{3} \cdot \frac{\ln(S_x \cdot S_y \cdot S_z) - 3 \cdot \ln(S_0)}{b} \Leftrightarrow \quad (4.9)$$

$$\langle ADC \rangle = -\frac{\ln(S_x \cdot S_y \cdot S_z)^{\frac{1}{3}} - \ln(S_0)}{b} \quad (4.10)$$

$$\text{where, } S = (S_x \cdot S_y \cdot S_z)^{\frac{1}{3}} \text{ denotes the trace} \quad (4.11)$$

$$\text{hence, } \langle ADC \rangle = -\frac{\ln\left(\frac{S}{S_0}\right)}{b}. \quad (4.12)$$

Tensor ADC calculation

The tensor ADC calculation is described in [Equation 4.3](#).

Series of diffusion weighted images and IVIM support

Beyond of the two ADC calculation schemes described in [Equation 4.49](#) and [Equation 4.50](#) for an array of diffusion weighted images using the normalization procedure elucidated in [Equation 4.48](#), a new normalization routine has been taken into account.

In this case, no \mathbf{b} value blocks have been used to avoid motion artifacts. Instead, only one b_0 waited image is available in the stack among all valued images, designated at index position ζ ([Equation 4.13](#)).

$$\ln(s_i) = \frac{\ln(s_i)}{\ln\left(\frac{s_0}{s_\zeta}\right)} \quad (4.13)$$

In [Section 4.2.2](#), the IVIM approach has been only used in a fixed variant due to low SNR. The developed software additionally offers a non fixed solution where three degrees of freedom are used for f , D and D^* .

Eventually, an array of GE weighted trace sequences is supported, as well.

Design of an automatic ducts and vessels segmentation

In (Re et al., 2011), the ducts and vessels segmentation is thoroughly described. The developed technique has been implemented into the software tool to more accurately differentiate between pancreatic carcinoma and healthy pancreatic tissue.

Bile and pancreatic ducts appear hypointense in f maps and are impeding the delineation between the adjacent pancreatic lesions and lead to errors during quantification. The bile, pancreatic ducts and vessels can be colour coded including the *IVIM* derived parameters f and D resulting in a bi-parametric value f, D .

The derived values of D and f were determined by the cut-off values of a ROC analysis including 42 patients with histologically confirmed adenocarcinoma of the pancreas. The values of the ducts and vessels were determined by an analysis of sample ROIs in the tumour, the gallbladder or major bile duct, the aorta, renal artery or vertebral artery (Re et al., 2011).

In [Figure 4.35](#), the logical circuit concerning the ducts and vessels segmentation is shown. The *fuse* symbol can be seen as a logical **AND**. It can be clearly seen that vessels appear hyperintense in the f map and hypointense in the D map. In contradiction to that, as already said, the gallbladder and the pancreatic ducts show up as hypointense regions in the f map and hyperintense in D .

Design of a plotting facility

A plotting facility plus additional value extraction has been designed to have a more detailed inspection into the decaying signal. This can be used to better evaluate the quality of the data and especially in the case of the sequence consisting of the \mathbf{b} value pairs used in the pancreas studies (Klauss et al., 2011, Lemke et al., 2009), the lung study (Koyama et al., 2011) and the head and neck cancer study (Hauser et al., 2011).

The *IVIM* experimental values for the differentiation between pancreatitis and pancreatic carcinoma

In this section, the results of the differentiation between pancreatitis and pancreatic carcinoma are shown. These results are related to the study by (Klauss et al., 2011), where the *IVIM* model and the *ADC* have been used. In this study, it has been elucidated that f was the most sensitive parameter (80 % sensitivity) for this delineation compared to *ADC* measurements with \mathbf{b} values of 200, 600 and 800.

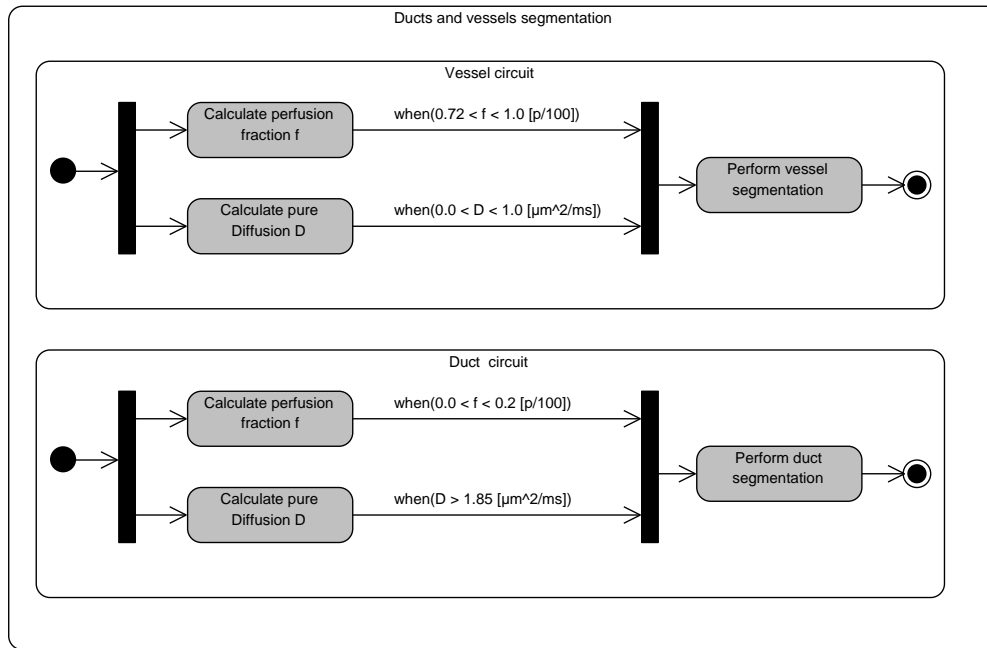


Fig. 4.35: Ducts and vessels segmentation

In the here depicted analysis, the R^2 (Equation 4.16) and integral parameter (Equation 4.17) have been used to perform this delineation.

The R^2 parameter is an index of linearity, normalized between 0 and 1. Large values indicate a strong linearity and can be used as an indicator for a mono exponential signal decay. This leads to a hypoperfused assumption. Clinical data derived from Klauss et al. (2011) indicate that the perfusion of pancreatic carcinoma is lower compared to pancreatitis and thus, the R^2 values for pancreatic carcinoma are supposed to be higher.

The integral parameter determines the numerical approximation of the integral of the signal decay within the perfusion weighted compartment. We assumed that the low perfusion affected compartment is determined by \mathbf{b} values below 200 (Le Bihan et al., 1988, 2008, Luciani et al., 2008).

On 10 patients, the diagnostic strength by means of receiver operating characteristic curve analysis of the two parameters has been elucidated using MedCalc (MedCalc Software, Mariakerke, Belgium).

$$C_y = \frac{1}{n} \sum_{i=1}^n (y_i - \bar{y})^2 \quad (4.14)$$

$$C_R = \frac{1}{n} \sum_{i=1}^n (y_i - \hat{y}_i)^2 \quad (4.15)$$

$$R^2 = 1 - \frac{c_R}{c_y} \quad (4.16)$$

$$\int_0^{200} \ln \left(\frac{S}{S_0} \right) db \quad (4.17)$$

4.3 Postprocessing

The postprocessing section describes the application of the developed software of the two studies. Firstly, the glioma study with the reproducible separation and quantification (Section 4.3.1) and secondly, the application of the IVIM model and reproducible derived parameters in diffusion weighted images (Section 4.3.2).

4.3.1 Application of the software for a reproducible separation and quantification of high- and low-proliferative areas in gliomas

In this section, the postprocessing consisting of 'Clustering' and 'Quantification' (Figure 4.1) is described.

Clustering

This section entails the objectivity test and the initialization procedure in 'Test for the objectivity of tumour clustering and initialization procedure'.

Test for the objectivity of tumour clustering and initialization procedure

Initialization test In Figure 4.36 the automated placement of clustering initiation seed points is illustrated. We used a maximum of 10 automatically drawn sample seeds starting from the center of gravity of the conservative ROIs for each tissue drawn by the physician in advance. We covered both conservative ROI in a broad way using the same manner.

Automatic initialization The fully automated initialization is given in Noe and Gee. (2001) and has been successfully tested. (Equation 4.18, Equation 4.19, Equation 4.20), where GTV describes the gross tumour volume, K the number of clusters, μ_k the mean, σ_k the variance and π_k the fraction of cluster k belonging to the whole Gaussian mixture model (Equation 4.21).

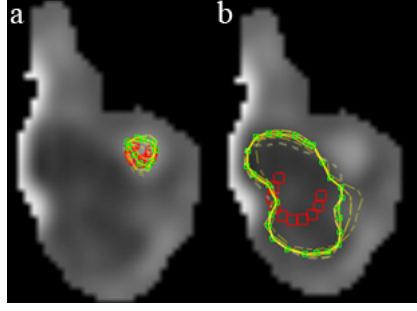


Fig. 4.36: Seed points in concentric circles, drawn around the center of gravity. Here the 10 sample seeds in the low-proliferating part (a) and in the high-proliferating part (b) for the first patient are shown

$$\mu_k = \frac{1}{K+1} \cdot [\max(GTV) - \min(GTV)] + \min(GTV) \quad (4.18)$$

$$\sigma_k = [\max(GTV) - \min(GTV)]^2 \quad (4.19)$$

$$\pi_k = \frac{1}{K} \quad (4.20)$$

$$p(x) = \sum_{k=1}^K \pi_k \mathcal{N}(x | \mu_k, \sigma_k) \quad (4.21)$$

Classification algorithm

For the classification algorithm, we used an Expectation Maximization algorithm (Bishop, 2006, Dempster et al., 1977, Hastie et al., 2009) applied to the normalized histogram of the *GTV* and used a Gaussian mixture model for classification. We used two variations of the EM clustering:

1. The Gaussian mixture model.
2. The Gaussian mixture model with additional partial volume class.

We used a superposition of two Gaussians, represented as a Gaussian mixture model, which is explained by the marginal or total probability $p(x)$ given in [Equation 4.22](#)

$$p(x) = \sum_{k=1}^K p(k) p(x|k) \quad (4.22)$$

More explicitly, if we are aiming to separate a high-proliferating cluster from a low-proliferating one, we can define the explicit marginal probability as denoted in [Equation 4.23](#).

$$p(x) = \pi_h \cdot p(x|h) + \pi_l \cdot p(x|l) \quad (4.23)$$

π_k is denoted as the mixing coefficient and because of the normalizations of the Gaussian components, Equation 4.22 yields for π_k , also known as the prior probability. To quantify the probabilistic ADC, we need the responsibilities or the posterior probability, determined by Equation 4.24. The general approach is described in Equation 3.43 and Equation 3.44 in Section 3.2.2.

$$\gamma_k(x) \equiv p(k|x) = \frac{p(k) \cdot p(x|k)}{\sum_{k=1}^K p(k) \cdot p(x|k)} = \frac{\pi_k \cdot \mathcal{N}(x|\mu_k, \sigma_k)}{\sum_{k=1}^K \pi_k \cdot \mathcal{N}(x|\mu_k, \sigma_k)} \quad (4.24)$$

The calculation of the posterior probability γ_k is also known as the Expectation step, where the members are being assigned to the cluster. The Maximization-Step uses the posterior probability to recalculate the model parameters (π_k, σ_k, μ_k) (Equation 4.25, Equation 4.26, Equation 4.27).

$$\mu_k^{new} = \frac{1}{N_k} \sum_{n=1}^N \gamma_k(x) x_n \quad (4.25)$$

$$\sigma_k^{new} = \frac{1}{N_k} \sum_{n=1}^N \gamma_k(x) (x_n - \mu_k^{new})^2 \quad (4.26)$$

$$\pi_k^{new} = \frac{N_k}{N} \quad (4.27)$$

Now, we do have the following Log-likelihood Equation to maximize:

$$\ln(p(X|\mu, \sigma, \pi)) = \sum_{n=1}^N \ln \left\{ \sum_{k=1}^K \pi_k \mathcal{N}(x|\mu_k, \sigma_k) \right\}. \quad (4.28)$$

N_k is determined in Equation 4.30 and explains the number of probabilistic pixels inside one cluster. N denotes the number of pixels of the whole GTV.

$$\pi_k = \frac{N_k}{N} \quad (4.29)$$

$$N_k = \sum_{n=1}^N \gamma_k(x) \quad (4.30)$$

Probabilistic quantification

The probabilistic quantification is preliminary discussed in [Section 3.2.3](#), including ([Equation 3.55](#), [Equation 3.56](#), [Equation 3.57](#), [Equation 3.58](#)) This quantification can be particularly also used for arbitrary quantities (e.g. the fractional anisotropy), replacing the *ADC* with this arbitrary quantification value, following (Stieltjes et al., 2006).

Then, we could determine the probabilistic mean *ADC* of the cluster \overline{ADC}_{prob} by

$$\overline{ADC}_{prob} \approx \overline{MD}_{prob} = \frac{1}{N_k} \cdot \sum_{n=1}^N \gamma_k(x_n) \cdot ADC(x_n) \quad (4.31)$$

Moreover, we determined the statistical errors for the mean values caused by image noise by calculating probabilistic second moments ([Equation 4.32](#)). Furthermore, we calculated the standardized probabilistic third ([Equation 4.33](#)) and fourth moments ([Equation 4.34](#)) to get additional information of the output probability distribution. The probabilistic volume ([Equation 4.35](#)) was calculated to get more information about the cluster size itself.

$$\mu_{prob}^2 = \frac{1}{N_k} \cdot \sum_{n=1}^N (x_n - \overline{ADC}_{prob})^2 \cdot \gamma(x_n) \quad (4.32)$$

$$\mu_{prob}^3 = \frac{\frac{1}{N_k} \cdot \sum_{n=1}^N (x_n - \overline{ADC}_{prob})^3 \cdot \gamma(x_n)}{\sigma_{prob}^3} \quad (4.33)$$

$$\mu_{prob}^4 = \frac{\frac{1}{N_k} \cdot \sum_{n=1}^N (x_n - \overline{ADC}_{prob})^4 \cdot \gamma(x_n)}{\sigma_{prob}^4} \quad (4.34)$$

$$volume_{prob} = N_k \cdot voxelsize^3 \quad (4.35)$$

The Gaussian mixture model with additional partial volume class was introduced in Noe and Gee. (2001). The complete model is described by three prior probabilities or mixing coefficients denoted for high-proliferating tumour, for low-proliferating tumour and for the mixture class to describe the partial volume effect class. Because of the normalization of the mixture class, the sum of

the prior probabilities or mixture parameters is 1. The signal of the mixture class is denoted as

$$S_m = (1 - \rho) \cdot S_l + \rho \cdot S_h \quad (4.36)$$

[Equation 4.36](#) can be understood as a relative fraction of each tissue represented within the image voxels (Noe and Gee., 2001). In this case, S represents the $\langle ADC \rangle$. Now, we do not have a superposition of only Gaussians any more. Instead we define the explicit marginal probability $p(x)$ by [Equation 4.37](#).

$$p(x) = \pi_h \cdot p(x|h) + \pi_l \cdot p(x|l) + \pi_m \cdot p(x|m) \quad (4.37)$$

$p(x|h)$ and $p(x|l)$ are modelled by Gaussian distributions, and $P(x|m)$ is modelled with the assumption that the mixture parameter ρ is uniformly distributed (Noe and Gee., 2001) as given in [Equation 4.38](#).

$$p(x|m) = \frac{1}{\sqrt{2\pi}} \int_0^1 \frac{1}{\sqrt{\rho^2 \sigma_l^2 + (1 - \rho)^2 \sigma_h^2}} e^{-0.5 \left(\frac{[x - [(1 - \rho) \cdot \mu_h + \rho \cdot \mu_l]]^2}{[(1 - \rho)^2 \cdot \sigma_h^2 + \rho^2 \cdot \sigma_l^2]} \right)} d\rho \quad (4.38)$$

The probabilistic quantification can be performed by ([Equation 4.24](#), [Equation 4.32](#), [Equation 4.33](#), [Equation 4.34](#) and [Equation 4.35](#)).

Application of the functional imaging technique such as perfusion as additional information

This section explains the 'Segmentation' and 'Quantification' concerning the additional functional imaging technique.

Segmentation

A region of interest was manually delineated by two experienced neuroradiologists to cover the enhancing lesion with approximately 1 cm of distance. A percentile thresholding algorithm was being applied on the integral of the probability density of the histogram to determine the upper bend and lower bend of the intensity to calculate the highest malignant fraction of the image f ([Equation 4.39](#)).

$$f = \left(\frac{1}{p} \right) \quad (4.39)$$

The normalized probability density is determined by [Equation 4.40](#) where n_g denotes the number of pixels having grayscale intensity g and n determines the total number of pixels.

$$p(g) = \left(\frac{n_g}{n}\right) \quad (4.40)$$

The cumulative normalized sum is calculated by [Equation 4.41](#).

$$c(g) = \int_0^g p(g) \quad (4.41)$$

To set the lower percentile bend of *ADC*, the threshold of the segmentation is set by [Equation 4.42](#).

$$c(T) = \frac{1}{p} \quad (4.42)$$

In the case of *rCBV*, we used the inverted image and performed the same percentile thresholding as in the *ADC* case to determine the upper bend of the histogram. Due to performance issues considering the fine trilinear interpolated voxelsize, we had to restrict the percentile thresholding and the quantification onto the given *GTV* slice and no thresholding or quantification on a large *VOI* was possible.

Exemplarily, we chose 30 % of the highest malignant regions in the two functional acquisitions.

Quantification

The quantification consists of the calculation of the following similarity indices onto the binarization of all of the resulting images.

- The Jaccard index: [Equation 4.43](#) (Jaccard, 1912) where *I* is determined by [Equation 4.44](#) and *U* denoted by [Equation 4.45](#) ([Equation 3.60](#)).
- The probability of the intersection pertaining to the full *GTV* segmentation of *ADC* and *rCBV*, is denoted by p_{rCBV} and p_{ADC} , respectively.
- The probability of the intersection pertaining to the mean of the full *GTV* segmentation of *ADC* and *rCBV*, respectively, is described by $\langle p_{rCBVADC} \rangle = \frac{|I|}{\frac{(ADC+rCBV)}{2}}$
- The quantification of the *ADC* and *rCBV*, which means, **number of voxels**, **min value**, **max value**, σ and μ , are calculated onto the full *GTV*, on $|I|$ projected on the *ADC* and *rCBV* and $|U|$ projected on *ADC* and *rCBV*.

$$J(ADC, rCBV) = \frac{|I|}{|U|} \quad (4.43)$$

$$I = ADC \cap rCBV \quad (4.44)$$

$$U = ADC \cup rCBV \quad (4.45)$$

$$p_{rCBV} = \frac{|I|}{rCBV} \quad (4.46)$$

$$p_{ADC} = \frac{|I|}{ADC} \quad (4.47)$$

4.3.2 Application of the IVIM model and reproducible derived parameters in diffusion weighted images

The postprocessing of the IVIM model and the reproducible derived parameters is depicted in this section. Firstly, in 'Registration', the registration process is elucidated in further detail and 'Quantification' depicts the quantification procedure.

Registration

We used an automatic serial linear rigid registration approach using normalized mutual information ([Section 3.2.5](#)) and a downhill simplex algorithm as an optimizer (Maes et al., 1997, Viola and Wells III, 1997). It has been applied onto the unweighted imagevector $\vec{u} = u_2 \cdots u_{10}$ onto u_1 in the set due to a higher signal to noise ratio. The transformation matrices \mathcal{T}_u can be applied interchangeably onto the weighted images due to an acquisition within the same breathhold and \mathbf{b} value prototype.

In the second approach, we limited the area used by the similarity measure by applying a 3D bounding box as a clipping region. This can be described as the local serial linear rigid registration approach.

Quantification

The following IVIM derived parameters have been determined: The mean ADC, calculated by using the following approaches:

1. Calculating the mean *ADC* by application of a linear least squares method (Elpelt and Hartung, 1992) (Equation 4.49) and a QR decomposition (Bishop, 2006, Hastie et al., 2009) for numerical stability using the following model, where the image vector \vec{y} consists of the normalized signals (Equation 4.48) in their respective breath hold phase. In a bi-exponential behavior of the signal decay, we use no restriction of the regression through (0,0), since the signal is approximated better in the non restricted model.
2. Calculating the mean *ADC* by using a (0,0) restriction using the fixed model (Equation 4.50). This model is being used if the signal is strongly linearly. From a physical point of view, the 0 value is artificially determined by normalization and has no standard deviation, so that it has to be preferred.

The minimization is being performed in both cases by applying Equation 4.51.

$$\ln(s_n) = \frac{\ln(s_i)}{\ln(s_0)} \quad (4.48)$$

$$\vec{y} = \begin{pmatrix} \ln(s_1) \\ \ln(s_2) \\ \vdots \\ \ln(s_n) \\ 0 \end{pmatrix} = \begin{pmatrix} 1 & b_1 \\ 1 & b_2 \\ \vdots & \vdots \\ 1 & b_n \\ 1 & 0 \end{pmatrix} \cdot \begin{pmatrix} \hat{\alpha} \\ \hat{\beta} \end{pmatrix} + \begin{pmatrix} e_1 \\ e_2 \\ \vdots \\ e_n \\ 0 \end{pmatrix}, X = \begin{pmatrix} 1 & b_1 \\ 1 & b_2 \\ \vdots & \vdots \\ 1 & b_n \\ 1 & 0 \end{pmatrix}, \hat{\theta} = \begin{pmatrix} \hat{\alpha} \\ \hat{\beta} \end{pmatrix} \quad (4.49)$$

$$\vec{y} = \begin{pmatrix} \ln(s_1) \\ \ln(s_2) \\ \vdots \\ \ln(s_n) \end{pmatrix} = \begin{pmatrix} b_1 \\ b_2 \\ \vdots \\ b_n \end{pmatrix} \cdot \hat{\beta} + \begin{pmatrix} e_1 \\ e_2 \\ \vdots \\ e_n \\ 0 \end{pmatrix}, X = \begin{pmatrix} b_1 \\ b_2 \\ \vdots \\ b_n \\ 0 \end{pmatrix} \quad (4.50)$$

$$\hat{\theta} = ((X^T \cdot X)^{-1}) \cdot X^T \cdot \vec{y} \Leftrightarrow \hat{\theta} = X^+ \cdot \vec{y} \quad (4.51)$$

The derived perfusion fraction f and the pure diffusion constant D have been determined by using a non-linear least squares approach by means of Levenberg Marquardt minimization of the residuals of the *IVIM* Equation (Equation 4.52) (Marquardt, 1963). The Jacobian Matrix \mathcal{J} is denoted by Equation 4.53 and has been used as an analytically determined descent using the partial derivatives in Equation 4.54. The minimization has been performed onto the normalized signals given in Equation 4.48.

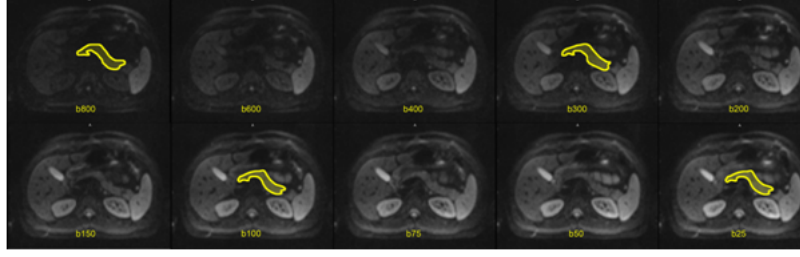


Fig. 4.37: Pancreas delineation in 2D on 3 sample ROIs $b_{100}, b_{300}, b_{800}$. b_{25} has been chosen as a reference ROI

$$\frac{S}{S_0} = (1 - f) \cdot e^{-b \cdot D} + f \cdot e^{-b \cdot (D + D^*)} \quad (4.52)$$

$$\mathcal{J}_{IVIM}(f, D, D^*) = \begin{pmatrix} \frac{\partial s_n}{\partial f} & \frac{\partial s_n}{\partial D} & \frac{\partial s_n}{\partial D^*} \\ \frac{\partial s_n}{\partial f} & \frac{\partial s_n}{\partial D} & \frac{\partial s_n}{\partial D^*} \\ \vdots & \vdots & \vdots \\ \frac{\partial s_n}{\partial f} & \frac{\partial s_n}{\partial D} & \frac{\partial s_n}{\partial D^*} \end{pmatrix} \quad (4.53)$$

$$\left[\begin{array}{c} \frac{\partial}{\partial f} = -e^{(-b \cdot D)} + e^{(-b \cdot (D + D^*))} \\ \frac{\partial}{\partial D} = -(1 - f) \cdot e^{(-b \cdot D)} b - f \cdot e^{(-b \cdot (D + D^*))} D \cdot b \cdot (D + D^*) \\ \frac{\partial}{\partial D^*} = -f \cdot e^{(-b \cdot (D + D^*))} \cdot D \cdot b \cdot (D + D^*) \end{array} \right] \quad (4.54)$$

The initialization values for the Levenberg Marquardt algorithm were determined as $f_{start} = 0.1$, for $d_{start} = 0.001$ and for $D^*_{start} = 0.01$. In the process, we used the following technique to derive the parameters: The perfusion fraction f and the pure diffusion coefficient D were free parameters, whereas the pseudo diffusion coefficient D^* was fixed to $20 \frac{\mu m^2}{ms}$, inferred from preliminary experiments of five healthy volunteers where all parameters were fitted.

The quantification values onto the specific VOI consist of **number of voxels**, **min value**, **max value**, μ and σ .

Evaluation

The significance of the reproducibility of f and the other *IVIM* derived parameters were proved by a Wilcoxon signed-rank test (Elpelt and Hartung, 1992). Moreover, the spatial alignment and therewith the plausibility of the image stack has been tested equivalently by this test. For this purpose, an overlap probability of the volume for the 4 images has been determined before and after the registration by [Equation 4.58](#). This method has been applied externally by a foreign software and the test has been performed by Graf et al. (2010).

$$\text{Let } P \text{ be a } m \times n \times o \text{ matrix.} \quad (4.55)$$

$$\text{and } X_i \text{ the matrix of image } i. \quad (4.56)$$

$$p_{ijk} = \frac{X_1 + X_2 + X_3 + X_4}{4} \quad (4.57)$$

$$\text{Overlap} = \frac{\sum_{i=1}^m \sum_{j=1}^n \sum_{k=1}^o p_{ijk}}{m \cdot n \cdot o} \quad (4.58)$$

Results

The results concerning the two basic studies are described here. Firstly, the evaluation of the glioma study is reported in 'A reproducible separation and quantification of high- and low-proliferative areas in gliomas' ([Section 5.1](#)). Secondly, The IVIM study evaluation is explained in 'The IVIM model and reproducible derived parameters' ([Section 5.2](#)).

5.1 A reproducible separation and quantification of high- and low-proliferative areas in gliomas

Firstly, this section entails the statistical test concerning the conservative ROIs and the ADC distribution analysis to prove the Gaussianity of the different clusters, given in [Section 5.1.1](#) and is further separated into a qualitative (1) ([Section 5.1.2](#)) and a quantitative evaluation (2) ([Section 5.1.3](#)).

5.1.1 Indication of conservative ROIS and ADC distribution analysis

The conservative ROIs to delineate high-proliferative and low-proliferative areas have been drawn by an experienced radiologist to indicate samples for these areas and to get an idea about the probability distribution in the different areas. In [Figure 5.1](#), the ADC distribution of conservative ROIs, averaged over 10 patients including high- and low-proliferating areas, is depicted. The averaging of the histograms is given in [Equation 5.1](#). Two properties can be derived from the two histograms. First, it can be seen that the two ADC distributions have distinct separable peaks. Second, through the application of a full range Gaussian fitting onto the single tumour entities and a χ^2 -test, the ADC distribution can be approximated properly by a Gaussian distribution. The full frequency is being used to achieve enough content in the different voxel value bins so that the χ^2 -test can be applied. This justifies the later use of a Gaussian mixture

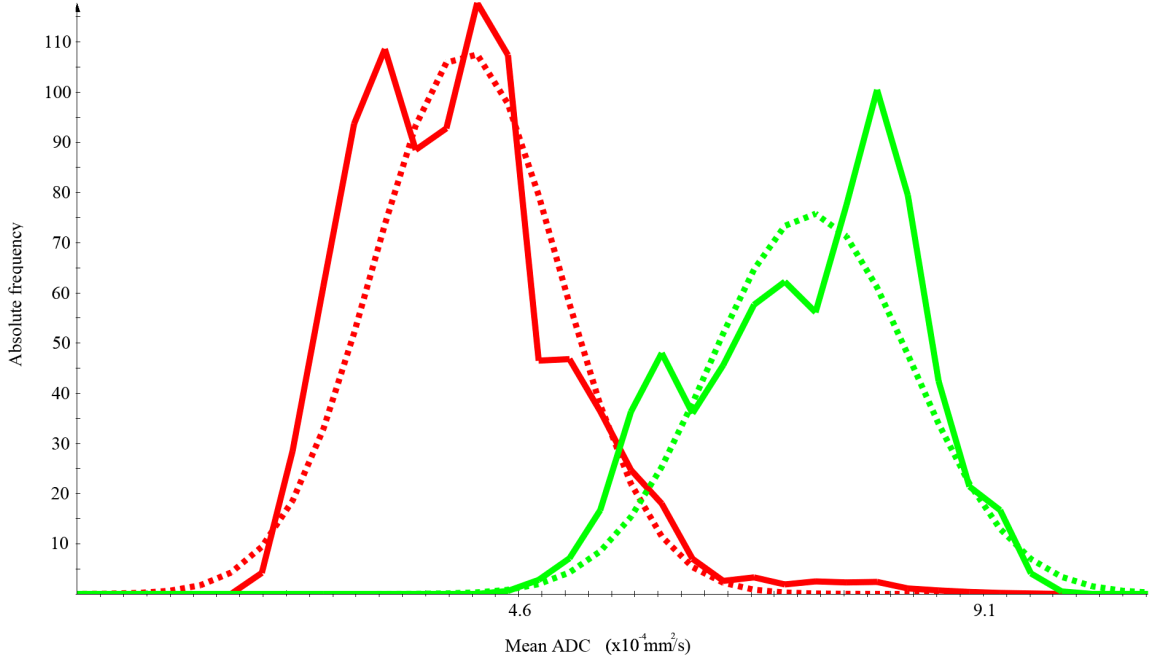


Fig. 5.1: Illustration of the ADC distribution in low- and high-proliferating areas. The red curve shows the ADC distribution in the high-proliferating area, the green curve represents the distribution in the low-proliferating area. Full range Gaussian fits are shown as dashed lines.

model for automated clustering of the two regions. The following values were found (μ denotes the mean value and σ specifies the standard deviation): High-proliferating tissue $\mu = 4.13 \cdot 10^{-4} \frac{mm^2}{s}$; $\sigma = 9.1 \cdot 10^{-5} \frac{mm^2}{s}$, Low-proliferating tissue $\mu = 7.26 \cdot 10^{-4} \frac{mm^2}{s}$; $\sigma = 9.9 \cdot 10^{-5}$. The χ^2 -test yields the following parameters: High-proliferating tissue $\chi^2(0.95; 100 - 3 = 97) = 121 > 89.1961$; Low-proliferating tissue $\chi^2(0.95; 100 - 3 = 97) = 121 > 85.9265$. The histograms with an equidistant discretization of 100 (bin size) \mathcal{H} were averaged and fitted with a Gaussian distribution using the toolkit root (root, CERN, Switzerland). The χ^2 -test was used to prove Gaussian distributions in the different areas using root (root, CERN, Switzerland).

$$\langle \mathcal{H} \rangle = \frac{1}{10} \cdot \sum_{i=1}^{10} \mathcal{H}_i \quad (5.1)$$

5.1.2 Qualitative evaluation

The qualitative evaluation is explained in this section. Firstly, it covers 'The GTV histogram model'. Here, a theoretical histogram model is being evaluated in terms of plausibility. Secondly, the 'Histogram clustering results' are analyzed qualitatively.

The GTV histogram model

Firstly, we constructed a theoretical Gaussian mixture model (Equation 4.21) and tried to elucidate a correlation between the theoretical model (Figure 5.2a) and the averaged GTV retrieved from the 10 patients (Figure 5.2b). The averaged GTV has been calculated by

$$\langle \mathcal{GTV} \rangle = \frac{1}{10} \cdot \sum_{i=1}^{10} \mathcal{GTV}_i \quad (5.2)$$

μ_k and σ_k have been retrieved and approximated by the Gaussian fitting of the averaged histograms given in Figure 5.1. Empirically, we chose the following parameters for the partial components of the Gaussian mixture model $\pi_k: \pi_{high} = 0.4, \pi_{low} = 0.3, \pi_{necrosis} = 0.15, \pi_{csf} = 0.15$. Qualitatively, we can say that the theoretical histogram (Figure 5.2a) consisting of the Gaussian mixture model fits well to the averaged GTV (Figure 5.2b). Thus, we have a further justification of the application of a Gaussian mixture model and the distribution of the components.

Histogram clustering results

In this section, the histogram clustering results are depicted. Firstly, we fill in on the background of the 'Clustering results using the standard Gaussian model' and secondly, the 'Clustering results using the Gaussian model plus partial volume class'.

Clustering results using the standard Gaussian model

The clustering results of three sample patients are illustrated here in consecutive order. The 'First sample patient', the 'Second sample patient' and the 'Third sample patient'.

First sample patient In Figure 5.3, the heterogeneous glioma of the first patient is shown. In (d), it can be clearly recognized that the low-proliferating region is overlapping the cerebrospinalfluid (light blue arrow). In (e), the posterior probability γ_k clustered high-proliferating (red colour) and low-proliferating

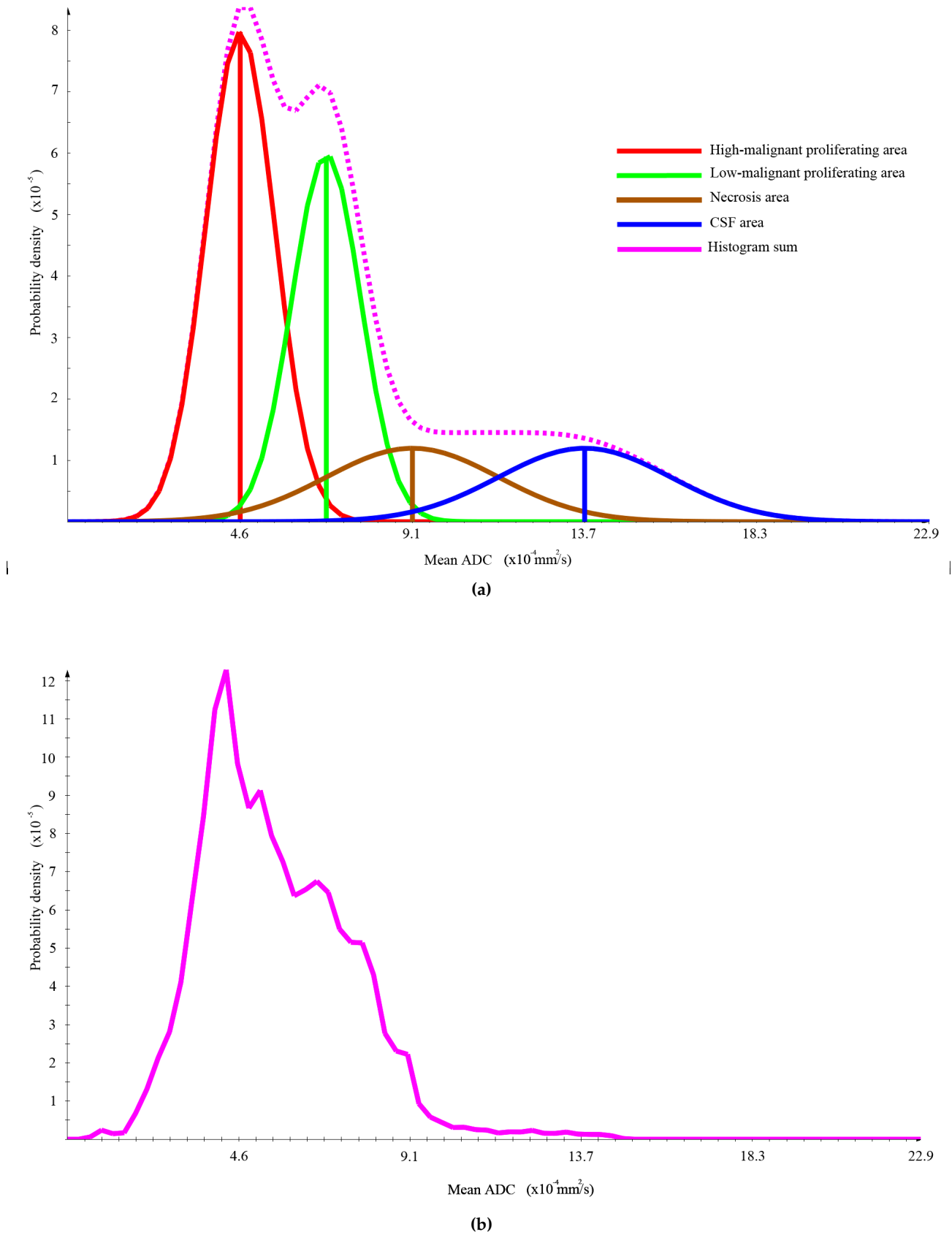


Fig. 5.2: (a) Theoretical histogram (taken from Simon et al. (2011)): Red determines the high-proliferating area, green the low-proliferating region, brown the necrosis area and blue the cerebrospinal fluid. The empirically determined fractions of the Gaussian mixture model are: $\pi_{high} = 0.4$, $\pi_{low} = 0.3$, $\pi_{necrosis} = 0.15$, $\pi_{csf} = 0.15$. The means are $\mu_{high} = 4.6 \cdot 10^{-4} \frac{mm^2}{sec}$, $\mu_{low} = 6.8 \cdot 10^{-4} \frac{mm^2}{sec}$, $\mu_{csf} = 9.2 \frac{mm^2}{sec}$, $\mu_{necrosis} = 13.7 \frac{mm^2}{sec}$. The standard deviations: $\sigma_{high} = 9.1 \cdot 10^{-5}$, $\sigma_{low} = 9.1 \cdot 10^{-5}$, $\sigma_{csf} = 2.3 \cdot 10^{-4}$ (b) Original histogram of GTVs: Consists of the averaged GTVs of the 10 patients

part (green colour) using a Gaussian mixture model and an application of the T2-FLAIR mask in combination with the necrosis threshold is shown (Equation 4.21). The regions are properly separated due to this suppression technique (see yellow arrows). Thanks to the T2-FLAIR mask, the cerebrospinal fluid cannot impede the clustering event within the *GTV* (see yellow arrows). The μ of the probability density (g) corresponds well to the conservative histogram in (f). However, the σ of the low-proliferating Gaussian seems to be higher than the conservative ROI and indicates that the found low-proliferating region exceeds the conservative ROI. In (h), it can be clearly identified that the probability density of the whole *GTV* fits well to the approximated sum of the Gaussians.

Second sample patient In Figure 5.4, we show a patient with a heterogeneous glioblastoma and the applied Gaussian clustering with applied FLAIR mask and necrosis threshold. In the centre of the high-proliferating part, necrosis is indicated by the light blue arrow and the surrounding orange circles. Figure 5.4e shows the clustering result after application of the necrosis threshold. A part of the necrotic areas shows up in the clustering as low-proliferating tumour (green colour). The necrosis threshold could only suppress them, partly. Additional expansion of the necrosis threshold would further reduce this erroneously clustered area but would also cancel out the low-proliferating area due to overlap in the *ADC* distribution of necrosis and low-proliferating tissue. Overall, the necrosis threshold improves the clustering result but is imperfect. (f) shows the conservative high-proliferating ROI and an automatically generated spike in the small apparent low-proliferating region due to a not ascertainable large enough visible conservative ROI. Therefore, the clustering could not be initialized by different seed points. In (g), the μ of the high-proliferating Gaussian (red curve) fits well to the conservative ROI. However, σ of the supposed to be high-proliferating region exceeds the conservative sample. The found low-proliferating μ and σ seem to be completely different compared to the automatic generated spike and indicate a high σ and a lower μ leading to an assumption of a partial volume effect. This assumption is further fortified by a strong similarity to a folded equally distributed partial volume class. The sum in (h) is indicating a proper fit to the histogram probability density.

Third sample patient In Figure 5.5, another heterogeneous glioma is depicted. Due to overlaps in the histogram of high-proliferating tissue and normal tissue (Figure 5.5d (blue arrows)), normal tissue is falsely classified as high-proliferating tumour (Figure 5.5e, yellow arrows). The μ and σ shown in (g) fit well to the conservative ROIs in (f). However, the σ of the high-proliferating curve in (g) exceeds the conservative ROI. In (h), we can see a good approximation of the histogram of the *GTV*.

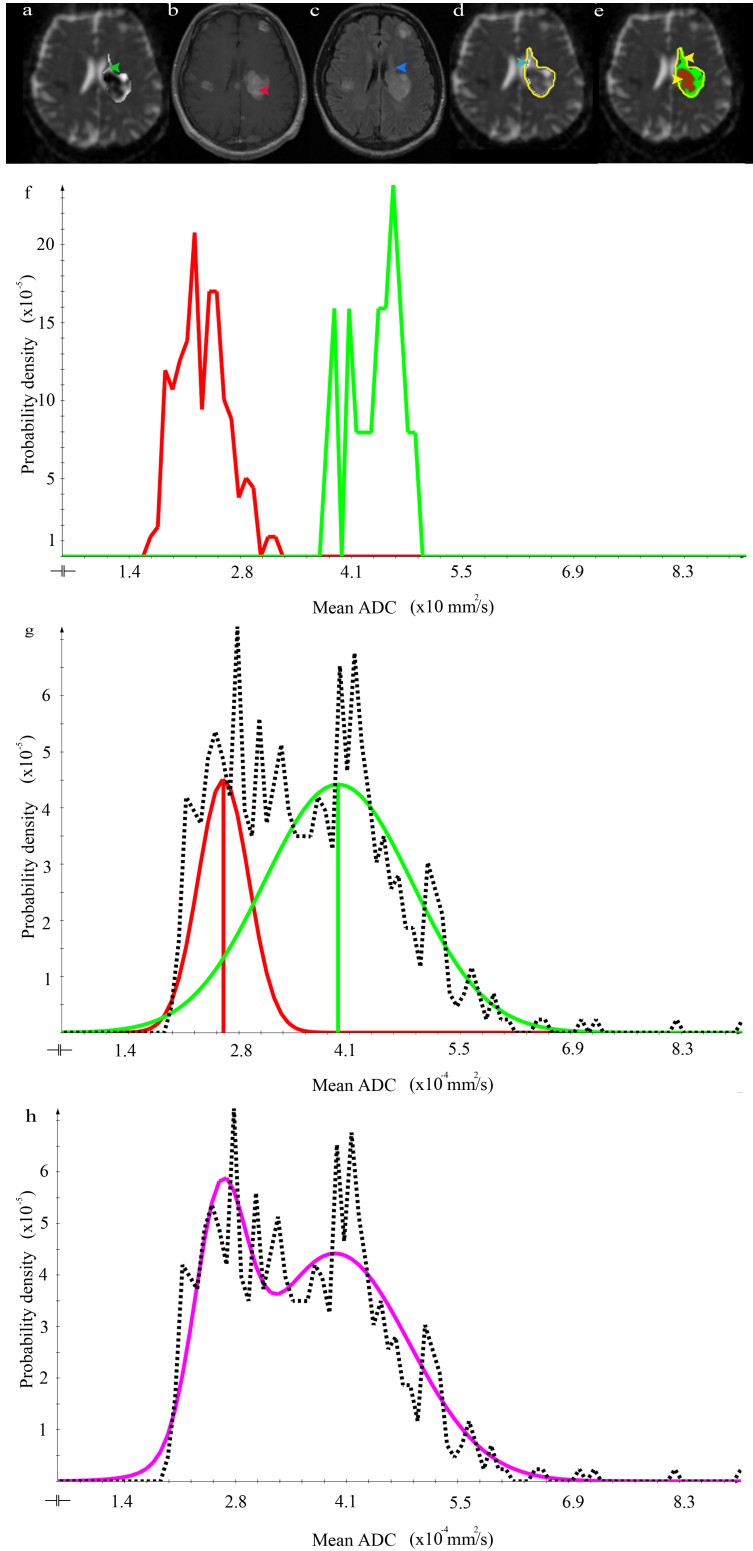


Fig. 5.3: Gauss clustering of first sample patient. (a) Axial ADC map with highlighted LUT within the tumour. The GTV is indicated by the green arrow, (b) Axial contrast enhanced T1-weighted image showing the high-proliferating part of the tumour (indicated by the red arrow). (c) Axial T2-FLAIR image showing the gross tumour volume (indicated by the dark blue arrow). (d) Outlined GTV in ADC map and overlapping cerebrospinal fluid with low-proliferating area of the tumour (see light blue arrow). (e) The ADC map with the clustering result showing the posterior probability using T2-FLAIR mask and necrosis threshold, resulting in a proper delineation (see yellow arrows). The low-proliferating part is indicated by green-colour and the high-proliferating part shows up in red. (f) Probability density histogram showing the conservative ROIs of the physician. The high-proliferating area is indicated by the red curve. The low-proliferating ROI in green. (g) The clustering result using the standard Gaussian mixture model (Equation 4.23). The high-proliferating area is indicated by the red Gaussian curve and the low-proliferating area by the green curve. The mean is highlighted by the vertical lines ($\mu_{high} = 2.6 \cdot 10^{-4} \frac{mm^2}{s}$, $\mu_{low} = 4.0 \cdot 10^{-4} \frac{mm^2}{s}$, $\sigma_{high} = 3.2 \cdot 10^{-5}$, $\sigma_{low} = 9.2 \cdot 10^{-5}$). The fractions of the mixture model are described as $\pi_{high} = 0.26$, $\pi_{low} = 0.74$. The corresponding histogram of the original GTV is shown as the black dashed probability density function. Both μ fit well to the conservative ROI but σ of the low-proliferative Gaussians exceeds the ROI shown in (f). (h) The whole added Gaussian mixture model (Equation 4.21) (magenta) fits well to histogram of the original GTV, the negative Log-likelihood (Equation 4.28) is denoted as -9.38. (taken from Simon et al. (2011))

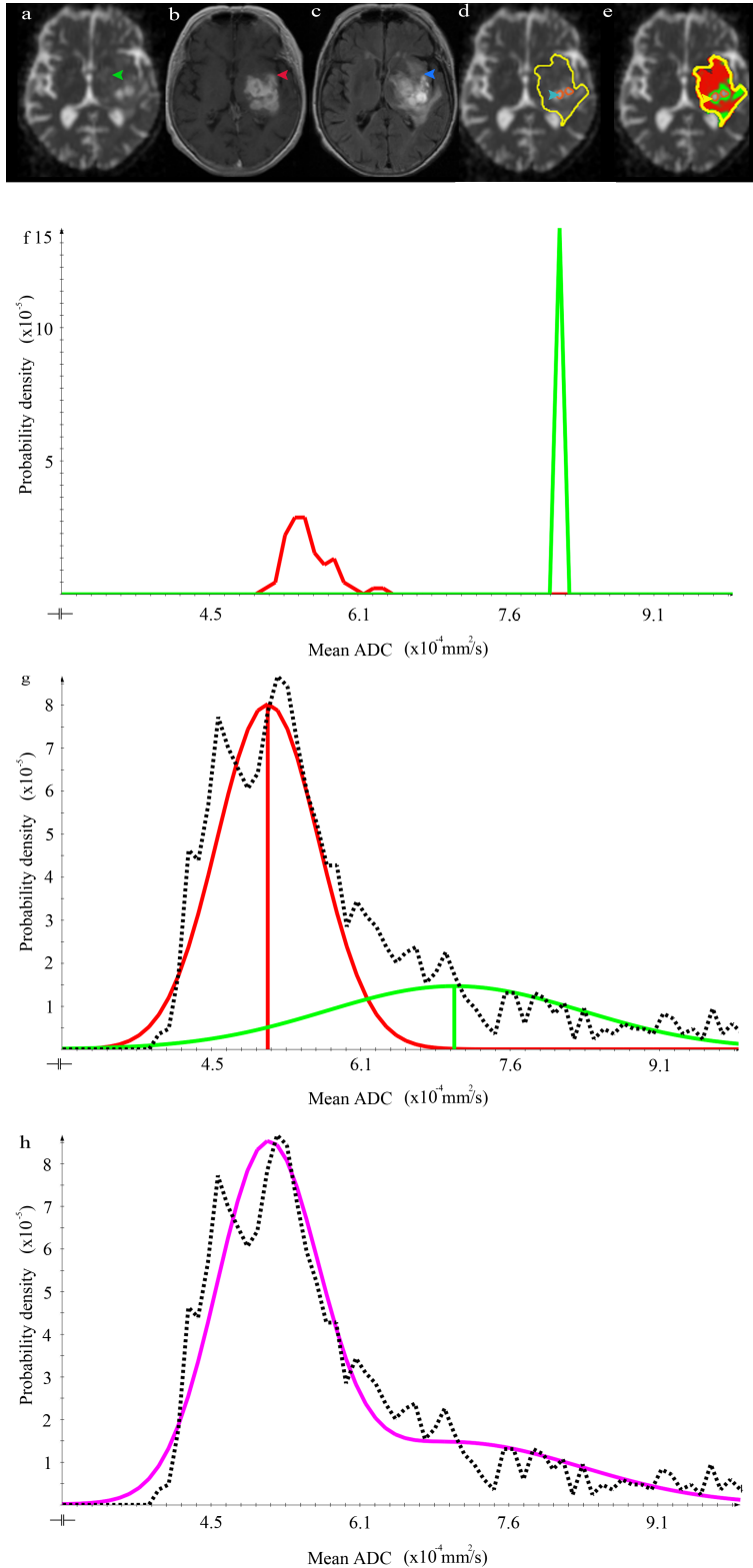


Fig. 5.4: Gauss clustering of second sample patient. (a) Axial ADC map showing the GTV, indicated by the green arrow, (b) Axial contrast enhanced T1-weighted image showing the high-proliferating part of the tumour (indicated by the red arrow). (c) Axial T2-FLAIR image showing the gross tumour volume (indicated by the dark blue arrow). (d) Outlined GTV in ADC map. Necrosis areas are indicated by the light blue arrow, surrounded by the orange circles. (e) The ADC map with the clustering result using model, described by Equation 4.23, with applied T2-FLAIR mask and necrosis threshold, resulting in an improved but imperfect necrosis suppression. The falsely clustered region is indicated by the blue arrow (necrosis is falsely clustered as low-proliferating tissue) (see yellow arrow) (f) Probability density histogram showing the conservative ROIs of the physician. The high-proliferating area is showed by the red curve. The physician could not indicate a proper large enough low-proliferating conservative area. Therefore, we used an automatic initialization (green spike). (g) The clustering result using the standard Gaussian mixture model (Equation 4.23). The high-proliferating area is indicated by the red Gaussian curve and the low-proliferating area by the green curve. μ is highlighted by the vertical lines ($\mu_{high} = 5.1 \cdot 10^{-4} \frac{mm^2}{sec}$, $\mu_{low} = 7.0 \cdot 10^{-4} \frac{mm^2}{sec}$, $\sigma_{high} = 5.1 \cdot 10^{-5}$, $\sigma_{low} = 1.3 \cdot 10^{-4}$). The fractions are determined as $\pi_{high} = 0.68$, $\pi_{low} = 0.32$. The green Gaussian curve is partly consisting of necrosis. μ of the high-proliferating Gaussian fits well to the conservative ROI. However, μ and σ of the low-proliferating Gaussian seem to be completely different. (h) The whole added Gaussian mixture model (Equation 4.21) (magenta) fits with histogram of the original GTV, the negative Log-likelihood (Equation 4.28) is denoted as -9.28 (taken from Simon et al. (2011))

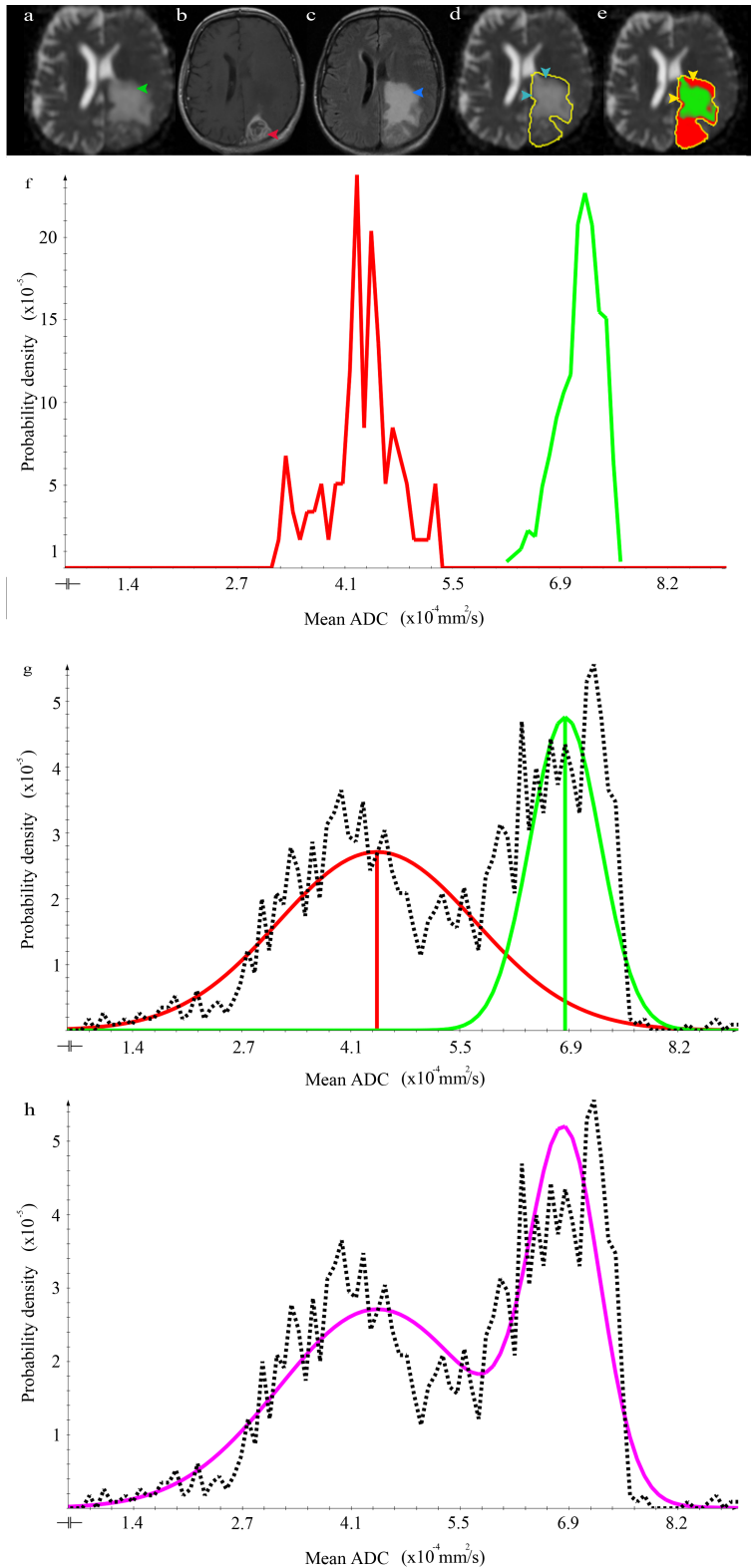


Fig. 5.5: Gauss clustering of third sample patient. (a) Axial ADC map indicating the GTV (green arrow). (b) Axial contrast enhanced T1-weighted image showing the high-proliferating part of the tumour (red arrow). (c) Corresponding axial T2-FLAIR image showing the gross tumour volume (dark blue arrow). (d) Outlined GTV in ADC map. Overlapping high-proliferating tumour with normal tissue is highlighted by the light blue arrows. (e) ADC map with the clustering result as overlay. High-proliferating tumour is clustered in red and low-proliferating tumour is clustered in green. The falsely clustered region is indicated by yellow arrows. (f) Probability density histogram showing the conservative ROIs of the physician. The high-proliferating area is showed by the red curve. The low-proliferating one by the green curve. (g) The clustering result using the standard Gaussian mixture model (Equation 4.23). The high-proliferating area is indicated by the red Gaussian curve and the low-proliferating area by the green curve. The mean is highlighted by the vertical lines. μ of both Gaussian curves fit well to the conservative ROIs, but σ of the high-proliferating clustered Gaussian exceeds the conservative sample ($\mu_{high} = 4.4 \cdot 10^{-4} \frac{mm^2}{sec}$, $\mu_{low} = 6.8 \cdot 10^{-4} \frac{mm^2}{sec}$, $\sigma_{high} = 1.2 \cdot 10^{-4}$, $\sigma_{low} = 4.4 \cdot 10^{-5}$). The fractions are determined as $\pi_{high} = 0.62$, $\pi_{low} = 0.38$ (h) The whole added Gaussian mixture model (Equation 4.21) (magenta) shows a very good approximation of the GTV, the negative Log-likelihood (Equation 4.28) is denoted as -9.68 (taken from Simon et al. (2011))

Clustering results using the Gaussian model plus partial volume class

This section elucidates the three sample patients with Gaussian model plus partial volume class, consecutively. The 'First sample patient', the 'Second sample patient' and finally, the 'Third sample patient' are being depicted.

First sample patient In [Figure 5.6](#), the partial volume approach is used ([Equation 4.37](#)). In (e), we can see the posterior probability γ_k of this model application. The low-proliferating area is indicated by green colour and the partial volume class by the blue colour. The high-proliferating area, depicted by red colour, is suppressed strongly by partial volume and hardly visible. The μ of the probability densities of the Gaussian curves still fit well to the histograms in (f). However, μ of the high-proliferating region is shifted to lower ADC values. Moreover, σ of the low-proliferating curve is still higher than that of the [Figure 5.3](#) and σ of the high-proliferating Gaussian is strongly reduced by the partial volume function. In (h), the sum of the mixture model is shown and still fits well to the histogram. Nonetheless, the spike, resulting from the high-proliferating part, seems to exceed the histogram. Overall, it can be clearly seen that the histogram sum clustering in [Figure 5.3](#) fits better to the original histogram GTV indicated by the black dashed lines.

Second sample patient [Figure 5.7](#) illustrates that the overlap between necrosis and low tumour can potentially be addressed by using the partial volume approach. The remaining falsely classified low-proliferating areas within the necrosis, can be reduced ([Figure 5.7e](#), yellow arrow). On the other hand, other apparent low-proliferating areas are now also classified as partial volume ([Figure 5.7e](#), magenta arrow). In (g), the μ of the high-proliferating Gaussian (red curve) fits well to the conservative ROI. The low-proliferating Gaussian curve is completely suppressed by the blue partial volume mixture and is not visible in the histogram, any more. The approximation in (h) seems to have the same fit to the original GTV histogram compared to [Figure 5.4](#).

Third sample patient In [Figure 5.8](#), the challenges in separation for 'high-proliferating tumour versus normal tissue' (Simon et al., 2009) are depicted and addressed by application of partial volume clustering. Due to overlaps in the histogram of high-proliferating tissue and normal tissue, normal tissue is falsely classified as high-proliferating tumour ([Figure 5.5c](#), yellow arrows). To overcome this problem, we used the partial volume clustering (Noe and Gee., 2001) assuming that the main part of the falsely clustered region can be understood as a partial volume effect between normal tissue and high-proliferating tissue. After application of this approach, the erroneous regions are reduced; however, there is still a small overlapping region between high-proliferating tumour and normal tissue. Interestingly, in the posterior part there seems to be a mixture

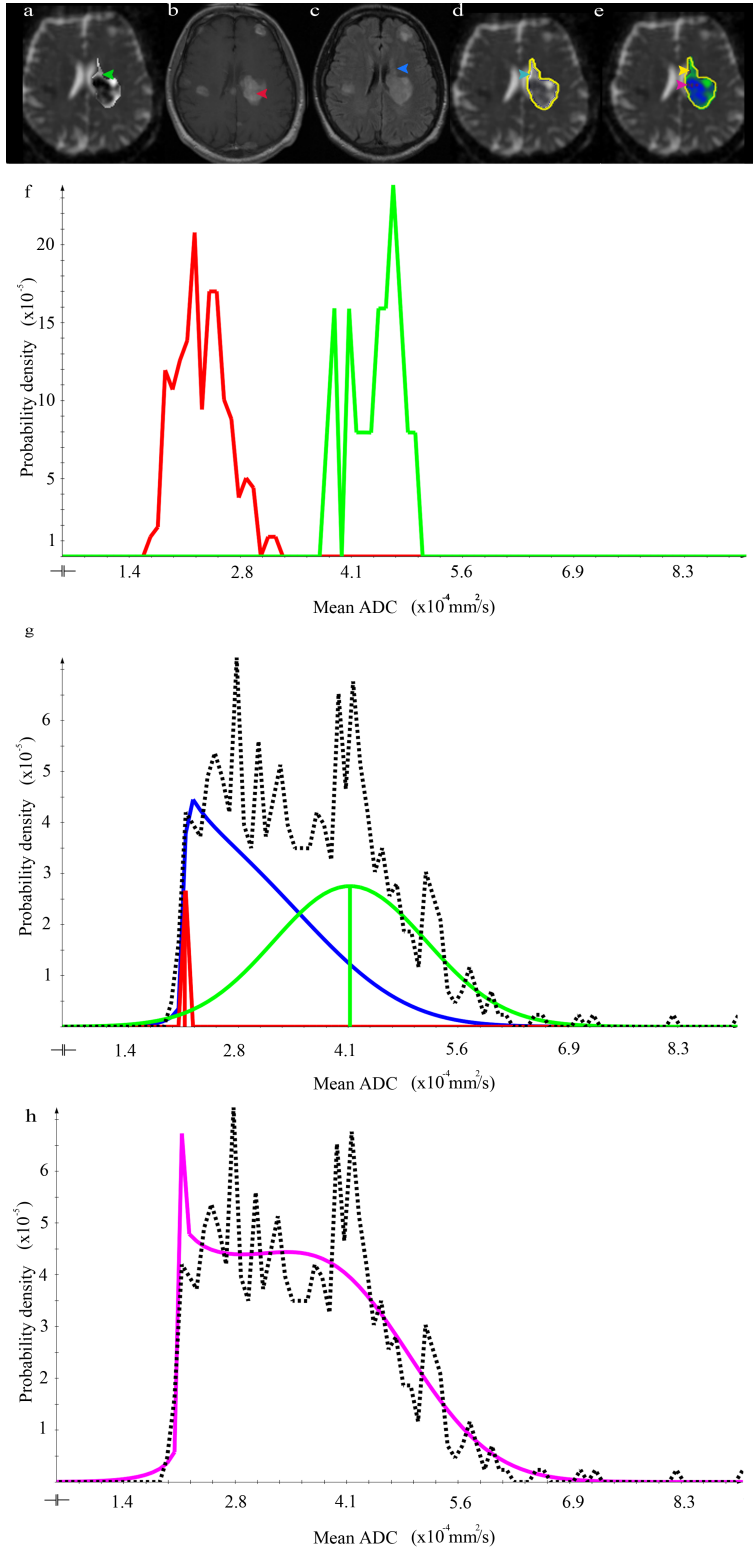


Fig. 5.6: Partial volume clustering of the first patient. (a) Axial ADC map indicating the GTV (green arrow). (b) T1-weighted image plus CA showing the high-proliferating part of the tumour (red arrow). (c) T2-FLAIR image showing the GTV (dark blue arrow). (d) Outlined GTV in ADC map. Overlapping low-proliferating tumour with CSF is highlighted by the light blue arrows. (e) ADC map with clustering result as overlay using the partial volume model. High-proliferating tumour is clustered in red and low-proliferating tumour in green. The partial volume class is indicated by the blue area and suppresses the high-proliferating tumour. The CSF cut off through T2-FLAIR mask is indicated by the yellow arrow. The magenta arrow indicates the rest of the high malignant tumour. (f) Histogram showing the conservative ROIs of the physician. The high-proliferating area is showed by the red curve. The low-proliferating by the green curve. (g) The clustering result using the partial volume mixture model (Equation 4.37). The high-proliferating area is indicated by the red curve and the low-proliferating by the green curve. The partial volume class is indicated by the blue function. μ is highlighted by the vertical lines. μ and σ of both Gaussian curves fit well to the conservative ROIs, but σ of the high-proliferating clustered Gaussian exceeds the conservative sample ($\mu_{high} = 2.1 \cdot 10^{-4} \frac{mm^2}{sec}$, $\mu_{low} = 4.1 \cdot 10^{-4} \frac{mm^2}{sec}$, $\sigma_{high} = 1.5 \cdot 10^{-6}$, $\sigma_{low} = 9.6 \cdot 10^{-5}$). The fractions are denoted as follows: $\pi_{high} = 0.01$, $\pi_{low} = 0.4$, $\pi_{pV} = 0.51$. Furthermore, the range of the high-proliferating area is strongly reduced due to the partial volume class, so that σ does not fit any more to the high-proliferating sample in (g). (h) The whole Gaussian mixture model (Equation 4.21) (magenta) shows a good approximation of the GTV. The negative Log-likelihood (Equation 4.28): -9.36. However, the spike of the high-proliferating Gaussian exceeds the histogram.

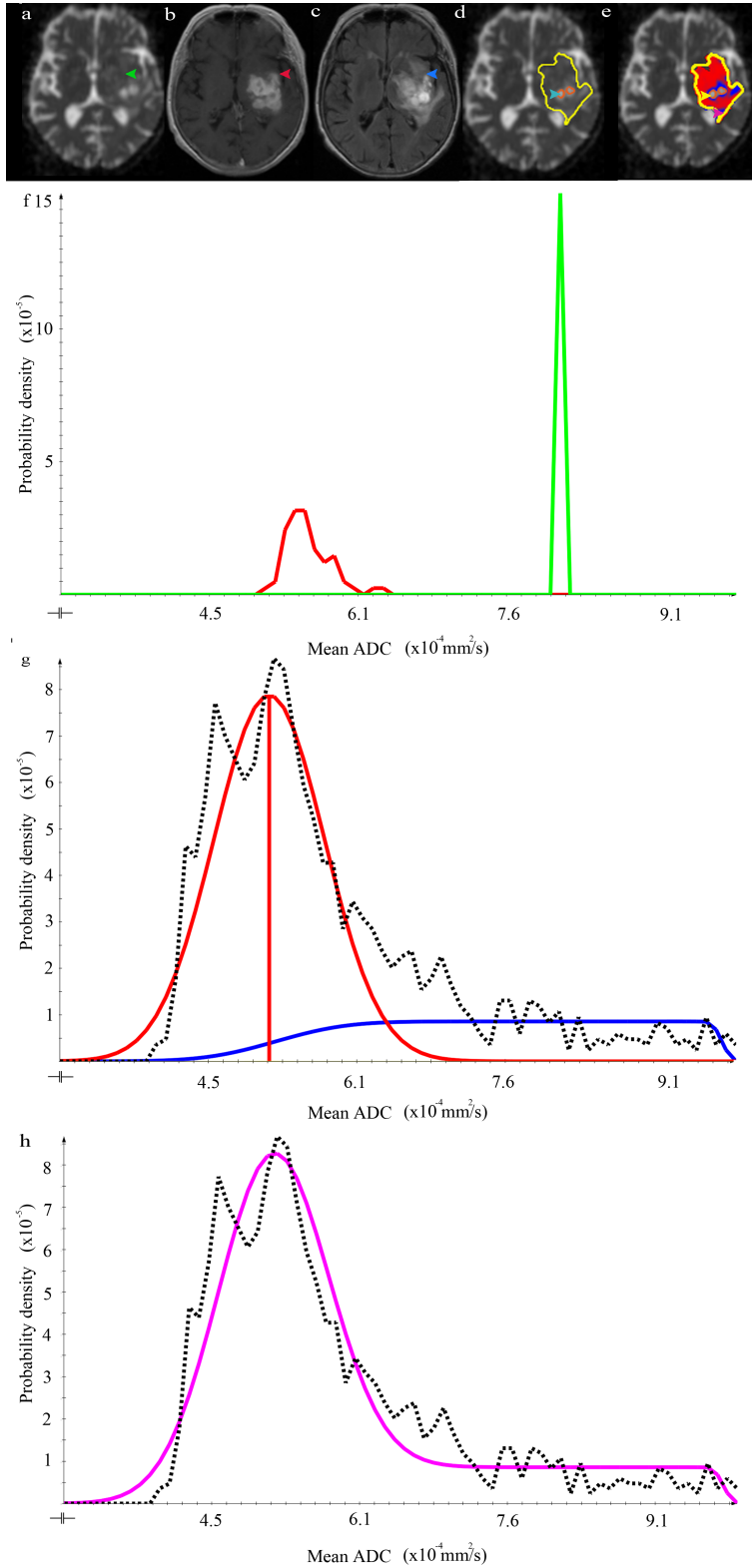


Fig. 5.7: Partial volume clustering of the second patient. (a) Axial ADC map image showing the GTV of the tumour (green arrow) (b) Axial contrast enhanced T1-weighted image showing the high-proliferating part of the tumour (red arrow). (c) Corresponding axial T2-FLAIR image showing the gross tumour volume (dark blue arrow) (d) Outlined GTV in ADC map. Necrosis areas are indicated by the light blue arrow, surrounded by the orange circles. (e) ADC map, applied PV clustering using uniformly distributed parameter to fold mixture class $p(a|m)$. High-proliferating tumour is clustered in red, partial volume leads to a clustered blue region. Surprisingly, no low proliferating tissue can be found (Equation 4.37). (f) Probability density histogram showing the conservative ROIs of the physician. The high-proliferating area is showed by the red curve. The physician could not indicate a proper large enough low-proliferating conservative area. Therefore, we used an automatic initialization (green spike). (g) The clustering result using the PV mixture model (Equation 4.23). The high-proliferating area is indicated by the red Gaussian curve and the low-proliferating area by the green curve. The PV clustering is shown by the blue curve. μ is highlighted by the vertical lines ($\mu_{high} = 5.2 \cdot 10^{-4} \frac{mm^2}{sec}$, $\mu_{low} = 9.9 \cdot 10^{-4} \frac{mm^2}{sec}$, $\sigma_{high} = 5.7 \cdot 10^{-5}$, $\sigma_{low} = 5.2 \cdot 10^{-6}$). The fractions are determined as $\pi_{high} = 0.74$, $\pi_{low} = 3.4 \cdot 10^{-5}$, $\pi_{PV} = 0.26$. μ of the high-proliferating Gaussian fits well to the conservative ROI. Through the strong partial volume suppression, μ and σ of the low-proliferating Gaussian is not visible any more. The partial volume curve in blue seems to cover the whole remaining area. (h) The whole added Gaussian mixture model (Equation 4.21) (magenta) fits with histogram of the original GTV, the negative Log-likelihood (Equation 4.28) is denoted as -9.28

between high-proliferating tumour and low-proliferating tumour, resulting in a relative fractional content in these voxels. The μ and σ shown in (g) still fit well to the conservative ROIs in (f). However, the σ of the high-proliferating curve in (g) still exceeds the conservative ROIs. The low-proliferating curve is strongly reduced by the partial volume assumption. In (h), we can see a good approximation of the histogram of the GTV, similar to [Figure 5.5](#) but with a reduced low-proliferating characteristic.

5.1.3 Quantitative evaluation

The qualitative assumptions in the last chapter are further supported by a quantitative analysis pertaining to 'The GTV histogram model' and the 'Histogram clustering results'. Furthermore, a statistical test is elaborated in 'Statistical analysis of clustering results'. Eventually, the result of an automatic initialization approach (Noe and Gee., 2001) is described in 'Result of automatic initialization approach'.

The GTV histogram model

In [Section 5.1.2](#), we elucidated the qualitative correlation between the theoretical Gaussian mixture model ([Figure 5.2a](#)) and the averaged original histogram of the GTV ([Figure 5.2b](#)). In this step, we tried to scrutinize if these histograms have plausible μ and fit well to values derived from literature. In Higano et al. (2006), the range of minimum ADC values in glioblastomas is depicted. The minimum range of the ADC is denoted as $6.2 - 11 \cdot 10^{-4} \frac{mm^2}{sec}$ and fits to the histograms. An example of necrosis could be found in Asao et al. (2005). The minimum value of the ADC necrosis group is determined as $10.4 \cdot 10^{-4} \frac{mm^2}{sec}$. The μ value of the cerebrospinal fluid matches well to Raffin et al. (2001). The range of the ADC is determined as $11.2 - 35.0 \cdot 10^{-4} \frac{mm^2}{sec}$.

Histogram clustering results

In this section, the clustering results concerning the 'standard Gaussian model' and the 'Clustering results using the Gaussian model plus partial volume class' are being elaborated.

Clustering results using the standard Gaussian model

Here, the clustering results of the three sample patients using the standard Gaussian model are being depicted in consecutive order. The 'First sample patient', the 'Second sample patient' and the 'Third sample patient'.

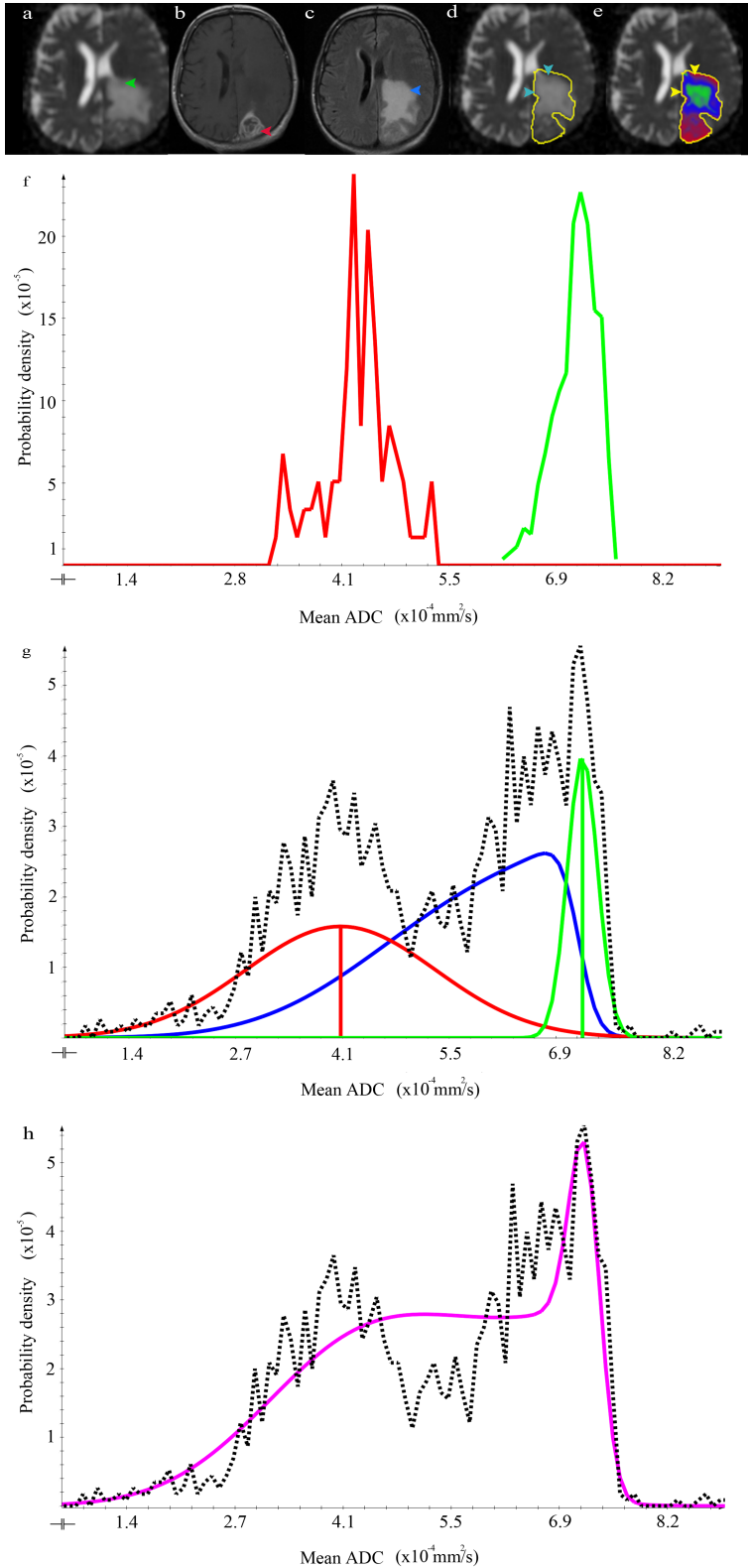


Fig. 5.8: (a) Axial ADC map showing the GTV of the tumour (green arrow). (b) Corresponding contrast enhanced T1-weighted image showing the high-proliferating part of the tumour (red arrow). (c) Axial T2-FLAIR image showing the gross tumour volume (dark blue arrow). (d) Outlined GTV in ADC map. Overlapping high-proliferating tumour with normal tissue is highlighted by the light blue arrows. (e) ADC map with the clustering result as overlay. Here, PV clustering was applied using uniformly distributed parameter ρ to fold mixture class $p(a|m)$. High-proliferating tumour is clustered in red, partial volume in blue and green depicts the low-proliferating part. The red arrow depicts the remaining but strongly reduced areas with a clustering error at the interface of low-proliferating tumour and healthy tissue. (f) Probability density histogram showing the conservative ROIs of the physician. The high-proliferating area is shown by the red curve. The low-proliferating one by the green curve. (g) The clustering result using the partial volume mixture model (Equation 4.37). The high-proliferating area is indicated by the red Gaussian curve and the low-proliferating area by the green curve. Partial volume is indicated by the blue curve. The mean is highlighted by the vertical lines. μ of both Gaussian curves still fit well to the conservative ROIs compared to Figure 5.5, but σ of the high-proliferating clustered Gaussian still exceeds the conservative sample. The partial volume curve suppresses a part of the low malignant tumour part ($\mu_{high} = 4.1 \cdot 10^{-4} \frac{mm^2}{sec}$, $\mu_{low} = 7.2 \cdot 10^{-4} \frac{mm^2}{sec}$, $\sigma_{high} = 1.2 \cdot 10^{-4}$, $\sigma_{low} = 1.9 \cdot 10^{-5}$). The fractions are determined as $\pi_{high} = 0.62$, $\pi_{low} = 0.38$, $\pi_{PV} = 0.50$. (h) The whole added Gaussian mixture model (Equation 4.21) (magenta) shows still a very good approximation of the GTV and similar to Figure 5.5, the negative Log-likelihood (Equation 4.28) is denoted as -9.68.

First sample patient The qualitative assumptions for [Figure 5.3](#) are further fortified by the quantitative parameters μ and σ . $\mu_{high} = 2.5 \cdot 10^{-4} \frac{mm^2}{sec}$ and $\mu_{low} = 4.0 \cdot 10^{-4} \frac{mm^2}{sec}$ fit to the ranges given by the conservative ROIs. μ_{high} seems to have a complete match with the μ derived from the conservative ROI. $\sigma_{low} = 3.2 \cdot 10^{-5}$ exceeds the conservative ROI sample but important is that it is not smaller than the given sample.

Second sample patient The hypotheses made in [Figure 5.4](#) are further supported by the parameters of μ and σ . μ_{high} of $5.1 \cdot 10^{-4} \frac{mm^2}{sec}$ fits in the range of the high-proliferating conservative ROI. μ_{low} of $7.0 \cdot 10^{-4} \frac{mm^2}{sec}$ is strongly shifted to the right compared to the conservative low-proliferating ROI. $\sigma_{high} = 5.1 \cdot 10^{-5}$ exceeds the conservative ROI. $\sigma_{low} = 1.3 \cdot 10^{-4} \frac{mm^2}{sec}$ is a very high standard deviation and no real peak can be found in the histogram of the GTV.

Third sample patient The quantitative evaluation of [Figure 5.5](#) supports the qualitative evaluation. $\mu_{high} = 4.4 \cdot 10^{-4} \frac{mm^2}{sec}$ and $\mu_{low} = 6.8 \frac{mm^2}{sec}$ fit perfectly well to the μ of the conservative ROIs in (f). The high $\sigma_{high} = 1.2 \cdot 10^{-4}$ exceeds the conservative ROI and $\sigma_{low} = 4.4 \cdot 10^{-5}$ matches perfectly well to the given sample.

Clustering results using the Gaussian model plus partial volume class

The quantitative measurements of the three sample patients are being depicted in this section in ascending order. The 'First sample patient', the 'Second sample patient' and the 'Third sample patient'.

First sample patient The qualitative analysis of [Figure 5.6](#) is further fostered by a quantitative evaluation. The difference between μ of the two areas is denoted as $5.0 \cdot 10^{-5} \frac{mm^2}{sec}$. The low-proliferating shift of μ results in $1.0 \cdot 10^{-5} \frac{mm^2}{sec}$. The strong suppression of the high-proliferating part is denoted by σ of approximately 95 %. $\sigma_{PVclustering}^{low} = 9.6 \cdot 10^{-5}$ has changed slightly by $4.0 \cdot 10^{-6}$. The assumption that [Figure 5.3](#) fits better to the original histogram GTV is further fortified by an improvement of the Log-likelihood of 0.02.

Second sample patient A further continuation of the qualitative analysis for [Figure 5.7](#) is made here quantitatively. The complete suppression of the low-proliferating area can be seen by a very high $\mu_{PVclustering}^{low} = 9.9 \cdot 10^{-4} \frac{mm^2}{sec}$, a very

low $\sigma_{PVclustering}^{low} = 5.2 \cdot 10^{-6} \frac{mm^2}{sec}$ and an extremely suppressed $\pi_{PVclustering}^{low} = 3.4 \cdot 10^{-5}$. The high-proliferating curve is shifted by $0.01 \cdot 10^{-4} \frac{mm^2}{sec}$ and σ is increased by approximately 10 %.

The accuracy of the GTV has not changed. This is proved by an equal negative Log-likelihood of -9.28.

Third sample patient The quantitative evaluation of [Figure 5.8](#) supports before made qualitative hypotheses. μ is reduced by $0.3 \cdot 10^{-4} \frac{mm^2}{sec}$ and $\sigma_{PVclustering}^{high} = 1.2 \cdot 10^{-4}$ did not change at all and still exceeds the conservative ROI. The low-proliferating curve is strongly reduced and shifted to the right. The values quantitatively support this: μ increased by $0.4 \cdot 10^{-4} \frac{mm^2}{sec}$ and σ is reduced by approximately 60%.

The Log-likelihood by the partial volume approach is the same compared to the pure Gaussian approach and denoted as -9.68.

Statistical analysis of clustering results

In [Figure 5.9](#) dotplots of the clustering test illustrated in [Figure 4.36](#) using Gaussian clustering ([Equation 4.23](#)) and partial volume clustering ([Equation 4.37](#)) are shown (StataCorp. (2009). Stata: Release 11. Statistical Software. College Station, TX: StataCorp LP.). The conservative ROIs of the physician have been used as a security margin to cut off totally implausible values. Specifically, the mean value of the minimum values $-\sigma$ and the maximum values $+\sigma$ have been used to define the criterion for the runaway values.

Gauss clustering

In [Figure 5.9\(a\)](#), the pure Gaussian clustering test applied onto the high-proliferating ROI is shown. We can see a strong spatially dot plot clustering of the clustering results per patient. 2 patients could be partly included. This justifies an objectivity of the clustering approach. The intraclass coefficient ([Section 3.2.4](#)) of further fortifies the reproducibility.

In [Figure 5.9\(b\)](#), the low-proliferating Gaussian clustering test is depicted. There is no patient who completely exceeds the security margin and 2 fractional outliers can be found. The dot plot clustering can be seen, as well. This justifies an objectivity assumption which is further supported by the ICC of 0.996.

Partial volume clustering

In [Figure 5.9\(c\)](#), the partial volume clustering test applied onto the high-proliferating ROI is illustrated. A fractional spatial clustering of the dotplots can be seen. However, there were 4 complete outliers and 4 fractional outliers. The ICC is denoted as 0.621 and we cannot speak of an objective clustering any more.

[Figure 5.9\(d\)](#) illustrates the partial volume clustering test applied onto the low-proliferating ROI. No dot plot clustering can be seen any more. We had 6 complete outliers and 4 fractional outliers. The ICC is denoted as 0.686 and the objectivity assumption of the clustering has to be rejected, completely.

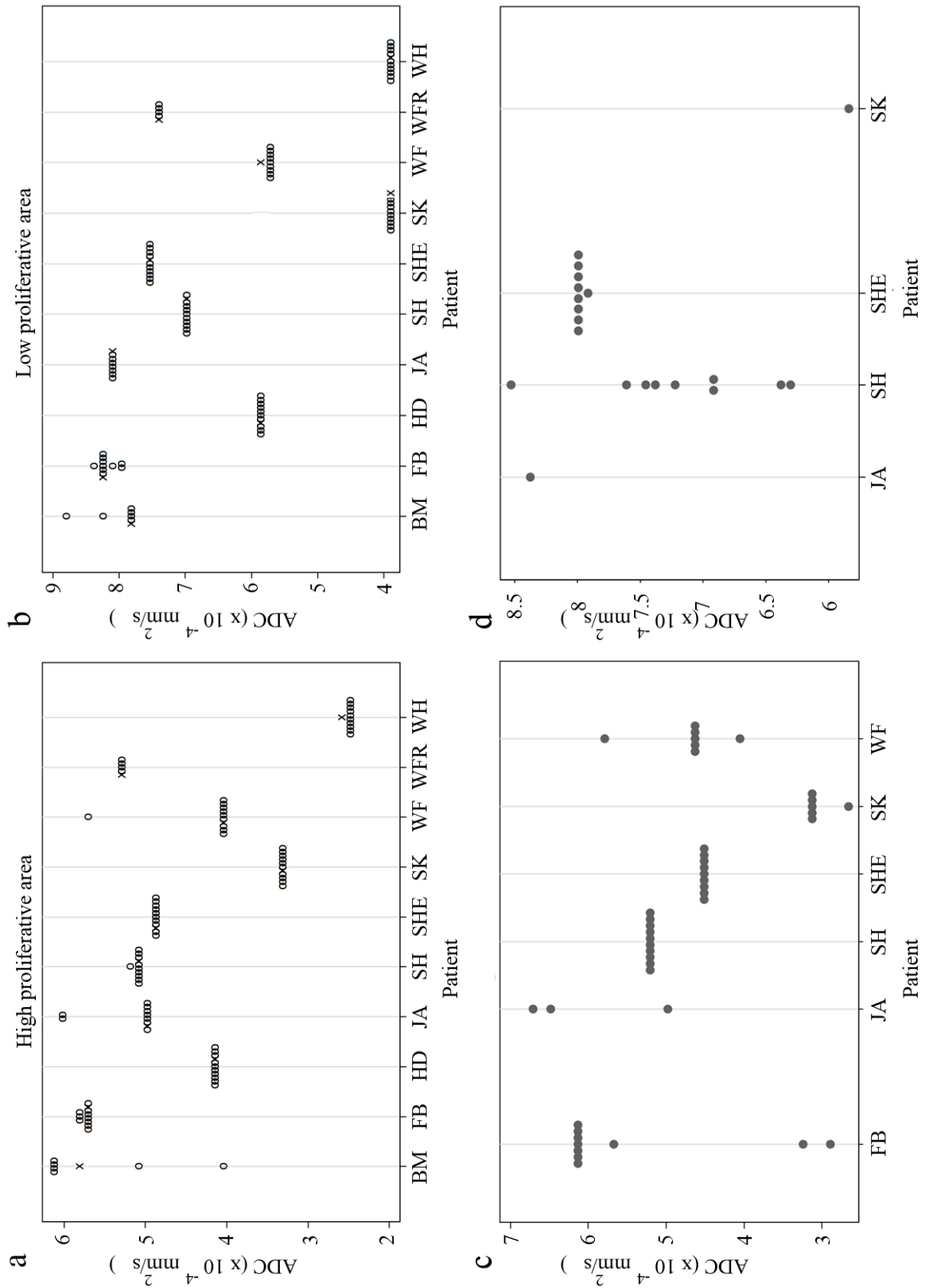


Fig. 5.9: Dotplots of the clustering results using conservative ROIs as a security margin. (a) The seedpoint test has been applied onto the high-proliferating region (Equation 4.23). No complete outlier. Fractional outliers: **BM** 4/10, **JA** 1/10. The ICC is denoted as 0.92. The results of the automatic clustering approach are denoted as grey crosses. (b) The seedpoint test has been applied onto the low-proliferating region. No complete outlier. Fractional outliers: **BM** 4/10, **WF** 1/10. The ICC is denoted as 0.996 (taken from Simon et al. (2011)). (c) The seedpoint test has been applied onto the high-proliferating region using the partial volume clustering (Equation 4.37). 4 complete outliers can be denoted: **BM**, **HD**, **WFR**, **WH**. Fractional outliers: **JA** 7/10, **SHE** 1/10, **SK** 4/10, **WF** 3/10. The ICC is denoted as 0.621. (d) Partial volume clustering test applied onto the low-proliferating tumour part. 6 complete outliers can be seen: **BM**, **FB**, **HD**, **WFR**, **WF**, **WH**. Fractional outliers: **JA** 9/10, **SH** 1/10, **SHE** 1/10, **SK** 9/10. The ICC is denoted as 0.686.

Result of automatic initialization approach

Since the clustering applied with a pure Gaussian mixture model (Equation 4.23) leads to an objective clustering, regarding the dotplots in Figure 5.9 and the ICCs, an automatic initialization is justified concerning the usage of this model. We tried the automatic initialization given in Equation 4.19 leading to results which can be compared to the spatial clustering of the dotplots in Figure 5.9(a) and Figure 5.9(b).

Altogether, the automatic clustering was successful in 10 of 10 cases of the pure Gaussian mixture model and fits perfectly to the spatial clustering of the dot-plots which justifies an objectivity assumption of the Gaussian clustering

5.1.4 Including functional imaging such as perfusion as additional information

The qualitative and quantitative evaluation while adding a functional imaging technique such as perfusion is entailed in this section. Firstly, the 'Qualitative evaluation' and secondly the 'Quantitative evaluation'.

Qualitative evaluation

In Figure 5.10, the qualitative evaluation is shown. In (a), the delineated glioblastoma encompassing the enhancing lesion including a 1 cm margin is shown. (b) depicts the set including the $maxCBV$ values in black and $minADC$ values in white. The intersection of both highest malignant areas is highlighted in grey. Qualitatively, it can be denoted that $maxCBV$ values were located mostly within the enhancing region. The $minADC$ was located in the surrounding area. This was the case in 14 of 20 patients. In six patients, these typical localizations could not be identified (Radbruch et al., 2011).

Quantitative evaluation

Quantitatively, it can be stated that the intersection showed an average overlap of $34.7 \pm 10.9\%$ (Radbruch et al., 2011).

5.2 The IVIM model and reproducible derived parameters

This section covers the results of the application of the IVIM model and the determination of reproducible parameters. Firstly, the evaluation of the intra-individual reproducibility is depicted in Section 5.2.1.

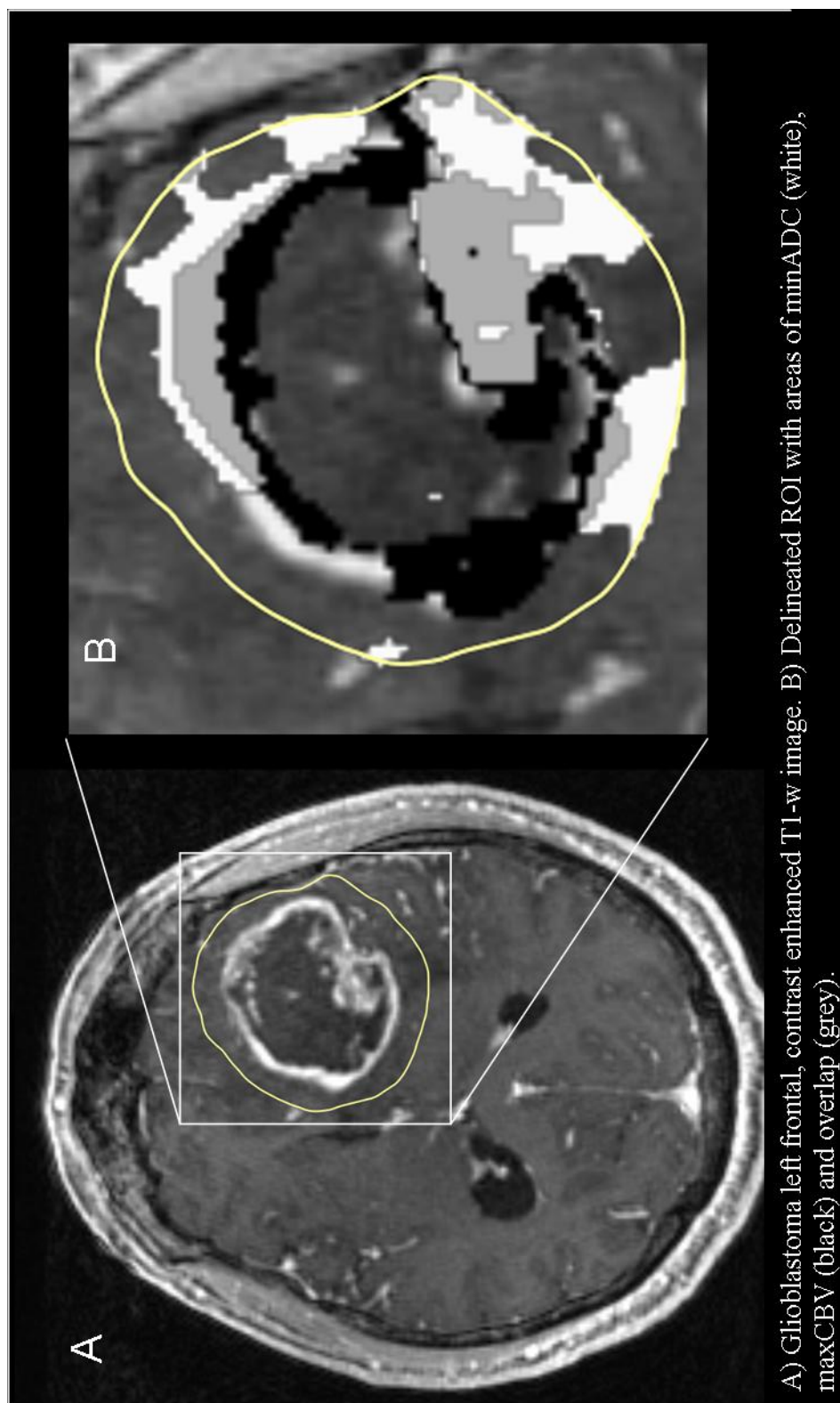


Fig. 5.10: Qualitative evaluation of the intersection concerning the rCBV study (taken from Radbruch et al. (2011))

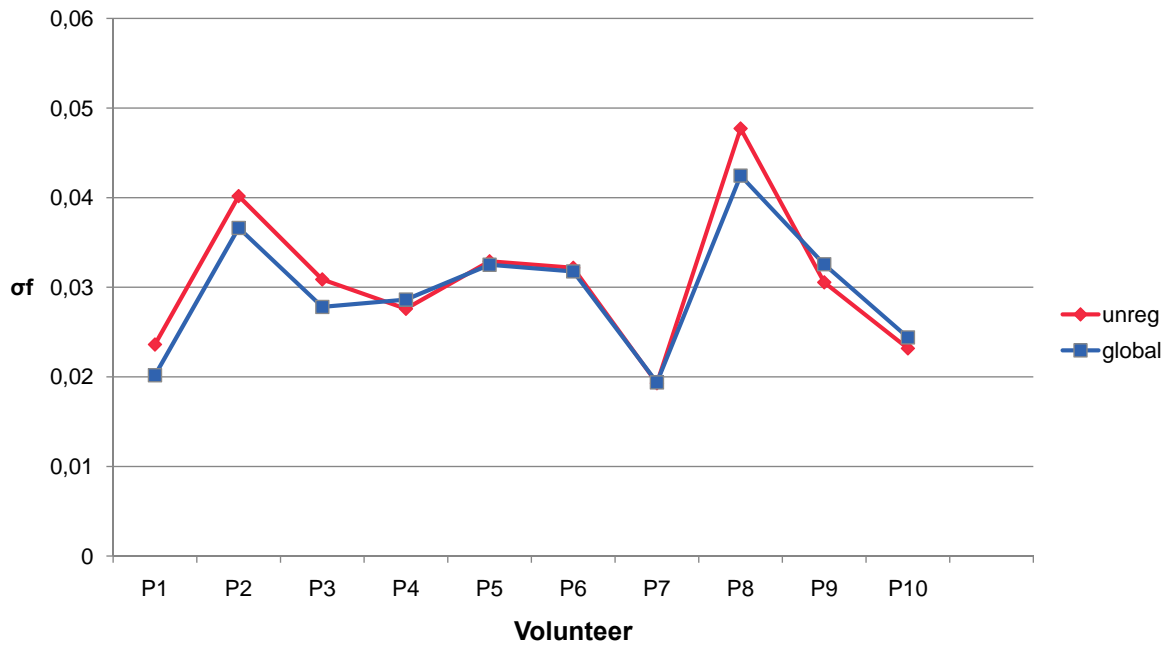


Fig. 5.11: The intra-individual reproducibility of f

The second part consists of the evaluation of the plausibility with help of an overlap probability (Section 5.2.2).

The third part elucidates the application of the IVIM approach onto more organs (Section 5.2.3) and this section finishes with the results of experimental derived values of the IVIM model (Section 5.2.4).

5.2.1 Evaluation of the intra-individual reproducibility

The intra-individual reproducibility of the derived parameters has been tested by evaluation of the three consecutive measurements comparing the parameters f , D and ADC . For calculating the ADC , we used the unrestricted model following Equation 4.49 due to an observed bi-exponential behavior of the signal decay in healthy pancreas. As described in Figure 4.16, we tested three approaches: the *unregistered approach* (1.), the *global registration approach* (2.) and the *local registration approach* (3.).

The results showed an improvement of the reproducibility in terms of a decrease in the standard deviation σ in all three parameters. Remarkably, σ_f showed a drop of over 3 % (Figure 5.11). Thus, we can state that rigid registration improves the reproducibility of f (Graf et al., 2010).

Applying a Wilcoxon signed-rank test (Elpelt and Hartung, 1992), all three parameters reach significance concerning σ of the three consecutive measure-

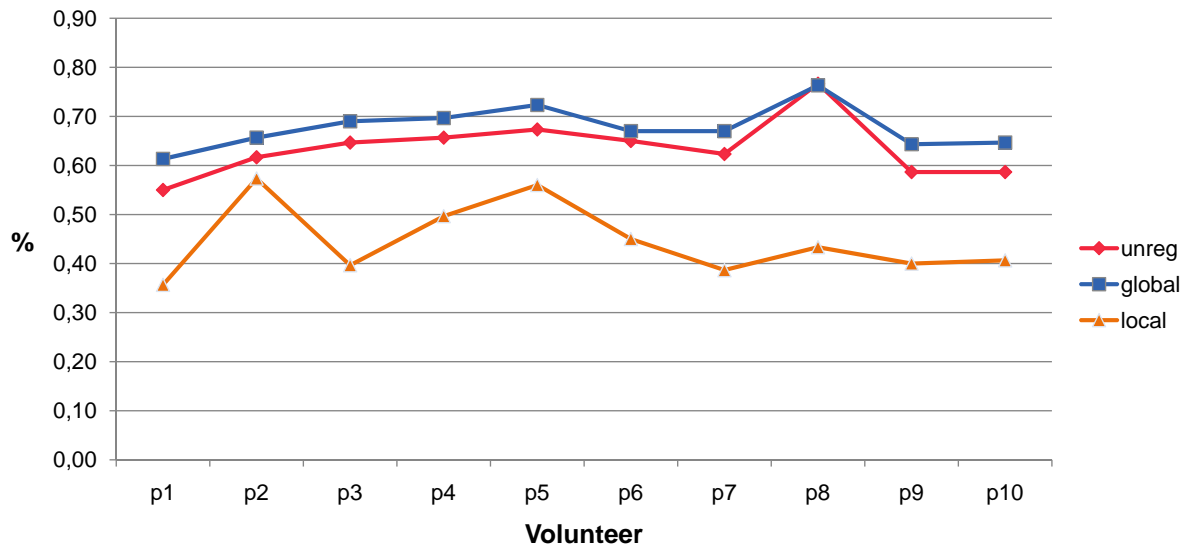


Fig. 5.12: 3D overlap probability per subject

ments. 72 2D samples out of the 140 of the 3D segmentation have been chosen for the significance proof. Thus, every derived observed parameter is more robust considering both registration approaches.

5.2.2 Evaluation of the plausibility

Figure 5.12 (taken from Graf et al. (2010)) shows the overlap probability using Equation 3.62 before and after applying the two mentioned registration algorithms. Averagely, the overlapping probability could be increased by more than 4 %, applying the global registration approach (Table 5.1) (taken from Graf et al. (2010)).

Unexpectedly, the local registration approach decreased the overlap probability of about 19 %.

Using a Wilcoxon rank sum test, we could prove the significance of the overlap increase.

5.2.3 Application of the IVIM approach onto several organs

This section covers the application of the IVIM approach onto several organs and is subdivided into a section which is describing the results of an additional mono-exponential fitting routine ('Adding an additional mono-exponential fitting routine and comparison to the IVIM fit').

Sample	Unregistered	Globally registered	Locally registered
1. subject	0.55	0.61	0.36
2. subject	0.62	0.66	0.57
3. subject	0.65	0.69	0.40
4. subject	0.66	0.70	0.50
5. subject	0.67	0.72	0.56
6. subject	0.65	0.67	0.45
7. subject	0.62	0.67	0.39
8. subject	0.77	0.76	0.43
9. subject	0.59	0.64	0.40
10. subject	0.59	0.65	0.41

Table 5.1: *Overlap probability of applied registration approaches*

Adding an additional mono-exponential fitting routine and comparison to the IVIM fit

This section shows results of the mono-exponential fitting routines described in [Equation 4.49](#) and [Equation 4.50](#) compared to the used Levenberg Marquardt fit of the IVIM equation ([Equation 4.52](#)).

Normalized signal decay in a pancreatic tumour

In this section the normalized signal decay in a pancreatic tumour is being evaluated by firstly 'Comparing signal decay against regression model' and secondly by 'Comparing signal decay against Levenberg Marquardt fit'.

Comparing signal decay against regression model In [Figure 5.13](#), the normalized signal decay in a pancreatic tumour is tested against both used regression models. It can be clearly seen that the non fixed model ([Equation 4.49](#)) outperforms in terms of accuracy, regarding the residual variance: $C_R = 0.00098 < 0.0034$. Nonetheless, there is no standard deviation at (0,0) because of the normalization procedure.

Comparing signal decay against Levenberg Marquardt fit The signal decay against the Levenberg Marquardt fit in a pancreatic tumour is shown in [Figure 5.14](#). It can be clearly seen that the Levenberg Marquardt algorithm starts at (0,0) and fits perfectly well to the algorithm approach of the restricted regression model.

Normalized signal decay in healthy pancreas

Comparing signal decay against regression model The normalized signal decay in healthy pancreas is compared against both regression models. In the healthy

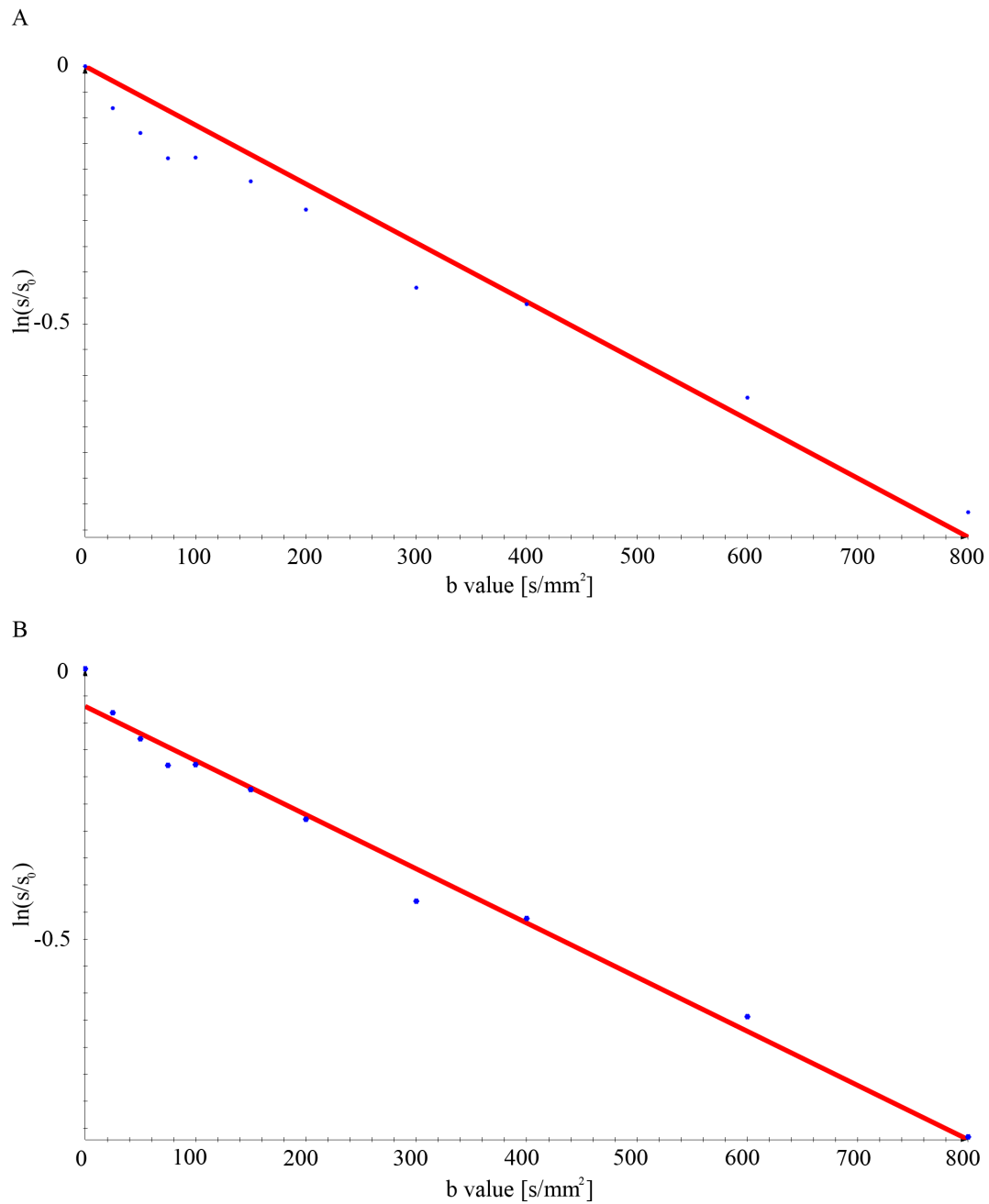


Fig. 5.13: Normalized signal decay in a pancreatic tumour: (A) Showing the normalized signal decay (blue dots) and the restricted regression using model (Equation 4.50) ($ADC=0.0012 > D=0.00095 \frac{mm^2}{sec}$, $C_R = 0.0034$) (B) Here, the non restricted model is shown (Equation 4.49) ($ADC=0.0011 > D=0.00095 \frac{mm^2}{sec}$, $C_R = 0.00098$)

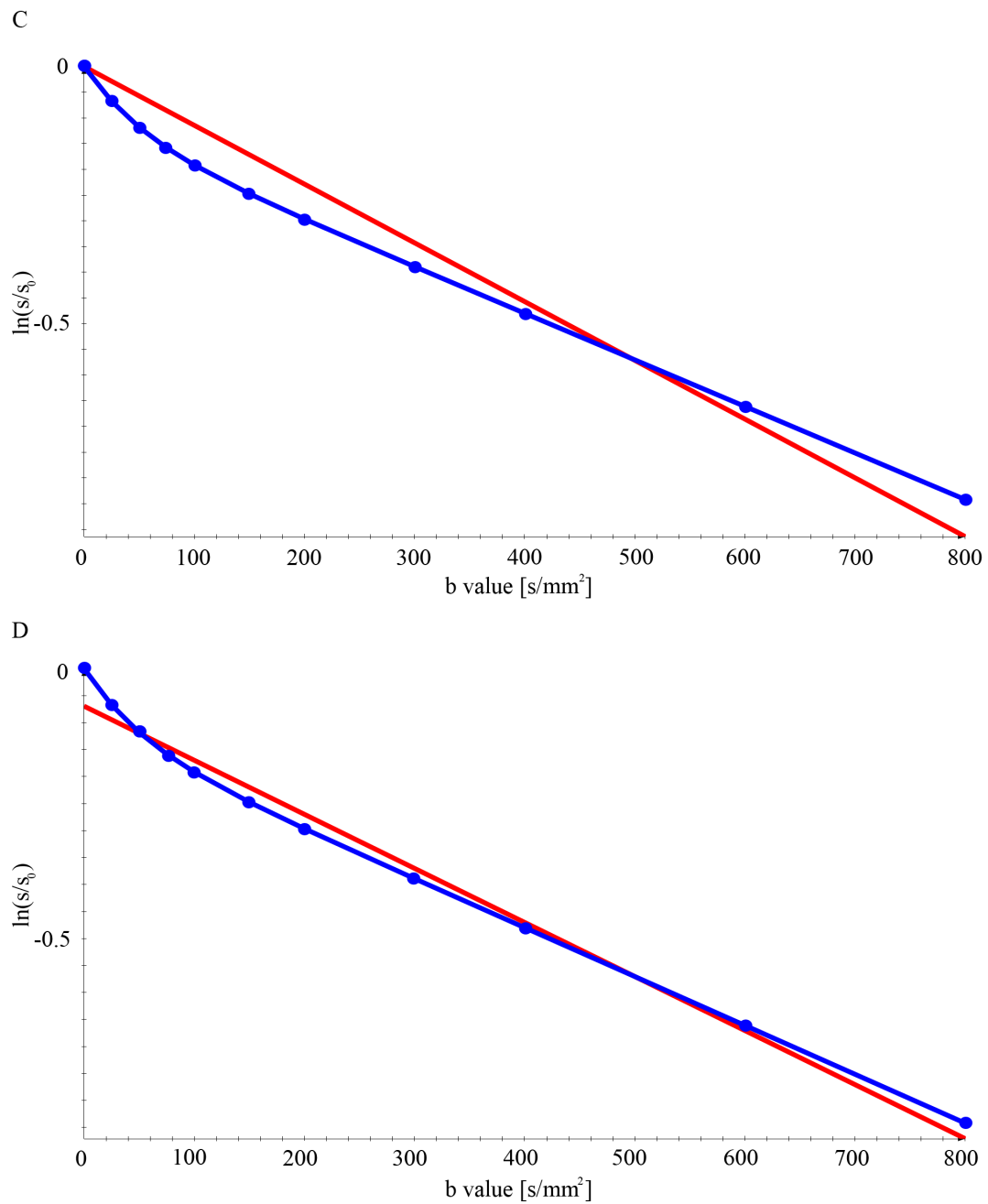


Fig. 5.14: Normalized signal decay in a pancreatic tumour: (C) The Levenberg Marquardt fit and the restricted model (Equation 4.50) (D) The Levenberg Marquardt fit and the non restricted model (Equation 4.49)

case, the difference is much stronger due to the prominent perfusion drop, happening at low \mathbf{b} values. Therefore, the residual variance difference is higher and expressed in $C_R = 0.015$ in the non fixed case compared to $C_R = 0.20$ in the fixed case (Figure 5.15, Figure 5.16).

Interestingly, the ADC value seems to be lower than the derived D . This is impossible from a physical point of view and happens due to the application of different model assumptions for the estimation of the ADC and D .

5.2.4 The IVIM experimental values for the differentiation between pancreatitis and pancreatic carcinoma

In this section the 'Qualitative evaluation' and 'Quantitative evaluation' of the two experimental derived parameters R^2 (Equation 4.16) and integral \mathcal{I} (Equation 4.49) is depicted.

Qualitative evaluation

The qualitative evaluation of the experimental values is depicted in this section. Firstly, 'The R^2 map and secondly, 'The integral map'.

The R^2 map

As predicted, the R^2 value is higher in pancreatic cancer than in pancreatitis. The pancreatic lesion can be delineated by a bright region (Figure 5.17a).

The integral map

The integral map for pancreatic carcinoma is shown in Figure 5.17b. In contradiction to the R^2 map, the carcinoma is shown as a dark area.

Quantitative evaluation

The R^2 map

Quantitatively, the R^2 parameter for pancreatic cancer is denoted as $\mu = 0.86 \pm 0.096$ compared to $\mu = 0.79 \pm 0.098$ but without significance applying a Wilcoxon rank sum test. The receiver operator characteristic curve analysis, depicted in Figure 5.18a, shows a sensitivity of 80 % and a specificity of 100 %.

The integral map

The integral parameter for pancreatic cancer is denoted by a value of $\mu = 0.32 \pm 0.10$ compared to $\mu = 0.36 \pm 0.06$. The Wilcoxon rank sum test did not show any significance. The receiver operator characteristic curve analysis (Figure 5.18b) shows a sensitivity of 60 % and a specificity of 100 %.

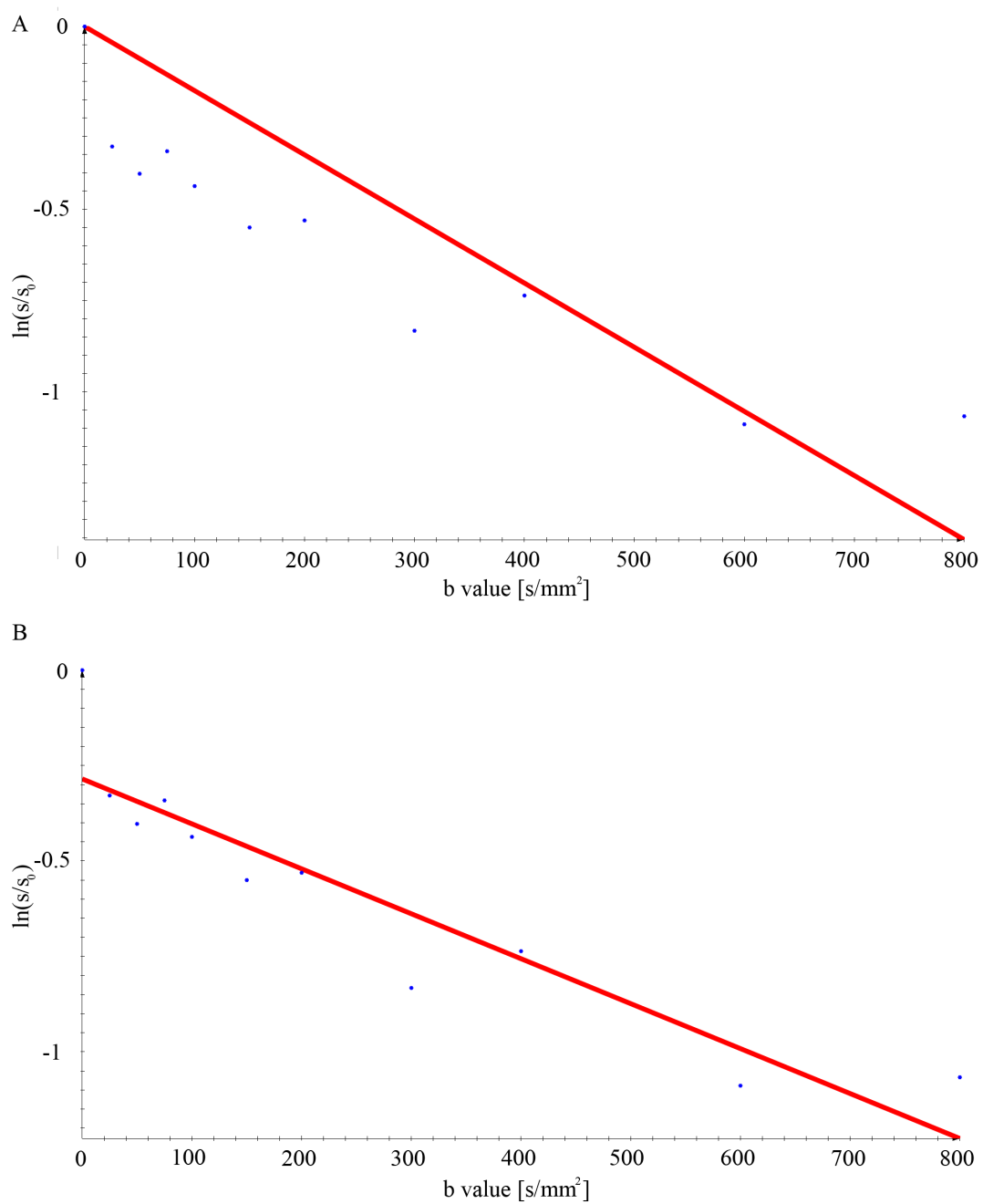


Fig. 5.15: Normalized signal decay in healthy pancreas: (A) Showing the normalized signal decay (blue dots) and the restricted regression using model (Equation 4.50) ($ADC=0.0019 > D=0.0012 \frac{mm^2}{sec}$, $C_R = 0.20$) (B) Here, the non restricted model is shown (Equation 4.49) ($ADC=0.0011 < D=0.0012 \frac{mm^2}{sec}$!, $C_R = 0.015$)

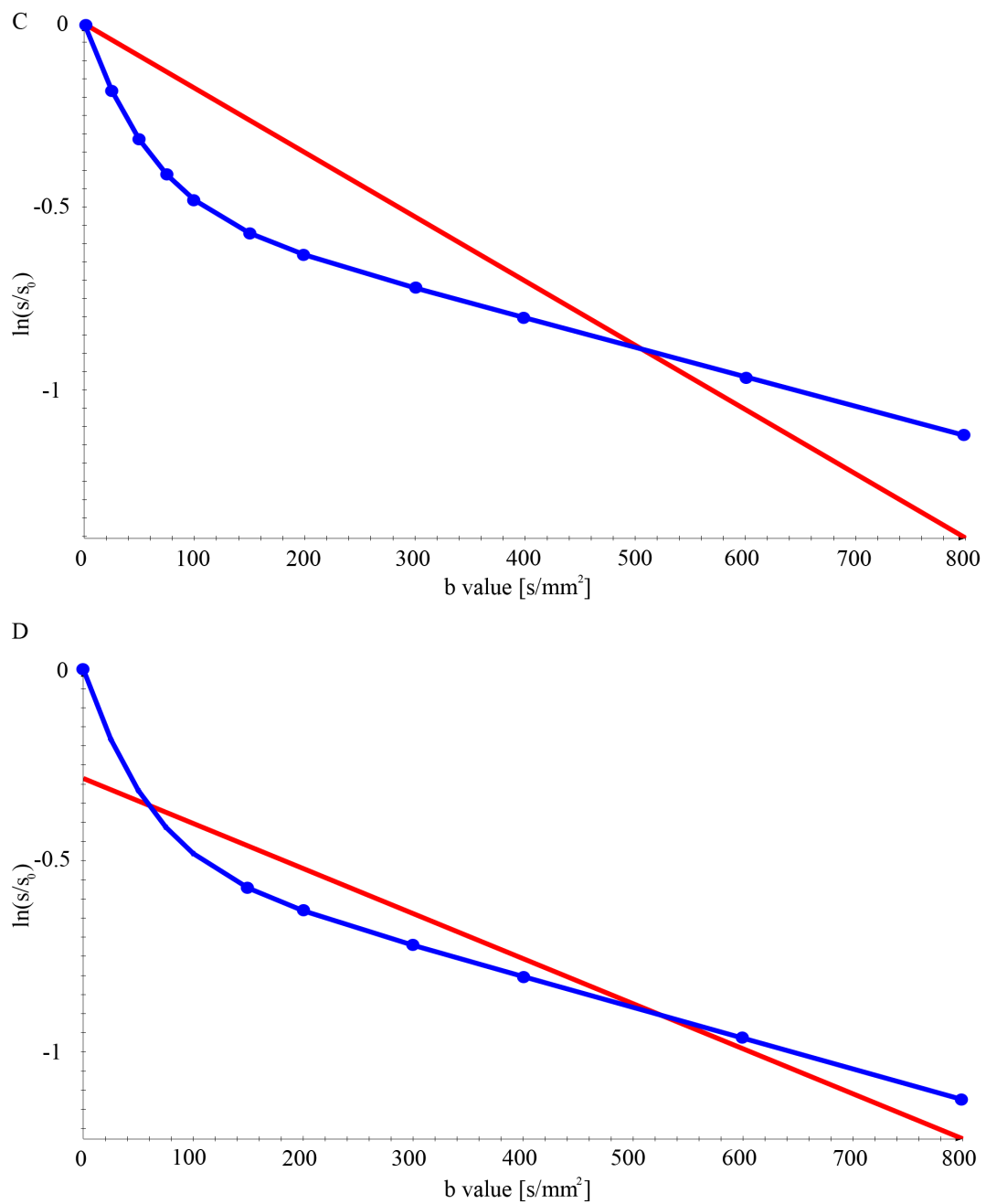


Fig. 5.16: Normalized signal decay in healthy pancreas: (A) The Levenberg Marquardt fit and the restricted model (Equation 4.50) (B) The Levenberg Marquardt fit and the non restricted model (Equation 4.49)

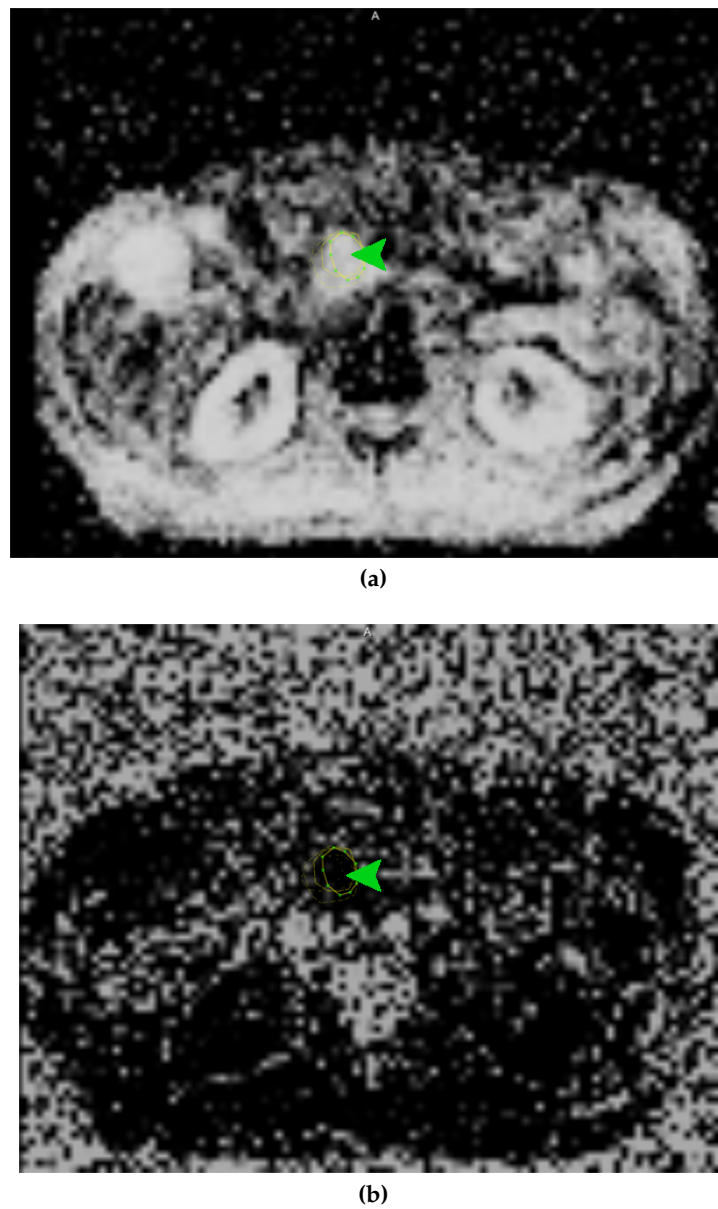
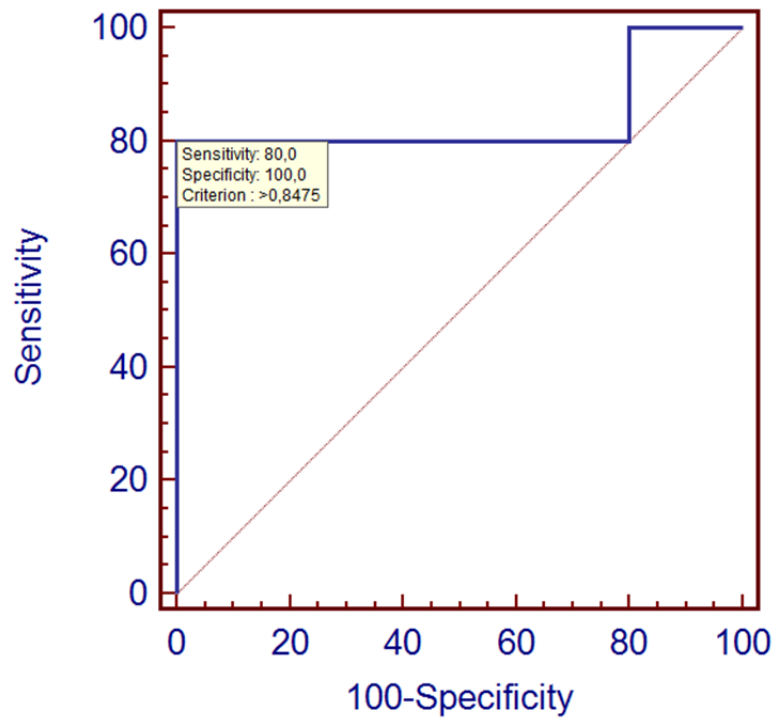
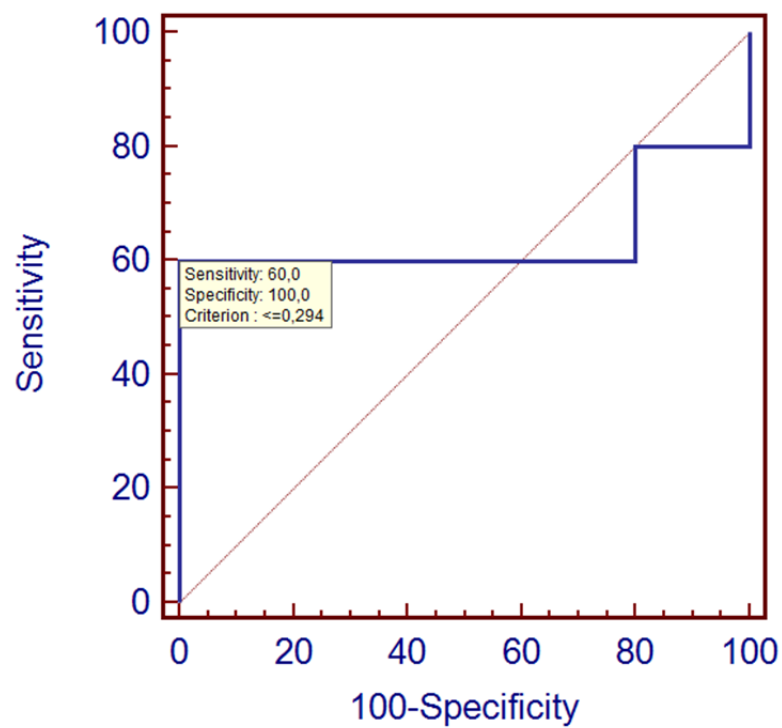


Fig. 5.17: (a) Pancreatic lesion (highlighted by the green arrow) in the R^2 map and (b) is depicting the integral map



(a)



(b)

Fig. 5.18: (a) Receiver operator characteristic curve analysis concerning the R^2 parameter and (b) is depicting the integral map

Discussion

In this chapter, the discussion concerning the separation and quantification of high- and low-proliferative areas ([Section 6.1](#)) and the reproducible evaluation of derived parameters of the *IVIM* model ([Section 6.2](#)) in diffusion weighted images, is depicted.

6.1 Separation and quantification of high- and low-proliferative areas in glioblastomas

This section fills in on the background of the separation and quantification of high- and low-proliferative areas in gliomas and discusses the results.

Firstly, the main activity is restated and the results with its limitations are described ([Section 6.1.1](#)).

Next, improvements of the used technique are succinctly explained ([Section 6.1.2](#)). Here, the application of additional contextual constraints are taken into account.

[Section 6.1.3](#) elucidates future research concerning this topic and gives some practical applications. E.g. an application in the field of radiotherapy is explained.

[Section 6.1.4](#) sums up the whole study and gives a slight and succinct conclusion of the achievement of a reproducible separation and quantification of high- and low-proliferative areas in glioblastomas.

6.1.1 Interpretation of the results and limitations

This section entails a restatement of the research results and interpretes them in a wider context ('Restatement of main activity and interpretation'). Secondly, the limitations of the study are described in 'Limitations'.

Restatement of main activity and interpretation

This section is subdivided into the clustering procedure only taking the *ADC* into account ('Clustering on *ADC* only') and adding a functional imaging technique such as perfusion ('Adding a multimodal technique such as perfusion').

Clustering on ADC only In this work, we show that low- and high-proliferating parts in high grade gliomas in diffusion weighted images can be successfully objectively delineated and probabilistically quantified by an Expectation Maximization algorithm and a superposition of two Gaussian distributions which are separable by their means. We validated this approach empirically on a sample of 10 patients. We propose an automatic and rapid approach which considers the heterogeneous nature of high grade gliomas.

The application of a Gaussian mixture model is validated firstly by a χ^2 test of the averaged high-proliferating and low-proliferating ROIs, yielding Gaussian distributions in the different areas (Figure 5.1).

Secondly, a theoretical Gaussian mixture model with empirically determined partial components compared qualitatively with the averaged *GTV* underlines the application of this mixture model. Quantitatively, we proved that the derived mean values of this theoretical model are plausible.

Through the application of a statistical algorithm with a Gaussian mixture model, we are able to probabilistically quantify areas of low- and high-proliferation in high grade gliomas. This unsupervised algorithm is plausible (justified by the qualitative evaluation (Section 5.1.2), provides a high reproducibility and objectivity, proven through the quantitative analysis (Section 5.1.3), a minimal human interaction, provided by an automatic initialization (Equation 4.18, Equation 4.19, Equation 4.20) and rapidness. Thus, it is well suited for the specific problem task to segment areas with gliding borders between high- and low-proliferating areas, normal tissue, necrotic areas and cerebrospinal fluid within heterogeneous high grade gliomas.

The posterior probability, which can be seen as a quality measurement of the complete approach, ensures a probabilistic quantification which allows for a reproducible quantification in the separated areas. The objectivity could be further validated by an application of an objectivity test with various initialization seeds within the low and high grade areas (see Figure 4.36). Furthermore, the reproducibility has been validated by the application of the spatial clustering of the dotplots (see Figure 4.36).

By application of a binary FLAIR mask, cerebrospinal fluid could be excluded and thus is not impeding the delineation and quantification procedure (Figure 5.3 and Figure 5.6). In this step, registration plays an important role, since the spatially matching of the morphologic FLAIR image and the functional diffusion weighted image is of great importance.

Besides of low- and high-proliferating parts, the heterogeneous tumour mass also includes necrotic areas. These necrotic areas could be suppressed by application of a histogram cut-off. However, the necrosis threshold is not completely satisfactory since it cannot suppress necrosis totally without additionally cutting off apparent low-proliferating tumour tissue (see [Figure 5.4](#) and [Figure 5.7](#)).

By adding an equally folded distributed partial volume class ([Section 3.1.6](#)) to the superposition of Gaussians, we could improve the delineation between high-proliferating regions and normal tissue. Although a part of the erroneous classified high-proliferating tissue can be classified as a partial volume effect, some of the thus found partial volume regions may be falsely assigned (see [Figure 5.7](#) and [Figure 5.8](#)). An explanation for the falsely assignment in [Figure 5.7](#) could be that the statistical amount of information is too low to find the low-proliferating class.

As recent studies show, manual ROI placement is impeded by the heterogeneous nature of high grade gliomas and additionally by partial volume effects e.g. (Higano et al., 2006, Sadeghi et al., 2004). Other methods similar to the Expectation Maximization statistical segmentation approach, like Support Vector Machines (SVMs) (Hongmin et al., 2007, Lee et al., 2005, Zhang et al., 2005), can also be used in an unsupervised fashion (Zhang et al., 2005). SVMs belong to so called discriminative decision task solutions, with a binary decision function, in contrast to our generative solution. In the case of SVMs, normally no posterior probability is being produced. This posterior probability can be seen as the quality measurement of the whole approach and thus, the lack of this posterior probability in SVMs obscures the qualitative evaluation of a given clustering result (Bishop, 2006). Discriminative algorithms excluding the SVMs, generate the posterior probability directly. Generative algorithms, like the presented Expectation Maximization algorithm with Gaussian mixture model, generate the joint probability $p(x) \cdot p(x|k)$ and the posterior probability is determined by normalization through the marginal probability $p(x)$. In our case, the crucial key issues of our specific problem task can be denoted as

1. finding gliding borders
2. performing an objective probabilistic quantification, while considering partial volume effects
3. human interaction

Concerning (1), usually, SVMs can only be used to separate sharp borders, also named linearly separable data, by finding a maximum margin between two classes. But by application of the called 'kernel trick' that data can be projected to a multidimensional space, called feature space (Bishop, 2006) and thus, also gliding borders can be found using SVMs.

Due to the discriminative fashion with a binary separation function, an objective

probabilistic quantification cannot be performed by a SVM alone. This can be seen as the main disadvantage of using SVMs as mentioned above. However, the probability can be approximated by fitting a sigmoid function (Platt, 1999).

With the used generative Expectation Maximization clustering applied on the probability distribution, we are able to perform an objective probabilistic quantification. Using this approach, new data points with low probability can be detected easily. This is known as outlier or novelty detection (Bishop, 2006). It is of special value in glioblastomas where gliding borders consisting of voxels with an extremely low probability are present. In the case of our additionally folded equally distributed probability class, we are also modelling the marginal probability in a special way and add a non Gaussian distribution to the superposition of Gaussians (Figure 5.6, Figure 5.7 and Figure 5.8). Concerning three, a one class SVM is also unsupervised, however if more than one class is expected, a supervised SVM approach is needed. For these supervised SVMs, time-consuming human interactions are necessary to label representative data samples for high and low-proliferative areas. Thus, given that at least three classes are present (high- and low-proliferative and partial volume), the EM approach is advantageous in terms of reduction of human interaction.

A prominent example for discriminative statistical algorithms without binary decision function, are perceptrons. In this case, the artificial neuronal networks can find gliding borders (1) due to solving the linear separation problem by application of multiple layers. As in the case of SVMs, they are also not applied on the histogram directly. Instead, the training data is based on derived bitmap features and the position information of the voxels (Dickson et al., 1997). A probabilistic quantification can be performed by using the posterior probability directly. The posterior probability is being determined by an application of multiple logistic regression on non linear data (Bishop, 2006).

Contrary to single class SVMs and our Expectation Maximization approach, multilayer perceptrons cannot be used in an unsupervised fashion. Instead, they perform a so called reinforcement learning to generate the appropriate output. Thus, concerning (3), they are disadvantageous.

Adding a multimodal technique such as perfusion By adding an additional multimodal imaging technique such as perfusion (Section 4.2.1), we could identify that the highest malignant areas, identified by ADC and $rCBV$, do not necessarily overlap spatially. An average overlap of only $34.7 \pm 10.9\%$ quantitatively supports this. The multispectral information provides additional information about the tumour biology. The location of min ADC in the surrounding tissue and max $rCBV$ values in the enhancing areas could be that low ADC values produce neoangiogenic factors which is leading to a 'trailing behind' of the

vascular-rich tumour border. This border is represented by high *CBV* values (Radbruch et al., 2011).

Limitations

The largest limitation of our algorithm is that the issue 'of overlapping intensities of normal tissue with high-proliferating areas' (Prastawa et al., 2003) (Section 3.3.1) is still not completely solved. Even if we assume an additional partial volume class, the overlapping still remains partially (Figure 5.7 and Figure 5.8).

A further limitation of the applied algorithm is that it only clusters globally on a GTV drawn on a 2 dimensional slice. An expand onto a 3 dimensional volume was successful. However, future research should extend this onto the whole brain, resulting in a 3d whole brain fully automated clustering algorithm which includes and defines contextual three dimensional constraints. This is further explained in Section 3.2.2.

The Gaussian mixture approximation is a result of the occurring Rician noise onto the pure MR signal (Section 5.8). Here, Rician assumptions onto the log signal, as well as direct Rician assumptions onto the derived values are valid (Fillard et al., 2007). However, more exact would be an application of a log Rician or at least a log Gaussian model in our case of a high *SNR* (Section 3.1.5) through averaging of 10 DTI datasets. This should be evaluated in further research.

6.1.2 Improvements of the used technique

Future research has to address the still occurring overlapping between necrosis versus low-proliferating and high-proliferating tissue and normal tissue. This may be addressed by algorithms that include prior knowledge and the addition of spatial and anatomical constraints (van Leemput, 2001) or in the tumour segmentation case (Lee et al., 2005), where a discriminative variant of the usually generative Markov Random Fields in combination with a *SVM* is used (Simon et al., 2011). The crucial problem pertaining to the overlapping issue is based on the independence assumption given in van Leemput (2001). It says that the tissue type of each voxel is independant from the tissue type of all of the other voxels which means that the *ADC* distribution of a voxel does not depend on the *ADC* probability distribution of any other voxel. Thus, there is no context in which the labels reside. This can be measured by the posterior probability to reflect the information of the Gaussian mixture model $\gamma_k(x) \equiv p(k|x)$. Hence, each voxel is classified independantly based only on the *ADC* probability density. If the *ADC* probability density between the different tissue types has an overlap, the intensity based classification will probably fail. By including contextual constraints, a Markov Random Field can provide a solution for

misclassified regions, particularly the misclassification of normal tissue as high-proliferating tissue.

The assumption of a generative Markov Random Field is roughly that each variable only directly depends on a few other neighbours (Perez et al., 1998) (Section 3.2.2). More specifically, we can say that a voxel which belongs to a specific area of proliferation, depends only on the proliferation rate in a special region, called a Markov blanket (Bishop, 2006). Thus, the prior probability π_k of a voxel belonging to the high- or low-proliferation area is not the same as in the intensity based independent case, it now depends on the classification of the surrounding voxels (van Leemput et al., 1999).

By application of the Markov Random Field and by changing the prior probability π_k in the way that configurations are preferred where neighbours for the same tumour-proliferating entity occur (van Leemput, 2001, van Leemput et al., 1999), the spatial context or the spatial clustering of the voxels is taken into account. Thus, the clustering is based on the intensity *and* the spatial context. In this way, outliers can be removed and the issue rose in Figure 5.3 and Figure 5.6 pertaining to the overlapping intensities of low-proliferating and high-proliferating tumour can be reduced.

Furthermore, by defining contextual constraints (van Leemput et al., 1999), the clustering can be additionally restricted and unlikely clustering results can be prevented such as:

- high tumour surrounded by low tumour or normal tissue
- normal tissue around high tumour
- high tumour around low tumour

A classification is needed that considers the single-site potentials $ssp(k|x) \equiv \gamma_k(x) \equiv p(k|x)$, reflecting the ADC probability distribution in terms of considering the Gaussian mixture model and additionally the pair potential, which is responsible for the spatial coupling, and can be denoted as $pp(k_i, k_j|X)$, where X represents all of the remaining variables in the image where we consider a 4 neighbourhood system (Li et al., 1995). A further approach would be to include a special labelling procedure, where the spatial couplings could be used to improve the clustering result in terms of accuracy (Lee et al., 2009a,b). More specifically, the cluster initialization procedure could be applied to perform such an initial labelling and thus results in a semi-supervised approach.

6.1.3 Future research and practical applications

The probabilistic ADC measurement in gliomas, as proposed here, can be used for the planning of resections and biopsies. Moreover, it can be applied in the context of modern radiotherapy techniques where intensity modulation is used

which can be used to adapt the local dose to the biological activity in heterogeneous tumour parts (Boyer et al., 2000, Ling et al., 2000).

The identified low-proliferating and high-proliferating parts might also be of use in a tumour growth model as described in Konukoglu et al. (2010) to more precisely estimate the proliferation rate in different tumour areas.

6.1.4 Conclusion

In conclusion, we presented a novel method for the objective delineation of high- and low-proliferating areas in high grade gliomas (Section 3.3.1, Section 3.2.1). We could show that this approach is rapid, reproducible and leads to an objective delineation with automatic initialization (Section 5.1.3), regarding heterogeneity, while accommodating for signal inhomogeneities and gliding borders of high grade gliomas. The partial volume recognizing method has been tested. However, the objectivity could not yet be proved (Section 5.1.3). The further evaluation pertaining to this subject has to be proven in future studies. Furthermore, the pure Gaussian automatic probabilistic quantification allows for an objective and reproducible extraction of the *ADC* values in the different clusters (Section 5.1.3).

The additional multimodal information in terms of perfusion, provides more information about tumour biology taking the vascular contribution into account (Radbruch et al., 2011). The highest malignant areas identified by *rCBV* and *ADC* do not necessarily overlap spatially. Thus, it can be denoted that areas of high-malignancy can be interpreted from a different point of view, regarding the used imaging technique and tumour specific property. To conclude, it can be said that the derived objective and reproducible *ADC* delivers just one important characteristic trait of the tumour.

These objective values, reflecting high-proliferating and low-proliferating regions in glioblastomas, have clinical relevance concerning therapy assessment and post-therapy follow up in terms of therapy modification.

6.2 The IVIM model and reproducible derived parameters in diffusion weighted images

This section discusses the main activity concerning the application of the *IVIM* model and the reproducible extraction of the derived parameters.

The interpretation of the results and its limitations are discussed consecutively which leads to a development of a non-invasive screening tool for the pancreas. (Section 6.2.1).

Furthermore, improvements of the technique are elucidated which expands the usage onto other organs (Section 6.2.2).

Section 6.2.3 sums up the whole study to conclude the approach towards a non-invasive screening tool while using diffusion weighted imaging.

6.2.1 Interpretation of the results and limitations

The interpretation of the results is divided into the determination of the derived IVIM parameters concerning the serial registration ('Determining reproducible derived parameters and serial registration'), the ducts and vessels segmentation ('The ducts and vessels segmentation'), the IVIM fit ('IVIM fit'), the additional experimental fitting routine ('Adding an additional mono-exponential fitting routine') and finishes with the determination of experimental derived parameters such as R^2 (Equation 4.16) and integral \mathcal{I} (Equation 4.17) ('The IVIM experimental values for the differentiation between pancreatitis and pancreatic carcinoma').

Determining reproducible derived parameters and serial registration

The section is subdivided into the 'Interpretation of the results' and 'Limitations'.

Interpretation of the results

In the IVIM study (Section 5.2), we prove that serial linear rigid registration of the \mathbf{b} values stack, leads to a significant increase in the IVIM derived parameters such as f (Figure 5.11), D and the ADC (Graf et al., 2010).

The second important result indicates that the plausibility, determined by an overlap probability, could also reach a significant improvement (Figure 5.11, and Table 5.12). Unexpectedly, the local registration approach could not succeed, since normalized mutual information is solely based on intensity values. A high similarity can occur in the metric, even if there is no anatomical overlap correlation.

Limitations

A limitation of the registration study is clearly that we did not include non rigid registration. That elastic organ motion has to be present, can be derived by the fact that the maximum overlap probability increased only from 72% to 77% (Figure 5.1) (Graf et al., 2010).

The ducts and vessels segmentation

As indicated in Re et al. (2011), it could be identified that the ducts and vessels segmentation improves the delineation of pancreatic lesions, regarding the elimination of adjacent ducts and vessels.

Moreover, Re et al. (2011) states that f is significantly higher in post segmentation (Switching from 0.16 to 0.17). This can be explained by the zero valued eliminated ducts.

Concerning the vessels, Re et al. (2011) could find out that the trend in Lemke et al. (2009), saying that D should be higher in tumour than in healthy tissue (tumour: $1.25 \frac{\mu m^2}{ms}$ compared to healthy tissue: $1.13 \frac{\mu m^2}{ms}$), was absent after elimination of the vessels (tumour: $1.16 \frac{\mu m^2}{ms}$ compared to healthy tissue: $1.13 \frac{\mu m^2}{ms}$).

The IVIM fit

This section, concerning the IVIM fit, is subdivided into 'Interpretation of the results' and 'Limitations'.

Interpretation of the results

As described in [Section 4.1.2](#), we fixed D^* to $20 \frac{\mu m^2}{ms}$ due to low SNR ([Section 3.1.5](#)). This restriction is further analyzed by Lemke et al. (2011), where an optimal distribution of \mathbf{b} values is discussed. In this work, Monte Carlo simulations were used and the error of the fit was used as an optimization criterion. σ_D^* , depicting the relative error in the Monte Carlo simulation, showed the highest error.

This result could be confirmed by in vivo conditions, measured in three healthy subjects (Lemke et al., 2011).

In Klauss et al. (2011), a direct histopathological comparison between the true diffusion constant D in 24 pancreatic carcinoma patients considering fibrosis was found which further fortifies the plausibility of the true diffusion constant D .

Limitations

Since D^* has been fixed due to the mentioned instability of the parameter, this fixation is limiting the quality of the derived parameters and results in a shift of f rather than an alteration of the found contrasts (Re et al., 2011). However, the automatic tumour delineation leads to a good automatic segmentation of the tumour, confirmed by radiologists. Moreover, the D^* parameter of $20 \frac{\mu m^2}{ms}$ in the pancreas, is comparable and reproducible (Re et al., 2011). This value is

comparable to other organs obtained from literature: brain: $D^* = 10 \frac{\mu\text{m}^2}{\text{ms}}$, kidney: $D^* = 15 \frac{\mu\text{m}^2}{\text{ms}}$ and liver: $D^* = 60 \frac{\mu\text{m}^2}{\text{ms}}$ Lemke et al. (2011).

Another limitation concerning the IVIM fit is the applied SNR (Section 3.1.5). Lemke et al. (2011) investigates an optimal \mathbf{b} value distribution dependant on the applied SNR. Three classes have been created here: b_{low} , b_{medium} and b_{high} . Furthermore, the SNR could be so low that a plausible three parameter fit is not feasible (Lemke et al., 2011).

Adding an additional mono-exponential fitting routine

In Section 4.1.2, we explain the application of the IVIM approach onto several organs and use two mono-exponential fitting routines for the ADC (Equation 4.50, Equation 4.49). As indicated in Section 4.1.2, the normalization procedure (Equation 4.48) of the IVIM equation leads to a strong (0,0) value, so that this value has to be fixed, since this value has no standard deviation. Moreover, the Levenberg Marquardt approach (Equation 4.54) used to determine the IVIM derived parameters, fixes the (0,0) value in the same way and is a second argument to use the the fixed model, defined in Equation 4.50. In the experiment in Figure 5.14 and Figure 5.15, we can clearly see that the fixed model, to determine the ADC, fits better to the IVIM parameters D and f .

However, in cases of a strong bi-exponential signal decay (e.g. in healthy pancreas: (Figure 5.15 and Figure 5.16)), the signal approximation seems to be better in the non-restricted model (Equation 4.49), regarding the residual variance C_r . In this case, D can be higher than ADC, which is impossible from a physical point of view.

Even in the tumour case (Figure 5.13, Figure 5.14), the non-fixed model is more exact.

The IVIM experimental values for the differentiation between pancreatitis and pancreatic carcinoma

Interpretation of the results

In Section 5.2.4, the experimental value R^2 (Equation 4.16) and \mathcal{I} (Equation 4.17) are evaluated and R^2 turned out to be the superior experimental parameter for the differentiation of mass forming pancreatitis and pancreatic carcinoma and is showing the same sensitivity than the perfusion fraction f reported in Klaus et al. (2011).

Limitations

Due to the small sample size, an evaluation of the significance of the differentiation and the expressiveness of the diagnostic performance is limited.

6.2.2 Improvements of results and future research

The improvements of the results and future research is divided into the following topics:

1. 'Determining reproducible derived parameters and serial registration'
2. 'The ducts and vessels segmentation'
3. 'The IVIM fit'
4. 'The IVIM experimental values for the differentiation between pancreatitis and pancreatic carcinoma'
5. 'Therapy issues concerning different organs'

Determining reproducible derived parameters and serial registration

The still recognizable organ motion leads to a warrantable use of elastic registration approaches. Future research should consider these advanced techniques for a more stable measurement of the parameters (Graf et al., 2010).

The reduction of the standard deviation in the pancreatic diseases, has to be confirmed in future studies in the course of a clinical study to evaluate the benefit of registration onto homogeneous ROIs reflecting pancreatic tumours and pancreatitis, respectively.

Since we are using images with a resolution of $100 \times 78 \times 14$ and the normalized mutual information metric (Maes et al., 1997, Viola and Wells III, 1997) (Section 3.2.5) needs a minimum set of statistical information, we recommend an increase of the used entropy, in terms of increasing the applied resolution (Graf et al., 2010).

The ducts and vessels segmentation

The ducts and vessels segmentation can be also performed by using an Expectation Maximization approach with multivariate Gaussian mixture model (Bishop, 2006, Dempster et al., 1977, Hastie et al., 2009) similar to the used machine learning algorithm in Section 5.1 but with multivariate Gaussians, reflecting D and f , respectively (Equation 3.39). This could be an appropriate technique if the biparametric f, D characteristic yields a multivariate Gaussian mixture (Re et al., 2011).

Furthermore, this segmentation approach could be extended on further organs.

The IVIM fit

To extend the *IVIM* approach onto more organs, we should consider to adjust the D^* parameter to appropriately fix the pseudo-diffusion to the respective organ.

Moreover, the technique elucidated in Lemke et al. (2011) should be taken into account. The SNR [Section 3.1.5](#) should be measured and taken into account to derive optimum \mathbf{b} values. Most importantly, a cut-off value for a critical SNR is warranted.

The IVIM experimental values for the differentiation between pancreatitis and pancreatic carcinoma

Future research, according to the experimental values R^2 ([Equation 4.16](#)) and the integral parameter \mathcal{I} ([Equation 4.17](#)), has to consider more patients for the differentiation to strengthen the informative value of the receiver operator characteristic curve analysis and to reach a significant difference between pancreatic carcinoma and pancreatitis, respectively.

Therapy issues concerning different organs

There were several studies which evaluated the *IVIM* derived parameters under therapy ([Section 4.1.2](#)). Future research should take a histology comparison into account to better estimate the real correspondent of the values regarding healthy tissue and tumourous tissue.

6.2.3 Conclusion

To conclude, we presented an approach for a robust and reproducible parameter quantification of *IVIM* derived parameters through linear rigid image registration ([Section 5.2.1](#)). Furthermore, this estimation could be further improved by an automatic ducts and vessels segmentation to exclude erroneous ducts and vessels ([Section 4.1.2](#)).

The *IVIM* fit procedure could be adjusted so that several organs are supported by two normalization procedures and the different *ADC* calculation schemes foster two different aspects of approximating the bi-exponential signal decay. Moreover, the quality of the data can be checked by a visualization of the signal decay and fits.

However, elastic organ motion (Schnabel and Rueckert, 2009) is not considered and will be a task for future developments. Moreover, the constant pseudo diffusion constant D^* is deviating among other organs so that this parameter has to be changeable by an adjustable parametrization of the software. Furthermore, the SNR ([Section 3.1.5](#)) should be a marker to define the optimum \mathbf{b} value distribution and to define a minimum criterion for the feasibility of the *IVIM* derived parameters. Due to the automatic detection of the data and the \mathbf{b} value extraction, arbitrary \mathbf{b} value distributions are supported by the software.

This leads to a development of a non-invasive screening tool ([Section 3.3.2](#)) to robustly characterize pancreatic diseases and other organs in the future.

Summary

7.1 Quantitative parameters derived from diffusion weighted imaging

First, in the glioma case, reproducible *ADC* measurements could be achieved. The developed software prototype could prove that this algorithm establishes objective measurements without user dependency (Section 4.1.1). Regarding the pure Gaussian mixture model (Equation 4.23), the objectivity assumption holds but the ICCs of the partial volume including model (Equation 4.38) do not justify this assumption.

Future research should also take this partial volume model into account to end up into a reproducible and partial volume recognizing method.

However, it has to be recognized that a combination of different parameters is important while deriving intrinsic parameters of gliomas. As described in the results in Section 5.1.4, the vascular contribution (*rCBV*) does not necessarily overlap spatially with the cellularity contribution designated as *ADC*.

Hence, future research should extend the objective determination of parameters in gliomas in direction of a multimodal or multispectral interpretation of the data. This could be feasible regarding a multi modal software platform such as **RONDO** (Woetzel et al., 2010).

In the *IVIM* study, we could show that the application of linear image registration improves the reproducibility and the plausibility of all *IVIM* derived parameters (Section 5.2.1 and Section 5.2.2). In the process, it has to be said that the crucial bottom line concerning the quantitative parameters can be denoted as indicated in Section 6.2.1. *High reproducibility of the parameters does not necessarily mean that these derived values are plausible, since the used metric for the registration is solely based on intensity values and does not include any spatial properties pertaining to the anatomical overlap.*

Concerning to the tumour ROI, the implemented ducts and vessels segmentation (Section 5.2.3) reduces the error-proneness of all parameters. As discussed

in Section 6.2.2, this technique could be further improved by machine learning algorithms.

However, as already described in Section 6.2.3, residual motion may be still present so that the reproducibility and plausibility could be still improved due to elastic deformations. Furthermore, D^* , concerning the used different organs and the \mathbf{b} value distribution pertaining to the SNR, could be adapted to further improve the derived values.

7.2 Reproducibility

The reproducibility of the *ADC* values in gliomas has been tested and validated while applying the pure Gaussian mixture model. The automatic seed point generation in combination with an ICC (Section 5.1.3) can be seen as a marker of reproducibility. The ICC in the high-proliferating and low-proliferating areas are approximately equal to recommendations by Tofts (2003) where an ICC of 0.9 is seen as a typical good value.

However, the ICC has a main drawback, concerning Tofts (2003): ‘The ICC is group dependant and can be completely different regarding other groups’. Furthermore, Tofts (2003) suggests to use the ‘within-subject variance’ in addition, calculated by $\frac{\sigma}{\mu}$ as a measurement of ‘within-subject reproducibility’ or the ‘confidence limits on a single measurement’.

A further drawback concerning the whole study is that the patient collective is quite small, so that the reproducibility message has to be seen with limitations.

So, future work could also incorporate the reproducibility regarding the value called *CV* and include more patients into the study.

The intra-individual reproducibility concerning the *IVIM* derived values has been evaluated by three consecutive measurements and could be significantly improved regarding their σ after a global linear registration (Section 5.2.1).

However, since the ROIs are user dependant and deviating like in the illustrated glioma cases (Section 3.2.1), the reproducibility could be improved while using automatic segmentation approaches to encompass the whole tumour ROI (Section 3.2.2).

A development of such a routine for automatically delineating the pancreatic tumour ROI could be investigated in further research.

7.3 Importance of this work for clinical applications

First and foremost, as indicated in Section 6.1.3, clinical applications of the reproducible measurements, are especially important for resections, biopsies

and radiation ([Section 3.1.7](#)), considering the highest proliferating areas. More specifically, IMRT can strongly improve of the herein represented separation or can be used to foster a derived tumour growth model.

As described in [Section 6.2.3](#), the reproducible measurements have to be further proved in a clinical setting, which means concerning the tumour or pancreatitis, to evaluate the direct clinical impact. In further studies, the impact of these improvements onto the diagnostic performance ([Section 3.2.4](#)) of the differentiation between the pancreatic diseases has to be derived.

All these developments lead to a final non-invasive clinical screening tool based on diffusion weighted imaging ([Section 3.3.2](#)).

List of Figures

3.1	An illustration of the spin	7
3.2	The affect of the bulk magnetization onto the proton.....	7
3.3	The spin echo train.....	11
3.4	An illustration of the EPI sequence	12
3.5	An illustration of the k space coverage of the EPI sequence	12
3.6	The Stejskal Tanner Sequence	16
3.7	Illustration of brain anisotropy of ischaemic stroke	18
3.8	Illustration of the intravoxel incoherent motion flow	23
3.9	Illustration of the independence property within a Markov Random Field	31
3.10	Illustration of a Markov blanket.....	32
3.11	An illustration of a ROC classification	37
3.12	Sample of a registration algorithm	40
3.13	The fixed and moving image.....	42
3.14	The mutual information	44
3.15	Illustration of a 3D brain	45
3.16	Illustration of a 3D abdomen.....	47
4.1	Activity diagram of the glioma study	53
4.2	Module description of the preprocessing modules	55
4.3	Module description of the initialization	56
4.4	Module description of the EM clustering	57
4.5	Module description of the histogram displaying and averaging... ..	58
4.6	UML description of DWIDetermineCOG and DWICreateCSOList	59
4.7	UML description of ProbabilisticADCQuantification.....	60
4.8	UML description of HistogramArithmeticConst and HistogramArithmetic	60
4.9	UML description of DWIGaussApproximation	61
4.10	UML description of the clustering prototype	62

4.11	Activity diagram of principal work flow concerning the <i>rCVB</i> study	64
4.12	Module description of the percentile thresholding	65
4.13	UML description of PythonPTileThresholding	66
4.14	An illustration of the percentile segmentation	68
4.15	An illustration of a sample quantification of the <i>rCBV</i> study	69
4.16	Activity diagram of the <i>IVIM</i> study	70
4.17	Module description of the registration modules	72
4.18	Module description of the registration modules part 2	72
4.19	Module based description of the quantification modules	73
4.20	UML diagram of the Python Sorter	74
4.21	UML discription of the registration modules	75
4.22	UML description of the quantification modules	76
4.23	Illustration of the bounding box registration	77
4.24	Module based description of additional quantification modules for <i>IVIM</i>	79
4.25	Module based description of the preprocessing modules	79
4.26	The ducts and vessels segmentation modules	80
4.27	The plotting module	81
4.28	<i>IVIM</i> quantification UML with additional normalizer	82
4.29	The plotting facility UML	83
4.30	The automatic preprocessing: Contouring	84
4.31	The automatic preprocessing: Ducts and vessels segmentation	85
4.32	The automatic preprocessing: Plotting of a 3D pancreatic lesion ..	87
4.33	Applied binary mask onto <i>ADC</i> map	89
4.34	The original sequence	91
4.35	Ducts and vessels segmentation	95
4.36	Seed points in concentric circles	97
4.37	Pancreas delineation in 2D on 3 sample ROIs	104
5.1	Illustration of the <i>ADC</i> distribution and Gaussian fits	107
5.2	Theoretical histogram of <i>GTV</i>	109
5.3	Gauss clustering of first sample patient	111
5.4	Gauss clustering of second sample patient	112
5.5	Gauss clustering of third sample patient	113
5.6	Partial volume clustering of the first patient	115
5.7	Partial volume clustering of the second patient	116
5.8	Partial volume clustering of the third patient	118
5.9	Dotplots of the clustering results using conservative ROIs as a security margin	121

5.10	Qualitative evaluation of the intersection concerning the $rCBV$ study	123
5.11	The intra-individual reproducibility of f	124
5.12	3D overlappability per subject	125
5.13	Normalized signal decay in pancreatic tumour in two models showing regression	127
5.14	Normalized signal decay in pancreatic tumour showing Levenberg Marquardt fit in two models	128
5.15	Normalized signal decay in healthy pancreas showing regression in two models	130
5.16	Normalized signal decay in healthy pancreas showing Levenberg Marquardt fit in two models	131
5.17	Pancreatic lesion represented by the experimental values of the $IVIM$ model	132
5.18	ROC analysis concerning the experimental values of the $IVIM$ model.....	133

List of Tables

3.1	Grading of brain tumours	46
3.2	Grading of pancreatic cancer: TNM classification	48
3.3	Grading of pancreatic cancer (tumour)	49
3.4	Grading of pancreatic cancer (nodes)	49
3.5	Grading of pancreatic cancer (metastasis)	49
4.1	Siemens MR sequences	92
5.1	Overlap probability of applied registration approaches	126

References

- Ades, T. et al. (2010). Cancer Facts and Figures. *American Cancer Society*. [48](#)
- Asao, C., Y. Korogi, M. Kitajima, T. Hirai, Y. Baba, K. Makino, M. Kochi, S. Morishita, and Y. Yamashita (2005). Diffusion-Weighted Imaging of Radiation-Induced Brain Injury for Differentiation from Tumor Recurrence. *Am J Neuroradiol* 26, 1455–1460. [117](#)
- Basser, P. J. and C. Pierpaoli (1996). Microstructural and Physiological Features of Tissues Elucidated by Quantitative-Diffusion-Tensor MRI. *Journal of magnetic resonance* 111(3), 209–219. [20](#)
- Bishop, C. M. (2006). *Pattern Recognition and Machine Learning*. New York: Springer. [3](#), [28](#), [29](#), [30](#), [31](#), [32](#), [33](#), [34](#), [51](#), [97](#), [103](#), [136](#), [137](#), [139](#), [144](#)
- Bloch, F. (1946, July). Nuclear Induction. *Physical Review* 70(7), 361–371. [8](#)
- Bourquain, H., A. Schenk, F. Link, B. Preim, G. Prause, and H.-O. Peitgen (2002). HepaVision2: A software assistant for preoperative planning in living-related liver transplantation and oncologic liver surgery. *Computer Assisted Radiology and Surgery* (2002), 341–346. [27](#)
- Boyer, A. et al. (2000). Intensity-Modulated Radiotherapy: Current Status and Issues of Interest. *Int J Radiat Oncol Biol Phys*. 51(4), 880–914. [140](#)
- Brunberg et al. (1995, February). In Vivo MR Determination of Water Diffusion Coefficients and Diffusion Anisotropy: Correlation with Structural Alteration in Gliomas of the Cerebral Hemispheres. *American Society of Neuroradiology* 16(2), 361–71. [21](#)
- Carr, H. Y. and E. Purcell (1954, May). Effects of Diffusion on Free Precession in Nuclear Magnetic Resonance Experiments. *Physical Review* 94(3). [11](#), [12](#), [15](#), [16](#)
- Chenevert, T. L., L. D. Stegman, J. M. Taylor, P. L. Robertson, H. S. Greenberg, A. Rehemtulla, and B. D. Ross (2000, December). Diffusion magnetic resonance imaging: an early surrogate marker of therapeutic efficacy in brain tumors. *J Natl Cancer Inst* 92(24), 2029–2036. [1](#), [21](#), [47](#)

- Damadian, R. (1971). Tumor Detection by Nuclear Magnetic Resonance. *Science* 171(3976), 1151–1153. [6](#)
- Dempster, A., N. Laird, and D. Rubin (1977). Maximum likelihood from incomplete data via the EM algorithm. *Journal of the Royal Statistical Society* 11(4), 1–38. [3](#), [28](#), [51](#), [97](#), [144](#)
- Dice, L. (1945). Measure of the Amount of Ecologic Association Between Species. *Ecology* 26(3), 297–302. [35](#)
- Dickson, S., B. T. Thomas, and P. Goddard (1997). Using neural networks to automatically detect brain tumours in MR images. *Int J Neural Syst.* 8(1), 91–99. [137](#)
- Elpelt, B. and J. Hartung (1992). *Grundkurs Statistkik, Lehr- und Übungsbuch der angewandten Statistik*. Oldenbourg Verlag München Wien. [15](#), [34](#), [38](#), [41](#), [87](#), [88](#), [103](#), [105](#), [124](#)
- Fabijanska, A., M. Janaszewski, P. M., and L. Babout (2009). Airway Tree Segmentation from CT Scans Using Gradient-Guided 3D Region Growing. *Lecture Notes in Computer Science* 5856(2009), 247–254. [27](#)
- Falcão, A. and K. Jayaram (2000). A 3D generalization of user-steered live-wire segmentation. *Medical Image Analysis* (2000), 389–402. [27](#)
- Fallini, A. (2010). ESMRMB School of MRI, DWI and brain tumors. School of mri, ESMRMB, School of MRI 2010.
http://www.esmrb.org/index.php?id=/en/school_of_mri.htm.
[3](#), [21](#), [27](#)
- Fattahi, R., N. Balci, W. Perman, et al. (2009). Pancreatic diffusion-weighted imaging(DWI): comparison between mass-forming focal pancreatitis (FP), pancreatic cancer (PC), and normal pancreas. *J Magn Reson Imaging* 29(2), 350–356. [25](#)
- Fawcett, T. (2004). ROC Graphs: Notes and Practical Considerations for Researches. *Kluwer Academic Publishers*. [36](#), [37](#), [38](#)
- Fillard, P., V. Arsigny, X. Pennec, and N. Ayache (2007). Clinical DT-MRI estimation, smoothing, and fiber tracking with log-Euclidean metrics. *IEEE transactions on medical imaging* 26(11), 1472–1482. [138](#)
- Giesel, F., T. Wüstenberg, A. Bongers, M. Weber, C. Zechmann, K. Baudendistel, H. Tengg-Kobligk, H. Hahn, M. Essig, and H.-U. Kauczor (2005). MR-basierte Methoden der funktionellen Bildgebung des zentralen Nervensystems. *Medizin Physik und Technik* 177, 714–730. [3](#), [90](#)
- Goodlett, C., P. Fletcher, W. Lin, and G. Gerig (2007). Quantification of measurement error in DTI: theoretical predictions and validation. *Med Image Comput Assist Interv* 10(1), 10–7. [14](#)
- GoogleLabs (2011a). Brain. Bodybrowser, GoogleLabs.
<http://bodybrowser.googlelabs.com>. [45](#)

- GoogleLabs (2011b). Pancreas, renal artery, aorta, gallbladder. Bodybrowser, GoogleLabs.
<http://bodybrowser.googlelabs.com>. 47
- Graf, M. and O. Nix (2009). A comparison and evaluation of several algorithms as part of a template matching registration method. In O. Dössel and W. C. Schlegel (Eds.), *World Congress on Medical Physics and Biomedical Engineering, September 7 - 12, 2009, Munich, Germany*, Volume 25/IV of *IFMBE Proceedings*, pp. 688–691. Springer. 42
- Grünberg, K., L. Grenacher, and M. Klauß (2011, February). Diffusionsbildgebung des Pankreas. *Der Radiologe* 51(3). 1, 25, 48
- Haacke, E., S. Mittal, Z. Wu, J. Neelavalli, and Y.-C. Cheng (2009). Susceptibility-Weighted Imaging: Technical Aspects and Clinical Application, Part 1. *American Society of Neuroradiology* 30(1), 19–30. 6
- Haacke, E. M., R. W. Brown, and M. Thompson (1999). *Magnetic resonance imaging Physical Principles and Sequence Design*. New York: John Wiley and Sons. 8, 9, 11, 12, 13
- Haenelt, K. (2007). Ähnlichkeitsmaße für Vektoren. Vorlesungsskript, Universität Darmstadt.
http://kontext.fraunhofer.de/haenelt/kurs/folien/Haenelt_VektorAehnlichkeit.ppt. 35
- Hahn, E. L. (1950, May). Spin Echoes. *Physical Review* 80(4). 6, 10, 15, 16
- Handl, A. (2002). *Multivariate Verfahren Theorie und Praxis multivariater Verfahren unter besonderer Berücksichtigung von S-PLUS*. Springer. 38
- Hastie, T., R. Tibshirani, and J. Friedman (2009). *The Elements of Statistical Learning, Data Mining, Inference, and Prediction*. New York: Springer. 3, 28, 29, 51, 97, 103, 144
- Hendee, W. and C. Morgan (1984). Magnetic resonance imaging. Part I – Physical principles. *Medical Progress* 141, 491–500. 5, 6
- Higano, S., X. Yun, T. Kumabe, M. Watanabe, S. Mugikura, A. Umetsu, A. Satol, Y. Takayuki, and S. Takahashi (2006). Malignant Astrocytic Tumors: Clinical Importance of Apparent Diffusion Coefficient in Prediction of Grade and Prognosis. *Radiology* 241(3), 839–846. 1, 26, 47, 117, 136
- Hongmin, C., R. Verma, Y. Ou, S. Lee, R. Melhem, and C. Davatzikos (2007). Cascaded segmentation of brain tumors using multi-modality MR profiles. In *Proceedings of the Joint Annual Meeting of the International Society of Magnetic Resonance in Medicine-ESMRMB*, Berlin, Germany. 27, 35, 136
- Hornak, J. P. (2011). The Basics of MRI. Online book, Rochester Institute of Technology.
<http://www.cis.rit.edu/htbooks/mri/index.html>. 6

- Jaccard, P. (1912). The distribution of flora in the alpine zone. *11*(2), 37–50. [35](#), [101](#)
- Jones, D. K. (2010a). ESMRMB School of MRI, DTI: Data Analysis. School of mri, ESMRMB, School of MRI 2010.
http://www.esmrb.org/index.php?id=/en/school_of_mri.htm. [2](#)
- Jones, D. K. (2010b). ESMRMB School of MRI, DTI Technique, Application. School of mri, ESMRMB, School of MRI 2010.
http://www.esmrb.org/index.php?id=/en/school_of_mri.htm. [15](#), [20](#)
- Kaus, M., S. K. Warfield, F. A. Jolesz, and R. Kikinis (1999). Adaptive Template Moderated Brain Tumor Segmentation in MRI. In *Email: x6wang@cs.ucsd.edu; Phone: 858 822 3739; Fax: 858 534 0177; ** Email: pphick@ucsd.edu; Phone: 858 534 8965; Fax: 858 534 0177; *** Email: bvjackson@ucsd.edu; Phone: 858 534 3358; Fax: 858 534 2294; **** Email: mbailey@sdsc.edu; Phone: 858 534 5142;*, pp. 102–105. Springer. [27](#)
- Kerekes, J. (2008). Receiver Operating Characteristic Curve Confidence Intervals and Regions. *IEEE Geoscience and remote sensing letters* *5*(2), 1–3–8. [36](#)
- Kindermann, R. and L. Snell (2000). *Markov Random Fields and Their Applications*. American Mathematical Society. [32](#)
- Kono, K., Y. Inoue, K. Nakayama, M. Shakudo, M. Morino, K. Ohata, K. Wakasa, and R. Yamada (2001). Microstructural and Physiological Features of Tissues Elucidated by Quantitative-Diffusion-Tensor MRI. *Am J Neuroradiology* *22*(6), 1081–1088. [21](#)
- Konukoglu, E., O. Clatz, B. H. Menze, M. Weber, B. Stieltjes, E. Mandonnet, H. Delingette, and N. Ayache (2010, January). Image Guided Personalization of Reaction-Diffusion Type Tumor Growth Models Using Modified Anisotropic Eikonal Equations. *IEEE Transactions On Medical Imaging* *29*(1), 77–95. [140](#)
- Krebs, C., K. Hüttmann, and C. Steinhäuser (2004). Ende einer Zweiklassengesellschaft. *Gehirn und Geist* *4*, 38–41. [44](#)
- Laun, F., K. Fritzsche, T. Kuder, and B. Stieltjes (2011). Einführung in die Grundlagen und Techniken der Diffusionsbildgebung. *Der Radiologe* *51*(3), 839–846. [15](#)
- Le Bihan, D. (2003). Looking into the functional architecture of the brain with diffusion mri. *Nature Reviews Neuroscience* *4*, 469–480. [17](#)
- Le Bihan, D. et al. (1988, August). Separation of diffusion and perfusion in intravoxel incoherent motion MR imaging. *Radiology* *168*(2), 497–505. [1](#), [6](#), [22](#), [23](#), [24](#), [95](#)

- Le Bihan, D. et al. (2008, December). Intravoxel incoherent motion perfusion MR imaging: a wake-up call. *Radiology* 249(3), 748–752. [1](#), [6](#), [17](#), [22](#), [24](#), [95](#)
- Lee, C., M. Schmidt, A. Murtha, A. Bistriz, J. Sander, and R. Greiner (2005). Segmenting Brain Tumors with Conditional Random Fields and Support Vector Machines. *Lecture Notes in Computer Science* 3765(2005), 469–478. [136](#), [138](#)
- Lee, N. et al. (2009a). Bayesian Transduction and Markov Conditional Mixtures for Spatiotemporal Interactive Segmentation. [139](#)
- Lee, N. et al. (2009b). Bayesian Transductive Markov Random Fields for Interactive Segmentation in Retinal Disorders. In O. Dössel and W. C. Schlegel (Eds.), *World Congress on Medical Physics and Biomedical Engineering, September 7 - 12, 2009, Munich, Germany*, Volume 25/IV of *IFMBE Proceedings*, pp. 227–230. Springer. [139](#)
- Lemke, A., B. Stieltjes, L. Schad, and F. Laun (2011, July). Towards an optimal distribution of b values for intravoxel incoherent motion imaging. *Magnetic Resonance Imaging* 19(6), 766–776. [22](#), [23](#), [142](#), [143](#), [145](#)
- Lettau, M., M. Laible, R. Barrows, S. Heiland, M. Bendszus, and S. Hähnel (2011). 3-T contrast-enhanced MR angiography with parallel imaging in cerebral venous and sinus thrombosis. *Journal of Neuroradiology* 11(4), 1–38. [5](#)
- Li, S. Z. et al. (1995). *Markov Random Fields, Modeling in Computer Vision*. Springer. [30](#), [32](#), [139](#)
- Ling, C., J. Humm, S. Larson, A. H., Z. Fuks, S. Leibel, and J. Koutcher (2000). Towards multidimensional radiotherapy (MD-CRT): biological imaging and biological conformality. *Int J Radiat Oncol Biol Phys.* 47(3), 547–548. [140](#)
- Louis, D., H. Ohgaki, O. Wiestler, W. K. Cavenee, P. Burger, A. Jouvet, B. W. Scheithauer, and P. Kleihues (2007, July). The 2007 WHO Classification of Tumours of the Central Nervous System. *Acta Neuropathol* 114, 97–109. [46](#)
- Luciani, A., A. Vignaud, M. Cavet, J. Tran Van Nhieu, A. Mallat, L. Ruel, A. Laurent, J.-F. Deux, P. Brugieres, and A. Rahmouni (2008). Liver Cirrhosis: Intravoxel Incoherent Motion MR Imaging - Pilot Study. *Radiology* 249(3), 891–899. [22](#), [23](#), [24](#), [95](#)
- Maes, F., A. Collignon, D. Vandermeulen, G. Marchal, and P. Suetens (1997). Multimodality image registration by maximization of mutual information. *IEEE transactions on medical imaging* 16(2). [43](#), [102](#), [144](#)
- Maintz, A. and M. Viergever (1997). A Survey of Medical Image Registration. *Medical Image Analysis* 2(1), 1–36. [39](#), [40](#), [41](#), [42](#)
- Mansfield, P. and A. A. Maudsley (2011). Medical imaging by NMR. *British Journal of Radiology* 50, 188–194. [6](#), [11](#)
- Marquardt, D. (1963). An algorithm for least-squares estimation of nonlinear parameters. *Journal of the Society for Industrial and Applied Mathematics* 11(2), 431–441. [103](#)

- Menze, B., K. van Leemput, D. Lashkari, M. Weber, N. Ayache, and P. Golland (2010). A Generative Model for Brain Tumor Segmentation in MultiModal images. *Med Image Comput Assist Interv* 13(2), 151–159. [28](#)
- Moffat, B. A., T. L. Chenevert, T. S. Lawrence, C. R. Meyer, T. D. Johnson, Q. Dong, C. Tsien, S. Mukherji, D. J. Quint, S. S. Gebarski, P. L. Robertson, L. R. Junck, A. Rehemtulla, and B. D. Ross (2005). Functional diffusion map: A noninvasive MRI biomarker for early stratification of clinical brain tumor response. *PNAS* 102(15), 5524–5529. [26](#)
- Moffat, B. A., D. E. Hall, J. Stojanovska, P. J. McConville, J. B. Moody, T. L. Chenevert, A. Rehemtulla, and B. D. Ross (2004). Diffusion imaging for evaluation of tumor therapies in preclinical animal models. *Magnetic Resonance Materials in Physics, Biology and Medicine* 17(3), 249–259. [1](#), [2](#), [21](#), [47](#)
- Mori, S. (2007). *Introduction to Diffusion Tensor Imaging*. Radarweg 29, PO Box 211, 1000 AE Amsterdam, The Netherlands: Elsevier. [1](#), [15](#), [17](#), [18](#), [19](#)
- Mori, S. and P. B. Barker (1999). Diffusion Magnetic Resonance Imaging: Its Principle and Applications. *The anatomical record (new anat.)* 257(3), 102–109. [1](#), [5](#), [6](#), [7](#), [15](#), [18](#)
- Noe, A. G. and C. Gee. (2001). Partial Volume Segmentation of Cerebral MRI Scans with Mixture Model Clustering. *Proceedings of the 17th International Conference on Information Processing in Medical Imaging*. [3](#), [14](#), [28](#), [35](#), [96](#), [99](#), [100](#), [114](#), [117](#)
- Perez, P. et al. (1998). Markov Random Fields and Images. *CWI Quarterly* 11(4), 413–437. [30](#), [139](#)
- Platt, J. C. (1999). Probabilistic Outputs for Support Vector Machines and Comparisons to Regularized Likelihood Methods. *Advances in Large Margin Classifiers*. [137](#)
- Pluim, J., A. Maintz, and M. Viergever (2003, July). Mutual information based registration of medical images: a survey. *IEEE transactions on medical imaging* 22(8), 986–1003. [43](#)
- Prastawa, M., E. Bullitt, S. Ho, and G. Gerig (2004, September). A brain tumour segmentation framework based on outlier detection. *Medical Image Analysis* 8, 275–283. [28](#)
- Prastawa, M., E. Bullitt, N. Moon, K. van Leemput, and G. Gerig (2003). Automatic Brain Tumour Segmentation by Subject Specific Modification of Atlas Priors. *Academic Radiology* 10, 1341–1348. [28](#), [43](#), [46](#), [138](#)
- Price, S., R. Jena, N. Burnet, P. Hutchinson, A. Dean, A. Pena, J. Pickard, T. Carpenter, and J. Gillard (2001). Improved Delineation of Glioma Margins and Regions of Infiltration with the Use of Diffusion Tensor Imaging: An Image-Guided Biopsy Study. *Am J Neuroradiology* 22(6), 1969–1974. [21](#)

- Rabi, I. I., S. Millman, P. Kusch, and J. Zacharias (1939). The Molecular Beam Resonance Method for Measuring Nuclear Magnetic Moments. *Physical Review* 22(6), 1969–1974. 6
- Raffin, L. S., L. A. Bacheschi, L. R. Machado, J. P. S. Nóbrega, C. C. Coelho, and C. Leite (2001). DIFFUSION-WEIGHTED MR IMAGING OF CYSTIC LESIONS OF NEUROCYSTICERCOSIS, a preliminary study. *Arq Neuropsiquiatr* 59(4), 839–846. 117
- Rana, A. and J. Wardlaw (2003). Apparent diffusion coefficient (ADC) measurements may be more reliable and reproducible than lesion volume on diffusion-weighted images from patients with acute ischaemic stroke-implications for study design. *Magnetic Resonance Imaging* 21(6), 617–624. 26
- Riches, S. et al. (2007). Diffusion Weighted Imaging of Androgen Deprivation Hormone Therapy for Prostate Cancer. In *Proceedings of the Joint Annual Meeting of the International Society of Magnetic Resonance in Medicine-ESMRMB*, Berlin, Germany. 1
- Riches, S., K. Hawtin, E. Charles-Edwards, and N. de Souza (2009). Diffusion-weighted imaging of the prostate and rectal wall: comparison of biexponential and monoexponential modelled diffusion and associated perfusion coefficients. *NMR Biomed* 22(3), 318–325. 23
- Riklin-Raviv, T., K. van Leemput, B. Menze, W. Wells III, and P. Golland (2010). Segmentation of image ensembles via latent atlases. *Medical Image Analysis* 14, 654–665. 28
- Sadeghi, N., C. D. D’Haene, M. Levivier, T. Metens, C. Maris, D. Wikler, D. Baleriaux, I. Salmon, and S. Goldman (2004). Apparent Diffusion Coefficient and Cerebral Blood Volume in Brain Gliomas: Relation to Tumor Cell Density and Tumor Microvessel Density Based on Stereotactic Biopsies. *American Journal of Neuroradiology* 29(3), 476–482. 26, 136
- Schlüter et al. (2005, September). Detection of Tumor Infiltration in Axonal Fiber Bundles Using Diffusion Tensor Imaging. *Int J Med Robot* 1(3), 80–86. 28, 33, 35
- Schnabel, J. and D. Rueckert (2009). Medical Image Registration. Lipari lecture, Lipari School on Computer Science.
<http://lipari.dipmat.unict.it/LipariSchool/CS>. 39, 40, 41, 44, 145
- Stadlbauer, A., C. Nimsky, S. Gruber, E. Moser, T. Hammen, T. Engelhorn, M. Buchfelder, and O. Ganslandt (2007, March). Diffusion-weighted MR Imaging of Intracerebral Masses: Comparison with Conventional MR Imaging and Histologic Findings. *American Journal of Neuroradiology* 28(3), 462–469. 21

- Stadnik et al. (2001, May). Diffusion-weighted MR Imaging of Intracerebral Masses: Comparison with Conventional MR Imaging and Histologic Findings. *AJNR* 22(5), 969–976. [2](#), [21](#)
- Stejskal, E. O. and J. E. Tanner (1965). Spin Diffusion Measurements: Spin Echoes in the Presence of a Time-Dependent Field Gradient. *The journal of chemical physics* 42(1), 288–292. [15](#), [16](#)
- Stieltjes, B., W. Kaufmann, P. van Zijl, K. Fredericksen, G. Pearlson, M. Solaiyappan, and S. Mori (2001). Diffusion tensor imaging and axonal tracking in the human brainstem. *NeuroImage* 14(3), 723–35. [24](#)
- Stieltjes, B., M. Schlüter, B. Diding, M.-A. Weber, H.-K. Hahn, P. Parzer, J. Rexilius, O. Konrad, H.-O. Peitgen, and M. Essig (2006). Diffusion tensor imaging in primary brain tumors: Reproducible quantitative analysis of corpus callosum infiltration and contralateral involvement using a probabilistic mixture model. *NeuroImage* 31(2), 531–542. [28](#), [33](#), [35](#), [44](#), [56](#), [99](#)
- Synowitz, M. (2008). Der Feind im Inneren. *Gehirn und Geist* 9, 56–59. [44](#), [46](#)
- Tien, R. D. et al. (1994, March). MR Imaging of High-Grade Cerebral Gliomas: Value of Diffusion-Weighted Echoplanar Pulse Sequences. *American Roentgen Ray Society* 162(3), 671–677. [21](#)
- Tofts, P. (2003). *Quantitative MRI of the Brain, Measuring changes caused by disease*. The Atrium, Southern Gate, Chichester, West Sussex PO19 5SQ, England: John Wiley and Sons Ltd. [1](#), [3](#), [5](#), [6](#), [7](#), [8](#), [11](#), [14](#), [15](#), [16](#), [17](#), [19](#), [20](#), [38](#), [148](#)
- van Leemput, K. (2001). Quantitative Analysis of Signal Abnormalities in MR Imaging for Multiple Sclerosis and Creutzfeldt-Jakob Disease. [3](#), [28](#), [30](#), [31](#), [32](#), [33](#), [35](#), [138](#), [139](#)
- van Leemput, K. et al. (1999, October). Automated Model-Based Tissue Classification of MR Images of the brain. *IEEE Transactions On Medical Imaging* 18(10), 897–908. [3](#), [30](#), [33](#), [139](#)
- Vincent, A., J. Herman, R. Schulick, H. R. Hruban, and M. Goggins (2011, May). Seminar Pancreatic cancer. *The lancet*. [48](#), [49](#)
- Viola, P. and V. Wells III (1997, April). Alignment by maximization of mutual information. *International Journal of Computer Vision* 24, 137–154. [39](#), [43](#), [102](#), [144](#)
- Woetzel, J., C. Thieke, M. Monz, K. Parodi, T. Twellmann, H.-O. Peitgen, K.-H. Küfer, W. Schlegel, and H.-P. Schlemmer (2010). Softwareplattform für die multimodale Diagnostik onkologischer Erkrankungen und Therapieoptimierung durch molekulare Bildgebung (DOT-MOBI). In *Tagungsband MediWING*. [92](#), [147](#)
- Zhang, J., E. Sigmund, H. Rusinek, H. Chandarana, Q. Chen, P. Storey, et al. (2009). Diffusion-weighted imaging of the prostate and rectal wall: compar-

- son of biexponential and monoexponential modelled diffusion and associated perfusion coefficients. *NMR Biomed* 22(3), 318–325. [23](#)
- Zhang, J. M., H. E. Kai-Kuang, and E. Meng (2005). Tumour segmentation from magnetic resonance imaging by learning via one-class support vector machine. *Conf Proc IEEE Eng Med Biol Soc.* 27, 136
- Zitová, B. and J. Flusser (2003). Image registration methods: a survey. *Image and Vision Computing* 21, 977–1000. [39](#)

Own cited Contributions

- Graf, M., D. Simon, A. Lemke, T. Re, F. Laun, and B. Stieltjes (2010). Evaluation of the value of registration on the reproducibility of Intra Voxel Incoherent Motion Imaging derived parameters. In N. Hodapp, J. Hennig, and M. Mix (Eds.), *Proceedings of the 41th annual meeting of the Deutsche Gesellschaft für medizinische Physik*, Freiburg, Germany.
- Grünberg, K., D. Simon, A. Lemke, T. Re, F. Laun, and B. Stieltjes (2011, March). Preliminary Results on the Influence of combined Chemoradiation on MR-Diffusion-weighted Imaging Parameters in Primary inoperable pancreatic carcinomas. In *Proceedings of the 23th annual meeting of the European Congress of Radiology*, Vienna, Austria.
- Hauser, T., M. Essig, F. Laun, M. Münter, A. Jenser, D. Simon, L. Gerigk, and B. Stieltjes (2011). Characterization and therapy monitoring of head and neck carcinomas using intravoxel incoherent motion parameters - initial results. In *Proceedings of the 97th annual meeting of the Radiological Society of North America*, Chicago, USA.
- Hillengass, J., T. Bäuerle, R. Bartl, M. Andrulis, F. McClanahan, F. Laun, C. Zechmann, R. Shah, B. Wagner-Gund, D. Simon, C. Heiss, K. Neben, A. Ho, H. Schlemmer, H. Goldschmidt, S. Delorme, and B. Stieltjes (2011, June). Diffusion-weighted imaging for non-invasive and quantitative monitoring of bone marrow infiltration in patients with monoclonal plasma cell disease: a comparative study with histology. *Br J Haematol* 153(6), 721–728.
- Klauss, M., M. Gaida, A. Lemke, K. Grünberg, D. Simon, S. Delorme, H. Kauczor, L. Grenacher, and B. Stieltjes (2011). Histopathological correlation of IVIM-derived true diffusion constant in patients with pancreatic carcinoma and chronic pancreatitis. In *Proceedings of the 19th annual meeting of the International Society for Magnetic Resonance Imaging*, Montreal, Canada.
- Klauss, M., A. Lemke, D. Simon, T. Re, M. N. Wente, F. B. Laun, H.-U. Kauczor, S. Delorme, L. Grenacher, and B. Stieltjes (2011, January). Intravoxel Incoher-

- ent Motion Imaging for the Differentiation between Mass Forming Pancreatitis and Pancreatic Carcinoma. *Investigative Radiology* 46(1), 57–63.
- Koyama, H., C. Hintze, J. Dinkel, M. Puderbach, M. Eichinger, C. Heußel, J. Biederer, H. Kauczor, D. Simon, and B. Stieltjes (2011). Diffusion Coefficients in Lung Abnormal Lesions: Evaluation with Intravoxel Incoherent Motion by Echo-planar MR Imaging. In *Proceedings of the 97th annual meeting of the Radiological Society of North America, Chicago, USA*.
- Lemke, A., F. Laun, D. Simon, B. Stieltjes, and L. Schad (2010, July). An in vivo verification of the intravoxel incoherent motion effect in diffusion-weighted imaging of the abdomen. *Magnetic Resonance in Medicine* 64(6), 1580–1585.
- Lemke, A., F. B. Laun, M. Klaus, T. Re, D. Simon, S. Delorme, L. R. Schad, and B. Stieltjes (2009, March). Differentiation of Pancreas Carcinoma From Healthy Pancreatic Tissue Using Multiple b-Values: comparison of apparent diffusion coefficient and intravoxel incoherent motion derived parameters. *Investigative Radiology* 44(12), 769–775.
- Radbruch, A., K. Lutz, D. Simon, B. Wiestler, P. Bäumer, B. Stieltjes, M. Graf, R. Floca, C. Hartmann, W. Wick, H.-P. Schlemmer, M. Bendszus, and S. Heiland (2011). Comparison of ADC Diffusion Maps and CBV Perfusion Maps in Patients with Newly Diagnosed Glioblastoma: Establishing Order in Heterogeneity. In *Proceedings of the 49th annual meeting of the American Society of Neuroradiology, Seattle, USA*.
- Re, T. J., M. Klaus, A. Lemke, F. Laun, D. Simon, S. Delorme, and B. Stieltjes (2009). Intravoxel Incoherent Motion (IVIM) f-maps of Pancreatic Lesions. *Siemens Magnetom Flash Magazine* 2, 26–32.
- Re, T. J., A. Lemke, M. Klaus, F. Laun, D. Simon, K. Grünberg, S. Delorme, L. Grenacher, R. Manfredi, R. Pozzi Mucelli, and B. Stieltjes (2011). Enhancing Pancreatic Adenocarcinoma Delineation in Diffusion Derived Intravoxel Incoherent Motion f-Maps Through Automatic Vessel and Duct Segmentation. *Magnetic Resonance in Medicine*. Epub ahead of print.
- Simon, D. et al. (2009). A Software Tool to Automatically Evaluate and Quantify Diffusion Weighted Images. In O. Dössel and W. C. Schlegel (Eds.), *World Congress on Medical Physics and Biomedical Engineering, September 7 - 12, 2009, Munich, Germany, Volume 25/IV of IFMBE Proceedings*, pp. 1194–1197. Springer.
- Simon, D., K.-H. Fritzsche, C. Thieke, J. Klein, P. Parzer, M.-A. Weber, and B. Stieltjes (2011, August). Diffusion weighted imaging based probabilistic segmentation of high and low proliferative areas in gliomas. *Cancer Imaging*. planned.
- Simon, D., J. Klein, J. Rexilius, and B. Stieltjes (2009). Objective tumour heterogeneity determination in gliomas. Volume 7260, pp. 72601X. SPIE. 89

A

Appendix

Listing A.1: *The partial volume class*

```
1
2  double DWIGaussApproximation::mixMean(const double mu1,
3  const double mu2, const double rho)
4  {
5      return (1.0 - rho) * mu1 + rho * mu2;
6  } // mixing the mu
7
8  double DWIGaussApproximation::mixVariance(const double covariance1,
9  const double covariance2, const double rho)
10 {
11     return (1.0 - rho) * (1.0 - rho) * covariance1 + rho * rho * covariance2;
12 } // always take the covariance or variance (mixing the covariance)
13
14
15 double DWIGaussApproximation::foldedMixtureClass(const double x,
16 const double p1, const double mu1,
17 const double mu2, const double covariance1, const double covariance2)
18 {
19     double dProbVal=0.0;
20     double mixed_mean=mu1;
21     double mixed_variance=covariance1;
22     double left=0.0; // the integral is defined by 0 to 1
23     double right=1.0; // compute new width
24     double width = right - left; // the width of the integral, in this case 1
25     int numberOfGridPoints=this->numberOfGridPoints->getIntValue();
26     double deltaRho = width / (double) (numberOfGridPoints-1);
27     double rho = left; // number of gridpoints
28     double segmentArea=0.0; // sum of individual trapezoids
29     double fXiMinusOne=0.0;
30     double fXi=0.0;
31     double xiMinusOne = 0.0;
32     double xi=0.0;
33     if (_myAllVolumeSwitch->getIntValue() != 0)
34         // All Volume switch has been turned on (Adding the first Gaussian)
35         dProbVal=this->gaussianFunction(x, mu1, covariance1);
36         //rho is zero, using the first mu
37     for (int k=0; k < numberOfGridPoints-2; k++) // gridpoints
38     { // using the trapezoid rule:
39         xiMinusOne=rho;
40         fXiMinusOne=this->gaussianFunction(x, mixed_mean, mixed_variance);
41         rho+=deltaRho;
```

```

42     mixed_mean=this->mixMean(mu1, mu2, rho); //mixing mu with appropriate rho
43     mixed_variance=this->mixVariance(covariance1, covariance2, rho);
44     //mixing covariance with appropriate rho
45     fXi=this->gaussianFunction(x, mixed_mean, mixed_variance);
46     xi=rho;
47     segmentArea= (xi-xiMinusOne)*(fXiMinusOne+fXi);
48     segmentArea *=0.5;
49     dProbVal+= segmentArea;
50 }
51 if (_myAllVolumeSwitch->getIntValue() !=0)
52 // All Volume switch has been turned on (Adding the second Gaussian)
53     dProbVal+=this->gaussianFunction(x, mu2, covariance2);
54     dProbVal*=p1;
55     return dProbVal; //perform multiplication with pi_1
56 }
57
58 double DWIGaussApproximation::gaussianFunction(const double x,
59 const double p1, const double p2, const double p3) // a Gaussian (root style)
60 {
61     return p1*TMath::Exp(-0.5*TMath::Power(((x-p2)/TMath::Sqrt(p3)),2));
62 }
63
64 double DWIGaussApproximation::gaussianFunction(const double x,
65 const double mu, const double covariance)
66 {
67     return ((1/TMath::Sqrt(2*ML_M_PI))*(1/TMath::Sqrt(covariance))*
68     TMath::Exp(-0.5*TMath::Power(((x-mu)/TMath::Sqrt(covariance)),2)));
69     // a Gaussian (generic style)
70 }

```

Curriculum Vitae

Personalien:

Name: Dirk Simon
Geburtsdatum: 17.01.1978
Geburtsort: Trier
Nationalität: Deutsch

Promotion:

seit 07 / 2008 Doktorat im Bereich der diffusionsgewichteten
Magnetresonanztomographie
Deutsches Krebsforschungszentrum (DKFZ)
Prof. Dr. Sabine Heiland
Neuroradiologie
Universität Heidelberg

Studium:

04 / 2004 - 06 / 2006 Studium Master of Science
Fachhochschule Trier
Abschluss: Master of Science
10 / 1999 - 10 / 2003 Studium der Angewandten Informatik
Fachhochschule Trier
Abschluss: Diplom Informatiker (FH)

Praxis und Weiterbildung:

01 / 2007 - 06 / 2008 Wissenschaftlicher Mitarbeiter
Deutsches Krebsforschungszentrum (DKFZ)
10 / 2005 - present Adept Technologies Inc. (former: MobileRobots Inc.):
ArAKin-Arm Kinematics
11 / 2004 - 12 / 2006 Assistent im Fachbereich Informatik
Fachhochschule Trier
10 / 2001 - 11 / 2004 Wissenschaftlicher Mitarbeiter
Agfa Healthcare (former: GWI Research GmbH)

Schulbildung:

08 / 1988 - 07 / 1998 Max-Planck Gymnasium
Trier
Abschluss: Abitur

Acknowledgements

This work is strongly interdisciplinary based and has been pursued within different groups, namely the Software Development for Integrated Diagnostics and Therapy (SIDT), supervised by Dr. Ralf Floca (former supervisor Dr. Oliver Nix and headed by Prof. Wolfgang Schlegel), the section for quantitative imaging-based disease characterization (headed by Dr. Bram Stieltjes), the radiology department, supervised by Prof. Heinz-Peter Schlemmer (co-supervised by Prof. Stefan Delorme, former supervisor: Prof. Hans-Ulrich Kauczor) and finally the group of experimental neuroradiology located in the head clinic, supervised by Prof. Sabine Heiland. An additional circle, where this work took place, is the Integrated Diagnostics and Therapeutic Center (IDTC) and the Dot Mobi cooperation headed by Dr. Dr. Christian Thieke as the project leader at the German Cancer Research Center.

Fore and foremost, I wish to thank the supervisors, co-supervisors and former supervisors of these groups, in particular Prof. Sabine Heiland for supervising this thesis, Prof. Hans-Ulrich Kauczor for being at the German Cancer Research Center, and all of the members of the groups. Second, I wish to particularly thank Dr. Bram Stieltjes in the section of quantitative imaging-based disease characterization for a strong support and for the feeling to be part of an interdisciplinary research team. Furthermore, in particular, I wish to thank Dr. Thomas Re for a lot of support, insights, Italian receipts and cooperative work during my PhD. Likewise, Markus Graf, residing in the SIDT group, for a cooperative work within the years of my PhD. Moreover, thanks to the physicists Dr. Andreas Lemke and Dr. Frederik Laun to gain insight into the interdisciplinary world of medical physics. Additional special thanks go to the MeVis group (Fraunhofer, MEVIS, Bremen) for development support, in particular the core development team: Marcus Barann, Dr. Tobias Boskamp, Gereon Frey, Olaf Konrad, Florian Link, Stephan Palmer, Uwe Siems and Wolf Spindler. Within the MeVis research group, I would especially like to thank Dr. Jan Klein for diffusion weighted imaging related tasks from a computer scientist's point of

view, as well as Dörte van Straaten for general support concerning the MeVis-Lab development environment. Moreover, thanks go to Dr. Klaus Fritzsche for computer science related questions. In terms of topics related to machine learning, I would greatly thank Dr. Michael Kelm and Dr. Frederik Kaster. For nice philosophical talks and for being a nice room-mate, I would further like to thank Stephan Kassemeyer. Kind regards go to all of the physicians and doctoral students who used my developed software research prototype, notably Dr. Katharina Grünberg, for a good interdisciplinary team work and for proofreading the medical part of pancreatic diseases. Furthermore, thanks to Alexander Radbruch for cooperative work in a subrelated project to this thesis.

Last but not least, I would like to thank my parents for their mental support. Thanks!